Advancements of Micro Gas Chromatographs and Their Core Components

by

Maxwell Li

A dissertation submitted in partial fulfillment
of the requirements for the degree of
Doctor of Philosophy
(Electrical and Computer Engineering)
in the University of Michigan
2021

Doctoral Committee:

Professor Xudong Fan, Co-Chair
Professor L. Jay Guo, Co-Chair
Professor Yogesh Gianchandani
Professor Katsuo Kurabayashi

Maxwell Li

maxli@umich.edu

ORCID iD: 0000-0002-6714-4143

Acknowledgements

I would like to acknowledge my advisor, Professor Xudong Fan, whom I have worked alongside for these past few years. He has provided me with many opportunities as well as given me a wealth of advice, both professional and personal, for which I am very grateful.

I would also like to thank my coadvisor, Professor Jay Guo, who has helped me a great deal in navigating the difficult details of my degree and in exploring different fields of study throughout my studies.

I wish to extend my gratitude to Professor Katsuo Kurabayashi, who has provided support on the development of key components of my research throughout my studies, and with whom I have collaborated on several projects as well.

I also wish to thank Professor Yogesh Gianchandani for discussions during useful courses and about critical sensing components in my research, which has helped me better understand and advance my research.

A special thanks to Dr. Hongbo Zhu, who mentored me during my first couple years in Professor Fan's group and helped guide me through the transition from student to researcher. I also appreciate the help from my lab coworkers, including Dr. Abhishek Ghosh, Dr. Ruchi Sharma, Dr. Menglian Zhou, Dr. Xiaolu Huang, and Dr. Jinyan She for collaborations on various system-level projects. I would like to acknowledge Ziqi Li for experimental help during my various projects, and Dr. Xiaotian Tan and Xuzhou Li for lab support as well as many useful discussions about my research. An additional thanks to Dr. Wenzhe Zang, Dr. Anandram Venkatasubramanian, and Xiaheng Huang for recent collaborations on challenging systems projects. I've had a wonderful time working in Professor Fan's lab and have learned a great deal throughout my entire time here.

I would like to thank the tool engineers at the Lurie Nanofabrication Facility, especially Kevin Owen, Shawn Wright, Katherine Beach, Vishva Ray, Caroline Patel, and Sandrine Martin for their hard work in training me and helping me accomplish and develop the challenging microfabrication procedures for my Ph.D.

A great thanks to the Michigan Center for Wireless Integrated MicroSensing & Systems center and the University of Michigan Electrical Engineering and Computer Science department for providing me financial support for my Ph.D.

Finally, I greatly appreciate the support of my family, especially my parents, throughout the entirety of my doctoral studies. I could not have accomplished my degree without their encouragement and advice and am very grateful to have had them by my side this whole time.

Table of Contents

List of Tables

List of Figures

List of Appendices

Abstract

The development of portable vapor sensors is of high interest for *in situ* and real-time chemical analysis. These sensors are targeted at industrial and environmental monitoring as well as point-of-care applications. Advances in microelectromechanical systems (MEMS) technologies has allowed for the miniaturization of benchtop gas chromatography (GC) into portable micro GC (μGC) systems that allow for field analysis. This dissertation details the development of critical μGC components, especially microcolumns and micro photoionization detectors (PIDs), along with their assembly into prototype μGC systems for *in situ* testing. Two different microcolumn coatings were developed to broaden the range of chemical separations suitable for μGC analysis, including a micro porous layer open tubular column for light compound analysis and micro ionic liquid column for simultaneous analysis of polar and nonpolar compounds. A new column coating method was also demonstrated to improve separation performance without the need for increasing column length or any auxiliary components. A micro helium desorption PID (μHDPID) fabrication process was developed to allow for the robust fabrication of universal vapor detectors, complementing the increased range of separations from the new microcolumn coatings. A high sensitivity PID system was also developed with sub-pg detection limits, comparable to or even surpassing that of benchtop flame ionization detectors. These components were assembled into two prototype systems, one for hydrogen and methane detection for breath analysis, and another ultracompact μGC system with the entire system capable of being contained within a 1.1 L box, including batteries, pumps, and electronic readout boards. Together, these developments are aimed at increasing the range of applications that can be targeted by μGC by broadening its separation and detection capabilities, as well as improving the sensing performance.

Chapter 1 Introduction

1.1 Background

Conventional analysis of vapor samples is commonly performed using gas chromatography (GC), which is a physical separation method used for environmental, clinical, and pharmaceutical analysis of compounds that can be vaporized around or below ~350 °C. Traditional benchtop GC analyzes the content of chemical mixtures by separating their components, which can be useful for chemical synthesis, monitoring of toxic compounds, and food testing. GC is also a powerful method for testing of breath and forensic samples due to capability for separation of hundreds of compounds at once. GC systems are equipped with long separation columns often of 30 or 60 m in length and typically use carrier gases of helium, nitrogen, or hydrogen to pass chemical mixtures through the columns, whereupon each individual component in the mixture is separated and detected at the output[1]. While these instruments provide powerful separation capabilities, their large weight (~200 kg) and size (>10s of L), high power (>2000 W), long analysis times (>30 min), and high cost (>$20000 secondhanded) limits their general use outside of controlled laboratory environments. Increasing interest has been directed toward the development of portable vapor sensing systems for rapid *in situ* analysis, which enables on-site and real-time monitoring. This is indispensable for applications such as point-of-care vapor analysis using human breath, or for industrial monitoring in construction sites, or petroleum pipeline detection of volatile hydrocarbons, or even for environmental monitoring of greenhouse and noxious gases[2-82]. Common to these are the need for high robustness and portability, which alleviate the requirement for extensive sample preparation and long lead times for laboratory analysis.

To date, research on portable vapor sensors has taken many diverse directions, including optical fiber and fluorescence[83-90], metal oxide/sulfide chemiresistive and organic[19,86,90-99], conductive polymer[100], surface acoustic wave[101,102], graphene and nanostructure[91,92,96,103-107

sensors, electronic noses[88,99,101,108-111] and other various sensor arrays[19,83,86,88,89,102,111-115], and ion mobility spectrometry[82,116]. While optical fiber and fluorescence based sensors detect changes in optical emission spectra when an analyte is adsorbed on a surface or absorbs light passing through it[83-90], metal oxide/sulfide chemiresistors, organometallics, conductive polymers, graphene and nanostructures, and surface acoustic wave resonators rely on surface adsorption, reactivity, or other interactions with chemical analytes in order to induce a physically detectable signal, such as a current, change in mass, resistance, or acoustic frequency shift[86,90,92-95,99-101,103,117]. In contrast, ion mobility spectrometers (IMS) rely on ion mobility in a specific carrier gas to separate (either in space or time) and thus identify ionized molecules[82,116]. These varying methods each have their own advantages and disadvantages. While the widespread use of metal oxides hinges on their low cost, compact size, and ease of use, one of the greatest disadvantages is poor analyte selectivity[86,90-93]. In fact, because various chemiresistors, organometallics, conductive polymers, and even nanomaterials all rely on surface interactions with chemical analytes, the specificity of detection is limited entirely by the interaction mechanism. This already poses an issue for the detection of single compounds (*e.g.* CO, SO_2), but for the analysis of more complex samples, a single sensor is unable to accommodate more than a few chemical species at once.

This has led to the development of sensor arrays and electronic noses, which use the data collected from sensors with many different chemical sensitivities to analyze chemical mixtures containing many components[19,83,86,88,89,99,102,104,108-115]. While these arrays may provide powerful analytical capabilities with high sensitivities in the ppm and ppb range, they require the use of complex data analysis for compound identification and are limited by the types of individual sensors used in the array. In particular, the lack of absolute calibration for these electronic noses usually requires confirmation by another analytical method, such as GC-MS, to account for drift and lack of more straightforward chemical identification. Electronic noses are thus typically used for identifying odor patterns, which can be useful for applications such as food and beverage analysis, but may be more difficult to use when identification of specific chemical species is necessary[88,99,108-111]. Other methods such as optical fiber sensors or IMS can identify chemicals if pre-made libraries are generated, but it is difficult for these technologies to identify more than several chemical analytes at once[83-85,88,89], presenting a problem for analysis of complex samples outside of laboratory settings.

Recent efforts have led to the miniaturization of benchtop GC into powerful micro gas chromatographs (μGC) geared at use for field applications[2-81]. Compared to other portable vapor sensors, μGC has demonstrated the greatest advantages in analytical capabilities for complex chemical mixtures. Analytical vapor sensors, under variable ambient conditions and outside of controlled laboratory environments, may encounter several tens or even hundreds of compounds of interest at once. Some applications, including environmental monitoring, water analysis, and hydrocarbon detection, require simultaneous identification of several or all of these compounds due to their chemical or biological relevance[2-82]. This can be difficult to achieve with other sensing paradigms, which rely on vapor sensors without any type of chromatographic separation. However, the development of microfabricated columns and miniaturized GC components has allowed for the modernization of traditional GC technology into portable μGC, which possess many of the capabilities of benchtop systems while allowing for on-site analysis. Details on conventional GC technology and a comparison to μGC are described in the following sections.

1.2 Gas chromatography components

Gas chromatograph devices are composed of three main components, namely one of several methods for injection, separation column for analysis of chemical analytes, and vapor sensor for chemical detection after separation. Benchtop GC systems additionally utilize a carrier gas typically of either high purity helium, nitrogen, or hydrogen to flow the analytes through the separation column. Details on these components are provided in the following sections. A schematic of a typical benchtop GC system is provided in **Figure 1.1**.

1.2.1 Injection methods

In any GC system, there must be some method for sample preparation and injection into the system itself so that the mixture is adequately volatilized and provided at desired concentrations. Some benchtop GCs, such as the Agilent 6890N, use a manual injection port where gas or liquid phase samples are sampled into a syringe and injected by hand into a split/splitless injection port. The injection port is heated, typically to >50 °C above the analyte boiling point to volatilize it. In splitless mode, the entirety of the sample is injected into the column, but results in broad injection peaks due to the large dead volume of the injector cylinder. Thus, split mode is usually

preferred to inject only a small fraction of the sample from the entire injector volume by controlling the flow resistance of the split path. This allows for narrowing of the peak width and improved chromatographic performance, but comes at the tradeoff of reducing the amount of analyte that reaches the detector, especially if higher split ratios (*e.g.* >100:1) are used[1]. A diagram of a split/splitless injector is provided in **Figure 1.2**.

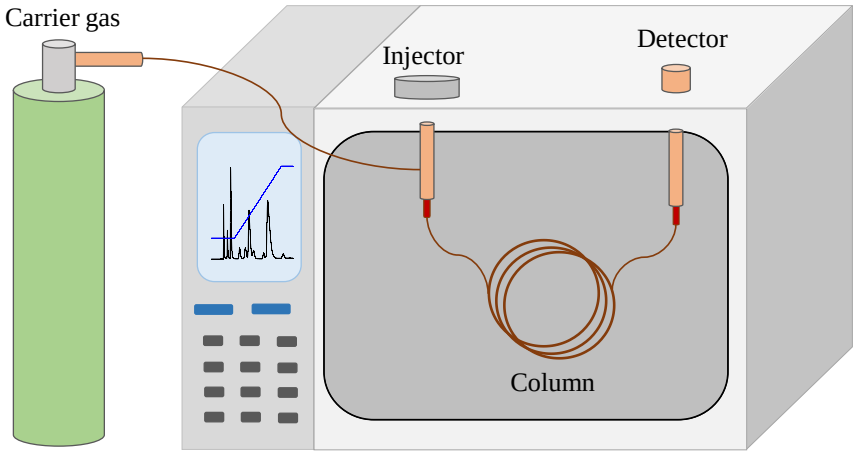

Figure 1.1. Benchtop gas chromatograph, composed of injector, column housed inside GC oven, and detector. The carrier gas pressure is controlled by a regulator and electronic pressure control.

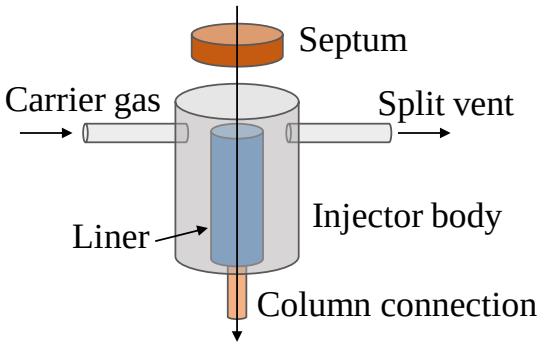

Figure 1.2. Split/splitless injector, with septum, split vent, glass liner, and column outlet interconnection. Manual injections are typically made with a syringe, which pierces the septum and injects the sample into the liner.

While convenient and easy to use, manual injection into split/splitless ports is inconsistent and can be a large source of error in an experiment. Thus, autosampling methods have been developed to work with techniques such as solid phase microextraction (SPME)[118,119], purge and

trap[120], thermal desorption[121-124], and sampling loops. Sampling loops are simple injectors that use a set volume in a cavity or tube enclosed by a six-port valve or by valves on either side. These loops contain no adsorbent material and deliver the same volume of sample for every injection, which can be useful for quantitative analysis. However, for many applications, some form of preconcentration is often desirable in order to improve the overall system sensitivity. One such technique is SPME, which is a static headspace sampling method that exposes a coated fused silica fiber to a sample (either gaseous or headspace above a liquid), whereupon the sample is adsorbed onto the surface and subsequently injected[118,119]. In contrast, purge and trap is a dynamic headspace sampling method, which involves purging the sample with an inert gas to volatilize the chemicals. The analytes are then adsorbed into a trap, which is a tube containing adsorbent materials. The trap is heated to release the analytes[120]. Thermal desorption is very similar in that analytes are adsorbed into a tube containing a thermally activated sorbent. The main difference is that thermal desorption sometimes is used to refer to samples directly pumped into the desorption tube, rather than being bubbled and volatilized from a liquid sample. In thermal desorption, there is often a second "cold trap" with a narrower bore size that collects the sample eluted from the first thermal desorption tube. This cold trap is usually held below room temperature and is rapidly heated to release the analytes, allowing for sharper injection widths than if the first trap were used alone[121-124].

1.2.2 Separation columns

The heart of the GC is the separation column, which is responsible for system's analytical capabilities. The column separates chemical analytes by chemical interactions with a stationary phase, where different partitioning of analytes between the stationary phase and mobile phase determines their retention time (*i.e.*, the amount of time it takes for a chemical to elute from the column). Two categories of columns are used for traditional GC, which are packed columns and capillary columns[125]. Packed columns are comparatively short tubes of metal, glass, Teflon, or other inert material in which packing bead supports are loaded and coated with a stationary phase. These were initially the only type of column used in GC instruments, but demonstrated comparatively poor efficiency compared to capillary columns due to flow turbulence from the packing material[125]. Development of capillary columns thus became of greater interest, and several types were developed, porous layer open tubular (PLOT) and wall coated open tubular

(WCOT), which are both useful for different applications depending on the analytes of interest. In PLOT columns, a porous layer of alumina, molecular sieve, or porous polymer is fixed on the side wall, allowing for a coating of high surface area and retention capability, which is especially useful for very volatile compounds. WCOT columns fix a stationary phase on the side wall with a thickness usually in the range of several tens of nm to a few µm and are broadly applicable to many environmental and industrial analyses. Since highly smooth and inert fused silica capillaries are used for these columns, longer columns of 30 or 60 m can be made with plate numbers ranging in the hundreds of thousands, as compared to packed columns which may only reach a few thousand[125]. A discussion of column performance parameters can be found in ***1.3.3 Column performance characteristics***.

GC stationary phases are most commonly categorized by polarity. While a great number of column stationary phases exist[126,127], the most well established and commonly used columns are the traditional poly(5%diphenyl/95%dimethyl siloxane) phase and the 100% polydimethyl siloxane (PDMS) phases due to their highly established use and wide ranging libraries. Other columns, such as polyethylene glycol (PEG) are used for separation of polar compounds, while PLOT columns are used for separation of light volatile compounds. A list of column stationary phases and their polarities are provided in **Figure 1.3**.

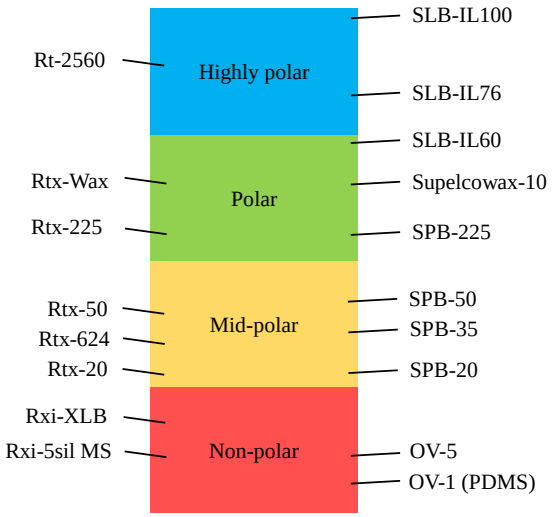

Figure 1.3. Column stationary phases categorized by polarity.

1.2.3 Vapor detectors

Upon elution from a GC column, separated chemical analytes must be transduced into a detectable signal by a vapor sensor. GC sensors, of course, are desired to have high sensitivity to chemical analytes, low noise, high linear dynamic range, fast response times, and low dark or background current. However, in addition and unlike for some other vapor sensors, the sensor at the outlet of a GC should be capable of detecting a broad range of chemicals due to the high number of chemical analytes eluting from the column. In some cases, volatile organic compounds (VOCs) of all types should be detected, while in others, even universal detection is desired. Thus, GC detectors most often do not use adsorption methods and rely on different mechanisms for sensing[128].

Currently, benchtop GC devices most widely employ flame ionization detectors (FIDs), thermal conductivity detectors (TCDs), electron capture devices (ECDs), and photoionization detectors (PIDs)[128]. The most widely used detector in current benchtop systems is the FID, which uses an oxidative hydrogen flame to burn organic molecules to produce ions, which are then collected by an electrode inside the ionization chamber[128]. The wide use of the FID is due to its nearly universal detection of organic molecules, as well as low detection limit (sub pg or sub ppb), near instantaneous response time, and linear dynamic range of at least 7 orders of magnitude.

TCDs are an older type of detector which use four heated filaments (to 400 °C, of which two are exposed to an inert carrier (He or H_2), and two are exposed to the sample. The filaments are connected by the Wheatstone bridge and act as resistors. When exposed to sample, the thermal conductivity of the ambient decreases, causing the filament temperature to increase and thus the resistance to increase as well, which can be measured by the Wheatstone bridge[128]. While providing nearly universal detection and nondestructive operation, the TCD possesses poor performance compared to the FID (ng to ppm level detection limit, 5 orders of magnitude linear dynamic range), and has different responses to different chemical analytes, thus requiring calibration.

ECDs are a relatively niche type of detector relying on a radioactive source to ionize the carrier gas into an electron beam, which flows into the detector cavity as a standing current. Samples passing through the cavity may deplete the standing current depending on their electron affinities, which necessitates calibration based on individual compounds. While the linear

dynamic range of ECDs may be small (around 4 orders of magnitude) and a radiation source is required[128], the ECD is capable of detection certain compounds (*e.g.*, halogenated compounds) down to extremely low levels, even to a few femtograms per second.

PIDs are powerful sensors that rely on ultraviolet photons generated from inert gas plasmas, most typically krypton, to ionize target samples into a collectible current via conductive electrodes. PIDs have been shown to possess competitive detection limit (sub-pg) and similar dynamic range compared to FIDs, with drawbacks being slightly lower response times and detection being limited by photon emission energy[129]. Although no compounds with ionization potentials above the photon emission energy can be detected, the PID is a non-destructive detector unlike the FID, allowing for use in the middle of the GC fluidic path, which can be useful for applications such as multi-dimensional GC. Additionally, unlike the FID, the PID does not require hydrogen and is much safer for portable instruments.

1.3 Gas chromatography principles

Having discussed the core components of the traditional GC system, a discussion of the theoretical background for GC separation and detection principles is summarized in the following sections. In addition, key GC and vapor sensor terminology is presented and performance metrics are discussed.

1.3.1 Retention theory

The core component of the GC is the separation column, which is responsible for the method's analytical capabilities. A theoretical basis for separation can be understood by each analyte having a different effective velocity through the column, which results in different elution times. This effective velocity, $u_{eff}(t)$, is dependent on the distribution of the analyte in the mobile and stationary phases of the column and can be expressed as

$$u_{eff}(t) = \frac{u_M(t)}{1 + k(t)}, \quad (1.1)$$

where $u_M(t)$ is the velocity in the mobile phase and $k(t)$ is the retention factor, given by

$$k(t) = \frac{t_r - t_m}{t_m} = \frac{K(t)}{\beta}. (1.2)$$

Retention factor $k(t)$ is a unitless measure of how much a compound is retained by a particular stationary phase. It can experimentally be measured from retention time t_r, the time an analyte elutes from the column, and holdup time (or dead time) t_m, which is the time it takes for the carrier gas to pass through the system. $k(t)$ is theoretically explained by distribution coefficient $K(t)$ and phase ratio β, with $K(t)$ defined as

$$K(t) = \frac{[C]_s}{[C]_m} = \exp\left(-\frac{\Delta G}{RT(t)}\right). (1.3)$$

$K(t)$ can be understood as the ratio between the molar concentration of analyte C in the stationary phase and the mobile phase, which is given theoretically by the thermodynamic interaction of the analyte with the stationary phase. R is the universal gas constant and $T(x,t)$ is the time dependent column temperature. ΔG is the Gibbs free energy change associated with an analyte moving from the stationary to mobile phase and can be calculated from the change in analyte enthalpy (ΔH) and entropy (ΔS)

$$\Delta G = \Delta H - T\Delta S. (1.4)$$

The ΔG of interaction with the stationary phase is different for each compound. The other component of retention factor $k(t)$ is the phase ratio β, defined by

$$\beta = \frac{\left(d_i - 2d_f\right)^2}{d_i^2 - \left(d_i - 2d_f\right)^2} \approx \frac{d_i}{4d_f}, for\ d_i \gg d_f, (1.5)$$

where d_i and d_f are the column inner diameter and the film thickness, respectively. Eq. 1.2 can thus be expressed as

$$k(t) = A\exp\left(\frac{\Delta G}{RT(t)}\right) \times d_f, (1.6)$$

where A is a constant for a given column. The time dependence of $k(t)$, $K(t)$, and $u_{eff}(t)$ in the prior equations arises from the time varying temperature of the column ambient, which can be varied for temperature programmed GC. The importance of Eq. 1.6 is detailed further in subsequent sections.

1.3.2 van Deemter Equation

The height equivalent to a theoretical plate (HETP) is a way to measure column efficiency and can be understood as the amount an analyte peak broadens as it travels along the column, normalized by the column length. The smaller the HETP for a given column, the better its per length efficiency and the higher its separation performance. HETP is related to several diffusion parameters by the van Deemter equation

$$HETP = A + \frac{B}{\mu} + C\mu = \left[2\lambda d_p\right] + \left[\frac{2D_m}{u_M}\right] + \left[\frac{1 + 6k + 11k^2}{24(1+k)^2}\frac{{d_c}^2 u_M}{D_m} + \frac{2k}{3(1+k)^2}\frac{{d_f}^2 u_M}{D_s}\right], \quad (1.7)$$

with A representing eddy diffusion, B as longitudinal diffusion, C as resistance to mass transfer, and u_M as the linear gas velocity. Expanded, the van Deemter equation includes particle shape λ, particle size d_p, mobile phase diffusion coefficient D_m, stationary phase diffusion coefficient D_s, capillary diameter d_c, film thickness d_f, and k as the retention factor[79].

Eddy diffusion is proportional to particle size and shape, which can be understood as channel asymmetry or imperfections in the case of WCOT columns, or particle beads for packed columns. Longitudinal diffusion is diffusion along the column length as the analyte band is propelled by the carrier gas. Increasing the linear carrier gas velocity decreases longitudinal diffusion. In contrast, resistance to mass transfer increases with increased carrier gas velocity, since a lower ratio of the analyte is in mobile phase and thus diffuses with higher velocity compared to the analyte remaining in stationary phase. This results in peak broadening and tailing, or peak asymmetry.

Using Eq. 1.7, the optimum flow velocity can be found theoretically by[79]

$$\mu_{opt} = \sqrt{2D_m\left[\frac{24(1+k)^2}{1+6k+11k^2}\frac{D_m}{{d_c}^2} + \frac{3(1+k)^2}{2k}\frac{D_s}{{d_f}^2}\right]}. \quad (1.8)$$

More typically, since the various coefficients and k may not be known for a particular compound, the optimal flow velocity is determined experimentally using van Deemter, or Golay, plots. By varying the flow velocity, obtaining several data points, and fitting a curve for Eq. 1.7, the optimal flow velocity can be determined for a particular column, type of separation, and type of carrier gas. A sample Golay plot is provided in **Figure 1.4**, with each diffusion term plotted separately for reference.

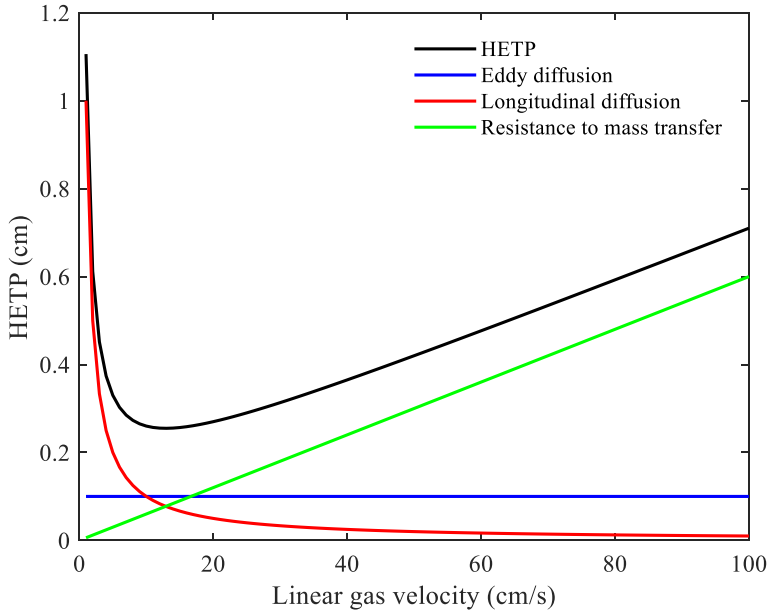

Figure 1.4. van Deemter or Golay plot. HETP varies as a function of various diffusion terms. A: Eddy diffusion, B: longitudinal diffusion, C: resistance to mass transfer. An optimal linear gas velocity can be determined to obtain the lowest HETP.

1.3.3 Column performance characteristics

Using the previously derived theory, column characteristics and separation performance metrics can be identified. Some important column performance parameters are provided in the following sections.

1.3.3a Resolution and peak capacity

The theoretical plate number N is a measure of total column efficiency (including length L), and is defined as

$$N = 5.545\left(\frac{t_R}{w_{0.5h}}\right)^2 = \frac{L}{HETP}, \quad (1.9)$$

with a larger N describing a more efficient column. t_R is the experimentally measured retention time and $w_{0.5h}$ is the experimentally determined full width at half maximum (FWHM). The resolution of a GC chromatogram is a measure of how well individual chemical peaks from the mixture are separated. Resolution R can be defined as

$$R = 2\frac{t_{R1} - t_{R2}}{w_1 + w_2} = 1.18\frac{t_{R1} - t_{R2}}{w_{0.5h1} + w_{0.5h2}} = \frac{1}{4}\sqrt{N}(\alpha - 1)\frac{k}{1 + k}. \text{ (1.10)}$$

The first two equations represent experimentally determined resolution, with t_{R1} and t_{R2} being the retention times of adjacent peaks, with base-to-base widths w_1 and w_2 or FWHMs $w_{0.5h1}$ and $w_{0.5h2}$. The more separated two peaks are and the narrower the peak widths, the higher the resolution. The third equation represents resolution determined from column parameters, with α as a separation factor which is a variable based on the stationary phase composition as well as its thickness. Eq. 1.10 shows that the higher the theoretical plate number (and smaller the HETP), the better the chromatographic resolution. Larger retention factors k also improve the resolution.

Any given chromatogram may contain tens or even hundreds of peaks. Summing over all resolutions yields the peak capacity for a column, which is a description of the column's overall separation capabilities for a set of compounds. Peak capacity PC can be defined simply as

$$PC = \sum R. \text{ (1.11)}$$

Peak capacities can be calculated based on a set of reference chemicals to compare the performances of different columns for specific applications. Higher peak capacities indicate a higher performance column for the application in question.

1.3.3b Column length

Theoretical plate number N is proportional to column length, but Eq. 1.10 shows that resolution scales as $\sqrt{N}$ and thus scales as $R \sim \sqrt{L}$. Thus, the per unit length separation capabilities are higher for shorter columns than for longer columns and long columns (*e.g.*, 60 or 100 m) are useful only when extremely high separation capabilities are required. Long columns come at the tradeoff of higher head pressures and longer analysis times, which may be prohibitive even for benchtop laboratory experiments. While analysis time can be reduced by increasing the flow rate or temperature ramping rate, separation then suffers as was shown in **Figure 1.4**.

1.3.3c Column diameter

Eq. 1.7 showed that HETP is proportional to the square of column inner diameter. Thus, as column inner diameter increases, the theoretical plate number N and column efficiency decrease. This can be understood by increased analyte interaction with the stationary phase interaction on

the side wall (due to decreased resistance to transverse mass transfer) if the diameter decreases. However, smaller inner diameters also increase the head pressure requirement for the same flow rate, as well as reduce the sample capacity due to the comparatively thinner coating thickness.

1.3.3d Stationary phase thickness

Eq. 1.7 showed that HETP is also proportional to the square of the stationary phase thickness, and thus thicker films result in decreased theoretical plate number. At the same time, retention factor k is directly proportional to film thickness. A column's separation capability R is a function of both of these effects and the ideal film thickness depends on the type of analysis required. Thicker films are capable of separating more volatile analytes due to increased retention and increase the sample capacity due to greater stationary phase volume. However, thicker films also increase the temperature required for elution of heavier analytes (thus increasing the analysis time) and have higher stationary phase bleeding at elevated temperatures. In general, the thinnest film thickness required for a specific application or separation is preferred (*i.e.*, when $k \gg 1$ for all analytes in question).

1.3.4 Sensor performance characteristics

Sensor characteristics are important for the overall detection performance of a GC device. Several vapor detectors were described in ***1.2.3 Vapor detectors***, each of which had performance advantages and disadvantages beyond only the detectable range of analytes. Several important sensor performance parameters are discussed as follows.

1.3.4a Detection limit

One of the most important sensor parameters for GC devices is the lowest detectable quantity of a particular analyte, also known as the detection limit. This is highly dependent on the sampling method and the vapor sensor, but is typically in the range of <1 pg for the gold standard FID, corresponding to sub-ppb level concentrations for many compounds even without preconcentration. Detection limit DL can be defined as

$$DL = \frac{Injected\ mass}{SNR_{3\sigma}}, \quad (1.12)$$

with $SNR_{3\sigma}$ as the signal to noise ratio using a standard deviation noise at 3 deviations (*i.e.*, 3σ). SNR can be calculated as the peak height divided by the 3σ noise.

1.3.4b Linear dynamic range and sensitivity

A sensor's linear dynamic range determines the range of concentrations that a GC system is capable of handling. While the detection limit is important for applications with extremely low concentrations (*e.g.*, forensics), the linear range is important for quantification of samples. At higher concentrations, sensor saturation may also occur, which can be detrimental to the lifetime of the sensor and prevent other signals from being detected. The linear dynamic range is the range of concentrations for which the sensor output linearly scales with the injected analyte quantity and is especially important for applications requiring quantification.

The sensitivity is the change in output signal divided by the change in input analyte mass (or concentration), which is the slope of the linear response in the linear dynamic range. This slope may be different for different analytes and thus requires calibration. For example, a correction factor (CF) is usually used for PIDs, normalized against isobutylene (CF = 1).

1.3.4c Drift

Sensor drift is the amount that a sensor reading may deviate from its initial value (*i.e.*, baseline) over time. This drift may be the result of ambient conditions, degradation due to humidity or oxygen, or electrode degradation. This may manifest as a baseline drift, increase in baseline noise, or reduction in signal height.

1.3.4d Response time

A sensor's response time is the time it takes for the sensor to reach 90% of the peak value from 10% of the peak height. The response time determines the accuracy of the actual recorded peak width. If a sensor's response time is similar to or longer than the actual peak width, the observed peak will be much broader than the actual eluted peak from the column. As the response time increases, peaks broaden and the degree of separation (*i.e.*, the chromatographic resolution) decreases.

1.4 Micro gas chromatography

1.4.1 Overview

While conventional benchtop GC provides powerful separation and detection performance for complex samples, the large size and weight of this technology prevents the use for *in situ* chemical analysis. The miniaturization of GC components has thus been of interest for the development of portable µGC devices. These systems have involved miniaturized valves and pumps, microfluidic tubing, and on-column heating to supplant the need for an oven. Crucially, the development of additional microfabrication technologies has also allowed for the development of microfluidic injectors, columns, and detectors, which reduces the footprint and power consumption of these GC components[2-7,9-12,14,15,17,20,24,30,34,36,40,42,44,45,47,49,51,54,60-62,64,76,80,130-132]. A discussion of each of these three µGC major components follows.

1.4.2 Miniaturized preconcentrators

Several GC injection methods were presented in ***1.2.1 Injection methods***, of which most automatic methods are applicable to µGC systems. While sampling loops are sometimes used as simple components for injection, by far the most common method are various forms of microfabricated or otherwise miniaturized preconcentrators[44,45,64,78,133-146]. Preconcentrators are essentially small scale versions of TD tubes, and are capable of both sampling and injection using the same microfabricated chip. Sampling involves generating a flow into the preconcentrator using a pump, where samples can be collected by various materials, typically activated charcoal (*e.g.*, Carbopack B or X, Carboxen 1000) or carbon nanostructures[36,44,45,64,72,78,133,138-142,144,145], or porous polymer materials (*e.g.*, Tenax TA)[121,135,136,146]. For injection, the carrier gas is flowed through the preconcentrator, which is then quickly heated to release the adsorbed chemicals. The more rapid the heating, the quicker the release and the sharper the injection peak width. The injected peak width is usually less than 1 second, but can be as fast as ~200 ms[44,145].

Preconcentrators often use multiple sorbents to capture a wider range of chemicals for analysis. For commonly used activated charcoals, the adsorption capability is proportional to the charcoal's surface area. Charcoals with low surface area typically can only trap compounds with lower volatilities, while charcoals with higher surface area can trap compounds with both low

and high volatilities. Due to their high adsorption capabilities, high surface area charcoals can become chemically poisoned by low volatility compounds, which can permanently remain in the charcoal and prevent it from trapping other compounds. Thus, sampling usually exposes the sample flow to low surface area charcoals first to trap the low volatility compounds. During injection, the preconcentrator is then flushed backward to first inject low volatility compounds into the column, ensuring a sharper injection peak for these analytes as well as preventing chemical poisoning of the sorbent beds. A depiction of a typical preconcentrator is provided in **Figure 1.5**.

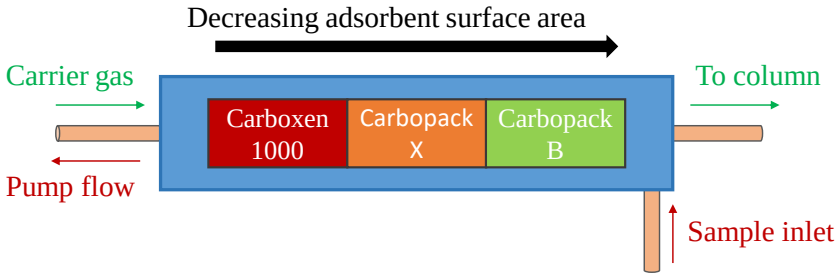

Figure 1.5. Miniaturized preconcentrator with 3 sorbent beds. The flow during sampling is depicted in red, while the flow during analysis is depicted in green. The two flows travel in opposite directions to ensure that chemical poisoning of high surface area sorbents does not occur.

1.4.3 Microfabricated columns

Traditional GC columns can provide powerful separation capabilities due to their long length, but this also results in long analysis times, high power consumption, and high head pressure requirements. These columns also use benchtop ovens and high pressure flow regulator systems, which greatly increases the footprint necessary for the use of these columns. Microfabrication technology has allowed for the replacement of these long capillary columns with MEMS-based planar microcolumns. Monolithic integration of small scale microcolumns with heaters and other micro-components has enabled highly uniform on-chip column heating for columns of up to 10 m in length, allowing for reduction of overall system power consumption and size by eliminating the accessory components usually required for benchtop systems[2-4,6,8,10,12,14,42,80,147]. Various microcolumn layouts, cross-sectional shapes, channel structures, stationary phase films, and coating methods have been explored, with detailed design parameters having been researched for microcolumn optimization.

1.4.3a Microcolumn layouts and cross-sectional shape

In a planar microcolumn, as opposed to a conventional column, the channel is etched or machined into a chip with a set pattern. Microcolumn layouts have included circular and square spirals, as well as serpentine patterns[148]. Literature has suggested that while gas permeability and unretained solute broadening is similar for all of these patterns, serpentine patterns may offer higher plate numbers and resolution[148]. A key aspect of column layout is avoiding sharp turns, which can lead to path length differences between the inner and outer parts of the channel, which then results in peak tailing as well as stationary phase pooling during coating.

Related to the above is the cross-sectional shape, which is ideally circularly symmetric as in capillary columns. However, microcolumns made using machining or etching techniques have rectangular cross sections due to fabrication limitations, which then results in path length differences due to channel asymmetry. Like sharp turns, rectangular cross-sections cause stationary phase pooling during coating, which further exacerbates peak tailing in microcolumns.

1.4.3b Channel fluidic structures

The majority of microcolumns have utilized wall-coated open tubular structures due to ease of fabrication and coating[7,8,11,15,36,45,61,62,80]. While microfabricated packed columns are difficult to make, the development of semi-packed columns using microfabricated posts inside the column channel has allowed for improved separation efficiency from reduced mass transfer distances, shorter column lengths (<1 m), and higher sample capacities compared to WCOT microcolumns[2,4,6,7,13,20,42,60]. However, semi-packed columns require higher head pressures (up to 100 psi) due to the increased flow resistance, which also can make conventional coating methods tricky to accomplish properly.

1.4.3c Column coating methods and materials

As with commercial capillary columns, the stationary phase for a microcolumn can be coated either statically or dynamically. In either case, a stationary phase mixture must first be prepared, most often as a polymerization mixture for polymer-based coatings. In dynamic coating, a plug is first created at the start of the column, where it is then forced through the column with low gas pressure. The coating speed must be slow and controlled to ensure a homogeneous coating and

uniform thickness. The thickness is determined by the coating speed and mixture viscosity, but is difficult to calculate directly.

In static coating, the entire column is filled with the coating mixture and one end is sealed. The other end is connected to a vacuum pump, which evaporates the solvent at a set temperature. As the solvent evaporates, the stationary phase is left behind on the wall – the coating process is completed once the solvent has completely dried. Again, the rate of evaporation must be controlled and slow to ensure a homogeneous coating. Unlike dynamic coating, the thickness of the coating can be calculated using

$$d_f = \frac{V_{column} \times C_{coating}}{\rho S}, \quad (1.13)$$

with V_{column} being the entire column channel volume, $C_{coating}$ as coating solution concentration (wt/wt), ρ as stationary phase density, and S as column inner surface area. Literature has suggested that static coating, while more complex, results in more uniform and higher quality coatings compared to dynamic coating[11,149,150].

Compared to the variety of stationary phase coatings and techniques used in commercial columns, microcolumns have drastically more limited options[127,151-153]. Currently in the literature, the most commonly used microcolumns are coated with either OV-1 or OV-5 coatings[2,5,7,8,11,15,42,45,64,80], with limited research having been directed at other coatings such as porous alumina deposited during microfabrication[40,54]. While these traditional PDMS or 5% phenyl stationary phases are useful for general purpose separations, exploration of different microcolumn stationary phases and coating techniques is critical to broadening the scope of portable μGC to more diverse and specialized separations.

1.4.4 Miniaturized detectors

Compared to benchtop detectors, miniaturized detectors have a key difference in lower footprint requirements, including size, auxiliary gas flows, and power consumption requirements. While the FID is a powerful benchtop GC detector, the use of high auxiliary gas flows, including extremely flammable H_2 gas, makes it difficult to practically miniaturize for portable GC devices. Other miniaturized vapor detectors have been developed for use in μGC, including miniaturized thermal conductivity detectors (TCDs), surface acoustic wave detectors, chemiresistors, chemicapacitors, and electron capture detectors[36,90-92,100,103,107,112,114,115,117,154-157].

These sensors were discussed in **1.1 Background**, most of which are commonly used as standalone vapor sensors, but can also theoretically be used as the vapor detector for a portable GC device. While the detection limits of these sensors can be down to a few ppm or tens of ppb[90-92,100,103,107,112,114,115,117,154-156], most of these miniaturized detectors are highly selective (*e.g.*, chemiresistors, chemicapacitors)[90-92,100,103,107,112,114,115,117,154-156] and require extensive calibration or array implementations (*e.g.*, electronic nose) for compatibility with portable μGC due to the broad range of compounds for analysis. These chemical sensor arrays require machine learning analysis for signals to be processed. Optical fiber and fluorescent sensors are powerful tools, but often impractical due to the delicate optics required for accurate measurements. Other analytical methods like IMS require robust libraries for identification, which are currently not well-studied. Other issues for miniaturization include the need for high auxiliary gas flows (helium) for sensors like TCDs, or high voltages for electron capture devices and heating for metal oxide sensors, which are less practical for portable systems with limited space and resources.

Currently, plasma-based photoionization detectors (PIDs) are among the most commonly used sensors for μGC systems[26,30,60,70,131,158-160]. Typical PIDs utilize sealed lamps (made of ultraviolet transparent materials such as LiF or MgF_2) containing noble or permanent gases (*e.g.*, xenon, krypton, and argon) to excite plasma and thereby generate photons ranging from 9.6 to 11.7 eV. Detection of analytes is determined by the energy of the emitted photons, where any compounds with ionization potentials below the emission energy may be ionized. PIDs have demonstrated high sensitivity (tens of pg), large dynamic range (up to 6 decades), low manufacturing cost, and fast response times (within 10s of ms) along with small size (few mL), which enables their suitable use in μGC[30,31,49,60,70,72,131,160].

1.5 Outlook

This chapter has summarized some of the background and motivation for the development of portable vapor sensors. In particular, compared to the convention benchtop gas chromatography technology used for chemical analysis, most portable sensors are limited in the range of compounds they can identify at once. Thus, portable μGC systems are of high interest to increase the capabilities of on-site chemical vapor analysis. Background and theory on gas chromatography allowed for insight into column design parameters, which are important for the development of microcolumns. A summary of miniaturization of core GC components was

provided, along with the state of current technology. Further development of μGC devices is aimed at improvement of individual microcomponents (*i.e.*, preconcentrator, column, detector, pumps, and valves), as well as improving overall system layout, robustness, and footprint. This thesis mainly discusses the development of miniaturized columns and detectors, with the aim of broadening the range of compounds and applications that μGC can target. Assembly of these components into complete portable systems is then aimed at demonstrating practical *in situ* use of these μGC devices.

1.6 References

(1) McNair, H. M.; Miller, J. M.; Snow, N. H.: *Basic Gas Chromatography, Third Edition*; John Wiley & Sons, Inc., 2019.

(2) Agah, M.; Lambertus, G. R.; Sacks, R.; Wise, K. High-speed MEMS-based gas chromatography. *JMemS* **2006**, *15*, 1371-1378.

(3) Haghighi, F.; Talebpour, Z.; Sanati-Nezhad, A. Through the years with on-a-chip gas chromatography: a review. *Lab Chip* **2015**, *15*, 2559-2575.

(4) Regmi, B. P.; Agah, M. Micro Gas Chromatography: An Overview of Critical Components and Their Integration. *Anal Chem* **2018**, *90*, 13133-13150.

(5) Zareian-Jahromi, M. A.; Ashraf-Khorassani, M.; Taylor, L. T.; Agah, M. Design, Modeling, and Fabrication of MEMS-Based Multicapillary Gas Chromatographic Columns. *JMemS* **2009**, *18*, 28-37.

(6) Akbar, M.; Restaino, M.; Agah, M. Chip-scale gas chromatography: From injection through detection. *Microsyst Nanoeng* **2015**, *1*.

(7) Lambertus, G.; Elstro, A.; Sensenig, K.; Potkay, J.; Agah, M.; Scheuering, S.; Wise, K.; Dorman, F.; Sacks, R. Design, fabrication, and evaluation of microfabricated columns for gas chromatography. *Anal Chem* **2004**, *76*, 2629-2637.

(8) Lambertus, G. R.; Fix, C. S.; Reidy, S. M.; Miller, R. A.; Wheeler, D.; Nazarov, E.; Sacks, R. Silicon microfabricated column with microfabricated differential mobility spectrometer for GC analysis of volatile organic compounds. *Anal Chem* **2005**, *77*, 7563-7571.

(9) Collin, W. R.; Serrano, G.; Wright, L. K.; Chang, H.; Nunovero, N.; Zellers, E. T. Microfabricated gas chromatograph for rapid, trace-level determinations of gas-phase explosive marker compounds. *Anal Chem* **2014**, *86*, 655-663.

(10) Kim, S. K.; Chang, H.; Zellers, E. T. Microfabricated gas chromatograph for the selective determination of trichloroethylene vapor at sub-parts-per-billion concentrations in complex mixtures. *Anal Chem* **2011**, *83*, 7198-7206.

(11) Reidy, S.; Lambertus, G.; Reece, J.; Sacks, R. High-performance, static-coated silicon microfabricated columns for gas chromatography. *Anal Chem* **2006**, *78*, 2623-2630.

(12) Luong, J.; Gras, R.; Shellie, R. A.; Cortes, H. J. Applications of planar microfluidic devices and gas chromatography for complex problem solving. *J Sep Sci* **2013**, *36*, 182-191.

(13) Ali, S.; Ashraf-Khorassani, M.; Taylor, L. T.; Agah, M. MEMS-based semi-packed gas chromatography columns. *Sensors Actuators B: Chem* **2009**, *141*, 309-315.

(14) Lewis, A. C.; Hamilton, J. F.; Rhodes, C. N.; Halliday, J.; Bartle, K. D.; Homewood, P.; Grenfell, R. J.; Goody, B.; Harling, A. M.; Brewer, P.; Vargha, G.; Milton, M. J. Microfabricated planar glass gas chromatography with photoionization detection. *J Chromatogr A* **2010**, *1217*, 768-774.

(15) Serrano, G.; Reidy, S. M.; Zellers, E. T. Assessing the reliability of wall-coated microfabricated gas chromatographic separation columns. *Sensors Actuators B: Chem* **2009**, *141*, 217-226.

(16) Hobbs, P. J.; Misselbrook, T. H.; Pain, B. F. Assessment of Odors from Livestock Wastes by a Photoionization Detector, an Electronic Nose, Olfactometry and Gas-Chromatography Mass-Spectrometry. *JAER* **1995**, *60*, 137-144.

(17) Wang, A.; Hynynen, S.; Hawkins, A. R.; Tolley, S. E.; Tolley, H. D.; Lee, M. L. Axial thermal gradients in microchip gas chromatography. *J Chromatogr A* **2014**, *1374*, 216-223.

(18) Baltazar, Q. Q.; Leininger, S. K.; Anderson, J. L. Binary ionic liquid mixtures as gas chromatography stationary phases for improving the separation selectivity of alcohols and aromatic compounds. *J Chromatogr A* **2008**, *1182*, 119-127.

(19) Zhong, Q.; Steinecker, W. H.; Zellers, E. T. Characterization of a high-performance portable GC with a chemiresistor array detector. *Analyst* **2009**, *134*, 283-293.

(20) Narayanan, S.; Rice, G.; Agah, M. Characterization of a micro-helium discharge detector for gas chromatography. *Sensors Actuators B: Chem* **2015**, *206*, 190-197.

(21) Poole, C. F. Chromatographic and spectroscopic methods for the determination of solvent properties of room temperature ionic liquids. *J Chromatogr A* **2004**, *1037*, 49-82.

(22) Grall, A. J.; Sacks, R. D. Column performance and stability for high-speed vacuum-outlet GC of volatile organic compounds using atmospheric pressure air as carrier gas. *Anal Chem* **1999**, *71*, 5199-5205.

(23) Gough, D. V.; Bahaghighat, H. D.; Synovec, R. E. Column selection approach to achieve a high peak capacity in comprehensive three-dimensional gas chromatography. *Talanta* **2019**, *195*, 822-829.

(24) Wang, J.; Bryant-Genevier, J.; Nuñovero, N.; Zhang, C.; Kraay, B.; Zhan, C.; Scholten, K.; Nidetz, R.; Buggaveeti, S.; Zellers, E. T. Compact prototype microfabricated gas chromatographic analyzer for autonomous determinations of VOC mixtures at typical workplace concentrations. *Microsystems & Nanoengineering* **2018**, *4*, 17101.

(25) Skog, K. M.; Xiong, F.; Kawashima, H.; Doyle, E.; Soto, R.; Gentner, D. R. Compact, Automated, Inexpensive, and Field-Deployable Vacuum-Outlet Gas Chromatograph for Trace-Concentration Gas-Phase Organic Compounds. *Anal Chem* **2019**, *91*, 1318-1327.

(26) Price, J. G. W.; Fenimore, D. C.; Simmonds, P. G.; Zlatkis, A. Design and operation of a photoionization detector for gas chromatography. *AnaCh* **2002**, *40*, 541-547.

(27) Dumas, T. Determination of Formaldehyde in Air by Gas-Chromatography. *J Chromatogr* **1982**, *247*, 289-295.

(28) Cavalcante, R. M.; de Andrade, M. V. F.; Marins, R. V.; Oliveira, L. D. M. Development of a headspace-gas chromatography (HS-GC-PID-FID) method for the determination of VOCs in environmental aqueous matrices: Optimization, verification and elimination of matrix effect and VOC distribution on the Fortaleza Coast, Brazil. *Microchem J* **2010**, *96*, 337-343.

(29) Contreras, J. A.; Wang, A.; Rockwood, A. L.; Tolley, H. D.; Lee, M. L. Dynamic thermal gradient gas chromatography. *J Chromatogr A* **2013**, *1302*, 143-151.

(30) Soo, J. C.; Lee, E. G.; LeBouf, R. F.; Kashon, M. L.; Chisholm, W.; Harper, M. Evaluation of a portable gas chromatograph with photoionization detector under variations of VOC concentration, temperature, and relative humidity. *J Occup Environ Hyg* **2018**, *15*, 351-360.

(31) Zhang, W.-q.; Li, H.; Zhang, Y.-j.; Bi, F.; Meng, L.-s.; Zhang, X.-m.; Mao, J.-y.; Cheng, N.-l.; Fang, B.; Yang, Y.; Chen, C.; Guo, K.-x.; Zhan, G.-e.; Sha, J.; Wang, X.-z. Fast Determination of Monocyclic Aromatic Hydrocarbons in Ambient Air Using a Portable Gas Chromatography–Photoionization Detector. *Chromatographia* **2017**, *80*, 1233-1247.

(32) Bartle, K. D. Film Thickness of Dynamically Coated Open-Tubular Glass Columns for Gas-Chromatography. *AnaCh* **1973**, *45*, 1831-1836.

(33) Boeker, P.; Leppert, J. Flow field thermal gradient gas chromatography. *Anal Chem* **2015**, *87*, 9033-9041.

(34) Lee, J.; Zhou, M.; Zhu, H.; Nidetz, R.; Kurabayashi, K.; Fan, X. Fully Automated Portable Comprehensive 2-Dimensional Gas Chromatography Device. *Anal Chem* **2016**, *88*, 10266-10274.

(35) Zhou, M.; Lee, J.; Zhu, H.; Nidetz, R.; Kurabayashi, K.; Fan, X. A fully automated portable gas chromatography system for sensitive and rapid quantification of volatile organic compounds in water. *RSC Advances* **2016**, *6*, 49416-49424.

(36) Qin, Y.; Gianchandani, Y. B. A fully electronic microfabricated gas chromatograph with complementary capacitive detectors for indoor pollutants. *Microsyst Nanoeng* **2016**, *2*, 15049.

(37) Mendoza, L. G.; Gonzalez-Alvarez, J.; Gonzalo, C. F.; Arias-Abrodo, P.; Altava, B.; Luis, S. V.; Burguete, M. I.; Gutierrez-Alvarez, M. D. Gas chromatographic analysis of fatty acid methyl esters of milk fat by an ionic liquid derived from L-phenylalanine as the stationary phase. *Talanta* **2015**, *143*, 212-218.

(38) Poole, C. F.; Lenca, N. Gas chromatography on wall-coated open-tubular columns with ionic liquid stationary phases. *J Chromatogr A* **2014**, *1357*, 87-109.

(39) Patil, R. A.; Talebi, M.; Sidisky, L. M.; Berthod, A.; Armstrong, D. W. Gas chromatography selectivity of new phosphonium-based dicationic ionic liquid stationary phases. *J Sep Sci* **2018**, *41*, 4142-4148.

(40) Akbar, M.; Shakeel, H.; Agah, M. GC-on-chip: integrated column and photoionization detector. *Lab Chip* **2015**, *15*, 1748-1758.

(41) Mahe, L.; Dutriez, T.; Courtiade, M.; Thiebaut, D.; Dulot, H.; Bertoncini, F. Global approach for the selection of high temperature comprehensive two-dimensional gas chromatography experimental conditions and quantitative analysis in regards to sulfur-containing compounds in heavy petroleum cuts. *J Chromatogr A* **2011**, *1218*, 534-544.

(42) Agah, M.; Potkay, J. A.; Lambertus, G.; Sacks, R.; Wise, K. D. High-performance temperature-programmed microfabricated gas chromatography columns. *JMemS* **2005**, *14*, 1039-1050.

(43) Gras, R.; Hua, Y.; Luong, J. High-throughput gas chromatography for volatile compounds analysis by fast temperature programming and adsorption chromatography. *J Sep Sci* **2017**, *40*, 1979-1984.

(44) Serrano, G.; Sukaew, T.; Zellers, E. T. Hybrid preconcentrator/focuser module for determinations of explosive marker compounds with a micro-scale gas chromatograph. *J Chromatogr A* **2013**, *1279*, 76-85.

(45) Yutao, Q.; Gianchandani, Y. B. iGC1: An Integrated Fluidic System for Gas Chromatography Including Knudsen Pump, Preconcentrator, Column, and Detector Microfabricated by a Three-Mask Process. *JMemS* **2014**, *23*, 980-990.

(46) Anderson, J. L.; Armstrong, D. W. Immobilized ionic liquids as high-selectivity/high-temperature/high-stability gas chromatography stationary phases. *Anal Chem* **2005**, *77*, 6453-6462.

(47) Sun, J.; Guan, F.; Cui, D.; Chen, X.; Zhang, L.; Chen, J. An improved photoionization detector with a micro gas chromatography column for portable rapid gas chromatography system. *Sensors Actuators B: Chem* **2013**, *188*, 513-518.

(48) Cacho, J. I.; Campillo, N.; Vinas, P.; Hernandez-Cordoba, M. Improved sensitivity gas chromatography-mass spectrometry determination of parabens in waters using ionic liquids. *Talanta* **2016**, *146*, 568-574.

(49) Lee, J.; Zhou, M.; Zhu, H.; Nidetz, R.; Kurabayashi, K.; Fan, X. In situ calibration of micro-photoionization detectors in a multi-dimensional micro-gas chromatography system. *Analyst* **2016**, *141*, 4100-4107.

(50) Amaral, M. S. S.; Marriott, P. J.; Bizzo, H. R.; Rezende, C. M. Ionic liquid capillary columns for analysis of multi-component volatiles by gas chromatography-mass spectrometry: performance, selectivity, activity and retention indices. *Anal Bioanal Chem* **2018**, *410*, 4615-4632.

(51) Regmi, B. P.; Chan, R.; Agah, M. Ionic liquid functionalization of semi-packed columns for high-performance gas chromatographic separations. *J Chromatogr A* **2017**, *1510*, 66-72.

(52) Pojjanapornpun, S.; Nolvachai, Y.; Aryusuk, K.; Kulsing, C.; Krisnangkura, K.; Marriott, P. J. Ionic liquid phases with comprehensive two-dimensional gas chromatography of fatty acid methyl esters. *Anal Bioanal Chem* **2018**, *410*, 4669-4677.

(53) Nan, H.; Anderson, J. L. Ionic liquid stationary phases for multidimensional gas chromatography. *TrAC, Trends Analyt Chem* **2018**, *105*, 367-379.

(54) Regmi, B. P.; Chan, R.; Atta, A.; Agah, M. Ionic liquid-coated alumina-pretreated micro gas chromatography columns for high-efficient separations. *J Chromatogr A* **2018**, *1566*, 124-134.

(55) Fanali, C.; Micalizzi, G.; Dugo, P.; Mondello, L. Ionic liquids as stationary phases for fatty acid analysis by gas chromatography. *Analyst* **2017**, *142*, 4601-4612.

(56) Mazzucotelli, M.; Bicchi, C.; Marengo, A.; Rubiolo, P.; Galli, S.; Anderson, J. L.; Sgorbini, B.; Cagliero, C. Ionic liquids as stationary phases for gas chromatography-Unusual selectivity of ionic liquids with a phosphonium cation and different anions in the flavor, fragrance and essential oil analyses. *J Chromatogr A* **2019**, *1583*, 124-135.

(57) Poole, C. F. Ionization-based detectors for gas chromatography. *J Chromatogr A* **2015**, *1421*, 137-153.

(58) Nan, H.; Zhang, C.; O'Brien, R. A.; Benchea, A.; Davis, J. H., Jr.; Anderson, J. L. Lipidic ionic liquid stationary phases for the separation of aliphatic hydrocarbons by comprehensive two-dimensional gas chromatography. *J Chromatogr A* **2017**, *1481*, 127-136.

(59) Pang, X.; Nan, H.; Zhong, J.; Ye, D.; Shaw, M. D.; Lewis, A. C. Low-cost photoionization sensors as detectors in GCxGC systems designed for ambient VOC measurements. *Sci Total Environ* **2019**, *664*, 771-779.

(60) Narayanan, S.; Rice, G.; Agah, M. A micro-discharge photoionization detector for micro-gas chromatography. *Microchimica Acta* **2013**, *181*, 493-499.

(61) Li, M. W.; Huang, X.; Zhu, H.; Kurabayashi, K.; Fan, X. Microfabricated ionic liquid column for separations in dry air. *J Chromatogr A* **2020**, *1620*, 461002.

(62) Li, M. W.; She, J.; Zhu, H.; Li, Z.; Fan, X. Microfabricated porous layer open tubular (PLOT) column. *Lab Chip* **2019**, *19*, 3979-3987.

(63) Nesterenko, E. P.; Burke, M.; de Bosset, C.; Pessutto, P.; Malafosse, C.; Collins, D. A. Monolithic porous layer open tubular (monoPLOT) capillary columns for gas chromatography. *RSC Adv* **2015**, *5*, 7890-7896.

(64) Manginell, R. P.; Bauer, J. M.; Moorman, M. W.; Sanchez, L. J.; Anderson, J. M.; Whiting, J. J.; Porter, D. A.; Copic, D.; Achyuthan, K. E. A monolithically-integrated µGC chemical sensor system. *Sensors (Basel)* **2011**, *11*, 6517-6532.

(65) Tolley, H. D.; Tolley, S. E.; Wang, A.; Lee, M. L. Moving thermal gradients in gas chromatography. *J Chromatogr A* **2014**, *1374*, 189-198.

(66) Shashkov, M. V.; Sidelnikov, V. N.; Bratchikova, A. A. New Stationary Ionic Liquid Phases with Quinolinium Cations for Capillary Gas Chromatography. *Anal Lett* **2020**, *53*, 84-101.

(67) Contreras, J. A.; Rockwood, A. L.; Tolley, H. D.; Lee, M. L. Peak sweeping and gating using thermal gradient gas chromatography. *J Chromatogr A* **2013**, *1278*, 160-165.

(68) Huang, K.; Han, X.; Zhang, X.; Armstrong, D. W. PEG-linked geminal dicationic ionic liquids as selective, high-stability gas chromatographic stationary phases. *Anal Bioanal Chem* **2007**, *389*, 2265-2275.

(69) Sanchez, J. M.; Sacks, R. D. Performance characteristics of a new prototype for a portable GC using ambient air as carrier gas for on-site analysis. *J Sep Sci* **2007**, *30*, 1052-1060.

(70) Verner, P. Photoionization detection and its application in gas chromatography. *J Chromatogr A* **1984**, *300*, 249-264.

(71) Ji, Z. H.; Majors, R. E.; Guthrie, E. J. Porous layer open-tubular capillary columns: preparations, applications and future directions. *J Chromatogr A* **1999**, *842*, 115-142.

(72) You, D. W.; Seon, Y. S.; Jang, Y.; Bang, J.; Oh, J. S.; Jung, K. W. A portable gas chromatograph for real-time monitoring of aromatic volatile organic compounds in air samples. *J Chromatogr A* **2020**, *1625*, 461267.

(73) Aldaeus, F.; Thewalim, Y.; Colmsjo, A. Prediction of retention times and peak widths in temperature-programmed gas chromatography using the finite element method. *J Chromatogr A* **2009**, *1216*, 134-139.

(74) Zhou, M.; Sharma, R.; Zhu, H.; Li, Z.; Li, J.; Wang, S.; Bisco, E.; Massey, J.; Pennington, A.; Sjoding, M.; Dickson, R. P.; Park, P.; Hyzy, R.; Napolitano, L.; Gillies, C. E.; Ward, K. R.; Fan, X. Rapid breath analysis for acute respiratory distress syndrome diagnostics using a portable two-dimensional gas chromatography device. *Anal Bioanal Chem* **2019**, *411*, 6435-6447.

(75) Sharma, R.; Zhou, M.; Hunter, M. D.; Fan, X. Rapid In Situ Analysis of Plant Emission for Disease Diagnosis Using a Portable Gas Chromatography Device. *J Agric Food Chem* **2019**, *67*, 7530-7537.

(76) Lussac, E.; Barattin, R.; Cardinael, P.; Agasse, V. Review on Micro-Gas Analyzer Systems: Feasibility, Separations and Applications. *Crit Rev Anal Chem* **2016**, *46*, 455-468.

(77) Seeley, J. V.; Bates, C. T.; McCurry, J. D.; Seeley, S. K. Stationary phase selection and comprehensive two-dimensional gas chromatographic analysis of trace biodiesel in petroleum-based fuel. *J Chromatogr A* **2012**, *1226*, 103-109.

(78) Lara-Lbeas, I.; Rodriguez-Cuevas, A.; Andrikopoulou, C.; Person, V.; Baldas, L.; Colin, S.; Le Calve, S. Sub-ppb Level Detection of BTEX Gaseous Mixtures with a Compact Prototype GC Equipped with a Preconcentration Unit. *Micromachines (Basel)* **2019**, *10*, 187-199.

(79) Blumberg, L. M.: *Temperature-programmed gas chromatography*; John Wiley & Sons, 2010.

(80) Reidy, S.; George, D.; Agah, M.; Sacks, R. Temperature-programmed GC using silicon microfabricated columns with integrated heaters and temperature sensors. *Anal Chem* **2007**, *79*, 2911-2917.

(81) Frink, L. A.; Armstrong, D. W. Water Determination in Solid Pharmaceutical Products Utilizing Ionic Liquids and Headspace Gas Chromatography. *J Pharm Sci* **2016**, *105*, 2288-2292.

(82) Borsdorf, H.; Mayer, T.; Zarejousheghani, M.; Eiceman, G. A. Recent Developments in Ion Mobility Spectrometry. *ApSRv* **2011**, *46*, 472-521.

(83) Walt, D. R. Bead-based optical fiber arrays for artificial olfaction. *Curr Opin Chem Biol* **2010**, *14*, 767-770.

(84) Wolfbeis, O. S. Fiber-optic chemical sensors and biosensors. *Anal Chem* **2000**, *72*, 81R-89R.

(85) Elosua, C.; Matias, I. R.; Bariain, C.; Arregui, F. J. Volatile organic compound optical fiber sensors: A review. *Sensors* **2006**, *6*, 1440-1465.

(86) Nazemi, H.; Joseph, A.; Park, J.; Emadi, A. Advanced Micro- and Nano-Gas Sensor Technology: A Review. *Sensors (Basel)* **2019**, *19*.

(87) Gao, M.; Tang, B. Z. Fluorescent Sensors Based on Aggregation-Induced Emission: Recent Advances and Perspectives. *ACS Sens* **2017**, *2*, 1382-1399.

(88) Li, Z.; Askim, J. R.; Suslick, K. S. The Optoelectronic Nose: Colorimetric and Fluorometric Sensor Arrays. *Chem Rev* **2019**, *119*, 231-292.

(89) Liu, T. H.; Miao, R.; Peng, H. N.; Liu, J.; Ding, L. P.; Fang, Y. Adlayer Chemistry on Film-based Fluorescent Gas Sensors. *Acta Physico-Chimica Sinica* **2020**, *36*.

(90) Zhou, X.; Lee, S.; Xu, Z.; Yoon, J. Recent Progress on the Development of Chemosensors for Gases. *Chem Rev* **2015**, *115*, 7944-8000.

(91) Mirzaei, A.; Leonardi, S. G.; Neri, G. Detection of hazardous volatile organic compounds (VOCs) by metal oxide nanostructures-based gas sensors: A review. *Ceram Int* **2016**, *42*, 15119-15141.

(92) Sun, Y. F.; Liu, S. B.; Meng, F. L.; Liu, J. Y.; Jin, Z.; Kong, L. T.; Liu, J. H. Metal oxide nanostructures and their gas sensing properties: a review. *Sensors (Basel)* **2012**, *12*, 2610-2631.

(93) Kumar, R.; Liu, X.; Zhang, J.; Kumar, M. Room-Temperature Gas Sensors Under Photoactivation: From Metal Oxides to 2D Materials. *Nanomicro Lett* **2020**, *12*, 164.

(94) Li, H. Y.; Zhao, S. N.; Zang, S. Q.; Li, J. Functional metal-organic frameworks as effective sensors of gases and volatile compounds. *Chem Soc Rev* **2020**, *49*, 6364-6401.

(95) Wenger, O. S. Vapochromism in organometallic and coordination complexes: chemical sensors for volatile organic compounds. *Chem Rev* **2013**, *113*, 3686-3733.

(96) Fang, X.; Zhai, T.; Gautam, U. K.; Li, L.; Wu, L.; Bando, Y.; Golberg, D. ZnS nanostructures: From synthesis to applications. *Prog Mater Sci* **2011**, *56*, 175-287.

(97) Pandey, S. Highly sensitive and selective chemiresistor gas/vapor sensors based on polyaniline nanocomposite: A comprehensive review. *Journal of Science: Advanced Materials and Devices* **2016**, *1*, 431-453.

(98) Majhi, S. M.; Mirzaei, A.; Kim, H. W.; Kim, S. S.; Kim, T. W. Recent advances in energy-saving chemiresistive gas sensors: A review. *Nano Energy* **2021**, *79*, 105369.

(99) Chiu, S. W.; Tang, K. T. Towards a chemiresistive sensor-integrated electronic nose: a review. *Sensors (Basel)* **2013**, *13*, 14214-14247.

(100) Bai, H.; Shi, G. Q. Gas sensors based on conducting polymers. *Sensors* **2007**, *7*, 267-307.

(101) McGinn, C. K.; Lamport, Z. A.; Kymissis, I. Review of Gravimetric Sensing of Volatile Organic Compounds. *ACS Sens* **2020**, *5*, 1514-1534.

(102) Ricco, A. J.; Crooks, R. M.; Osbourn, G. C. Surface acoustic wave chemical sensor arrays: New chemically sensitive interfaces combined with novel cluster analysis to detect volatile organic compounds and mixtures. *Acc Chem Res* **1998**, *31*, 289-296.

(103) Singh, E.; Meyyappan, M.; Nalwa, H. S. Flexible Graphene-Based Wearable Gas and Chemical Sensors. *ACS Appl Mater Interfaces* **2017**, *9*, 34544-34586.

(104) Wang, T.; Huang, D.; Yang, Z.; Xu, S.; He, G.; Li, X.; Hu, N.; Yin, G.; He, D.; Zhang, L. A Review on Graphene-Based Gas/Vapor Sensors with Unique Properties and Potential Applications. *Nanomicro Lett* **2016**, *8*, 95-119.

(105) Konvalina, G.; Haick, H. Sensors for breath testing: from nanomaterials to comprehensive disease detection. *Acc Chem Res* **2014**, *47*, 66-76.

(106) Schroeder, V.; Savagatrup, S.; He, M.; Lin, S.; Swager, T. M. Carbon Nanotube Chemical Sensors. *Chem Rev* **2019**, *119*, 599-663.

(107) Kauffman, D. R.; Star, A. Carbon nanotube gas and vapor sensors. *Angew Chem Int Ed Engl* **2008**, *47*, 6550-6570.

(108) Scott, S. M.; James, D.; Ali, Z. Data analysis for electronic nose systems. *Microchimica Acta* **2006**, *156*, 183-207.

(109) Rock, F.; Barsan, N.; Weimar, U. Electronic nose: current status and future trends. *Chem Rev* **2008**, *108*, 705-725.

(110) Baldwin, E. A.; Bai, J.; Plotto, A.; Dea, S. Electronic noses and tongues: applications for the food and pharmaceutical industries. *Sensors (Basel)* **2011**, *11*, 4744-4766.

(111) Di Natale, C.; Paolesse, R.; Martinelli, E.; Capuano, R. Solid-state gas sensors for breath analysis: a review. *Anal Chim Acta* **2014**, *824*, 1-17.

(112) Grate, J. W. Acoustic wave microsensor arrays for vapor sensing. *Chem Rev* **2000**, *100*, 2627-2648.

(113) Jurs, P. C.; Bakken, G. A.; McClelland, H. E. Computational methods for the analysis of chemical sensor array data from volatile analytes. *Chem Rev* **2000**, *100*, 2649-2678.

(114) Albert, K. J.; Lewis, N. S.; Schauer, C. L.; Sotzing, G. A.; Stitzel, S. E.; Vaid, T. P.; Walt, D. R. Cross-reactive chemical sensor arrays. *Chem Rev* **2000**, *100*, 2595-2626.

(115) Spinelle, L.; Gerboles, M.; Kok, G.; Persijn, S.; Sauerwald, T. Review of Portable and Low-Cost Sensors for the Ambient Air Monitoring of Benzene and Other Volatile Organic Compounds. *Sensors (Basel)* **2017**, *17*.

(116) Zrodnikov, Y.; Rajapakse, M. Y.; Peirano, D. J.; Aksenov, A. A.; Kenyon, N. J.; Davis, C. E. High Asymmetric Longitudinal Field Ion Mobility Spectrometry Device for Low Power Mobile Chemical Separation and Detection. *Anal Chem* **2019**, *91*, 5523-5529.

(117) Wales, D. J.; Grand, J.; Ting, V. P.; Burke, R. D.; Edler, K. J.; Bowen, C. R.; Mintova, S.; Burrows, A. D. Gas sensing using porous materials for automotive applications. *Chem Soc Rev* **2015**, *44*, 4290-4321.

(118) Reyes-Garces, N.; Gionfriddo, E.; Gomez-Rios, G. A.; Alam, M. N.; Boyaci, E.; Bojko, B.; Singh, V.; Grandy, J.; Pawliszyn, J. Advances in Solid Phase Microextraction and Perspective on Future Directions. *Anal Chem* **2018**, *90*, 302-360.

(119) Lord, H.; Pawliszyn, J. Evolution of solid-phase microextraction technology. *J Chromatogr A* **2000**, *885*, 153-193.

(120) Soria, A. C.; García-Sarrió, M. J.; Sanz, M. L. Volatile sampling by headspace techniques. *TrAC, Trends Anal Chem* **2015**, *71*, 85-99.

(121) Gallego, E.; Roca, F. J.; Perales, J. F.; Sanchez, G.; Esplugas, P. Characterization and determination of the odorous charge in the indoor air of a waste treatment facility through the evaluation of volatile organic compounds (VOCs) using TD-GC/MS. *Waste Manag* **2012**, *32*, 2469-2481.

(122) Stadler, S.; Stefanuto, P. H.; Brokl, M.; Forbes, S. L.; Focant, J. F. Characterization of volatile organic compounds from human analogue decomposition using thermal desorption coupled to comprehensive two-dimensional gas chromatography-time-of-flight mass spectrometry. *Anal Chem* **2013**, *85*, 998-1005.

(123) Zhao, Y.; Kreisberg, N. M.; Worton, D. R.; Teng, A. P.; Hering, S. V.; Goldstein, A. H. Development of an In Situ Thermal Desorption Gas Chromatography Instrument for Quantifying Atmospheric Semi-Volatile Organic Compounds. *Aerosol Sci Technol* **2012**, *47*, 258-266.

(124) Isaacman, G.; Kreisberg, N. M.; Yee, L. D.; Worton, D. R.; Chan, A. W. H.; Moss, J. A.; Hering, S. V.; Goldstein, A. H. Online derivatization for hourly measurements of gas- and particle-phase semi-volatile oxygenated organic compounds by thermal desorption aerosol gas chromatography (SV-TAG). *Atmos Meas Tech* **2014**, *7*, 4417-4429.

(125) Rahman, M.; El-Aty, A.; Choi, J.-H.; Shin, H.-C.; Shin, S. C.; Shim, J.-H.: Basic Overview on Gas Chromatography Columns. 2015.

(126) Supelco. GC Column Selection Guide[Online early access]2013.

(127) Vickers, A. K.: PLOT Column Selection. 2000.

(128) Hartmann, C. H. Gas Chromatography Detectors. *AnaCh* **2012**, *43*, 113A-125A.

(129) Driscoll, J. N. Evaluation of a New Photoionization Detector for Organic-Compounds. *J Chromatogr* **1977**, *134*, 49-55.

(130) Ghosh, A.; Johnson, J. E.; Nuss, J. G.; Stark, B. A.; Hawkins, A. R.; Tolley, L. T.; Iverson, B. D.; Tolley, H. D.; Lee, M. L. Extending the upper temperature range of gas chromatography with all-silicon microchip columns using a heater/clamp assembly. *J Chromatogr A* **2017**, *1517*, 134-141.

(131) Zhu, H.; Nidetz, R.; Zhou, M.; Lee, J.; Buggaveeti, S.; Kurabayashi, K.; Fan, X. Flow-through microfluidic photoionization detectors for rapid and highly sensitive vapor detection. *Lab Chip* **2015**, *15*, 3021-3029.

(132) Zhu, H.; Zhou, M.; Lee, J.; Nidetz, R.; Kurabayashi, K.; Fan, X. Low-Power Miniaturized Helium Dielectric Barrier Discharge Photoionization Detectors for Highly Sensitive Vapor Detection. *Anal Chem* **2016**, *88*, 8780-8786.

(133) Pijolat, C.; Camara, M.; Courbat, J.; Viricelle, J.; Briand, D.; Derooij, N. Application of carbon nano-powders for a gas micro-preconcentrator. *Sensors Actuators B: Chem* **2007**, *127*, 179-185.

(134) Yeom, J.; Field, C. R.; Bae, B.; Masel, R. I.; Shannon, M. A. The design, fabrication and characterization of a silicon microheater for an integrated MEMS gas preconcentrator. *Journal of Micromechanics and Microengineering* **2008**, *18*, 125001.

(135) McCartney, M. M.; Zrodnikov, Y.; Fung, A. G.; LeVasseur, M. K.; Pedersen, J. M.; Zamuruyev, K. O.; Aksenov, A. A.; Kenyon, N. J.; Davis, C. E. An Easy to Manufacture Micro Gas Preconcentrator for Chemical Sensing Applications. *ACS Sens* **2017**, *2*, 1167-1174.

(136) Akbar, M.; Wang, D.; Goodman, R.; Hoover, A.; Rice, G.; Heflin, J. R.; Agah, M. Improved performance of micro-fabricated preconcentrators using silica nanoparticles as a surface template. *J Chromatogr A* **2013**, *1322*, 1-7.

(137) Manginell, R. P.; Adkins, D. R.; Moorman, M. W.; Hadizadeh, R.; Copic, D.; Porter, D. A.; Anderson, J. M.; Hietala, V. M.; Bryan, J. R.; Wheeler, D. R.; Pfeifer, K. B.; Rumpf, A. Mass-Sensitive Microfabricated Chemical Preconcentrator. *JMemS* **2008**, *17*, 1396-1407.

(138) Camara, E. H. M.; Breuil, P.; Briand, D.; Guillot, L.; Pijolat, C.; de Rooij, N. F. Micro gas preconcentrator in porous silicon filled with a carbon absorbent. *Sensors Actuators B: Chem* **2010**, *148*, 610-619.

(139) Camara, E. H.; Breuil, P.; Briand, D.; de Rooij, N. F.; Pijolat, C. A micro gas preconcentrator with improved performance for pollution monitoring and explosives detection. *Anal Chim Acta* **2011**, *688*, 175-182.

(140) Wei-Cheng, T.; Pang, S. W.; Chia-Jung, L.; Zellers, E. T. Microfabricated preconcentrator-focuser for a microscale gas chromatograph. *JMemS* **2003**, *12*, 264-272.

(141) Martin, M.; Crain, M.; Walsh, K.; McGill, R. A.; Houser, E.; Stepnowski, J.; Stepnowski, S.; Wu, H.-D.; Ross, S. Microfabricated vapor preconcentrator for portable ion mobility spectroscopy. *Sensors Actuators B: Chem* **2007**, *126*, 447-454.

(142) Wei-Cheng, T.; Chan, H. K. L.; Chia-Jung, L.; Pang, S. W.; Zellers, E. T. Multiple-stage microfabricated preconcentrator-focuser for micro gas chromatography system. *JMemS* **2005**, *14*, 498-507.

(143) Wong, M. Y.; Cheng, W. R.; Liu, M. H.; Tian, W. C.; Lu, C. J. A preconcentrator chip employing mu-SPME array coated with in-situ-synthesized carbon adsorbent film for VOCs analysis. *Talanta* **2012**, *101*, 307-313.

(144) Gràcia, I.; Ivanov, P.; Blanco, F.; Sabaté, N.; Vilanova, X.; Correig, X.; Fonseca, L.; Figueras, E.; Santander, J.; Cané, C. Sub-ppm gas sensor detection via spiral μ-preconcentrator. *Sensors Actuators B: Chem* **2008**, *132*, 149-154.

(145) Bryant-Genevier, J.; Zellers, E. T. Toward a microfabricated preconcentrator-focuser for a wearable micro-scale gas chromatograph. *J Chromatogr A* **2015**, *1422*, 299-309.

(146) Alfeeli, B.; Taylor, L. T.; Agah, M. Evaluation of Tenax TA thin films as adsorbent material for micro preconcentration applications. *Microchem J* **2010**, *95*, 259-267.

(147) Narayanan, S.; Agah, M. Fabrication and Characterization of a Suspended TCD Integrated With a Gas Separation Column. *JMemS* **2013**, *22*, 1166-1173.

(148) Radadia, A. D.; Salehi-Khojin, A.; Masel, R. I.; Shannon, M. A. The effect of microcolumn geometry on the performance of micro-gas chromatography columns for chip scale gas analyzers. *Sensors Actuators B: Chem* **2010**, *150*, 456-464.

(149) Boogaerts, T.; Verstappe, M.; Verzele, M. Experiments with Static and Dynamic Coating Procedures for Glass Capillary Columns. *J Chromatogr Sci* **1972**, *10*, 217-219.

(150) Yang, L.; Qin, M.; Yang, J.; Zhang, G.; Wei, J. Review on stationary phases and coating methods of MEMs gas chromatography columns. *Rev Anal Chem* **2020**, *39*, 247-259.

(151) Restek's PLOT Column Family - The Benchmark for Performance. https://www.restek.com/Technical-Resources/Technical-Library/Petroleum-Petrochemical/Restek-s-PLOT-Column-Family-PCSS1163G-UNV.

(152) Ji, Z.; Hutt, S. A new bonded porous polymer PLOT U column with increased polarity. *J Chromatogr Sci* **2000**, *38*, 496-502.

(153) Sidel'nikov, V. N.; Nikolaeva, O. A.; Platonov, I. A. Stationary Phases Deposition on the Planar Columns Capillaries. *Prot Met Phys Chem* **2015**, *51*, 1065-1075.

(154) Szulczyński, B.; Gębicki, J. Currently Commercially Available Chemical Sensors Employed for Detection of Volatile Organic Compounds in Outdoor and Indoor Air. *Environments* **2017**, *4*, 21.

(155) Cho, B.; Lee, K.; Jo, E.; Kim, J. Detection of Mixed BTEX With Suppressed Reaction Specificity Using Tin Oxide Nanoparticles Functionalized by Multi-Metalloporphyrins. *IEEE Sens J* **2019**, *19*, 11791-11796.

(156) Mirzaei, A.; Kim, J.-H.; Kim, H. W.; Kim, S. S. Resistive-based gas sensors for detection of benzene, toluene and xylene (BTX) gases: a review. *Journal of Materials Chemistry C* **2018**, *6*, 4342-4370.

(157) Carapezza, E. M.; Patel, S. V.; Hobson, S. T.; Cemalovic, S.; Mlsna, T. E. Chemicapacitive microsensors for detection of explosives and TICs. **2005**, *5986*, 59860M.

(158) Freedman, A. N. The photoionization detector: Theory, performance and application as a low-level monitor of oil vapour. *J Chromatogr A* **1980**, *190*, 263-273.

(159) Driscoll, J. N.; Duffy, M. Photoionization detector: A versatile tool for environmental analysis. *Chromatography* **1987**, *2*, 21-27.

(160) Coelho Rezende, G.; Le Calvé, S.; Brandner, J. J.; Newport, D. Micro photoionization detectors. *Sensors Actuators B: Chem* **2019**, *287*, 86-94.

Chapter 2 Microcolumn Development for Portable µGC

2.1 Introduction

2.1.1 Background

Conventional separation and analysis of volatile compounds is commonly performed using benchtop gas chromatography (GC) systems equipped with long separation columns often of 30 or 60 m in length. While these long columns provide powerful separation capabilities, they also result in long analysis times, high power consumption, and high head pressure requirements, which hinders the use of benchtop GC for on-site analysis and real-time monitoring. Miniaturized and microfabricated columns for micro gas chromatography (µGC) are thus currently in development to address these issues and enable GC use in field applications[1-13]. Monolithic integration of these microcolumns with heaters and other micro-components allows for dead volume minimization and rapid, highly uniform column heating, enabling their use for fast, low-power, and portable µGC technology[1-3,5,7,9,11,13-16]. More recently, optimization of fluidic channel layouts, column chip material, and channel cross-section shapes has improved microcolumn efficiency[1,3,4,6], while integration with temperature and pressure sensors has allowed for better characterization and control over column temperature and flow rate[1,3,7,14,16].

Current limitations that inhibit the more widespread use of microcolumns include stationary phase pooling in sharp corners (resulting in peak broadening)[1,3,4,6], lack of fine control over temperature and pressure programming[1,14,16], and limited variety of stationary phase coatings and techniques (when compared to commercial capillary columns)[17-20]. Currently in the literature, the most commonly used microcolumns are coated with either OV-1 or OV-5 coatings[1,4,6,7,10,14,16,21-23], with limited research having been directed at other coatings. While these traditional polydimethylsiloxane or 5% phenyl stationary phases are useful for general purpose separations, exploration of different microcolumn stationary phases and coating techniques is especially

critical to both improving the performance of and broadening the scope of portable μGC to more diverse and specialized separations.

This chapter discusses the development of microcolumn coatings targeting portable μGC environmental analysis as well as improving microcolumn performance and robustness. Focus is placed on analysis of a broad range of target chemicals, along with column performance and degradation in the presence of potentially harsh ambient conditions, especially humidity. Ultimately, development of different microcolumn coatings and coating techniques is aimed at expanding the range of practical applications that portable μGC systems can target. Some important applications and characteristics of special interest are discussed in following sections.

2.1.2 Microcolumn fabrication

The microcolumn fabrication process used in this chapter is shown in **Figure 2.1(A)**. A 3 μm thick layer of thermal oxide was grown on a double side polished silicon wafer and subsequently patterned using standard lithography processes. The exposed oxide was etched away in buffered hydrofluoric acid. The photoresist then was removed, and the wafer was aligned and patterned again to expose the inlets and outlets. A 160 μm deep trench was created via deep reactive ion etching. The photoresist was stripped again, and deep reactive ion etching was applied to the entire pattern area. The final column width and depth were both 160 μm, and the width and depth of the inlets and outlets were 400 μm. The final column length was 5 m. The wafer was subsequently anodically bonded with Borofloat 33 glass at 350 °C under vacuum. The heater was deposited on the back side of the column through physical vapor deposition and patterned by lift-off. Photos of the column and heater are provided in **Figure 2.1(B)**. Individual deactivation and coating methods are discussed subsequently.

2.1.3 Connection interface

The connection interface between microcolumn and other components is particularly important as a fragile interconnect prone to leakage or outgassing. A special interconnection method was developed to improve the robustness of the microcolumn connection interface. First, fused silica capillaries with outer diameters of 380 μm and inner diameters of 250 μm were inserted into the inlet and outlet of the microcolumn. Previously, adhesives such as Hysol® epoxy, polyimide, and Duraseal have been explored to form connection interfaces between

capillaries and microcolumn chips. While Hysol® epoxy can withstand the shear force induced by thermal expansion mismatch between adhesive and column at 300 °C, strong outgassing prevents operation beyond 200 °C. Polyimide is a thermally stable and outgassing-free material commonly used for GC column outer surface coating. However, poor adhesion between polyimide and silicon results in leakage after thermal cycling, which is exacerbated when the microcolumn is under high head pressure. Thus, a two-step gluing method using both polyimide and Hysol® epoxy was developed to form the connection interface (**Figure 2.2**).

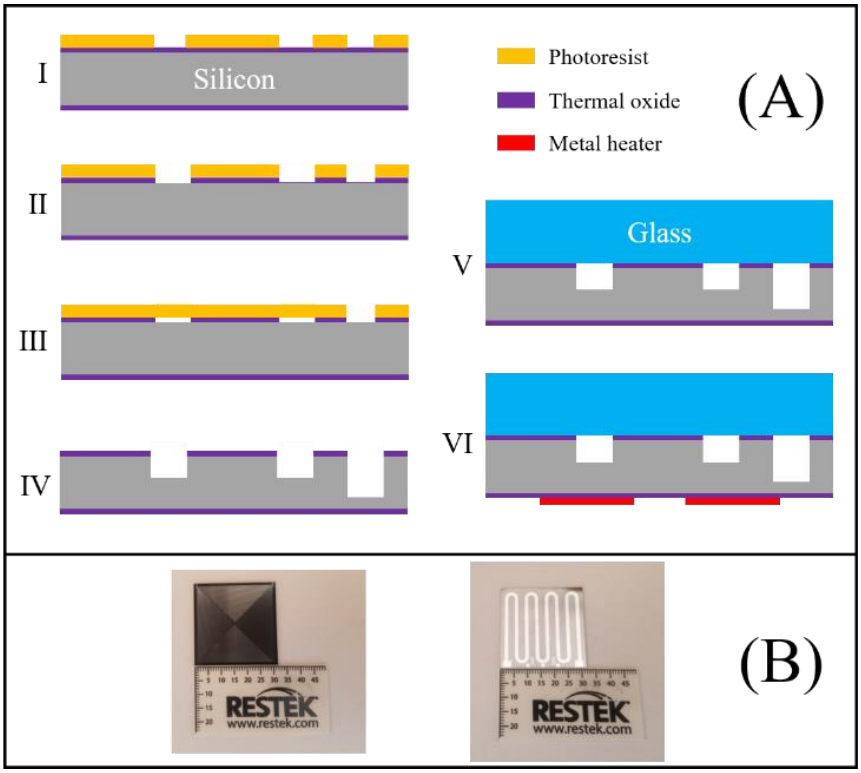

Figure 2.1. (A) Microcolumn fabrication processes. I. Soft mask of photoresist exposing both column and inlets/outlets. II. Creation of oxide hard mask through DRIE. III. Soft mask exposing only inlets/outlets for DRIE etching to 160 µm. IV. DRIE on the entire pattern area to etch inlets/outlets to 400 µm and column to 160 µm. V. Anodic bonding with Pyrex glass to seal the column. VI. Metal heater deposition on column backside. (B) Photographs of the front (column) and back (heater) sides of the microcolumn. The final column width and depth were both 160 µm. The total column length was 5 m.

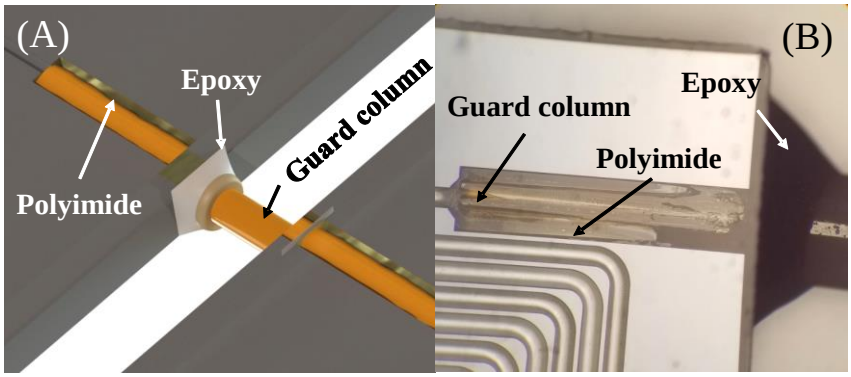

Figure 2.2. (A) Illustration of hybrid adhesive connection ports. (B) Photo of the connection port.

Polyimide was first applied to the outer capillary surface, serving as an "O-ring" to prevent chemicals released by Hysol® epoxy from entering the microcolumn. The capillaries were inserted into microcolumn inlet and outlet, and the chip was heated at 120 °C overnight to further cure the polyimide. Hysol® epoxy was subsequently applied to the outer surface of the connection interface and cured at 250 °C for two hours until the epoxy had become dark brown. Hysol® epoxy was then again applied to the outer surface of the connection interface and cured again at 250 °C for one hour. The connection was tested using a helium leak detector after 15 cycles up to 300 °C (ramping from 120 °C to 300 °C at 30 °C per min) and showed no signs of leakage or damage.

2.2 Microfabricated Porous Layer Open Tubular (PLOT) Column

2.2.1 Background

One of the major applications for portable μGC is environmental analysis of highly volatile compounds. EPA Methods 502, 524.2, and 8260 (B, C, D) list a wide range of volatile organic compounds (VOCs) that have varying degrees of toxicity or carcinogenicity; other light volatiles such as formaldehyde and light hydrocarbons are also of interest as common toxic air pollutants[24-31]. Since many common types of columns (e.g., packed, various polysiloxane and polyethylene glycol stationary phases) only weakly retain these light VOCs, porous layer open tubular (PLOT) columns have been developed as an alternative for separating these

compounds[17-19,24,32-42]. Previous research has highlighted alumina, molecular sieves, carbon sieves, metal-organic frameworks, covalent-organic frameworks, and porous polymers as PLOT column stationary phase materials[32,33,35-38]. Alumina is known to possess high specificity to light hydrocarbon VOCs, while molecular sieve stationary phases are capable of separating fixed gases such as O_2, N_2, and noble gases[17,19,32,35,37]. Divinylbenzene (DVB) polymers do not separate these compounds as strongly, but their excellent stability in the presence of moisture is a highly desirable property for field analysis, where varying ambient conditions can affect μGC separation characteristics[17,18,32,35,37]. Although many capillary based PLOT columns have been researched extensively and are now commercially available, little research has been directed towards the development of microfabricated PLOT columns for portable μGC, which considerably limits μGC applicability to analysis and monitoring of highly volatile VOCs.

This section reports the design, fabrication, and evaluation of a microfluidic PLOT column (μPLOT) with a DVB-based stationary phase. The fabrication and column coating procedures are detailed herein, and three benchmarks, i.e., separation of high volatility alkanes, formaldehyde solution, and organic solvents, are shown to demonstrate the μPLOT's ability to separate high volatility VOCs. Characterization of moisture and temperature robustness is also performed. These benchmarks show how the μPLOT can significantly broaden applications of μGC in field and environmental analysis of high volatility toxic and carcinogenic VOCs due to its small footprint, high moisture resilience, and rapid separation capabilities.

2.2.2 Experimental

2.2.2a PLOT microcolumn coating

The microcolumn was coated based on an optimized procedure adapted from previous research[33,43]. Prior to coating, the column was silanized by eight repeated injections of hexamethyldisilazane vapor under a 0.5 mL/min flow of helium. Following silanization, the column was washed sequentially with dichloromethane, water, and acetone. Subsequently, the column was filled with a 30 wt.-% solution of 3-(trimethoxysilyl)propyl methacrylate in acetone—in order to promote adhesion of the coating solution to the column wall—and left to react at room temperature overnight. The column was then washed with acetone and dried using nitrogen.

A polymerization mixture of 32% DVB, 8% styrene, 52% 1-octanol, 8% toluene, and azobisisobutyronitrile (1% wt. of DVB) was prepared and heated at 60 °C for 20 hours. The column was filled with solution, then dry air was used to push the solution out at a rate of 1 cm/min (approx. 2 psi pressure, see **Figure 2.3(A)**). A dummy column was attached to the end of the column during this process in order to maintain constant flow resistance. The column was subsequently purged with dry air and crosslinked at 80 °C for 2 hours, followed by post deactivation using hexamethyldisilazane and subsequent baking at 200 °C for 2 hours. The coating process was repeated by filling the column with the same polymerization mixture and pushing the solution out at 1 cm/min, this time without a dummy column (approx. 2 psi pressure). The second coating step ensured a sufficient coating thickness and enhanced the separation capability of the μPLOT. The column was crosslinked, deactivated, and baked again (200 °C for 2 hours followed by 300 °C for 2 hours). A photo of the coated column is provided in **Figure 2.3(B)**.

2.2.2b Experimental setup

The μPLOT was evaluated on all separations in an Agilent 6890 benchtop GC equipped with an injection port and a flame ionization detector (FID). Temperature ramping was controlled by the GC oven. Ultra-high purity 5.0 grade helium was used as the carrier gas.

2.2.3 μPLOT characterization

2.2.3a PLOT stationary phase characterization

To characterize the polymer stationary phase, the μPLOT was frozen in liquid nitrogen and cut open. The stationary phase was imaged by scanning electron microscopy (SEM), which allowed for observation of the polymer's porous nature (**Figure 2.3(C)**). The stationary phase tends to pool around the corners of the microcolumn, which does not occur for regular capillary columns (**Figure 2.3(D)**). The average film thickness along the column wall is estimated by approximately calculating the area of the stationary phase pooled at the corners (using triangular approximations) and dividing by the total cross-section border length (~630 μm). This yielded an average film thickness of 1.83 μm. Experimentation with the coating thickness showed that the second coating step described in the "Microcolumn coating" section is important to ensure a

porous layer with sufficient thickness. Inferior separation performance was observed with μPLOT columns with a single coating step.

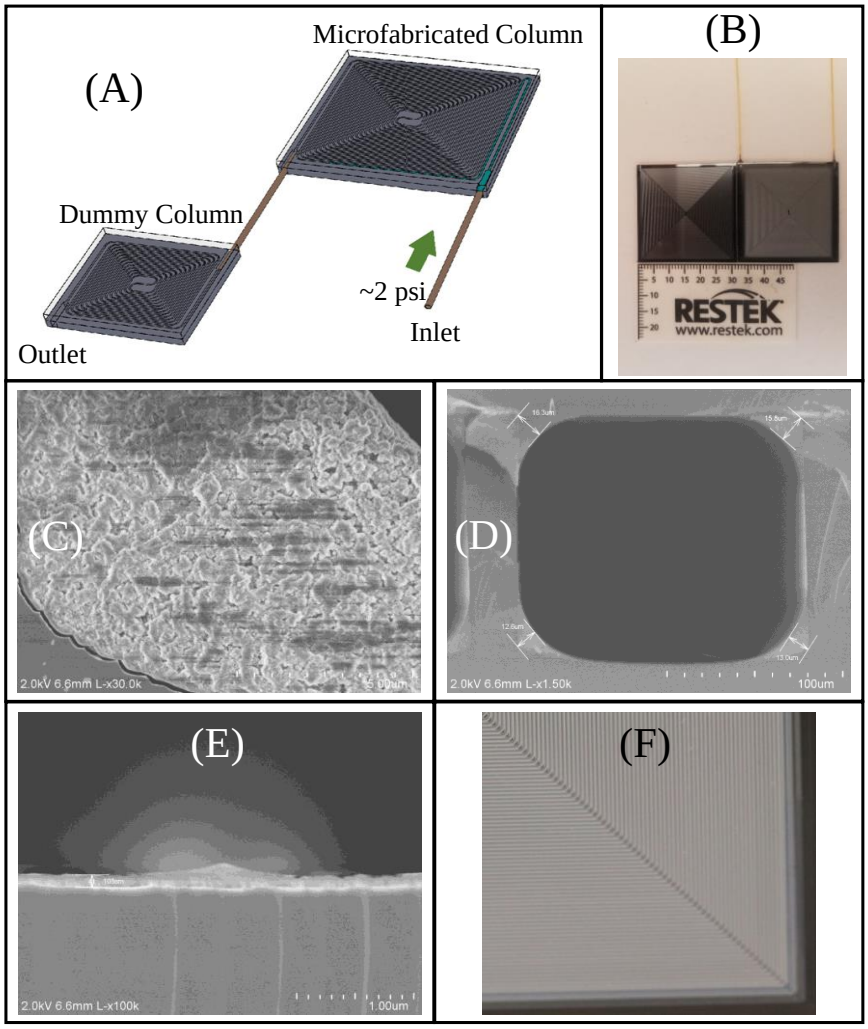

Figure 2.3. (A) Microcolumn coating setup. The column was statically coated by filling with the polymerization mixture and subsequently pushing the mixture out with a pressure of 2 psi. The microcolumn was coated a second time using the same 2 psi pressure and the same polymerization mixture without the dummy column. (B) Photograph of the μPLOT (right) with an uncoated microcolumn (left) for comparison. (C) SEM image of μPLOT porous polymer coating inside the silicon channel. (D) Image of film coating on the channel cross section, with stationary phase pooling observed at column corners. The thickest porous layer at the corner ranges from about 13-16 μm. The average thickness of the porous layer along the border is about

1.83 µm. (E) Zoom in of the column wall with a coating thickness of approximately 108 nm. This thickness was not included in the calculation for average film thickness due to being much smaller than the amount of stationary phase pooled at the column corners. (F) Zoom in of the coated column surface pattern.

2.2.3b Separation of high volatility alkanes

The ability to separate light hydrocarbons is essential for GC columns and has applications in the petroleum industry, feedstock products, and environmental monitoring[11,24,35,36,38,39]. This benchmark presents analysis of highly volatile alkanes, C_1 to C_6. The temperature was ramped from 40 °C to 160 °C at 30 °C per min at a carrier gas flow rate of 3 mL/min (measured at 40 °C). The resulting chromatogram is presented in **Figure 2.4**. All six alkanes are clearly separated by the µPLOT, with retention times and full widths at half maxima (FWHMs) reported in **Table 2.1**. Tailing factors are also provided and are used for discussion in 2.2.3d Separation of organic solvents and moisture robustness.

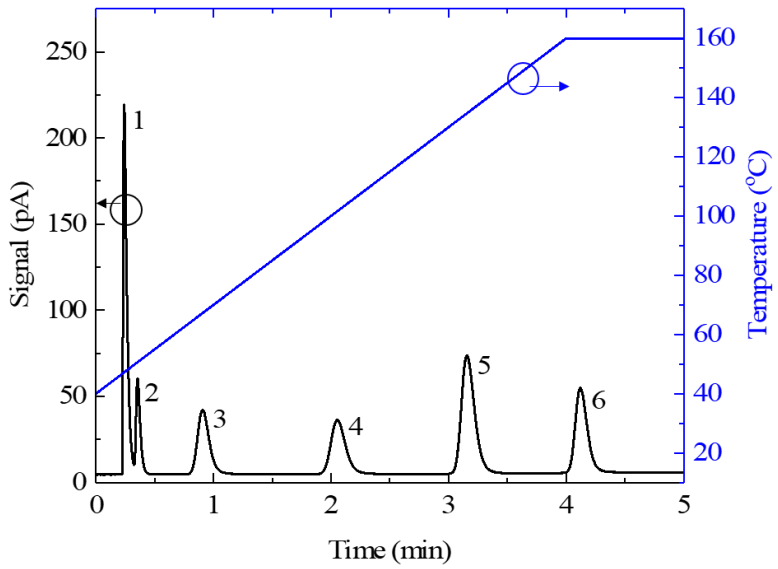

Figure 2.4. Separation of light alkanes. A splitless injection of 10 µL of headspace vapor from a mixture of the 6 alkanes was made. Carrier gas flow rate: 3 mL/min at 40 °C. 1. Methane; 2. Ethane; 3. Propane; 4. Butane; 5. Pentane; 6. Hexane. Analysis is provided in **Table 2.1**.

	Retention Time (min)	FWHM (min)	Tailing Factor
Methane(1)	0.2416	0.0337	2.5372
Ethane(2)	0.3551	0.0385	1.3229*
Propane(3)	0.9083	0.1088	1.2687
Butane(4)	2.0521	0.1370	1.2694
Pentane(5)	3.1556	0.1245	1.3325
Hexane(6)	4.1236	0.1140	1.2838

Table 2.1. Analysis of µPLOT separation of C_1 to C_6 alkanes. Not all tailing factors could be directly calculated using Eq. 2.2; these are marked with a * and are calculated by using the lowest possible peak height instead (ethane(2): 9%).

2.2.3c Formaldehyde separation

Formaldehyde is a colorless, odorous gas widely used in building materials and household products, and also serves as a preservative for tissue fixation. A causal relationship between exposure to formaldehyde and cancer in humans has been determined by various epidemiological studies, leading to increasing concern over industrial and environmental monitoring of airborne exposure[25-31,44]. Previous research has shown that sensitive formaldehyde detection is possible via portable GC separation using a Restek Q-BOND PLOT column[45].

The following benchmark (**Figure 2.5**) demonstrates the µPLOT's ability to replicate this separation, suggesting that the µPLOT may be used as an alternative to commercial capillary columns for portable µGC devices. A mixture of formaldehyde solution (containing, additionally, water and methanol), ethanol, and 1-propanol was used for injection. The temperature was ramped from 120 °C to 180 °C at 30 °C per min with a carrier gas flow rate of 1.1 mL/min (measured at 120 °C). The formaldehyde peak is relatively small, and the water peak is absent due to the FID's poor sensitivity to these chemicals. **Figure 2.5** shows that formaldehyde is fully separated from methanol, ethanol, and 1-propanol with a retention time of 1.389 min and peak FWHM of 0.073 min. Resolutions between adjacent peaks (defined by Eq. 2.1) are provided in **Table 2.2**.

$$R = 1.18 \times \frac{t_2 - t_1}{w_1 + w_2}, (2.1)$$

where t_1 and t_2 are the retention times of the first and second peaks, respectively. w_1 and w_2 are the FWHMs of the first and second peaks, respectively.

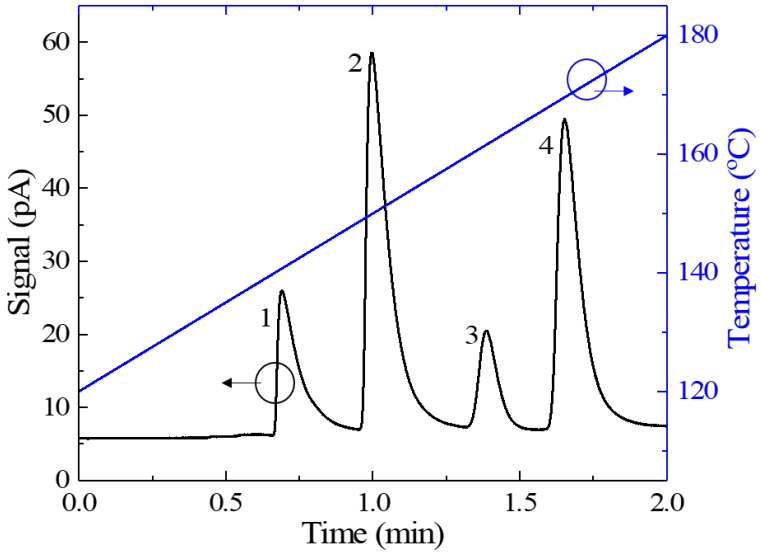

Figure 2.5. Separation of formaldehyde from methanol, ethanol, and 1-proponal. 200 µL of headspace vapor from a formaldehyde solution (37 wt.-% in water with 10-15% of methanol as a stabilizer) was mixed with 50 µL of headspace vapor from a mixture of ethanol and 1-propanol and injected in splitless mode. Carrier gas flow rate: 1.1 mL/min at 120 °C. 1. Methanol; 2. Ethanol; 3. Formaldehyde; and 4. 1-propanol. Analysis is provided in **Table 2.2**.

Since pure formaldehyde is highly reactive, stress testing of the µPLOT was performed by repeated injections of formaldehyde vapor to assess potential column degradation. The formaldehyde solution was heated to 80 °C to increase the sample volatility prior to injection. 200 µL vapor samples were drawn from the headspace and injected 30 times using the same temperature profile and flow rate as above. The formaldehyde solution was then allowed to cool, and separation of methanol, ethanol, 1-propanol, and formaldehyde was performed again post-stress testing. Analysis of retention times, FWHMs, and resolutions shows that injection of formaldehyde vapor caused no significant degradation of the column stationary phase (see **Table**

2.2, p-values between pre- and post- stress testing are all above 0.6, with a significance level of p = 0.05).

	Pre-Stress Test	Post-Stress Test	p-value
Methanol[(1)] RT	0.6748±0.014	0.6735±0.009	0.916
Methanol[(1)] FWHM	0.0752±0.005	0.0747±0.001	0.867
Ethanol[(2)] RT	0.9657±0.022	0.9583±0.017	0.709
Ethanol[(2)] FWHM	0.0783±0.004	0.0796±0.004	0.712
Formaldehyde[(3)] RT	1.3552±0.025	1.3476±0.018	0.726
Formaldehyde[(3)] FWHM	0.0773±0.005	0.0785±0.004	0.791
1-Propanol[(4)] RT	1.6100±0.033	1.6101±0.018	0.995
1-Propanol[(4)] FWHM	0.0878±0.005	0.0884±0.004	0.863
Resolution (1,2)	2.2472±0.186	2.1820±0.126	0.672
Resolution (2,3)	2.9636±0.173	2.9134±0.155	0.744
Resolution (3,4)	1.8288±0.166	1.8598±0.097	0.784

Table 2.2. Analysis of µPLOT separation of methanol[(1)], ethanol[(2)], formaldehyde[(3)], and 1-propanol[(4)] pre- and post- stress testing. Retention times (RT), FWHMs, and resolutions are provided as averages over 5 runs with corresponding standard deviations. p-values are calculated between pre- and post- stress testing values, with significance taken at p = 0.05. All p-values are greater than 0.6, showing no significant difference after stress testing with formaldehyde vapor.

2.2.3d Separation of organic solvents and moisture robustness

This benchmark has two main purposes. First, organic solvents are used in a wide variety of industries (e.g., pharmaceuticals, manufacturing, and agriculture), many of which are listed as toxic or carcinogenic. Real time monitoring of these compounds by portable µGC would be facilitated by efficient separation via the µPLOT. Second, the stability and performance of separation columns—especially those for field applications—in the presence of moisture is of concern for samples containing water or solvents. Since moisture can affect retention times and result in peak tailing and broadening, a hydrophobic stationary phase (i.e., DVB) can reduce the severity of these effects. In this benchmark, a sample of ten solvents (**Table 2.3**) was separated

by the µPLOT, as shown in **Figure 2.6**. The temperature was ramped from 140 °C to 200 °C at 30 °C per min with a carrier gas flow rate of 1.1 mL/min (measured at 140 °C). Retention times and peak FWHMs are provided in **Table 2.3**.

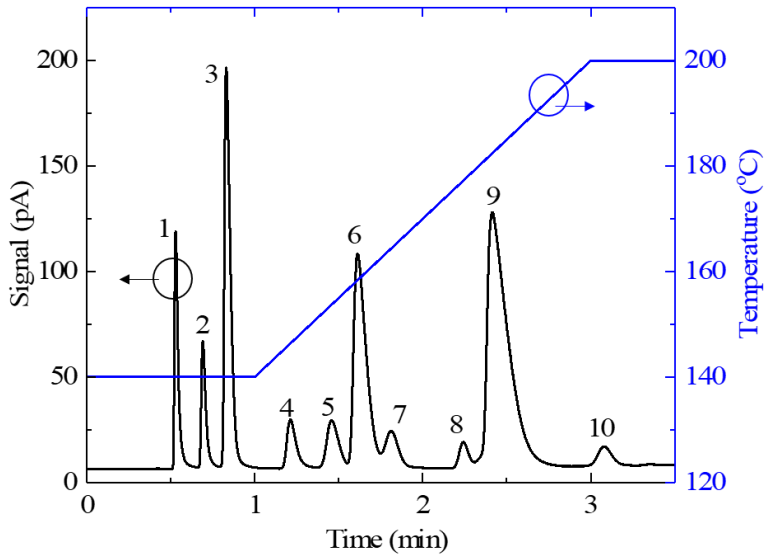

Figure 2.6. Separation of organic solvents. A splitless injection of 100 µL of headspace vapor from a mixture of the 10 solvents was made. Carrier gas flow rate: 1.1 mL/min at 140 °C. 1. Methanol; 2. Ethanol; 3. Dichloromethane; 4. 2-butanone; 5. 1-propanol; 6. 1,2-dichloroethane; 7. Chloroform; 8. 1-butanol; 9. 1,4-dioxane; 10. Tetrachloroethylene. Analysis is provided in **Table 2.3**.

Robustness against moisture was assessed by examining peak shapes. **Table 2.3** also reports the tailing factor (defined in Eq. 2.2) for each peak.

$$TF = \frac{p_t - p_f}{2(p_m - p_f)}, \quad (2.2)$$

where p_f is time of the peak front (at 5% of peak height), p_t is the time of the peak tail (also at 5% of peak height), and p_m is the time of the peak maximum (*i.e.* retention time).

A tailing factor of 1 represents a perfectly symmetric peak, but is not expected from the µPLOT due to stationary phase pooling in sharp microcolumn corners. The tailing factors in **Table 2.3** are instead compared to tailing factors calculated from the alkanes separation (**Table 2.1**), a gaseous sample containing no moisture. While, on average, tailing factors for the solvent

separation are higher than those for the alkane separation, peaks of similar heights (e.g., methane and methanol/dichloromethane, butane, and 2-butanone/tetrachloroethylene) show comparable tailing factors. This suggests that the effects of peak broadening and tailing in the solvent separation, if due to moisture, are relatively minor and may be byproducts of other factors such as separation parameters (temperature, flow rate), sampling injection amount, and varying retention for polar and nonpolar compounds.

	Retention Time (min)	FWHM (min)	Tailing Factor
Methanol(1)	0.5291	0.0222	1.9737
Ethanol(2)	0.6907	0.0282	1.7977
Dichloromethane(3)	0.8301	0.0388	1.8842
2-Butanone(4)	1.2122	0.0605	1.4656
1-Propanol(5)	1.4587	0.0785	1.2607*
1,2-Dichloroethane(6)	1.6109	0.0827	1.8831
Chloroform(7)	1.8119	0.0908	1.0093*
1-Butanol(8)	2.2416	0.0618	1.1705*
1,4-Dioxane(9)	2.4166	0.1317	2.1957
Tetrachloroethylene(10)	3.0791	0.0922	1.1676

Table 2.3. Retention times, FWHMs, and tailing factors of organic solvents separated by the µPLOT. Not all tailing factors could be directly calculated using Eq. 2; these are marked with a * and are calculated by using the lowest possible peak height instead (1-propanol(5): 11%, chloroform(7): 42%, 1-butanol(8): 27%).

Further assessment of the µPLOT's stability in the presence of moisture was examined by adding water to injected samples. 100 µL of headspace vapor from a formaldehyde solution (diluted to 20 wt.-% in methanol) was injected, along with 0, 100, 200, 300, and 400 µL of water vapor. The water was heated to 80 °C in order to increase the partial pressure in the headspace. The temperature was ramped from 90 °C to 150 °C at 30 °C per min with a carrier gas flow rate

of 2 mL/min (measured at 90 °C). Sample chromatograms are provided in **Figure 2.7(A)** and **(B)** (injections with 0 and 400 µL of water vapor). Retention times, peak widths, and tailing factors are analyzed in **Figure 2.8**. p-values between injections with 0 and 400 µL of water vapor are provided in **Table 2.4(A)** (significance taken at p = 0.05). All retention times and FWHMs show no significant difference when moisture is added to the sample, demonstrating the µPLOT's moisture resistance. Alkanes C_3 to C_6 were also injected with 0 and 500 µL of water vapor (heated to 80 °C) with a temperature ramping profile of 100 °C to 160 °C at 30 °C per min with a carrier gas flow rate of 1.3 mL/min (measured at 100 °C). Sample chromatograms are shown in **Figure 2.7(C)** and **(D)** and analysis is provided in **Table 2.4(B)**. No significant differences in retention times or FWHMs were observed. Additional information is provided in **Appendix A**.

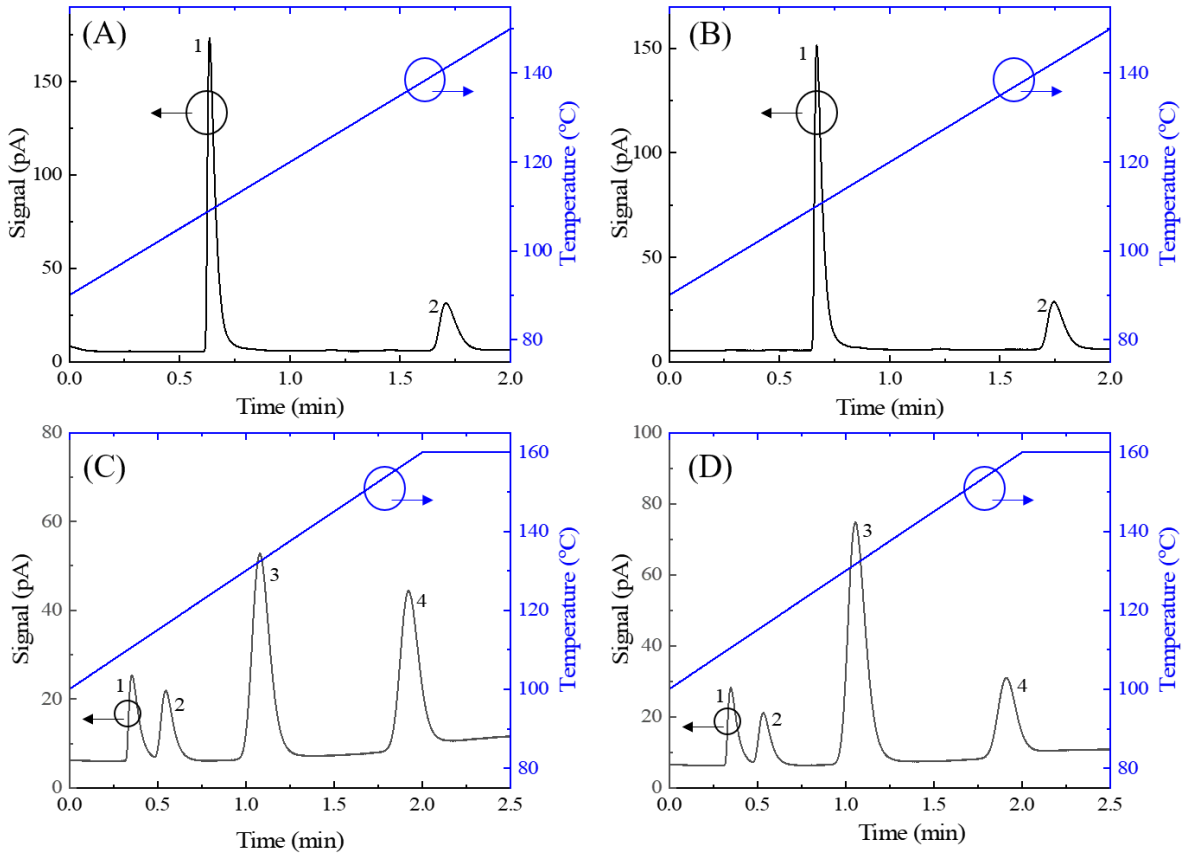

Figure 2.7. Separation of methanol[(1)] and formaldehyde[(2)] with no added moisture (A) and with 400 µL of additional water vapor (B). 100 µL of methanol and formaldehyde vapor was obtained from the headspace of the previously used formaldehyde solution diluted to 20 wt.-% in methanol. Carrier gas flow rate: 2 mL/min at 90 °C. Separation of propane[(1)], butane[(2)],

pentane[3], and hexane[4] with no added moisture (C) and with 500 µL of additional water vapor (D). A splitless injection of 5 µL of headspace vapor from a mixture of the alkanes was made. Carrier gas flow rate: 1.3 mL/min at 100 °C.

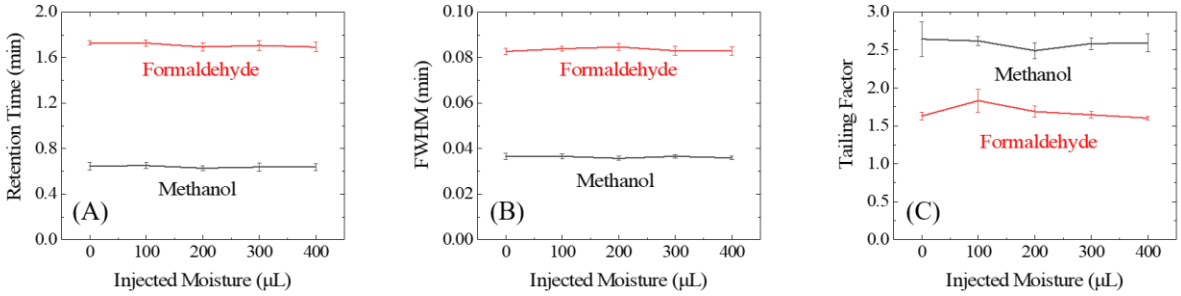

Figure 2.8. Methanol and formaldehyde retention times (A), FWHMs (B), and tailing factors (C) with 0 and 400 µL of injected moisture. Error bars represent one standard deviation and are calculated from 5 repetitions.

(A)	p-value
Methanol[1] RT	0.573
Methanol[1] FWHM	0.526
Formaldehyde[2] RT	0.554
Formaldehyde[2] FWHM	0.904
(B)	
Propane[1] RT	0.740
Propane[1] FWHM	0.419
Butane[2] RT	0.751
Butane[2] FWHM	0.947
Pentane[3] RT	0.732
Pentane[3] FWHM	0.704
Hexane[4] RT	0.710
Hexane[4] FWHM	0.457

Table 2.4. (A) p-values between retention times (RTs) and FWHMs of methanol and formaldehyde with no added moisture and 400 µL of added water vapor (5 runs each). (B) p-

values between RTs and FWHMs for C_3 to C_6 with no added moisture and 500 µL of added water vapor (5 runs each). Significance was taken at p = 0.05; all p-values are over 0.4, showing no significant difference in performance with added moisture.

2.2.3e Temperature robustness

The column's performance under high temperature was also analyzed by temperature ramping from 100 °C (held for 0.5 min) to 300 °C at 30 °C per minute with a carrier gas flow rate of 2 mL/min (measured at 100 °C). The bleed profile is provided in **Figure 2.9**. The average baseline ranged from 5.845 pA (measured from 0.01 to 0.5 min) to 15.374 pA (measured from 8 to 8.5 min). The relatively low stationary phase bleeding at 300 °C suggests that the µPLOT can be operated at high temperatures for separation of heavier compounds. However, operation at 300 °C with the µPLOT should be limited to a short amount of time. After heating the column to 250 °C for 3 hours, some degradation in performance was observed (only 9 of the solvents could be separated, with 1,2-dichloroethane and chloroform being coeluted with the same experimental parameters as in **Figure 2.6**). The column is robust at 210 °C, capable of sustaining over 14 h of operation at this temperature without noticeable degradation.

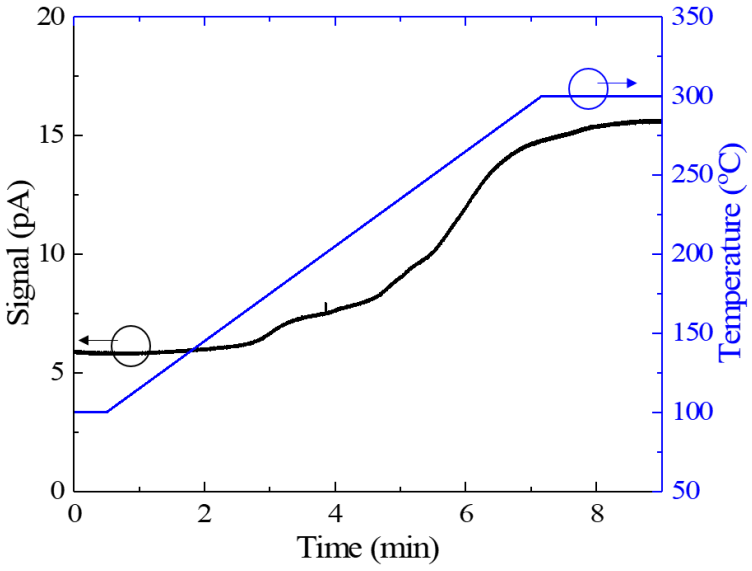

Figure 2.9. µPLOT bleed profile with temperature ramping to 300 °C.

2.2.3f Separation performance

The µPLOT's separation performance was compared with a commercial Restek Q-BOND PLOT column (see **Figure 2.10** and **Table 2.5**) by measuring each columns' height equivalent to the theoretical plate (HETP) with methanol and butane. The µPLOT's HETPs for methanol and butane were 1.156 and 0.974 mm, respectively, compared to the Q-BOND's 0.697 and 0.617 mm. The µPLOT's HETP is up to 66% higher than the Q-BOND's, which is likely due to stationary phase pooling (see *2.2.3a PLOT stationary phase* characterization) resulting in broader peaks and greater peak tailing. Another possible cause could be particles trapped within the column channel, which trap analytes and further increase broadening. Lower HETPs can be achieved by tuning the coating thickness.

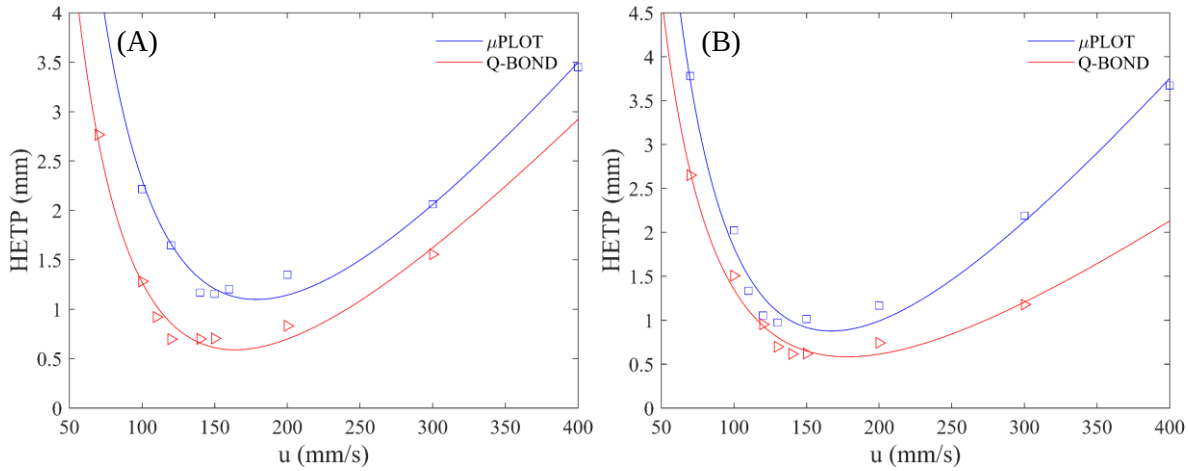

Figure 2.10. Golay plots with HETPs measured for µPLOT and a 5 m long RESTEK Q-BOND. (A) HETP for methanol at a temperature of 105 °C. (B) HETP for butane at a temperature of 130 °C. See **Table 2.5** for more information.

2.2.4 µPLOT summary

The microfabrication and coating of a chip-based PLOT column has been described herein. This µPLOT column demonstrated separation of light alkanes, formaldehyde solution, and organic solvents as well as robustness to moisture and temperatures of at least 210 °C. Combined with the µPLOT's small footprint, the ability to efficiently separate a wide range of highly volatile compounds makes the µPLOT highly suited for use in portable GC field analysis. In particular, the µPLOT can broaden µGC applicability to on-site monitoring of toxic and

carcinogenic compounds, many of which are light VOCs that are difficult to separate with other common stationary phases in existing microcolumns (e.g., polysiloxane or polyethylene glycol based). By enabling a method for real-time analysis of these VOCs, online environmental and pollution control also becomes possible.

	HETP (mm)
µPLOT in this work (Methanol)	1.156
µPLOT in this work (Butane)	0.974
Restek Q-BOND (Methanol)	0.697
Restek Q-BOND (Butane)	0.617
Ref. [46] (Butane)[46]	~0.2
Ref. [34] (Methanol)[34]	~0.25
Refs. [47] and [48] (Butane)[47,48]	~0.35

Table 2.5. Height equivalents to theoretical plates (HETPs) for divinylbenzene-based PLOT (µPLOT, Q-BOND, and Refs. [46] and [34]) and silica-based (Refs. [47] and [48]) porous layer columns. HETPs for the µPLOT and Q-BOND were measured based on optimized values obtained from Golay plots (see **Figure 2.10**). Other HETPs were estimated based on plots provided in the respective references.

2.3 Microfabricated Ionic Liquid Column for Separations in Dry Air

2.3.1 Background

While many advances have been made in recent years regarding the microfabrication and miniaturization of microcolumns, most current µGC stationary phase coating materials have low oxygen and moisture robustness, which leads to separation performance degradation with increased peak broadening and tailing[49]. These traits necessitate the use of bulky helium or nitrogen carrier gas cartridges and result in relatively large and heavy µGC systems. This increased size and weight are less suitable for field applications (especially those that require long-term unmanned operation). Previous studies have demonstrated systems using a carrier gas of ambient air[16,21,49-56]. However, these systems only permitted a limited selection of column

coating materials and temperature ranges (sometimes up to 150-200 °C[16,21,50,53-55], but not above this range especially for extended periods), which prohibits the general-purpose use of these systems in vapor sensing of a greater range of volatile compounds. Thus, in order to improve μGC portability and performance, it is necessary to develop microcolumns utilizing stationary phases capable of withstanding high moisture and oxygen exposure. Such stationary phases will allow for a broader range of VOC analysis using fewer μGC accessory components.

Previous work has demonstrated the versatile use of ionic liquids (IL) in GC separations, most notably as highly tunable compounds with unique separation capabilities[57-81]. By modifying the structure of the cation or anion, ILs can be tuned for separation of fatty acid methyl esters (FAMEs)[64,69,78,81-85], chiral compounds[67,74,80], nonpolar analytes[66,67,86], or aromatics and fragrances[57,59,63,65,72,73,76,81]. Some ILs also exhibit affinities to both dipolar and nonpolar solutes[59,70,74], allowing for separation of analytes of varying polarities with a single column. While the flexibility of different ILs is useful for development of highly tailored microcolumns, their moisture[62,67,70,73,77,80,87-90] and oxygen[58,59,73,75,79] resilience (or, ability to separate moisture and compounds containing oxygen – especially reactive oxygens such as formaldehyde) are greatly beneficial for microcolumns in portable GC systems. Many other column coatings are adversely impacted by moisture in samples and may require some form of moisture filtration; reactivity with oxygen at higher temperatures also necessitates the use of N_2, He, or H_2 carrier gas cartridges. By utilizing a suitable IL film instead, it becomes possible to develop a μGC device for which these accessories are no longer necessary, thus reducing the system's size and weight. Furthermore, the high-temperature resilience of many ILs[57,59,61,67,72,77,91-93] allows for more rapid separation of heavier compounds and therefore faster μGC analysis times. Some tradeoffs for eliminating the carrier gas cartridge may include addition of hydrocarbon filters, moisture filters for some systems (e.g. to maintain preconcentrator cleanliness rather than only prevent IL degradation), and particulate filters. These, however, can be inserted as inline fluidic or even microfluidic components, allowing them to be much smaller than the comparatively large carrier gas cartridge.

This section reports the design, fabrication, and evaluation of a wall coated open tubular microfluidic phosphonium ionic liquid (μIL) column. Fabrication and column coating procedures are detailed herein, and six separations, *i.e.*, separation of alcohols, chloroalkanes, aldehydes, aromatics, alkanes, and FAMEs, demonstrate the ionic liquid column's ability to separate both

polar and nonpolar compounds of varying volatilities using dry air as the carrier gas. Moisture and oxygen robustness characterized in the presence of dry air also show little to no column degradation due to moisture and slow degradation by oxygen at high temperatures. By showing the ability to separate a wide variety of compounds using a carrier gas of dry air, the μIL column demonstrates applicability to a wide range of μGC applications (*e.g.,* 2D μGC or ultracompact portable GC) by alleviating the need for auxiliary carrier gas cartridges through its high oxygen resilience.

2.3.2 Experimental

2.3.2a IL microcolumn coating

Prior to coating, the microcolumn was silanized by eight repeated injections of liquid hexamethyldisilazane under a 0.5 mL/min flow of helium at a temperature of 90 °C. Following silanization, the column was washed sequentially with dichloromethane, water, and acetone. A solution of ammonium hydrogen peroxide (APM) was prepared from a mixture of 10 mL of deionized water, 0.1 mL of H_2O_2 solution (30% w/w in aqueous solution), and 0.1 mL of NH_4OH (28-30% NH_3 w/w). 100 μL of the APM mixture was flowed through the column at a flow rate of 20 cm/min in order to roughen the silicon surface[94]. The column was then washed with acetone. Subsequently, a saturated solution of sodium chloride in dichloromethane was prepared at room temperature, sonicated, then diluted by adding 1 mL of solution to 5 mL of dichloromethane (and sonicated again)[95]. The column was filled with solution, allowed to stand for 2 hours, then emptied with dry air at a flow velocity of 5 cm/min.

400 mg of trihexyl(tetradecyl)phosphonium bis(trifluoromethyl sulfonyl)amide was added to 2 mL of diluted sodium chloride in dichloromethane (see above). The column was dynamically coated by filling with 300 μL of solution, then pushing the liquid out at a rate of 1 cm/min (approx. 5 psi pressure, see **Figure 2.3(A)** for fluidic connection). The column was subsequently purged with dry air and dried under a helium flow of 0.3 mL/min at 100 °C for 2 hours. The column was then aged at 200 °C for another 2 hours. A second column was coated using the same procedure, but using a further diluted sodium chloride solution for salt deposition (1 mL to 8 mL of dichloromethane) and a diluted ionic liquid solution (200 mg of ionic liquid added to 2 mL of solution) to demonstrate the capability for coating columns with different retention

characteristics. The second column was used for moisture and dry air stress testing analysis (see *2.3.3c Oxygen and moisture robustness*).

2.3.2b Experimental setup

The µIL column was evaluated on all separations in an Agilent 6890 benchtop GC equipped with an injection port and a flame ionization detector (FID). Manual injections were made, and the injection port was set to splitless unless otherwise stated. Temperature ramping was controlled by the GC oven. Dry air was used as the carrier gas.

2.3.3 µIL characterization

2.3.3a Separation of alcohols, chloroalkanes, aromatics, and aldehydes

This benchmark presents analysis of alcohols, chloroalkanes, aromatics, and aldehydes, *i.e.* separation of various groups of polar compounds. The following temperature ramping profiles were used: 30 °C (held for 1 min) to 190 °C, 40 °C (held for 2 min) to 190 °C, 50 °C (held for 1 min) to 170 °C, and 30 °C (held for 1 min) to 210 °C for alcohols, chloroalkanes, aromatics, and aldehydes, respectively. All temperature ramping rates were set to 30 °C/min and all flow rates were 2 mL/min (measured at each initial temperature). Resulting chromatograms are presented in **Figure 2.11**. All analytes are clearly separated by the µIL column, with retention times and FWHMs reported in **Table 2.6**. Golay plots for methanol and chlorobutane at 80 °C (isothermal) were generated (**Figure 2.12**) and optimized HETPs of 0.87 mm (k = 1.21 at 15 cm/s) and 0.95 mm (k = 1.42 at 7 cm/s) were obtained for methanol and chlorobutane, respectively, representing 1147 and 1051 plates per meter.

2.3.3b Separation of fatty acid methyl esters and alkanes

Trihexyl(tetradecyl)phosphonium bis(trifluoromethyl sulfonyl)amide columns have previously shown to offer efficient separation of fatty acid methyl esters (FAMEs)[64,69,78,81,82,84,85], which is useful for characterization of fats and oils in food. The following experiment (**Figure 2.13**) demonstrates the µIL column's ability to separate FAMEs from C6:00 to C15:00 with temperature ramping from 120 °C to 345 °C at 30 °C per min. The carrier gas flow rate was set to 2 mL/min at 120 °C. All FAMEs were fully separated, with retention times and FWHMs provided in **Table 2.7**. The average baseline signal varied from 5.51 pA (measured from 0.01 to

0.5 min) to 24.72 pA (measured from 7.2 to 7.5 min). A Golay plot for methyl caproate (C6:00) was obtained at 160 °C (isothermal, **Figure 2.12**) and an optimized HETP of 0.32 mm (k = 1.32 at 7 cm/s) was achieved, representing 3132 plates per meter.

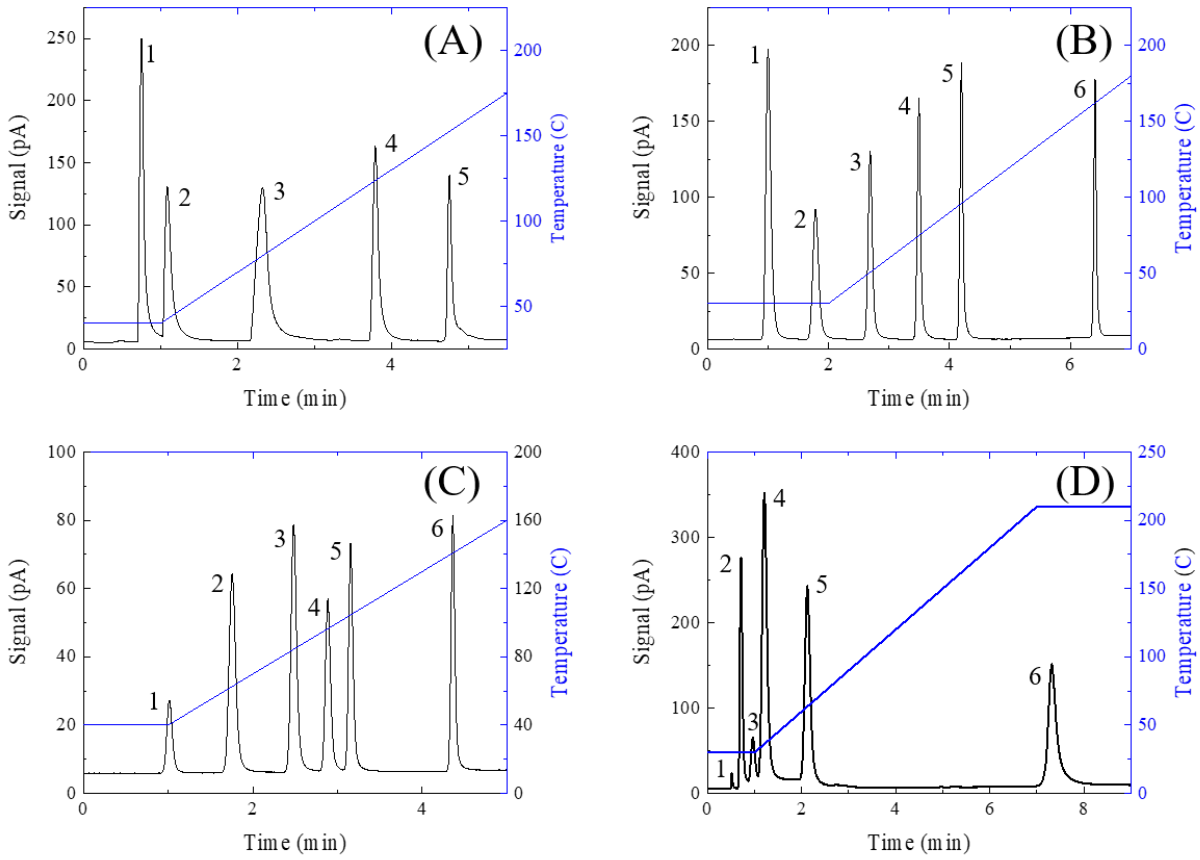

Figure 2.11. Separation of alcohols (A), chloroalkanes (B), aromatics (C), and aldehydes (D). Splitless injections of 0.04 µL of mixture liquids were made. Carrier gas flow rates: 2 mL/min at each initial temperature. Compound lists, elution orders, retention times, and FWHMs are provided in **Table 2.6**.

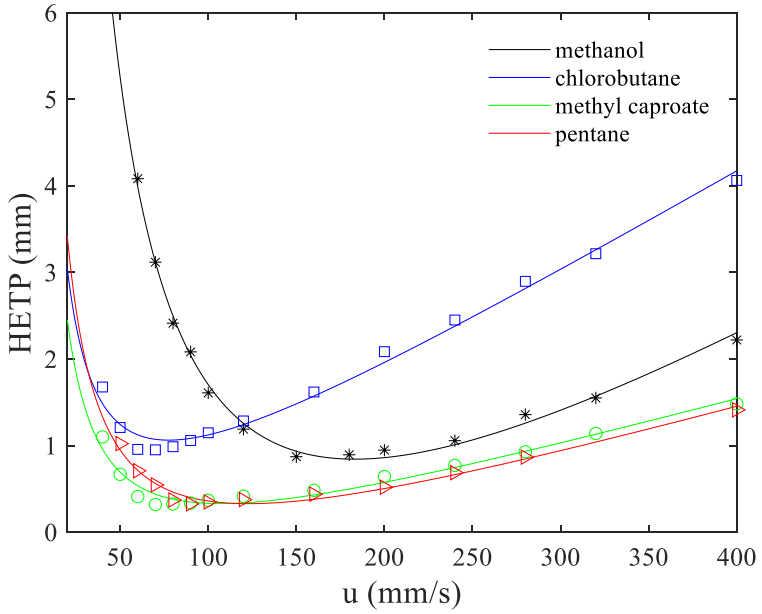

Figure 2.12. Golay plots for methanol, chlorobutane, methyl caproate, and pentane. The temperature was set to 80 °C for methanol and chlorobutane, 160 °C for methyl caproate, and 60 °C for pentane (isothermal at each temperature). Optimized HETPs: methanol – 0.87 mm; chlorobutane – 0.95 mm; methyl caproate – 0.32 mm; pentane – 0.33 mm.

(A)	RT	FWHM	(B)	RT	FWHM
(1) Methanol	0.754	0.0677	(1) Chlorobutane	1.000	0.1060
(2) Ethanol	1.088	0.0955	(2) Chloropentane	1.787	0.1220
(3) Propanol	2.324	0.1820	(3) Chlorohexane	2.690	0.0895
(4) Butanol	3.791	0.0890	(4) Chloroheptane	3.495	0.0703
(5) Pentanol	4.755	0.0648	(5) Chlorooctane	4.198	0.0612
			(6) Chlorododecane	6.407	0.0523
(C)			(D)		
(1) Benzene	1.011	0.0835	(1) Formaldehyde	0.514	0.0328
(2) Toluene	1.755	0.0987	(2) Acetaldehyde	0.710	0.0685
(3) Styrene	2.478	0.0837	(3) Methanol	0.962	0.1032
(4) Ethylbenzene	2.885	0.0787	(4) Propionaldehyde	1.210	0.1298
(5) o-Xylene	3.152	0.0658	(5) Butyraldehyde	2.123	0.1452
(6) 1,2-dichlorobenzene	4.360	0.0573	(6) Benzaldehyde	7.320	0.2145

Table 2.6. Retention times (RTs) and FWHMs of µIL separation of alcohols (A), chloroalkanes (B), aromatics (C), and aldehydes (D). Analytes are provided in order of elution for each separation. All values are provided in minutes.

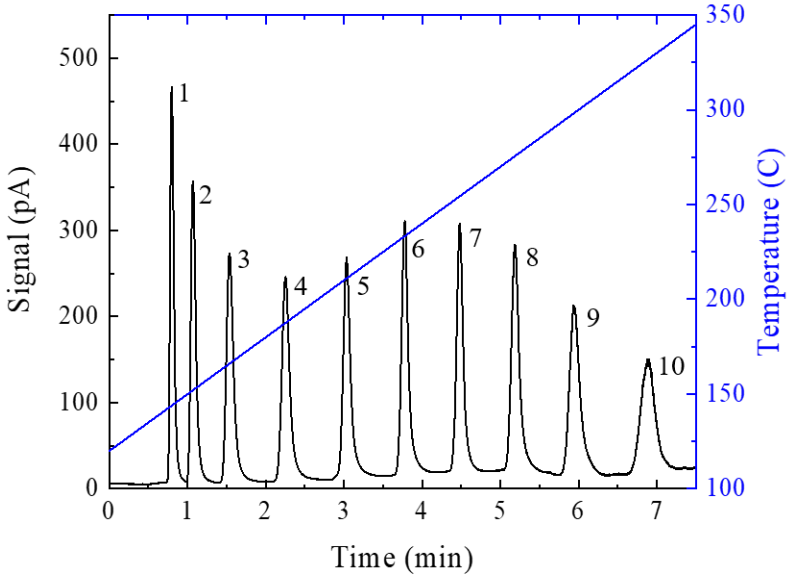

Figure 2.13. Separation fatty acid methyl esters. A splitless injection of 0.1 µL mixture liquid was made using a carrier gas flow rate of 2 mL/min at 120 °C. 1. C6:00; 2. C7:00; 3. C8:00; 4. C9:00; 5. C10:00; 6. C11:00; 7. C12:00; 8. C13:00; 9. C14:00; 10. C15:00. Analysis is provided in **Table 2.7**.

	RT	FWHM
(1) C6:00	0.797	0.0607
(2) C7:00	1.069	0.0809
(3) C8:00	1.536	0.1127
(4) C9:00	2.251	0.1159
(5) C10:00	3.033	0.1116
(6) C11:00	3.777	0.1058
(7) C12:00	4.477	0.1030
(8) C13:00	5.184	0.1213
(9) C14:00	5.936	0.1610
(10) C15:00	6.880	0.2270

Table 2.7. Retention times (RTs) and FWHMs of µIL column separation of FAMEs. All values are provided in minutes.

Analysis of alkanes ranging from C_5 to C_{24} was also performed, demonstrating the µIL column's ability to separate nonpolar analytes (note that FAMEs are also relatively nonpolar compared to the groups of analytes listed in the previous section). **Figure 2.14** demonstrates separation of these alkanes using a temperature ramping profile from 50 °C (held for 0.5 min) to 345 °C at 45 °C per min. The carrier gas flow rate was set to 3 mL/min at 50 °C. Again, all alkanes were fully separated, with C_5 and C_6 notably separated at 50 °C. Retention times and FWHMs are provided in **Table 2.8**. An optimized HETP of 0.33 mm (k = 0.68 at 9 cm/s) was obtained for pentane at 60 °C (isothermal, **Figure 2.12**), representing 3055 plates per meter. The average baseline signal varied from 5.63 pA (measured from 0.01 to 0.5 min) to 28.2 pA (measured from 12 to 12.6 min). Together with the baseline bleeding measured from the FAMEs separation, the µIL column's low bleed at 345 °C suggests that the column is stable at high temperatures for at least short periods, enabling rapid analysis of heavier compounds.

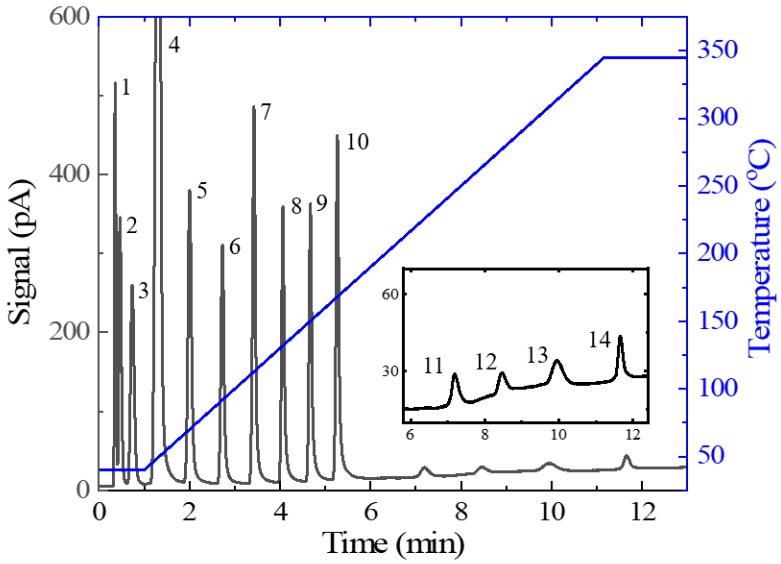

Figure 2.14. Separation C_5 to C_{24} alkanes. A splitless injection of 0.1 µL mixture liquid was made using a carrier gas flow rate of 3 mL/min at 50 °C. 1. Pentane; 2. Hexane; 3. Heptane; 4. Octane; 5. Nonane; 6. Decane; 7. Undecane; 8. Dodecane; 9. Tridecane; 10. Tetradecane; 11. Octadecane; 12. Eicosane; 13. Docosane; 14. Tetracosane. The inset provides a zoom-in of the octadecane, eicosane, docosane, and tetracosane peaks. Analysis is provided in **Table 2.8**.

	RT	FWHM
(1) C_5	0.357	0.0422
(2) C_6	0.465	0.0652
(3) C_7	0.733	0.1015
(4) C_8	1.313	0.1145
(5) C_9	2.002	0.0998
(6) C_{10}	2.729	0.0872
(7) C_{11}	3.427	0.0805
(8) C_{12}	4.066	0.0765
(9) C_{13}	4.674	0.0768
(10) C_{14}	5.272	0.0783
(11) C_{18}	7.191	0.2065
(12) C_{20}	8.473	0.2148
(13) C_{22}	9.963	0.3348
(14) C_{24}	11.652	0.1587

Table 2.8. Retention times (RTs) and FWHMs of µIL separation of C_5 to C_{24} alkanes. All values are provided in minutes.

2.3.3c Oxygen and moisture robustness

The µIL column's robustness to oxygen was tested by conditioning in dry air under elevated temperatures. Dry air was flowed through the column for 3 periods of 16 hours at 180 °C, 200 °C, and 220 °C for a total of 48 hours of conditioning. The flow rate was set to 0.5 mL/min at each temperature. Degradation in performance was analyzed on C_8 to C_{14} alkanes using a temperature profile of 40 °C (held for 1 min) to 190 °C at a temperature ramping rate of 30 °C/min with a flow rate of 2 mL/min measured at 40 °C. Chromatograms for the initial separation, after 16 hours (at 180 °C), after 32 hours (*i.e.,* 16 hours of 200 °C after the prior 16 hours), and after 48 hours (*i.e.,* 16 hours of 220 °C after the prior 32 hours) are provided in **Figure 2.15** (note that a mixture of C_5 to C_{14} was used, but since C_5 to C_7 were not well separated, only C_8 to C_{14} were analyzed).

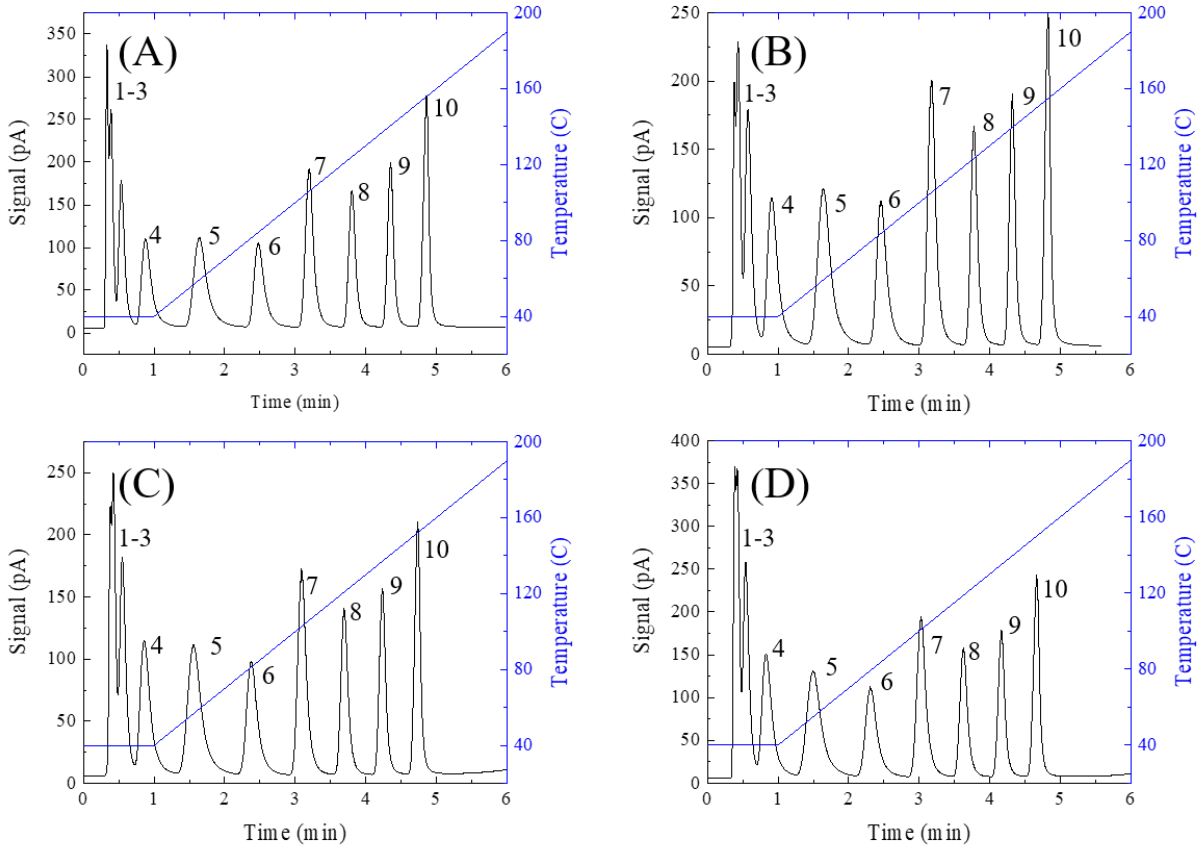

Figure 2.15. Separation of C_5 to C_{14} alkanes prior to conditioning (A), after 16 hours (B), after 32 hours (C), and after 48 hours (D). Splitless injections of 0.04 µL of mixture liquids were made. Carrier gas flow rate: 2 mL/min at 40 °C. 1. Pentane; 2. Hexane; 3. Heptane; 4. Octane; 5. Nonane; 6. Decane; 7. Undecane; 8. Dodecane; 9. Tridecane; 10. Tetradecane. Analysis is provided in **Table 2.9**.

Retention times and FWHMs were both gradually reduced with continuous conditioning and could not be directly compared to the original separation. Instead, resolutions between adjacent peaks (*e.g.*, between C_8 and C_9) were calculated using Eq. 2.1. A summation over all resolutions from C_8 to C_{14} (*i.e.*, $R_{\frac{C8}{C9}} + R_{\frac{C9}{C10}} + \cdots R_{\frac{C13}{C14}}$) yielded the peak capacity for each chromatogram (averaged over 5 runs). A gradual decrease in peak capacity was observed, from 18.05 prior to conditioning to 16.44 post-conditioning, a decrease of 8.92% after 48 hours of exposure to dry air at elevated temperatures (**Table 2.9**). In comparison, the peak capacity of a microfabricated OV-5-coated column was found to degrade from 37.28 to 30.32 after 16 hours of exposure to dry

air at 200 °C, representing an 18.67% decrease in performance (**Table 2.10**). When considering the maximum temperature used for this alkane separation (up to C_{14}), the column spends no more than 2 minutes above 180 °C on each run; therefore, the 48 hours of conditioning represents at least ~1500 runs with only an 8.92% reduction in performance. This low degradation rate demonstrates the μIL column's high robustness to oxygen in dry air, allowing for operation using a dry air carrier gas over extended periods. The lifetime of at least 48 hours of operation at elevated temperatures is expected to be more than sufficient for most portable GC applications.

	Peak Capacity
Initial	18.05
At 16 hours	17.92
At 32 hours	17.23
At 48 hours	16.44

Table 2.9. μIL column peak capacities calculated for C_8 to C_{14} alkanes after 16, 32, and 48 hours of exposure to dry air. Peak capacities are calculated by summing all resolutions between adjacent peaks (*i.e.,* summing resolutions between C_8/C_9, C_9/C_{10}… C_{13}/C_{14}). Peak capacity decreases with increased exposure to dry air, degrading by 8.92% at 48 hours.

	Peak Capacity
Initial	37.28
At 8 hours	33.02
At 16 hours	30.32

Table 2.10. Peak capacities of a microfabricated OV-5-coated column calculated for C_8 to C_{14} alkanes after 8 and 16 hours of exposure to dry air. Peak capacity decreases with increased exposure to dry air, degrading by 18.67% at 16 hours.

Finally, for field applications, a separation column's performance in the presence of moisture is of concern, especially for samples containing water and solvents. While moisture can affect

retention times and result in peak tailing and broadening (for normal columns such as OV-1 or OV-5 columns), ionic liquids have previously been shown to provide reasonable moisture resilience and the capacity to separate water[62,67,70,73,77,80,87,88]. To verify this, C_{10} to C_{14} alkanes were injected with and without added moisture (added concurrently into the syringe containing the alkane sample) using a temperature ramping profile of 100 °C (held for 0.5 min) to 220 °C at 60 °C/min with a flow rate of 1.2 mL/min (measured at 100 °C). 0.025 µL injections were made with no moisture, with 500 µL of water vapor (heated to 80 °C to increase the partial pressure in headspace), and with 1 µL of added liquid water (5 repetitions for each case). Sample chromatograms are provided in **Figure 2.16**. Comparisons between retention times and FWHMs between dry injections and injections with moisture were made using paired Student's t-tests and converting resulting T-scores to p-values. These retention times, FWHMs, and p-values are provided in **Table 2.11**. Peak capacities are provided in **Table 2.12**.

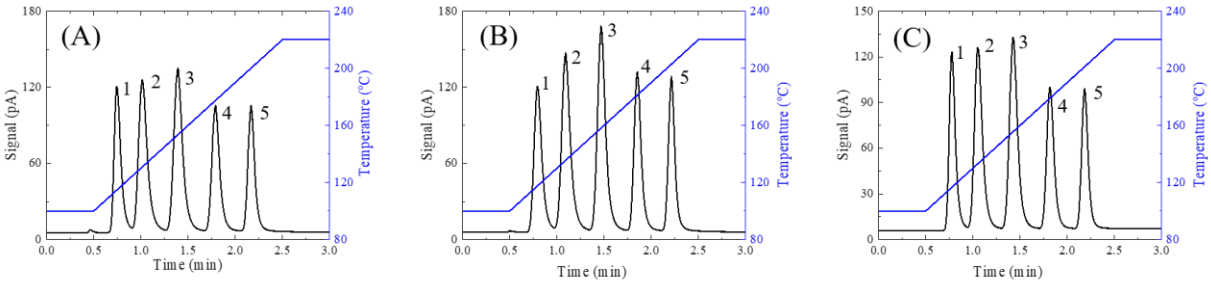

Figure 2.16. Example separations of C_{10} to C_{14} alkanes pre-stress testing with no added moisture (A), with 1 µL of added liquid water (B), and post-stress testing after 100 liquid water injections (C). Splitless injections of 0.025 µL mixture liquid were made using a carrier gas flow rate of 1.2 mL/min at 100 °C. Analysis is provided in **Table 2.11** and **Table 2.12**.

The only two significant differences observed were FWHM broadenings of 19% and 10% for C_{10} and C_{11} with liquid water injection **(Table 2.11**). However, the overall peak capacity was unaffected (**Table 2.12**), suggesting that the overall column performance was not degraded significantly. Degradation by long-term injection of moisture was also examined via 100 repeated injections of 0.2 µL of liquid water. The column temperature was set to 120 °C during injection with a flow rate of 1.2 mL/min. Injections were made once per minute. Retention times, FWHMs, and p-values are provided in **Table 2.13**, with no significant differences observed after

50 or 100 injections. Analysis of peak capacities (**Table 2.12**) corroborates this result, showing that the μIL column does not significantly degrade under long-term moisture exposure.

	RT (Dry)	FWHM (Dry)	RT (vapor)	FWHM (vapor)	p-value (vapor)	RT (liquid)	FWHM (liquid)	p-value (liquid)
C_{10}	0.737	0.0890	0.726	0.0921	0.31/0.47	0.724	0.1058	0.53/0.01
C_{11}	1.000	0.1162	0.999	0.1151	0.97/0.51	1.019	0.1279	0.44/0.03
C_{12}	1.372	0.1196	1.379	0.1193	0.75/0.88	1.411	0.1191	0.30/0.91
C_{13}	1.777	0.1053	1.770	0.1044	0.73/0.77	1.807	0.1008	0.28/0.30
C_{14}	2.158	0.0921	2.156	0.0910	0.91/0.65	2.182	0.0881	0.27/0.17

Table 2.11. Retention times (RTs), FWHMs, and p-values of C_{10} to C_{14} alkanes with no added moisture, 500 μL of added water vapor, and 1 μL of added liquid water. The water vapor was heated to 80 °C prior to injection in order to increase the partial pressure in headspace. RTs and FWHMs are provided in minutes. All values are calculated based on 5 runs. p-values were obtained by comparing moisture separations with dry separations, with significance taken at p = 0.05. p-values are provided as RT/FWHM; the only two significant values were for FWHMs for C_{10} and C_{11} with liquid water injection. FWHM broadenings of 19% and 10% were observed for C_{10} and C_{11}, respectively. No broadening was observed for vapor injection.

	Peak Capacity	p-value
Dry	7.783	-
Vapor	7.871	0.498
Liquid	7.842	0.788
50 injections	7.915	0.342
100 injections	8.037	0.086

Table 2.12. Peak capacities calculated for C_{10} to C_{14} alkanes for dry injections (control), with 500 μL of added water vapor, 1 μL of added liquid water, after 50 injections of liquid water, and after 100 injections of liquid water. Peak capacities are calculated by summing all resolutions

between adjacent peaks. p-values are calculated from 5 runs for each set of injections and significance is taken at p = 0.05. No significant differences in peak capacity were observed for either moisture injection or after stress testing.

	RT (Dry)	FWHM (Dry)	RT (50 inj)	FWHM (50 inj)	p-value (50 inj)	RT (100 inj)	FWHM (100 inj)	p-value (100 inj)
C_{10}	0.737	0.0890	0.725	0.0892	0.431/ 0.824	0.745	0.0846	0.656/ 0.104
C_{11}	1.000	0.1162	0.983	0.1132	0.420/ 0.127	1.006	0.1123	0.832/ 0.082
C_{12}	1.372	0.1196	1.355	0.1172	0.398/ 0.380	1.378	0.1153	0.840/ 0.108
C_{13}	1.777	0.1053	1.760	0.1026	0.279/ 0.380	1.779	0.0999	0.956/ 0.127
C_{14}	2.158	0.0921	2.140	0.0903	0.180/ 0.308	2.151	0.0877	0.718/ 0.080

Table 2.13. Retention times (RTs), FWHMs, and p-values of C_{10} to C_{14} alkanes prior to stress testing, after 50 injections, and after 100 injections. RTs and FWHMs are provided in minutes. All values are calculated based on 5 runs. p-values were obtained by comparing separations after stress testing with dry separation, with significance taken at p = 0.05. p-values are provided as RT/FWHM; no significant differences in RTs or FWHMs were observed.

2.3.4 µIL summary

The microfabrication and coating of a chip-based µIL column has been described herein. The µIL column enabled separation of alcohols, chloroalkanes, aromatics, aldehydes, fatty acid methyl esters, and alkanes at temperatures up to 345 °C using dry air as the carrier gas. The column's long-term robustness against oxygen was examined by 48 hours of dry air exposure at temperatures up to 220 °C with a degradation of only 8.92% observed. The column also exhibited robustness to moisture, with no observed degradation of separation performance by high moisture concentrations or long-term moisture exposure. The ability to efficiently separate a wide range of both polar and nonpolar compounds along with resilience to moisture and oxygen make the µIL column highly suited for use in portable GC field analysis. Finally, future

integration of the μIL column into μGC systems is expected to significantly facilitate development of ultracompact, portable GC devices by alleviating the need for auxiliary carrier gas cartridges and moisture filters.

2.4 Peak Focusing Based on Stationary Phase Thickness Gradient

2.4.1 Background

In GC wall coated capillary separation columns, vapor interactions between the gas phase and a stationary phase coated on a capillary wall allow for retention of analytes. Analytes traveling along the column encounter longitudinal and transverse mass transfer, which results in peak broadening, decreasing GC resolution and increasing the possibility of co-elution. Typically, proper selection of the column stationary phase (to allow for sufficient analyte interaction and retention)[36,70,96,97], application of temperature-programmed profiles[98-100], and split/splitless sample injection[98] allow for improvement of chromatograph separation and resolution. In some cases, however, these methods are insufficient to achieve a desired separation. For example, in portable GC, limited carrier gas supplies prevent use of split injections, while fine control over temperature programming is both difficult and limited by system power capacity[14,101]. Furthermore, even for specialized separations (*e.g.*, separation of highly volatile compounds by porous layer open tubular columns[17,35,36]), it can be difficult to fully separate the complete range of relevant compounds, especially considering the limited column length and short time of analysis for portable microsystems. An additional method for improving column separation is therefore desirable.

Negative temperature gradient separation (NTGS)[102] is one method that has been shown to improve column performance by sharpening elution peaks[103-109]. In NTGS, the column inlet is heated, and a temperature gradient is generated via thermal exchange with the ambient. Since the temperature is lower toward the column outlet, the peak front travels more slowly than its tail, resulting in overall focusing. This effect can be optimized by tuning different temperature profiles along the column, allowing for high versatility under different conditions[102-109]. However, due to NTGS reliance on thermal exchange, focusing varies with ambient temperature, humidity, air convection rate, and packing material thermal conductivity, reducing repeatability and predictability (especially if complex temperature profiles are used). Sophisticated heat

control modules can be used to stabilize the temperature gradient, but add additional size, weight, complexity, and cost to the GC device. Additionally, energy loss due to the aforementioned thermal exchange is a relevant detriment for systems with limited resources (*e.g.*, portable devices). Furthermore, separation of high volatility compounds often requires near ambient temperatures, which disallows generation of a temperature gradient and thus inhibits the NTGS effect. Therefore, although versatile and tunable, NTGS usage for certain applications (*e.g.*, portable GC) may be limited and challenging.

This section presents an alternative method for peak focusing via a positive stationary phase thickness gradient (*i.e.*, increased film thickness toward the outlet), as illustrated in **Figure 2.17(A)**. With the increased stationary phase thickness toward the outlet, the peak front travels more slowly than its tail, resulting in overall peak focusing. Herein, theory and simulation are first provided to explain underlying focusing mechanisms. Subsequently, the peak focusing effect is experimentally demonstrated by using a 5 m long film thickness gradient column (FTGC) created from a deactivated capillary column dynamically coated with a 5% phenyl stationary phase. Four sets of experiments are performed to characterize the FTGC's peak focusing abilities. An overall focusing rate of up to 28.2% was observed. Focusing of high volatility compounds at room temperature was also achieved.

2.4.2 Peak focusing theory

A theoretical explanation for peak focusing is provided in this section. Detailed simulation will be presented in the next section.

The effective velocity, $\boldsymbol{u_{eff}(x,t)}$, of an analyte at a location *x* (the distance from the column inlet) and a given time $\boldsymbol{t}$ is given by

$$u_{eff}(x,t) = \frac{u_M(x,t)}{1+k(x,t)}, \quad (2.3)$$

where $\boldsymbol{u_M(x,t)}$is the velocity of the mobile phase and $\boldsymbol{k(x,t)}$ is the retention factor:

$$k(x,t) = \frac{K(x,t)}{\beta(x)}, \quad (2.4)$$

with distribution coefficient $K(t)$ defined as

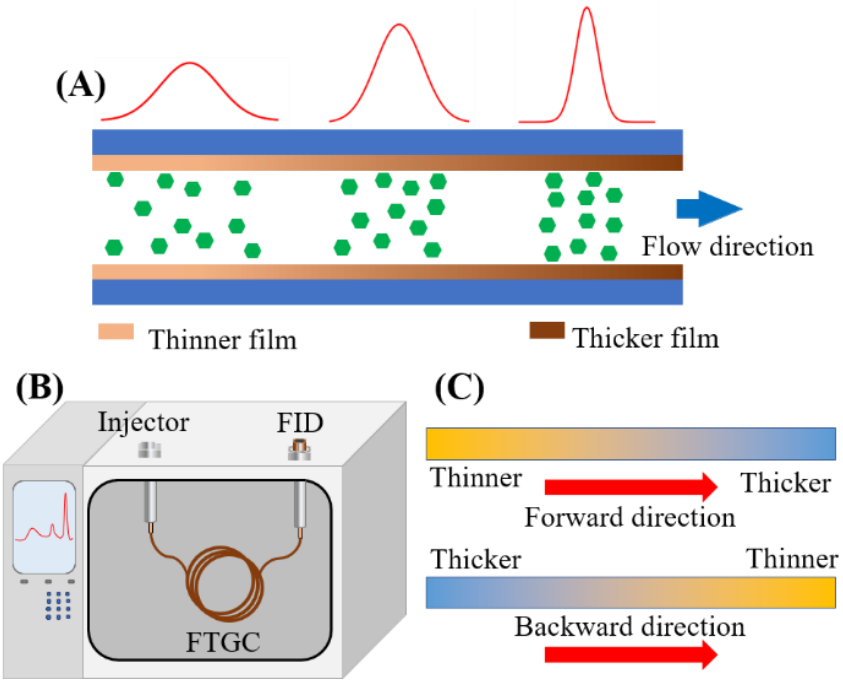

Figure 2.17. (A) Depiction of peak focusing by FTGC. A thinner to thicker film focuses an analyte peak as it travels along the column. (B) Setup for column performance evaluation. The column was installed in an Agilent 6890 benchtop GC equipped with a flame ionization detector. (C) Illustration of forward and backward modes. Columns were tested in one direction first, then reversed. Comparisons are made between chromatograms obtained from the two modes.

$$K(x,t) = \exp\left(\frac{\Delta G}{RT(x,t)}\right), (2.5)$$

where R is the universal gas constant and $T(x,t)$ is the time dependent column temperature at location x. ΔG is the Gibbs free energy change associated with an analyte moving from the stationary to mobile phase and can be calculated from the change in analyte enthalpy (ΔH) and entropy (ΔS)

$$\Delta G = \Delta H - T\Delta S. (2.6)$$

The phase ratio β is defined by

$$\beta = \frac{\left(d_i - 2d_f\right)^2}{d_i^2 - \left(d_i - 2d_f\right)^2} \approx \frac{d_i}{4d_f}, for\ d_i \gg d_f, (2.7)$$

where d_i and $d_f(x)$ are the column inner diameter and the film thickness, respectively. Eq. 2.4 can thus be expressed as

$$k(x,t) = A\exp\left(\frac{\Delta G}{RT(x,t)}\right) \times d_f(x), \text{(2.8)}$$

where A is a constant for a given column. The retention factor change along the column, $\delta k(x,t)$, can be written as

$$\frac{\frac{\delta k(x,t)}{\delta x}}{k(x,t)} = -\frac{\Delta H}{RT(x,t)}\frac{\frac{\delta T(x,t)}{\delta x}}{T(x,t)} + \frac{\frac{\delta d_f(x)}{\delta x}}{d_f(x)}. \text{(2.9)}$$

Eq. 2.9 shows that the fractional increase of the retention factor, $\frac{\delta k}{k}$, along the column in distance δx has two contributions: a negative temperature gradient given by the first term and a positive film thickness gradient given by the second term. This retention factor gradient ($\frac{\delta k}{k}$) is related to a velocity gradient by Eq. 2.3; thus, both a negative temperature gradient and a positive film thickness gradient result in a velocity difference between the front and tail of a band, allowing for band focusing (*i.e.*, the spatial distribution of an analyte experiences a spatially varying velocity gradient). At the outlet, the band is observed as a time varying peak during elution, which can be narrower than the corresponding peak from an unfocused band. In other words, peak focusing (an observable quantity) occurs as a result of band focusing within the column. The equivalency of these two gradients can be expressed as

$$-\frac{\Delta H}{RT(x,t)}\frac{\delta T(x,t)}{T(x,t)} = \frac{\delta d_f(x)}{d_f(x)}. \text{(2.10)}$$

Figure 2.18 plots the equivalent temperature gradient for C_{10} for various fractional film thickness gradients and column temperatures based on Eq. 2.10. **Figure 2.19** shows the equivalent temperature gradient for C_{10}, C_{12}, and C_{14} at various temperatures and a fractional film thickness gradient of 50%.

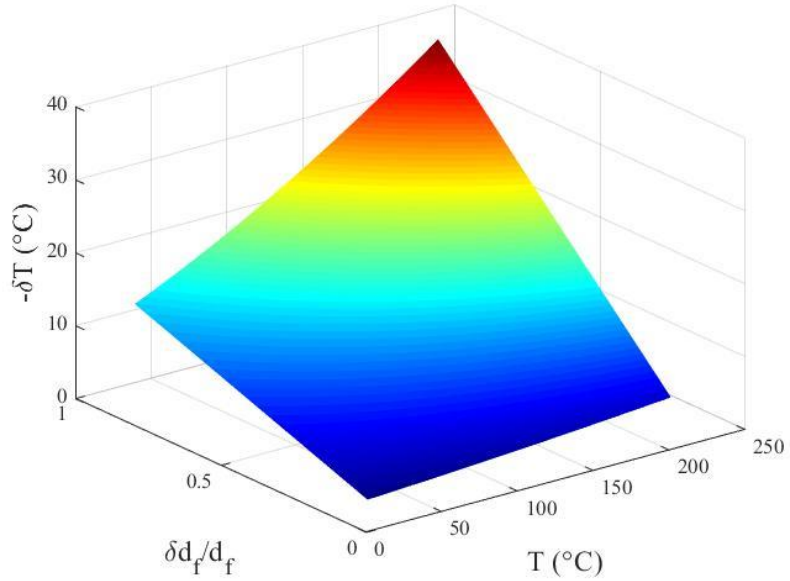

Figure 2.18. Equivalent column temperature gradient (ΔT) calculated using Eq. 2.10 and the Gibbs energy parameters listed in **Table 2.14** for C_{10} under isothermal separation for various fractional film thicknesses and column temperatures.

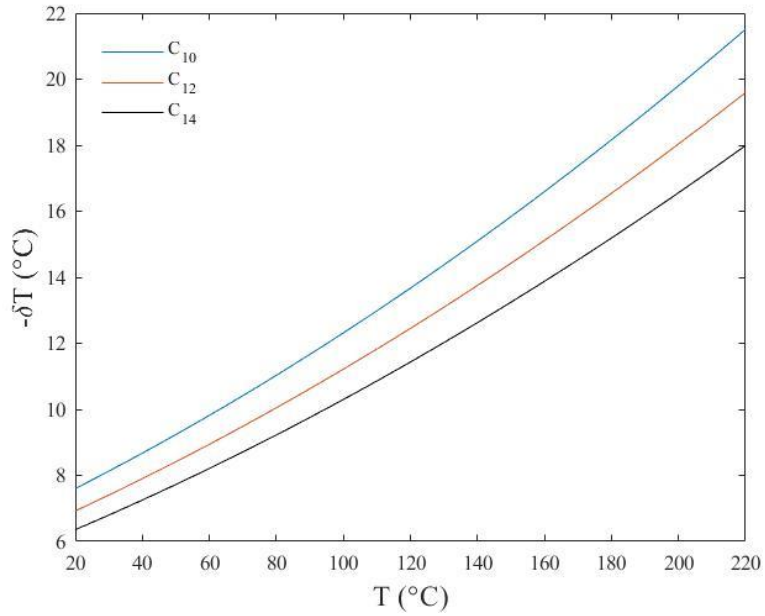

Figure 2.19. Equivalent column temperature gradient for C_{10}, C_{12}, and C_{14} using Eq. 2.10 and the Gibbs energy parameters listed in **Table 2.14** for various column temperatures for a 50% (i.e., $\frac{\boldsymbol{\delta d_f}}{\boldsymbol{d_f}} = 0.5$) film thickness gradient.

	C_{10}	C_{12}	C_{14}
$\Delta \boldsymbol{S}$ (*J/mol/K*)	74.3	76.8	79.3
$\Delta \boldsymbol{H}$ (*kJ/mol*)	47	51.6	56.2

Table 2.14. Entropy ($\Delta \boldsymbol{S}$) and enthalpy ($\Delta \boldsymbol{H}$) of evaporation of C_{10}, C_{12}, and C_{14} for a (5%-phenyl)-dimethyl polysiloxane film[100].

The film thickness gradient has several advantages over temperature gradient-based peak focusing. First, the film thickness gradient is independent of column temperature, allowing for focusing of analytes of any volatilities at any operation temperatures. High volatility compounds, especially, are difficult to focus with NTGS, but can be accomplished with an FTGC. Second, while the temperature gradient may vary with heater and ambient conditions (such as heater arrangement, heat dissipation, column size/weight, column channel arrangement, and ambient temperature and air flow), the film thickness gradient is always constant and allows for more reliable and repeatable GC operation (less susceptible to environmental effects). Finally, the FTGC can be used without extra accessories (such as heaters or coolers, which are required for NTGS), which significantly reduces device complexity for future integration. However, despite these advantages, film thickness gradient based separation is less versatile than NTGS since the gradient is fixed, whereas a temperature gradient can be adjusted by changing the heat source and/or drain. In addition, the increased film thickness toward the column outlet may result in slower mass transfer, potentially offsetting the peak focusing effect. The mass transfer effect is examined in the following simulation.

2.4.3 Simulation

For this simulation, no temperature gradient (*i.e.,* NTGS) is considered; only a film thickness gradient is analyzed. The time dependent concentration c of an analyte peak traveling along a column is determined by solving the transient convection-diffusion equation[110]

$$\frac{\partial c}{\partial t} = -\frac{\partial}{\partial x}\left(u_{eff}c\right) + \frac{\partial}{\partial x}\left(D_{eff}\frac{\partial c}{\partial x}\right), (2.11)$$

where $u_{eff}(x,t)$ is given in Eq. 1.1. The effective diffusion, D_{eff}, can be calculated from local dispersion, D, and the retention factor $k(x,t)$

$$D_{eff}(x,t) = \frac{D(x,t)}{1+k(x,t)} (2.12)$$

$$D = D_M(x,t) + \frac{1}{2}\left[\frac{1+6k(x,t)+11k(x,t)^2}{24\left(1+k(x,t)\right)^2}\frac{d_i^2}{D_M(x,t)} + \frac{2k(x,t)}{3\left(1+k(x,t)\right)^2}\frac{d_f(x,t)^2}{D_S(x,t)}\right]u_M(x,t)^2, (2.13)$$

with d_f as the film thickness and D_M as the mobile phase diffusion constant. Note that D includes both longitudinal and transverse mass transfer/diffusion. $D_M(x,t)$ can be expressed as

$$D_M(x,t) = D_C\frac{T(t)^{1.75}}{p(x)} = 5\times 10^4 D_S(x,t), (2.14)$$

with diffusion constant D_C (dependent on molar weights and atomic and structural diffusion volumes of analytes and mobile phase molecules) and D_S as the stationary phase diffusion constant[110]. Local pressure $p(x)$ is determined from inlet and outlet pressures p_{in} and p_{out}

$$p(x) = \sqrt{p_{in}^2 - (p_{in}^2 - p_{out}^2)\frac{x}{L}}, (2.15)$$

with L being the length of the column. u_M, the velocity in mobile phase is given by

$$u_M(x,t) = \frac{d_i^2}{16\eta(t)L}\frac{1}{p(x)}(p_{in}^2 - p_{out}^2), (2.16)$$

with viscosity η provided as a function of reference viscosity η_0 at temperature T_0 and gas type dependent exponent α_n:

$$\eta(t) = \eta_0\left(\frac{T(t)}{T_0}\right)^{\alpha_n}. (2.17)$$

In Eq. 2.14, temperature $T(x,t)$ is provided as $T(t)$ under the assumption that the temperature remains the same along the column at a given time t. Eq. 2.11 can be solved by applying a finite difference model to discrete time (t) and position (i) vectors

$$\frac{\partial c}{\partial t} \rightarrow \frac{\partial C}{\partial t} = \frac{C_{i,t+1} - C_{i,t}}{\Delta t} \quad (2.18)$$

$$\frac{\partial c}{\partial x} \rightarrow \frac{\partial C}{\partial x} = \frac{C_{i+1,t} - C_{i,t}}{\Delta x} \quad (2.19)$$

$$\frac{\partial^2 c}{\partial x^2} \rightarrow \frac{\partial^2 C}{\partial x^2} = \frac{C_{i+1,t} - 2C_{i,t} + C_{i-1,t}}{(\Delta x)^2}, \quad (2.20)$$

with Δx and Δt being simulation distance and time step sizes. Combining these yields

$$C_{i,t+1} = C_{i,t} + \Delta t \left(-u_{eff}(i,t) \frac{C_{i+1,t} - C_{i,t}}{\Delta x} \right) + \Delta t \left(D_{eff}(i,t) \frac{C_{i+1,t} - 2C_{i,t} + C_{i-1,t}}{(\Delta x)^2} \right). \quad (2.21)$$

The solution to Eq. 2.21 produces the time dependent movement of an analyte peak along the column.

To simulate Eq. 2.21, several boundary conditions must be set. First, at $t = 0$, the injected peak has a Gaussian peak shape, i.e.,

$$C(x,0) = \frac{1}{\sigma\sqrt{2\pi}} e^{-\frac{(x-3\sigma)^2}{2\sigma^2}}, \quad (2.22)$$

where σ is the initial dispersion. Note that the initial peak at time t = 0 is at x = 3σ. At the column inlet, after the initial injection, no additional analyte is injected into the column:

$$C(0,t) = 0. \quad (2.23)$$

At the column outlet, the last mesh concentration is approximately the same as the one to the left (since it cannot be calculated by Eq. 2.18), i.e.,

$$C(L,t) = C(L - \Delta x, t). \quad (2.24)$$

Peak retention times and FWHMs can be measured at the column outlet (*i.e.*, $x = L$) by observing that, using Eq. 2.21, a spatially varying concentration is used to construct a two-dimensional concentration matrix varying with both position and time. By observing concentration along the second dimension (*i.e.,* in time), a vector of concentration varying with time can be obtained, corresponding to a signal obtained from a detector at the outlet. The maximal value (varying with time) corresponds to the elution/retention time, and FWHMs can be measured by observing the times at which the concentration is half the peak value.

2.4.4 Experimental

2.4.4a Experimental setup

The FTGC was installed in an Agilent 6890 benchtop GC equipped with an FID (**Figure 2.17(B)**). Ultra-high purity helium was used as the carrier gas. Evaluation of the peak focusing effect was performed with analytes injected from the thinner coating end (forward mode, *i.e.*, traveling from thinner to thicker film) or thicker coating end (backward mode, *i.e.*, traveling from thicker to thinner film), as illustrated in **Figure 2.17(C)**. A uniform thickness column (film thickness same as the averaged thickness) was also evaluated using the same setup for comparison. All experiments were performed using constant pressure temperature programming. Temperature programing methods and head pressures are provided in **Table 2.15**.

	Initial Temperature (°C)	Final Temperature (°C)	Ramping Rate (°C/min)	Head Pressure (psi, mL/min)
Simulation	40	240	30	3.45, N/A
Uniform thickness control	60	180	30	3.45, 2.7
Alkane mixture (forward)	60	180	30	3.45, 2.7
Alkane mixture (equal time backward)	60	148	22	3.45, 2.7
Aromatics mixture (forward)	45	105	30	3.45, 2.9
Aromatics mixture (equal time backward)	45	90	20	3.45, 2.9
High Volatility Alkanes	26	26	0	2.20, 2.0

Table 2.15. Temperature programming profiles and head pressures for simulation, uniform thickness control, separation of alkanes C_7 to C_{16}, separation of aromatics, and separation of high volatility alkanes (C_5 and C_6).

2.4.4b Column coating

OV-1 (75% w/w), OV-17 (10% w/w), and Dow SYLGARD™ 184 reagent B (15% w/w, crosslinker) were dissolved in dichloromethane to create a 2% (w/w) coating solution

(effectively a 5% phenyl stationary phase). A 5 m long capillary column (250 µm i.d.) was silanized prior to coating by 8 repeated injections of hexamethyldisilazane (HMDS) vapor. Subsequently, an 80 µL coating solution was loaded into the capillary from the column inlet via a syringe pump (**Figure 2.20(A)**). A 5-psi positive pressure was applied from the inlet to drive the coating solution towards the outlet. A negative 2-psi vacuum pressure was applied to the outlet through a 1 m dummy column (250 µm i.d.), which ensured a constant coating plug speed. During coating, the small volume of low boiling point dichloromethane evaporated rapidly under vacuum, progressively increasing the coating solution concentration, and hence the film thickness, as the coating solution plug moved from column inlet to outlet[111]. After coating, dry air was continuously flowed through the column for 2 hours, followed by crosslinking at 80 °C for another 2 hours and subsequent deactivation using HMDS. The column was then aged at 230 °C for 3 hours under a helium flow of 0.5 mL/min. Using the same method, a column with a uniform thickness film was coated using a 1% (w/w) coating solution (same composition as above, but diluted) and applying a 5-psi positive pressure from the inlet to drive the coating solution toward the outlet (without applying a vacuum).

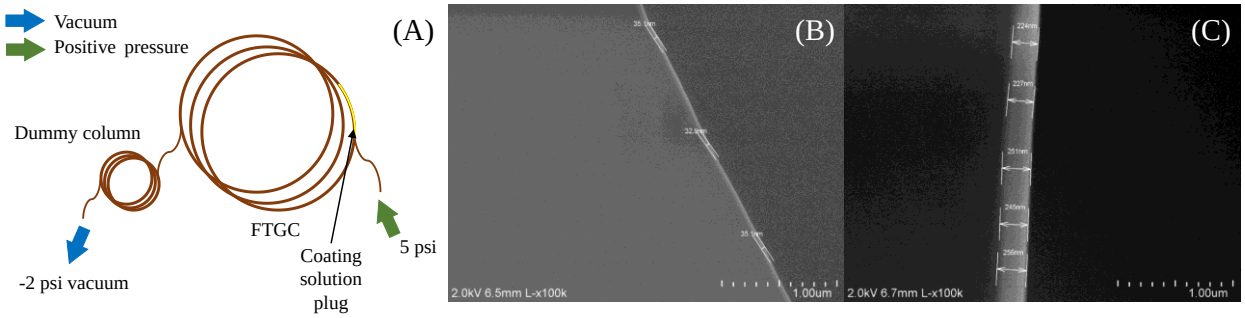

Figure 2.20. (A) FTGC coating setup. The column was dynamically coated by partially filling with a coating solution plug and subsequently pushing the mixture out with a pressure of 5 psi. While pushing the solution out, a vacuum pressure of -2 psi was applied to the outlet to vaporize the solvent. (B) SEM image close to the column inlet with a film thickness of 34 nm. (C) SEM image close to the column outlet with a film thickness of 241 nm.

2.4.4c Simulation setup

Simulation of separation of C_8 to C_{15} in forward and backward modes as well as using a uniform thickness equivalent to the average gradient film thickness was performed (separation conditions in **Table 2.15**). The film thickness varied from 34 nm to 241 nm for a 5 m column (inlet to outlet for forward mode and vice versa for backward mode, see *2.4.5b Stationary phase gradient* characterization). Additional simulation parameters for C_8 to C_{15} interactions with the stationary phase are provided in **Appendix B**[112]. Calculation of retention factor $k(x,t)$ requires a value for distribution coefficient $K(t)$ (Eq. 1.2), which is estimated based on values in Ref. [112]. Simulated retention times and FWHMs are provided in **Table 2.16** and resolutions are provided in **Table 2.17**. Analysis is provided in *2.4.5 Characterization of film thickness gradient*.

	RT_{fwd}	$FWHM_{fwd}$	RT_{bkwd}	$FWHM_{bkwd}$	RT_{uni}	$FWHM_{uni}$
C_8	0.460	0.0382	0.439	0.0684	0.449	0.0519
C_9	0.731	0.0473	0.697	0.0995	0.714	0.0704
C_{10}	1.157	0.0574	1.113	0.1296	1.136	0.0885
C_{11}	1.639	0.0656	1.560	0.1487	1.615	0.1005
C_{12}	2.106	0.0713	2.055	0.1584	2.082	0.1073
C_{13}	2.591	0.0763	2.541	0.1640	2.568	0.1120
C_{14}	3.050	0.0807	3.001	0.1679	3.027	0.1158
C_{15}	3.460	0.0842	3.411	0.1708	3.437	0.1186

Table 2.16. Simulated retention times (RTs) and full widths at half maxima (FWHMs) for C_8 to C_{15} in forward and backward modes. RTs and FWHMs for a uniform coating thickness are also provided for reference. The temperature was ramped from 40 °C at a rate of 30 °C/min with a head pressure of 3.45 psi. Column length was 5 m. All values are provided in minutes. Additional analysis is provided in **Table 2.17**.

	R_{fwd}	R_{bkwd}	R_{diff}	R_{uni}
C_8/C_9	3.744	1.814	1.930	2.554
C_9/C_{10}	4.808	2.147	2.661	3.133
C_{10}/C_{11}	4.619	2.020	2.599	2.992
C_{11}/C_{12}	4.024	1.787	2.237	2.647
C_{12}/C_{13}	3.884	1.779	2.105	2.615
C_{13}/C_{14}	3.448	1.634	1.814	2.379
C_{14}/C_{15}	2.932	1.429	1.503	2.065
PC	27.459	12.610	-	18.385

Table 2.17. Simulated resolutions (R) between adjacent peaks for C_8 to C_{15} in forward and backward modes and for uniform thickness. Forward mode resolutions are all larger than backward mode and uniform thickness resolutions. The difference in resolution is defined as $R_{diff} = R_{fwd}-R_{bkwd}$.

2.4.5 Characterization of film thickness gradient

2.4.5a Commercial column control

A Restek RTX-5 column was used for separation of C_7 to C_{16} alkanes in forward and backward modes as a control, with no difference in separation expected (separation conditions provided in **Table 2.15**. p-values for retention times and FWHMs (over 5 runs) were calculated using a paired Student's t-test and converting the resulting T-score to a p-value. Significance was taken at p = 0.05; no significant differences between forward and backward modes were observed for any analyte peak (**Table 2.18**). Similarly, no significant differences between forward and backward modes were observed for C_7-C_{15} when an Agilent DB-1MS column (data not shown) was used.

2.4.5b Stationary phase gradient characterization

To characterize the thickness of the stationary phase, the FTGC was first frozen in liquid nitrogen and several pieces were scored off. Scanning electron microscopy (SEM) images were taken close to the column inlet (thinner film) and outlet (thicker film). **Figure 2.20(B)** and **(C)** show that the film thickness increases from 34 nm to 241 nm from the inlet to the outlet, a gradient of approximately 41 nm/m. The uniform thickness column was also characterized at both the inlet and outlet with a film thickness of 131 nm at both column ends.

	Forward RT/FWHM	Backward RT/FWHM	p-values RT/FWHM
C_7	0.331/0.028	0.330/0.028	0.85/0.68
C_8	0.397/0.033	0.395/0.034	0.66/0.54
C_9	0.524/0.036	0.522/0.036	0.65/0.95
C_{10}	0.741/0.036	0.740/0.036	0.79/0.79
C_{11}	1.054/0.033	1.054/0.033	0.78/0.93
C_{12}	1.442/0.031	1.441/0.030	0.87/0.46
C_{13}	1.859/0.030	1.856/0.031	0.67/0.76
C_{14}	2.286/0.031	2.284/0.031	0.60/0.97
C_{15}	2.702/0.032	2.700/0.031	0.58/0.93
C_{16}	3.100/0.030	3.097/0.031	0.55/0.82

Table 2.18. Retention times, FWHMs, and p-values for Restek RTX-5 column between forward and backward modes (averaged over 5 runs). All values are provided in minutes. No significant difference is observed between forward and backward modes.

2.4.5c Peak focusing on alkane mixture

The FTGC's peak focusing capabilities were evaluated by separation of a C_7 to C_{16} alkane mixture. 0.025 µL of liquid was used for injection at a split ratio of 5:1. The same separation conditions were used for forward mode, the uniform thickness column, and backward mode (denoted as "identical parameters backward mode", see **Table 2.15** – alkane mixture). Example chromatograms are shown in **Figure 2.21**.

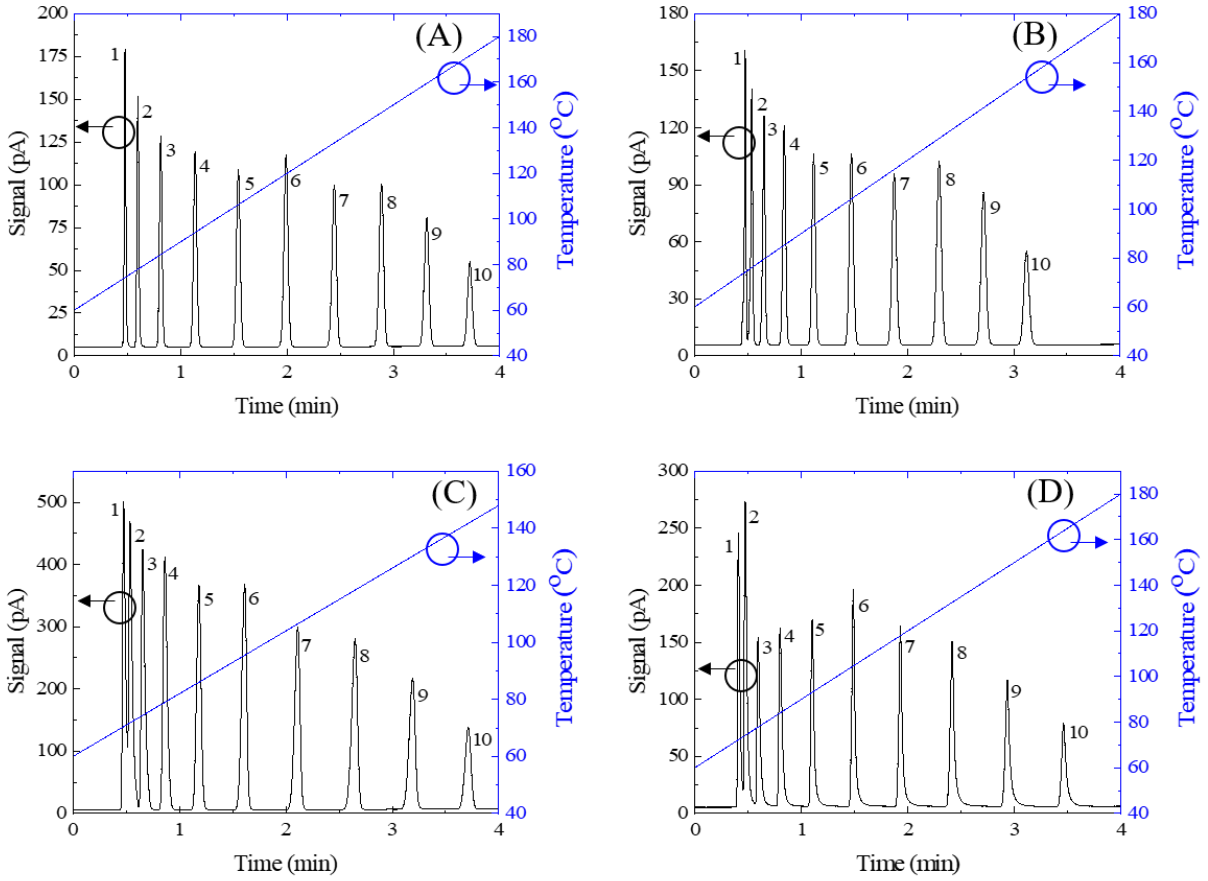

Figure 2.21. Separation of a C_7 to C_{16} alkane mixture in forward (A), identical parameters backward (B), and equal time backward (C) modes, and using a uniform thickness column (D). 0.025 µL of mixture liquid was injected into the injection portable for an Agilent 6890 benchtop GC. Carrier gas head pressure: 3.45 psi (2.7 mL/min at 60 °C).

Figure 2.21 shows that analyte peaks in forward mode, for the uniform thickness column, and in identical parameters backward mode elute at different times, which is consistent with simulation (**Table 2.16**). This is due to the fact that separation conditions for a given analyte are different between the two modes, which in turn are different from the uniform thickness column. In forward mode, the analyte is first exposed to the thinner film at low temperatures before reaching the thicker film at high temperatures, exactly opposite of what the analyte experiences in backward mode. In the uniform thickness column, analytes experience the same film thickness at all temperatures. As a result, retention times for analytes in these two modes and in the

uniform column are different and peak FWHMs are not directly comparable. Instead, resolutions between adjacent peaks (*e.g.*, C_7 and C_8, C_8 and C_9, *etc.*) are used to analyze separation performance. Resolutions in identical parameters backward mode and for the uniform column are subtracted from corresponding resolutions in forward mode; the resolution differences (*i.e.*, $R_{forward} - R_{identical\ parameters\ backward}$ or $R_{forward} - R_{uniform}$) between all adjacent peak pairs (averaged over 5 runs) are plotted in **Figure 2.22.** p-values for resolution differences are calculated using a paired Student's t-test (average of 5 runs in all modes) and converting the resulting T-score to a p-value (see **Table 2.19**).

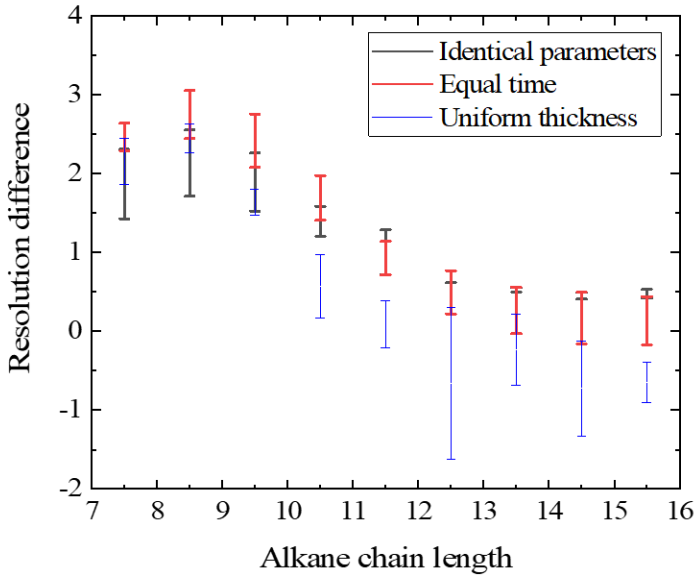

Figure 2.22. Resolution differences between forward and identical parameters and equal time backward modes, and a uniform thickness column for C_7 to C_{16} alkanes.

Significance is taken at p = 0.05, showing that forward mode has significantly higher resolution between all pairs of adjacent peaks when compared to identical parameters backward mode. This is corroborated by simulation (**Table 2.17**), which also demonstrates higher resolutions in forward mode, meaning that in the same time interval, forward mode can contain more peaks than backward mode. Uniform thickness column resolutions are lower than forward mode resolutions up to C_{10}/C_{11}, but uniform resolution is higher for the C_{15}/C_{16} pair. Analysis of overall performance is provided below.

Alkane pair	p-values		
	IP	ET	Uniform
C_7/C_8	0.001	9.77e-6	1.20e-4
C_8/C_9	5.27e-4	5.46e-5	1.18e-5
C_9/C_{10}	5.08e-4	1.39e-4	4.06e-5
C_{10}/C_{11}	1.27e-4	2.79e-4	0.046
C_{11}/C_{12}	7.38e-5	9.6e-4	0.585
C_{12}/C_{13}	5.35e-5	0.023	0.244
C_{13}/C_{14}	3.28e-6	0.146	0.358
C_{14}/C_{15}	2.80e-5	0.359	0.074
C_{15}/C_{16}	7.24e-5	0.430	0.006

Table 2.19. p-values between forward mode and uniform thickness, identical parameters (IP) backward, and equal time (ET) backward modes for C_7 to C_{16} alkanes separation. Significance is taken at p = 0.05. All p-values are significant between forward and IP backward mode, while p-values for C_7 to C_{13} are significant for ET backward mode. Forward mode resolutions are significantly higher than uniform thickness resolutions up to C_{10}/C_{11}, while uniform thickness resolution is significantly higher for C_{15}/C_{16}.

To further account for the discrepancy between retention times, a second set of chromatograms was obtained by lowering the backward mode ramping rate to ensure that C_{16} (the last eluted analyte) eluted at the same time as in forward mode (this is denoted as "equal time backward mode", see **Table 2.15** – separation conditions, **Figure 2.21** – chromatograms, **Figure 2.22** – resolution differences, **Table 2.19** – p-values). Again, forward mode provides significantly higher resolution for alkane pairs between C_7 and C_{13} (results obtained from 5 runs), but performs similarly to equal time backward mode for C_{13} to C_{16}. While forward mode does not outperform equal time backward mode (or the uniform thickness column) for all *local* resolutions (*i.e.*, between adjacent alkane pairs), forward mode has a significantly higher peak capacity (PC), defined as the sum over all resolutions (**Table 2.20**), compared to all other modes. Analysis of the focusing rate, defined as

$$FR = \frac{PC_{forward} - PC_{backward/uniform}}{PC_{backward/uniform}}, \quad (2.25)$$

shows that forward mode demonstrates overall focusing rates of approximately 11.7%, 26.8%, and 29.8% when compared with the uniform thickness column, identical parameters backward mode, and equal time backward mode, respectively.

Forward peak capacity	49.34±0.841
Backward peak capacity (IP)	38.90±0.831
p-value (IP)	1.73e-4
Focusing rate (IP)	26.84%
Backward peak capacity (ET)	38.02±2.400
p-value (ET)	4.62e-4
Focusing rate (ET)	29.76%
Uniform peak capacity	44.18±0.483
p-value (uniform)	1.63e-4
Focusing rate (uniform)	11.67%

Table 2.20. Peak capacities, p-values, and focusing rates between forward mode and identical parameters (IP) and equal time (ET) backward modes, and uniform thickness for C_7 to C_{16} alkanes separation in Figure 2.21. Significance is taken at p = 0.05. Peak capacity in forward mode is significantly higher than peak capacities in all other modes.

2.4.5d Peak focusing on aromatics mixture

FTGC peak focusing was also analyzed on separation of an aromatics mixture containing benzene, toluene, ethylbenzene, o-xylene, and 1,3-dichlorobenzene. 0.025 µL of mixture liquid was injected at a split ratio of 5:1 (separation conditions provided in **Table 2.15** – aromatics mixture). Example chromatograms are shown in **Figure 2.23** and resolution differences are

shown in **Figure 2.24**. Local resolution difference p-values (calculated from 5 runs) are provided in **Table 2.21**. Peak capacities, p-values, and focusing rates are provided in **Table 2.22**, showing that forward mode has significantly higher peak capacity compared to all other modes. Thus, regardless of whether separation parameters are kept constant (and analytes elute faster in identical parameters backward mode) or changed to ensure that the last compound elutes at the same time (in forward and equal time backward modes), separation performance in forward mode is always better than in either backward mode. Forward mode also outperforms the uniform thickness column, demonstrating a focusing rate of 28.2% (**Table 2.22**). Thus, overall, forward mode (*i.e.*, a positive film thickness gradient) demonstrates the ability to improve separation peak capacity.

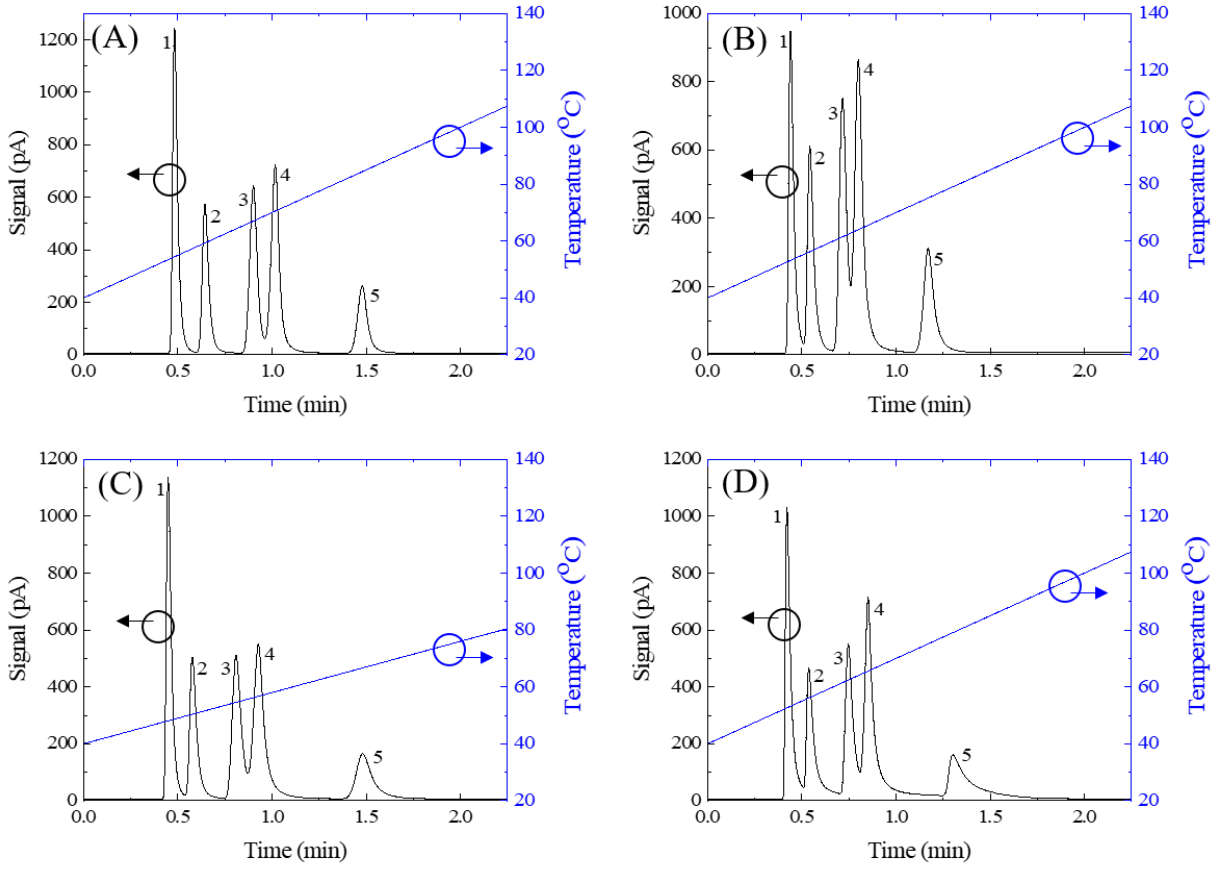

Figure 2.23. Separation of an aromatics mixture in forward (A), identical parameters (B), and equal time backward (C) modes, and using a uniform thickness column (D). 0.025 µL of mixture liquid was injected with a carrier gas head pressure of 3.45 psi (2.9 mL/min at 45 °C). 1.

Benzene (B); 2. Toluene (T); 3. Ethylbenzene (E); 4. o-Xylene (X); 5. 1,3-dichlorobenzene (DCB).

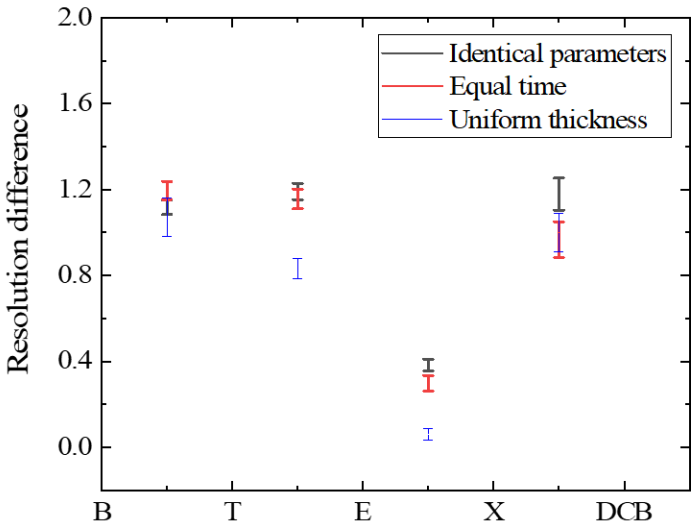

Figure 2.24. Resolution differences between forward and identical parameters backward and equal time backward modes, and a uniform thickness column for aromatics separation. Resolution difference is always positive, indicating that separation in forward mode is always better than separation in all other modes.

	p-values (IP)	p-values (ET)	p-values (Uniform)
B/T	3.08e-7	5.56e-7	1.83e-5
T/E	3.84e-7	9.28e-7	4.20e-6
E/X	9.32e-6	8.28e-5	0.012
X/DCB	5.95e-6	2.06e-5	2.28e-5

Table 2.21. p-values between forward mode and uniform thickness, identical parameters backward (IP), and equal time backward (ET) modes for aromatics separation. See **Figure 2.23** for elution order and abbreviations. Significance is taken at p = 0.05. All p-values show significantly improved resolution in forward mode.

2.4.5e Temperature ramping effects

To demonstrate how temperature ramping rate affects peak focusing, separation of C_7 to C_{10} with four different ramping rates (0, 10, 20, and 30 °C/min, ramped from 60 °C without holding) was performed in forward mode, identical parameters backward mode, and using the uniform thickness column. The head pressure was 3.45 psi (2.7 mL/min at 60 °C), and the split ratio was 15:1 for all separations (0.025 µL mixture liquid injection). The void time was measured by methane injection and was found to be 0.36 min for all ramping rates. Resolutions and focusing rates for each temperature profile are provided in **Table 2.23** (averages over 5 runs).

Forward peak capacity	13.47±0.089
Backward peak capacity (IP)	9.59±0.060
p-value (IP)	1.60e-7
Focusing rate (IP)	40.35%
Backward peak capacity (ET)	9.85±0.093
p-value (ET)	1.56e-6
Focusing rate (ET)	36.73%
Uniform peak capacity	10.50±0.146
p-value (uniform)	1.13e-5
Focusing rate (uniform)	28.22%

Table 2.22. Peak capacities, p-values, and focusing rates between forward mode and identical parameters (IP) and equal time (ET) backward modes, and uniform thickness for aromatics separation in **Figure 2.23**. Significance is taken at p = 0.05. Separation in forward mode is significantly better than separation all other modes.

In forward mode, at higher temperature ramping rates, analytes encounter relatively higher temperatures by the time they reach the thicker stationary phase closer to the column outlet. The

analyte thus spends less time in the thicker film and peak broadening is reduced. In backward mode, analytes first encounter the thicker stationary phase at lower temperatures before flowing to the thinner stationary phase at higher temperatures. Peak broadening from low thickness stationary phases is already low; therefore, the overall decrease in peak broadening due to increased temperature is lower in backward mode. Thus, the focusing rate increases with increased temperature ramping rate, up to 61.9% comparing forward and backward modes and 68.1% comparing forward mode and uniform thickness at a rate of 30 °C/min.

Ramping rate (°C/min)	$R_{fwd}/R_{bkwd}/R_{uni}$ (C_7/C_8)	$R_{fwd}/R_{bkwd}/R_{uni}$ (C_8/C_9)	$R_{fwd}/R_{bkwd}/R_{uni}$ (C_9/C_{10})	$PC_{fwd}/PC_{bkwd}/PC_{uni}$	Focusing rate (bkwd/uni)
0	4.59/3.40/ 2.74	5.86/4.68/ 4.86	6.73/5.68/ 7.43	17.18/13.76/ 15.02	24.85%/ 14.36%
10	4.60/3.18/ 2.73	5.80/4.40/ 4.42	6.65/5.38/ 6.69	17.05/12.96/ 13.84	31.56%/ 21.63%
20	4.43/2.86/ 2.53	5.51/3.94/ 4.02	6.39/4.88/ 5.77	16.32/11.68/ 12.32	39.73%/ 37.25%
30	4.01/2.14/ 1.84	5.30/3.16/ 2.85	6.11/4.22/ 4.48	15.41/9.52/ 9.17	61.87%/ 68.09%

Table 2.23. Resolutions (R), peak capacities (PC), and focusing rates for forward mode, identical parameters backward mode, and uniform thickness for C_7 to C_{10} separation at various temperature ramping rates. The initial temperature was 60 °C for all separations and the carrier gas head pressure was 3.45 psi (2.7 mL/min at 60 °C). 0.025 µL of mixture liquid was injected using a split ratio of 15:1.

2.4.5f Focusing for high volatility compounds

Unlike NTGS, an FTGC gradient is capable of focusing peaks at low temperatures, where a temperature gradient is difficult to generate. To demonstrate this, room temperature isothermal separation (**Table 2.15**) of C_5 and C_6 was performed (**Figure 2.25**). Resolutions, p-values, and focusing rates are provided in **Table 2.24** (values averaged over 5 runs). A focusing rate of 40.2% was achieved with an average forward mode resolution of 2.97 and uniform thickness

resolution of 2.12. Note that for NTGS, the same peak focusing effect for high volatility compounds is difficult to achieve since only small temperature gradients can be generated at low operating temperatures.

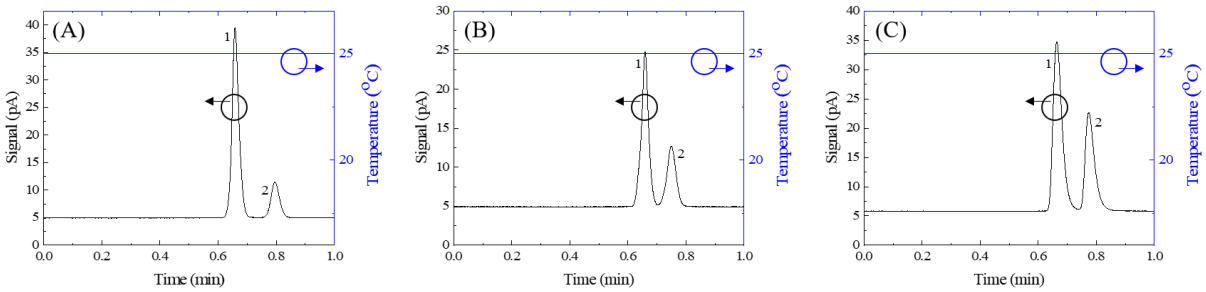

Figure 2.25. Room temperature (26 °C) isothermal separation of C_5 and C_6 in forward mode (A), identical parameters backward (B) mode, and using a uniform thickness column (C). 0.2 µL of vapor obtained from the headspace of a C_5 and C_6 mixture was injected using a carrier gas head pressure of 2.2 psi (2 mL/min).

Forward resolution	2.97±0.140
Backward resolution	1.85±0.055
p-value (backward)	1.17e-4
Focusing rate (backward)	60.4%
Uniform resolution	2.12±0.049
p-value (uniform)	4.87e-4
Focusing rate (uniform)	40.2%

Table 2.24. Resolutions, p-values, and focusing rates for forward mode, backward mode, and uniform thickness for room temperature (26 °C) C_5 and C_6 separation. Significance is taken at p = 0.05.

2.4.6 FTGC summary

Development and evaluation of a stationary phase thickness gradient column technique that enables peak focusing has been detailed herein. Experimental results were corroborated by theoretical analysis and simulation, showing increased separation performance of various compounds in forward mode, including focused separation of high volatility compounds at room temperature. Compared to NTGS, the FTGC has advantages in larger applicable temperature and compound volatility ranges, simple operation without accessories, less dependence on ambient conditions, and greater compactness. This stationary phase thickness gradient technique can be facilely applied to wide-ranging GC applications and can be used for stationary phases of any materials or thicknesses, provided only that a gradient can be generated. Furthermore, this technique is applicable to both regular circular cross-sectioned capillary columns and rectangular cross-sectioned microfabricated columns, thus additionally demonstrating applicability to microcolumns for μGC.

2.5 Conclusion

This chapter has detailed the development of microcolumn coatings targeting portable μGC environmental analysis. Coating of two different microcolumn stationary phases (PLOT and phosphonium ionic liquid) demonstrated separation of a broad range of compounds including specialty separations of light VOCs. Column resistance to humidity and even oxygen resilience from the μIL column were demonstrated, showing potential robustness to harsh ambient conditions. The development of these coatings is expected to expand the range of practical applications that portable μGC systems can target, as well as reduce the number of accessory components required for carrier gas and air filtering if the μIL column is used. Furthermore, the film thickness gradient coating technique introduced in this chapter allows for improvement of column performance without increasing the column length or involving extra active components such as for negative temperature gradient separation, both of which are challenging or not practical for portable μGC. Altogether, these developments are aimed at improving the separation capabilities and performance of microcolumns for miniaturized gas analysis systems.

For more specialized and selective separations (i.e., more suited to specific groups of chemicals), highly tunable PLOT and ionic liquid coatings can be altered to increase the polarity for more polar separations, or even altered to separated chiral compounds, and essential oils and

fragrances. These may be especially useful for multidimensional µGC, when paired with a more conventional column such as nonpolar OV-1 or OV-5. Future improvements may also target improved separation performance. This can be accomplished by tuning the coating thickness by increasing or decreasing the number of coatings depending on the required application, as well as by altering the column length. While thicker coatings and longer columns can improve separation performance, however, this comes at the cost of increased separation time and power consumption for portable systems. Further improvements may target peak tailing and broadening due to stationary phase pooling, which can be addressed with additional microfabrication steps to etch column channels with more rounded corners.

2.6 Experimental materials

All benchmark reagents were purchased from Sigma-Aldrich (St. Louis, MO), Cal Gas Direct (Huntington Beach, CA), and Restek (Bellefonte, PA). Benchmark reagents: analytical standard grade methanol, ethanol, propanol, butanol, pentanol, dichloromethane, 1,2-dichloroethane, 2-butanone, chloroform, 1,4-dioxane, tetrachloroethylene, formaldehyde solution, acetaldehyde, propionaldehyde, butyraldehyde, benzaldehyde, 1-chlorobutane, 1-chloropentane, 1-chlorohexane, 1-chloroheptane, 1-chlorooctane, 1-chlorododecane, benzene, toluene, styrene, ethylbenzene, o-xylene, 1,2-dichlorobenzene, 1,3-dichlorobenzene, nitrobenzene, C_5 to C_{16}, methyl caproate, *n*-Paraffin mix C_{18}, C_{20}, C_{22}, C_{24} (P/N 47108) (Sigma Aldrich). Methane, ethane, propane, butane (Cal Gas Direct). FAME #7 Mix (P/N 35016), FAME #8 Mix (P/N 35017) (Restek).

Coating reagents: divinylbenzene, octanol, toluene, styrene, azobisisobutyronitrile, acetone, 3-(trimethoxysilyl)propyl methacrylate; dichloromethane, trihexyl(tetradecyl)phosphonium bis(trifluoromethyl sulfonyl)amide, ammonium hydroxide, hydrogen peroxide, sodium chloride tablets (Sigma Aldrich). Vinyl modified OV-1 (P/N 6001), and OV-17 (P/N 6017) (Ohio Valley Specialty Company; Marietta, OH).

Hysol® 1C™ Epoxy and Dow SYLGARD™ 184 reagent B (Ellsworth Adhesive; Germantown, WI). Polyimide sealing resin (P/N 23817) (Sigma-Aldrich). Deactivated fused silica tubing (P/N 10010) with 250 µm inner diameter (Restek). Rt-Q-BOND PLOT column (P/N 19765, cut to 5 m in length) and RTX-5 column (P/N 10205, cut to 5 m in length with 250 µm inner diameter and 0.1 µm film thickness) (Restek). DB-1MS column (P/N 122-0162, cut to

5 m in length with 250 µm inner diameter and 0.25 µm film thickness) (Agilent; Santa Clara, CA). N-type silicon wafers (P/N 1095, 100 mm diameter, 500 µm thickness) and Borofloat 33 glass (P/N 517) (University Wafer). All materials were used as purchased without further purification or modification.

2.7 References

(1) Agah, M.; Lambertus, G. R.; Sacks, R.; Wise, K. High-speed MEMS-based gas chromatography. *JMemS* **2006**, *15*, 1371-1378.

(2) Haghighi, F.; Talebpour, Z.; Sanati-Nezhad, A. Through the years with on-a-chip gas chromatography: a review. *Lab Chip* **2015**, *15*, 2559-2575.

(3) Regmi, B. P.; Agah, M. Micro Gas Chromatography: An Overview of Critical Components and Their Integration. *Anal Chem* **2018**, *90*, 13133-13150.

(4) Zareian-Jahromi, M. A.; Ashraf-Khorassani, M.; Taylor, L. T.; Agah, M. Design, Modeling, and Fabrication of MEMS-Based Multicapillary Gas Chromatographic Columns. *JMemS* **2009**, *18*, 28-37.

(5) Akbar, M.; Restaino, M.; Agah, M. Chip-scale gas chromatography: From injection through detection. *Microsyst Nanoeng* **2015**, *1*.

(6) Lambertus, G.; Elstro, A.; Sensenig, K.; Potkay, J.; Agah, M.; Scheuering, S.; Wise, K.; Dorman, F.; Sacks, R. Design, fabrication, and evaluation of microfabricated columns for gas chromatography. *Anal Chem* **2004**, *76*, 2629-2637.

(7) Lambertus, G. R.; Fix, C. S.; Reidy, S. M.; Miller, R. A.; Wheeler, D.; Nazarov, E.; Sacks, R. Silicon microfabricated column with microfabricated differential mobility spectrometer for GC analysis of volatile organic compounds. *Anal Chem* **2005**, *77*, 7563-7571.

(8) Collin, W. R.; Serrano, G.; Wright, L. K.; Chang, H.; Nunovero, N.; Zellers, E. T. Microfabricated gas chromatograph for rapid, trace-level determinations of gas-phase explosive marker compounds. *Anal Chem* **2014**, *86*, 655-663.

(9) Kim, S. K.; Chang, H.; Zellers, E. T. Microfabricated gas chromatograph for the selective determination of trichloroethylene vapor at sub-parts-per-billion concentrations in complex mixtures. *Anal Chem* **2011**, *83*, 7198-7206.

(10) Reidy, S.; Lambertus, G.; Reece, J.; Sacks, R. High-performance, static-coated silicon microfabricated columns for gas chromatography. *Anal Chem* **2006**, *78*, 2623-2630.

(11) Luong, J.; Gras, R.; Shellie, R. A.; Cortes, H. J. Applications of planar microfluidic devices and gas chromatography for complex problem solving. *J Sep Sci* **2013**, *36*, 182-191.

(12) Ali, S.; Ashraf-Khorassani, M.; Taylor, L. T.; Agah, M. MEMS-based semi-packed gas chromatography columns. *Sensors Actuators B: Chem* **2009**, *141*, 309-315.

(13) Lewis, A. C.; Hamilton, J. F.; Rhodes, C. N.; Halliday, J.; Bartle, K. D.; Homewood, P.; Grenfell, R. J.; Goody, B.; Harling, A. M.; Brewer, P.; Vargha, G.; Milton, M. J. Microfabricated planar glass gas chromatography with photoionization detection. *J Chromatogr A* **2010**, *1217*, 768-774.

(14) Agah, M.; Potkay, J. A.; Lambertus, G.; Sacks, R.; Wise, K. D. High-performance temperature-programmed microfabricated gas chromatography columns. *JMemS* **2005**, *14*, 1039-1050.

(15) Narayanan, S.; Agah, M. Fabrication and Characterization of a Suspended TCD Integrated With a Gas Separation Column. *JMemS* **2013**, *22*, 1166-1173.

(16) Reidy, S.; George, D.; Agah, M.; Sacks, R. Temperature-programmed GC using silicon microfabricated columns with integrated heaters and temperature sensors. *Anal Chem* **2007**, *79*, 2911-2917.

(17) Restek's PLOT Column Family - The Benchmark for Performance. https://www.restek.com/Technical-Resources/Technical-Library/Petroleum-Petrochemical/Restek-s-PLOT-Column-Family-PCSS1163G-UNV.

(18) Ji, Z.; Hutt, S. A new bonded porous polymer PLOT U column with increased polarity. *J Chromatogr Sci* **2000**, *38*, 496-502.

(19) Vickers, A. K.: PLOT Column Selection. 2000.

(20) Sidel'nikov, V. N.; Nikolaeva, O. A.; Platonov, I. A. Stationary Phases Deposition on the Planar Columns Capillaries. *Prot Met Phys Chem* **2015**, *51*, 1065-1075.

(21) Serrano, G.; Reidy, S. M.; Zellers, E. T. Assessing the reliability of wall-coated microfabricated gas chromatographic separation columns. *Sensors Actuators B: Chem* **2009**, *141*, 217-226.

(22) Yutao, Q.; Gianchandani, Y. B. iGC1: An Integrated Fluidic System for Gas Chromatography Including Knudsen Pump, Preconcentrator, Column, and Detector Microfabricated by a Three-Mask Process. *JMemS* **2014**, *23*, 980-990.

(23) Manginell, R. P.; Bauer, J. M.; Moorman, M. W.; Sanchez, L. J.; Anderson, J. M.; Whiting, J. J.; Porter, D. A.; Copic, D.; Achyuthan, K. E. A monolithically-integrated µGC chemical sensor system. *Sensors (Basel)* **2011**, *11*, 6517-6532.

(24) Pelz, N.; Dempster, N. M.; Shore, P. R. Analysis of low molecular weight hydrocarbons including 1,3-butadiene in engine exhaust gases using an aluminum oxide porous-layer open-tubular fused-silica column. *J Chromatogr Sci* **1990**, *28*, 230-235.

(25) Kerns, W. D.; Pavkov, K. L.; Donofrio, D. J.; Gralla, E. J.; Swenberg, J. A. Carcinogenicity of formaldehyde in rats and mice after long-term inhalation exposure. *Cancer Res* **1983**, *43*, 4382-4392.

(26) Dumas, T. Determination of Formaldehyde in Air by Gas-Chromatography. *J Chromatogr* **1982**, *247*, 289-295.

(27) Harrison, S. Determination of Small Amounts of Formaldehyde in Acetaldehyde. *Analyst* **1967**, *92*, 773-&.

(28) Tang, X.; Bai, Y.; Duong, A.; Smith, M. T.; Li, L.; Zhang, L. Formaldehyde in China: production, consumption, exposure levels, and health effects. *Environ Int* **2009**, *35*, 1210-1224.

(29) Salthammer, T.; Mentese, S.; Marutzky, R. Formaldehyde in the indoor environment. *Chem Rev* **2010**, *110*, 2536-2572.

(30) Swenberg, J. A.; Kerns, W. D.; Mitchell, R. I.; Gralla, E. J.; Pavkov, K. L. Induction of squamous cell carcinomas of the rat nasal cavity by inhalation exposure to formaldehyde vapor. *Cancer Res* **1980**, *40*, 3398-3402.

(31) Songur, A.; Ozen, O. A.; Sarsilmaz, M. The toxic effects of formaldehyde on the nervous system. *Rev Environ Contam Toxicol* **2010**, *203*, 105-118.

(32) de Zeeuw, J.; de Nijs, R. C. M.; Henrich, L. T. Adsorption Chromatography on PLOT (Porous-Layer Open-Tubular) Columns: A New Look at the Future of Capillary GC. *J Chromatogr Sci* **1987**, *25*, 71-83.

(33) Sýkora, D.; Peters, E. C.; Svec, F.; Fréchet, J. M. J. "Molded" porous polymer monoliths: A novel format for capillary gas chromatography stationary phases. *Macromol Mater Eng* **2000**, *275*, 42-47.

(34) Nesterenko, E. P.; Burke, M.; de Bosset, C.; Pessutto, P.; Malafosse, C.; Collins, D. A. Monolithic porous layer open tubular (monoPLOT) capillary columns for gas chromatography. *RSC Adv* **2015**, *5*, 7890-7896.

(35) Ji, Z. H.; Majors, R. E.; Guthrie, E. J. Porous layer open-tubular capillary columns: preparations, applications and future directions. *J Chromatogr A* **1999**, *842*, 115-142.

(36) Patrushev, Y. V.; Sidelnikov, V. N. Selection of the porous layer open tubular columns for separation of light components in comprehensive two-dimensional gas chromatography. *J Chromatogr A* **2018**, *1579*, 83-88.

(37) Zhang, J.; Chen, J.; Peng, S.; Peng, S.; Zhang, Z.; Tong, Y.; Miller, P. W.; Yan, X. P. Emerging porous materials in confined spaces: from chromatographic applications to flow chemistry. *Chem Soc Rev* **2019**, *48*, 2566-2595.

(38) Mugo, S. M.; Huybregts, L.; Mazurok, J. Adjustable Methacrylate Porous Monolith Polymer Layer Open Tubular Silica Capillary Microextraction for the Determination of Polycyclic Aromatic Hydrocarbons. *Anal Lett* **2016**, *49*, 1824-1834.

(39) Gras, R.; Hua, Y.; Luong, J. High-throughput gas chromatography for volatile compounds analysis by fast temperature programming and adsorption chromatography. *J Sep Sci* **2017**, *40*, 1979-1984.

(40) Yu, C.; Svec, F.; Frechet, J. M. J. Towards stationary phases for chromatography on a microchip: Molded porous polymer monoliths prepared in capillaries by photoinitiated in situ polymerization as separation media for electrochromatography. *Electrophoresis* **2000**, *21*, 120-127.

(41) Causon, T. J.; Shellie, R. A.; Hilder, E. F.; Desmet, G.; Eeltink, S. Kinetic optimisation of open-tubular liquid-chromatography capillaries coated with thick porous layers for increased loadability. *J Chromatogr A* **2011**, *1218*, 8388-8393.

(42) Blumer, M. Preparation of porous layer open tubular columns by dynamic coating and rapid conditioning. *AnaCh* **2002**, *45*, 980-982.

(43) Svec, F.; Kurganov, A. A. Less common applications of monoliths. III. Gas chromatography. *J Chromatogr A* **2008**, *1184*, 281-295.

(44) Daoud Agha Dit Daoudy, B.; Al-Khayat, M. A.; Karabet, F.; Al-Mardini, M. A. A Robust Static Headspace GC-FID Method to Detect and Quantify Formaldehyde Impurity in Pharmaceutical Excipients. *J Anal Methods Chem* **2018**, *2018*, 4526396.

(45) Zhu, H. B.; She, J. Y.; Zhou, M. L.; Fan, X. D. Rapid and sensitive detection of formaldehyde using portable 2-dimensional gas chromatography equipped with photoionization detectors. *Sensors Actuators B: Chem* **2019**, *283*, 182-187.

(46) Korolev, A. A.; Shiryaeva, V. E.; Popova, T. P.; Kozin, A. V.; D'yachkov, I. A.; Kurganov, A. A. Macroporous polymeric monoliths as stationary phases in gas adsorption chromatography. *Polym Sci Ser A* **2006**, *48*, 779-786.

(47) Korolev, A. A.; Shiryaeva, V. E.; Popova, T. P.; Kurganov, A. A. Effect of the pressure of the carrier gas on the parameters of the van deemter equation for monolithic silica gel gas chromatography columns. *Russ J Phys Chem* **2006**, *80*, 781-785.

(48) Korolev, A. A.; Shiryaeva, V. E.; Popova, T. P.; Kurganov, A. A. A study of the efficiency of monolithic silica gel capillary columns for gas chromatography. *Russ J Phys Chem* **2006**, *80*, 609-614.

(49) Grall, A. J.; Sacks, R. D. Column performance and stability for high-speed vacuum-outlet GC of volatile organic compounds using atmospheric pressure air as carrier gas. *Anal Chem* **1999**, *71*, 5199-5205.

(50) Serrano, G.; Sukaew, T.; Zellers, E. T. Hybrid preconcentrator/focuser module for determinations of explosive marker compounds with a micro-scale gas chromatograph. *J Chromatogr A* **2013**, *1279*, 76-85.

(51) Zhang, W.-q.; Li, H.; Zhang, Y.-j.; Bi, F.; Meng, L.-s.; Zhang, X.-m.; Mao, J.-y.; Cheng, N.-l.; Fang, B.; Yang, Y.; Chen, C.; Guo, K.-x.; Zhan, G.-e.; Sha, J.; Wang, X.-z. Fast Determination of Monocyclic Aromatic Hydrocarbons in Ambient Air Using a Portable Gas Chromatography–Photoionization Detector. *Chromatographia* **2017**, *80*, 1233-1247.

(52) Pirsa, S. Design of a portable gas chromatography with a conducting polymer nanocomposite detector device and a method to analyze a gas mixture. *J Sep Sci* **2017**, *40*, 1724-1730.

(53) Zhong, Q.; Steinecker, W. H.; Zellers, E. T. Characterization of a high-performance portable GC with a chemiresistor array detector. *Analyst* **2009**, *134*, 283-293.

(54) Skog, K. M.; Xiong, F.; Kawashima, H.; Doyle, E.; Soto, R.; Gentner, D. R. Compact, Automated, Inexpensive, and Field-Deployable Vacuum-Outlet Gas Chromatograph for Trace-Concentration Gas-Phase Organic Compounds. *Anal Chem* **2019**, *91*, 1318-1327.

(55) Sanchez, J. M.; Sacks, R. D. Performance characteristics of a new prototype for a portable GC using ambient air as carrier gas for on-site analysis. *J Sep Sci* **2007**, *30*, 1052-1060.

(56) Defiant Technologies, I. *FROG-4000TM Chemical Analysis System*2015.

(57) Baltazar, Q. Q.; Leininger, S. K.; Anderson, J. L. Binary ionic liquid mixtures as gas chromatography stationary phases for improving the separation selectivity of alcohols and aromatic compounds. *J Chromatogr A* **2008**, *1182*, 119-127.

(58) Poole, C. F. Chromatographic and spectroscopic methods for the determination of solvent properties of room temperature ionic liquids. *J Chromatogr A* **2004**, *1037*, 49-82.

(59) Seeley, J. V.; Seeley, S. K.; Libby, E. K.; Breitbach, Z. S.; Armstrong, D. W. Comprehensive two-dimensional gas chromatography using a high-temperature phosphonium ionic liquid column. *Anal Bioanal Chem* **2008**, *390*, 323-332.

(60) Pello-Palma, J.; Gonzalez-Alvarez, J.; Gutierrez-Alvarez, M. D.; Dapena de la Fuente, E.; Mangas-Alonso, J. J.; Mendez-Sanchez, D.; Gotor-Fernandez, V.; Arias-Abrodo, P. Determination of volatile compounds in cider apple juices using a covalently bonded ionic liquid coating as the stationary phase in gas chromatography. *Anal Bioanal Chem* **2017**, *409*, 3033-3041.

(61) Dhanesar, S. C.; Coddens, M. E.; Poole, C. F. Evaluation of Tetraalkylammonium Tetrafluoroborate Salts as High-Temperature Stationary Phases for Packed and Open-Tubular Column Gas-Chromatography. *J Chromatogr* **1985**, *349*, 249-265.

(62) Poole, C. F.; Poole, S. K. Extraction of organic compounds with room temperature ionic liquids. *J Chromatogr A* **2010**, *1217*, 2268-2286.

(63) Zhao, X.; Tan, K.; Xing, J. A flexible and convenient strategy for synthesis of ionic liquid bonded polysiloxane stationary phases. *J Chromatogr A* **2019**, *1587*, 197-208.

(64) Mendoza, L. G.; Gonzalez-Alvarez, J.; Gonzalo, C. F.; Arias-Abrodo, P.; Altava, B.; Luis, S. V.; Burguete, M. I.; Gutierrez-Alvarez, M. D. Gas chromatographic analysis of fatty

acid methyl esters of milk fat by an ionic liquid derived from L-phenylalanine as the stationary phase. *Talanta* **2015**, *143*, 212-218.

(65) Patil, R. A.; Talebi, M.; Sidisky, L. M.; Berthod, A.; Armstrong, D. W. Gas chromatography selectivity of new phosphonium-based dicationic ionic liquid stationary phases. *J Sep Sci* **2018**, *41*, 4142-4148.

(66) Zhang, C.; Ingram, I. C.; Hantao, L. W.; Anderson, J. L. Identifying important structural features of ionic liquid stationary phases for the selective separation of nonpolar analytes by comprehensive two-dimensional gas chromatography. *J Chromatogr A* **2015**, *1386*, 89-97.

(67) Anderson, J. L.; Armstrong, D. W. Immobilized ionic liquids as high-selectivity/high-temperature/high-stability gas chromatography stationary phases. *Anal Chem* **2005**, *77*, 6453-6462.

(68) Amaral, M. S. S.; Marriott, P. J.; Bizzo, H. R.; Rezende, C. M. Ionic liquid capillary columns for analysis of multi-component volatiles by gas chromatography-mass spectrometry: performance, selectivity, activity and retention indices. *Anal Bioanal Chem* **2018**, *410*, 4615-4632.

(69) Regmi, B. P.; Chan, R.; Agah, M. Ionic liquid functionalization of semi-packed columns for high-performance gas chromatographic separations. *J Chromatogr A* **2017**, *1510*, 66-72.

(70) Nan, H.; Anderson, J. L. Ionic liquid stationary phases for multidimensional gas chromatography. *TrAC, Trends Analyt Chem* **2018**, *105*, 367-379.

(71) Regmi, B. P.; Chan, R.; Atta, A.; Agah, M. Ionic liquid-coated alumina-pretreated micro gas chromatography columns for high-efficient separations. *J Chromatogr A* **2018**, *1566*, 124-134.

(72) Mazzucotelli, M.; Bicchi, C.; Marengo, A.; Rubiolo, P.; Galli, S.; Anderson, J. L.; Sgorbini, B.; Cagliero, C. Ionic liquids as stationary phases for gas chromatography-Unusual selectivity of ionic liquids with a phosphonium cation and different anions in the flavor, fragrance and essential oil analyses. *J Chromatogr A* **2019**, *1583*, 124-135.

(73) Cagliero, C.; Bicchi, C.; Cordero, C.; Liberto, E.; Rubiolo, P.; Sgorbini, B. Ionic liquids as water-compatible GC stationary phases for the analysis of fragrances and essential oils. *Anal Bioanal Chem* **2018**, *410*, 4657-4668.

(74) Berthod, A.; Ruiz-Angel, M. J.; Carda-Broch, S. Ionic liquids in separation techniques. *J Chromatogr A* **2008**, *1184*, 6-18.

(75) Shashkov, M. V.; Sidelnikov, V. N.; Bratchikova, A. A. New Stationary Ionic Liquid Phases with Quinolinium Cations for Capillary Gas Chromatography. *Anal Lett* **2020**, *53*, 84-101.

(76) Huang, K.; Han, X.; Zhang, X.; Armstrong, D. W. PEG-linked geminal dicationic ionic liquids as selective, high-stability gas chromatographic stationary phases. *Anal Bioanal Chem* **2007**, *389*, 2265-2275.

(77) Berthod, A.; Ruiz-Angel, M. J.; Carda-Broch, S. Recent advances on ionic liquid uses in separation techniques. *J Chromatogr A* **2018**, *1559*, 2-16.

(78) Delmonte, P.; Fardin Kia, A. R.; Kramer, J. K.; Mossoba, M. M.; Sidisky, L.; Rader, J. I. Separation characteristics of fatty acid methyl esters using SLB-IL111, a new ionic liquid coated capillary gas chromatographic column. *J Chromatogr A* **2011**, *1218*, 545-554.

(79) Ragonese, C.; Sciarrone, D.; Tranchida, P. Q.; Dugo, P.; Mondello, L. Use of ionic liquids as stationary phases in hyphenated gas chromatography techniques. *J Chromatogr A* **2012**, *1255*, 130-144.

(80) Shamsi, S. A.; Danielson, N. D. Utility of ionic liquids in analytical separations. *J Sep Sci* **2007**, *30*, 1729-1750.

(81) Talebi, M.; Patil, R. A.; Sidisky, L. M.; Berthod, A.; Armstrong, D. W. Variation of anionic moieties of dicationic ionic liquid GC stationary phases: Effect on stability and selectivity. *Anal Chim Acta* **2018**, *1042*, 155-164.

(82) Weatherly, C. A.; Zhang, Y.; Smuts, J. P.; Fan, H.; Xu, C.; Schug, K. A.; Lang, J. C.; Armstrong, D. W. Analysis of Long-Chain Unsaturated Fatty Acids by Ionic Liquid Gas Chromatography. *J Agric Food Chem* **2016**, *64*, 1422-1432.

(83) Kozai, T. D.; Kipke, D. R. Insertion shuttle with carboxyl terminated self-assembled monolayer coatings for implanting flexible polymer neural probes in the brain. *J Neurosci Methods* **2009**, *184*, 199-205.

(84) Pojjanapornpun, S.; Nolvachai, Y.; Aryusuk, K.; Kulsing, C.; Krisnangkura, K.; Marriott, P. J. Ionic liquid phases with comprehensive two-dimensional gas chromatography of fatty acid methyl esters. *Anal Bioanal Chem* **2018**, *410*, 4669-4677.

(85) Fanali, C.; Micalizzi, G.; Dugo, P.; Mondello, L. Ionic liquids as stationary phases for fatty acid analysis by gas chromatography. *Analyst* **2017**, *142*, 4601-4612.

(86) Nan, H.; Zhang, C.; O'Brien, R. A.; Benchea, A.; Davis, J. H., Jr.; Anderson, J. L. Lipidic ionic liquid stationary phases for the separation of aliphatic hydrocarbons by comprehensive two-dimensional gas chromatography. *J Chromatogr A* **2017**, *1481*, 127-136.

(87) Cacho, J. I.; Campillo, N.; Vinas, P.; Hernandez-Cordoba, M. Improved sensitivity gas chromatography-mass spectrometry determination of parabens in waters using ionic liquids. *Talanta* **2016**, *146*, 568-574.

(88) Frink, L. A.; Armstrong, D. W. Water Determination in Solid Pharmaceutical Products Utilizing Ionic Liquids and Headspace Gas Chromatography. *J Pharm Sci* **2016**, *105*, 2288-2292.

(89) Frink, L. A.; Armstrong, D. W. The utilisation of two detectors for the determination of water in honey using headspace gas chromatography. *Food Chem* **2016**, *205*, 23-27.

(90) Frink, L. A.; Armstrong, D. W. Determination of Trace Water Content in Petroleum and Petroleum Products. *Anal Chem* **2016**, *88*, 8194-8201.

(91) Poole, C. F.; Lenca, N. Gas chromatography on wall-coated open-tubular columns with ionic liquid stationary phases. *J Chromatogr A* **2014**, *1357*, 87-109.

(92) Mahe, L.; Dutriez, T.; Courtiade, M.; Thiebaut, D.; Dulot, H.; Bertoncini, F. Global approach for the selection of high temperature comprehensive two-dimensional gas chromatography experimental conditions and quantitative analysis in regards to sulfur-containing compounds in heavy petroleum cuts. *J Chromatogr A* **2011**, *1218*, 534-544.

(93) Yao, C.; Anderson, J. L. Retention characteristics of organic compounds on molten salt and ionic liquid-based gas chromatography stationary phases. *J Chromatogr A* **2009**, *1216*, 1658-1712.

(94) Knotter, D. M.; de Gendt, S.; Mertens, P. W.; Heyns, M. M. Silicon surface roughening mechanisms in ammonia hydrogen peroxide mixtures. *J Electrochem Soc* **2000**, *147*, 736-740.

(95) Dhanesar, S. C.; Coddens, M. E.; Poole, C. F. Surface Roughening by Sodium-Chloride Deposition for the Preparation of Organic Molten-Salt Open Tubular Columns. *J Chromatogr Sci* **1985**, *23*, 320-324.

(96) Gough, D. V.; Bahaghighat, H. D.; Synovec, R. E. Column selection approach to achieve a high peak capacity in comprehensive three-dimensional gas chromatography. *Talanta* **2019**, *195*, 822-829.

(97) Seeley, J. V.; Bates, C. T.; McCurry, J. D.; Seeley, S. K. Stationary phase selection and comprehensive two-dimensional gas chromatographic analysis of trace biodiesel in petroleum-based fuel. *J Chromatogr A* **2012**, *1226*, 103-109.

(98) Giardina, M.; McCurry, J. D. Comparison of Temperature Programmable Split/Splitless and Cool On-Column Inlets for the Determination of Glycerol and Glycerides in Biodiesel by Gas Chromatography with Flame Ionization Detection. *J Chromatogr Sci* **2016**, *54*, 683-688.

(99) Snow, N. H. Temperature programmed GC: Why are all those peaks so sharp? *LCGC North America* [Online early access]2019.

(100) Blumberg, L. M.: *Temperature-programmed gas chromatography*; John Wiley & Sons, 2010.

(101) Reidy, S.; George, D.; Agah, M.; Sacks, R. Temperature-Programmed GC Using Silicon Microfabricated Columns with Integrated Heaters and Temperature Sensors. *Anal Chem* **2007**, *79*, 2911-2917.

(102) Zhukhovitskii, A. A.; Zolotareva, O. V.; Sokolov, V. A.; Turkel'taub, N. M. New method of chromatographic analysis. *Dokl Akad Nauk SSSR* **1951**, *77*, 435-438.

(103) Blumberg, L. M. Limits of Resolution and Speed of Analysis in Linear Chromatography with and without Focusing. *Chromatographia* **1994**, *39*, 719-728.

(104) Contreras, J. A.; Wang, A.; Rockwood, A. L.; Tolley, H. D.; Lee, M. L. Dynamic thermal gradient gas chromatography. *J Chromatogr A* **2013**, *1302*, 143-151.

(105) Contreras, J. A.; Rockwood, A. L.; Tolley, H. D.; Lee, M. L. Peak sweeping and gating using thermal gradient gas chromatography. *J Chromatogr A* **2013**, *1278*, 160-165.

(106) Tolley, H. D.; Tolley, S. E.; Wang, A.; Lee, M. L. Moving thermal gradients in gas chromatography. *J Chromatogr A* **2014**, *1374*, 189-198.

(107) Boeker, P.; Leppert, J. Flow field thermal gradient gas chromatography. *Anal Chem* **2015**, *87*, 9033-9041.

(108) Wang, A.; Hynynen, S.; Hawkins, A. R.; Tolley, S. E.; Tolley, H. D.; Lee, M. L. Axial thermal gradients in microchip gas chromatography. *J Chromatogr A* **2014**, *1374*, 216-223.

(109) Ghosh, A.; Johnson, J. E.; Nuss, J. G.; Stark, B. A.; Hawkins, A. R.; Tolley, L. T.; Iverson, B. D.; Tolley, H. D.; Lee, M. L. Extending the upper temperature range of gas chromatography with all-silicon microchip columns using a heater/clamp assembly. *J Chromatogr A* **2017**, *1517*, 134-141.

(110) Aldaeus, F.; Thewalim, Y.; Colmsjo, A. Prediction of retention times and peak widths in temperature-programmed gas chromatography using the finite element method. *J Chromatogr A* **2009**, *1216*, 134-139.

(111) Bartle, K. D. Film Thickness of Dynamically Coated Open-Tubular Glass Columns for Gas-Chromatography. *AnaCh* **1973**, *45*, 1831-1836.

(112) Gonzalez, F. R.; Gagliardi, L. G. Distribution coefficients of n-alkanes measured on wall-coated capillary columns. *J Chromatogr A* **2000**, *879*, 157-168.

Chapter 3 Miniaturized Photoionization Detectors

3.1 Introduction

3.1.1 Background

Micro gas chromatography (μGC) devices target rapid *in situ* analysis of volatile organic compounds (VOCs) and require sensitive vapor detectors for a broad range of applications such as environmental monitoring, gas leak detection, and healthcare. Over the past few decades, a variety of miniaturized vapor detectors have been developed for use in μGC, including miniaturized thermal conductivity detectors (TCDs), surface acoustic wave detectors, chemiresistors, chemicapacitors, and electron capture detectors[1-15]. Although many advances have been made toward reducing the footprint and operating costs (power and gas consumption) of these detectors, the largest issue is their poor sensitivity compared to the flame ionization detectors (FIDs) widely used in benchtop GC systems, which μGC systems aim to supplement or replace. While FIDs may possess detection limits on the order of sub pg or sub ppt concentrations (*e.g.*, considering a mass of ~1 pg in 1 L volume), most miniaturized detectors have detection limits around a few ppm or at best tens of ppb[1-13]. Furthermore, many miniaturized detectors are highly selective (*e.g.*, chemiresistors, chemicapacitors)[1-13] and require extensive calibration or array implementations for compatibility with portable μGC due to the broad range of compounds for analysis. Other issues for miniaturization include the need for high auxiliary gas flows (helium/hydrogen) for sensors like TCDs and FIDs, or high voltages for electron capture devices and heating for metal oxide sensors, which are impractical for portable systems with limited space and resources.

In addition to the above, plasma-based photoionization detectors (PIDs) are commonly used for detection of highly volatile compounds in gas monitoring and analysis applications[16-23]. Typical PIDs utilize sealed lamps (made of ultraviolet transparent materials such as LiF or

MgF_2) containing noble or permanent gases (e.g., xenon, krypton, and argon) to excite plasma and thereby generate photons ranging from 9.6 to 11.7 eV. Detection of analytes is determined by the energy of the emitted photons, where any compounds with ionization potentials below the emission energy may be ionized. Unlike other miniaturized gas sensors, PIDs have demonstrated high sensitivity (down to 10s of pg), large dynamic range (up to 6 decades), low manufacturing cost, and fast response times (within 10s of ms) along with small size (few mL), which enables their suitable use in μGC[18-22,24-26]. In particular, Zhu *et al*. reported a microfabricated μPID device demonstrating single digit pg detection limits, tens of milliseconds response time, and low operating voltage (6 VDC)[21], showing great advantages for use in portable μGC.

While μPIDs exhibit many advantages compared to other miniaturized GC-compatible detectors, these sensors still have drawbacks in sensing performance (typically no lower than tens of pg) and limited photon energy (<11.7 eV). These aspects prevent detection of low concentration chemicals as well as chemicals with high ionization energies, respectively, which limits the scope of portable GC to a more specific set of applications. In contrast, the capability of conventional benchtop FIDs to ionize virtually all organic compounds of interest with sub-pg detection limits allows for analysis of a much broader range of applications, such as trace vapor detection, light hydrocarbons, and high ionization potential solvents, which current μPIDs cannot analyze. Further improvement of μPID performance is required for μGC-PID systems to be competitive with the current conventional benchtop GC-FID method.

This chapter focuses on the development of miniaturized photoionization detectors for μGC environmental analysis. Herein, development of μPID sensors is specifically aimed at detection of additional types of compounds, including high ionization potential compounds and even volatile inorganic compounds. Furthermore, improvement of μPID performance targets improving overall system sensitivity, thereby improving the detection limit and capability for detecting trace chemicals. These advancements aim to complement the previously introduced microcolumns by allowing for sensing of additional compounds for wider ranging and more specialized analyses. Details on these applications and specific μPID designs follow in the subsequent sections.

3.1.2 Circuit configuration

Due to the applicability of μPIDs to portable gas sensing, a small-scale circuit was developed in-house to accompany the small footprint of these sensors. The same circuit was used for all devices presented in this chapter. The circuit generates a stabilized high-voltage AC signal of about 0.9 kV with a frequency of 83.6 kHz for plasma generation. This circuit (**Figure 3.1(A)**) was designed using a NE555 astable multivibrator coupled with a step up transformer (ZS1052(H), Excelitas Technologies) through an n-channel MOSFET (IRF740SPBF). On the readout side, a bias voltage of 24 V was applied to the collection electrodes, where the current was then recorded by reading out a voltage drop across an external resistance circuit equivalent to ~102 MΩ. The voltage drop was further amplified using an INA122UA amplifier circuit, as shown in **Figure 3.1(B)**. A low pass filter with a cutoff frequency of 1.5 Hz was applied to the output of the amplification circuit. Notably, the supply voltage to the entire circuit was only 24 VDC, allowing for integration into low voltage, battery-operated portable systems. The total circuit cost was around only ~$250 (including both excitation and readout) and can be further reduced in the future with mass production ($100 – $150).

3.2 Integrated Microfluidic Helium Discharge Photoionization Detectors

3.2.1 Background

Regular PIDs, which generate photons with energies ranging from 9.6 to 11.7 eV, have seen increasing use in portable GC systems as highly sensitive volatile organic compound (VOC) detectors. Despite their many advantages, however, their limited photon energy prevents detection of chemicals with high ionization energies. More recently, research has been directed toward development of helium discharge PIDs (HDPIDs), which use helium flows to generate plasma that emits photons ranging from 13.5 to 17.5 eV[27-50]. In comparison with regular 10.6 eV or 11.7 eV PIDs, HDPIDs have been shown to efficiently ionize and detect virtually all volatile chemicals of interest[28,31,32,38,39,46], including those with ionization potentials close to or above 11.7 eV (e.g., methane and carbon tetrachloride). This provides a significant advantage over conventional lamp based PIDs, which cannot detect high ionization potential compounds such as formaldehyde or methane.

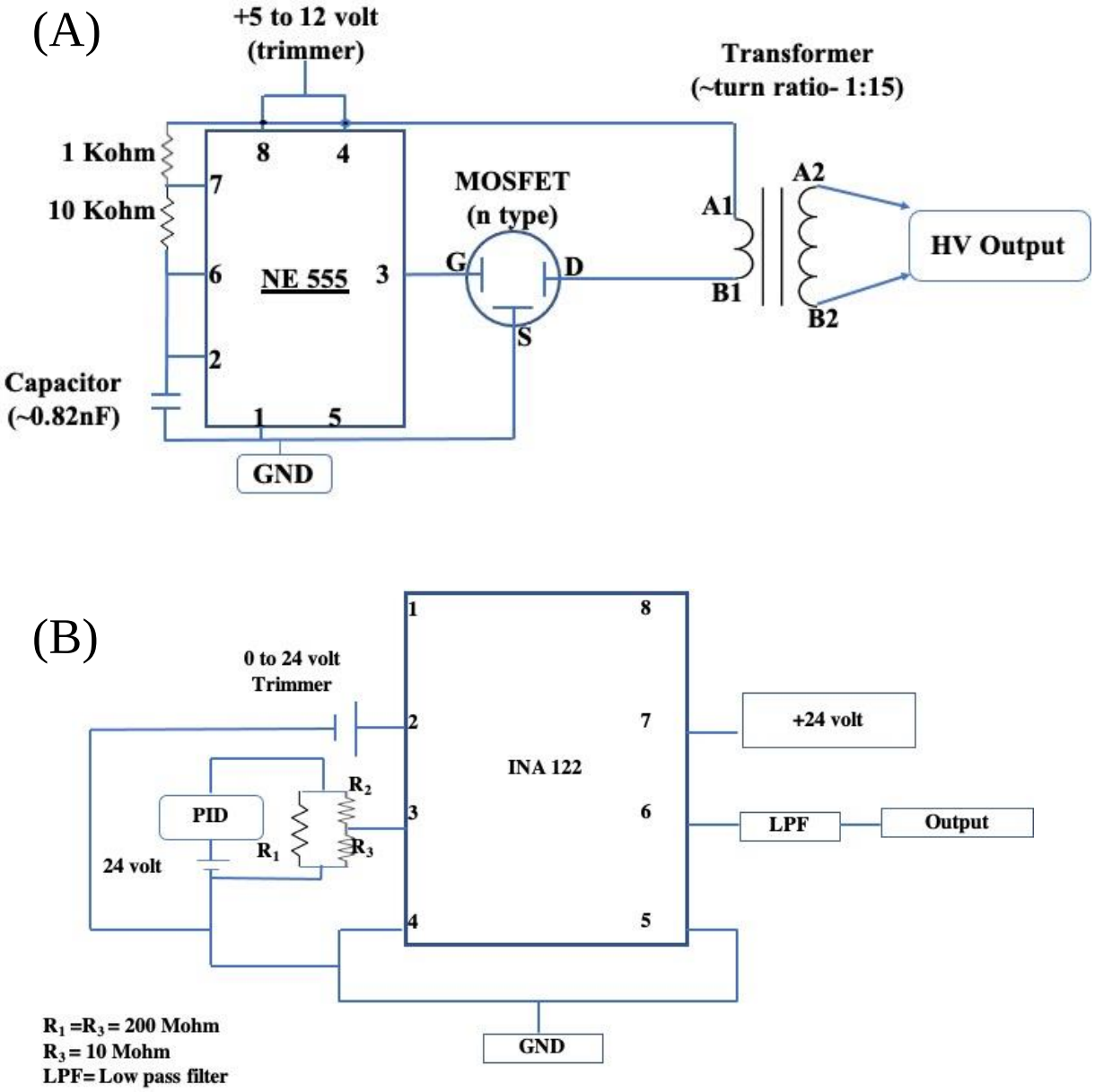

Figure 3.1. (A) Plasma generation circuit. The HV output is an AC signal with an amplitude of ~0.9 kV and a frequency of 83.6 kHz. (B) Amplification circuit. The supply voltage is 24 VDC. The collection electrodes are biased with 24 V. The voltage is read out through the network of R_1, R_2, and R_3, which have an equivalent resistance of ~102 MΩ. The low pass filter cutoff frequency is 1.5 Hz. PID – photoionization detector.

In particular, dielectric barrier discharge (DBD) plasma generation using high voltage (~10s-100s kV) and high frequency (up to several MHz) along with usage of dielectric materials to

protect the electrode surface from the discharge plasma has allowed for highly homogeneous discharge and long electrode lifetime[35,36,45,46,48-50]. These improve device performance (especially noise) and durability. Other methods such as pulsed or direct current discharge are also commonly applied for plasma generation[27,28,30-34,37,38,40,41,43,44,51], where either pulsed or continuous high voltages are used to generate helium ions. In the case of direct current discharge plasmas, most excitation voltages are in the range of a few hundred V[30,40,41,48], while pulsed discharge plasmas utilize pulses on the ms (occasionally μs) timescale to excite the plasma[28,32-34,43,44,48,51]. However, in pulsed or direct current discharge, the lack of dielectric protecting the electrode surface (present in DBD) means that high energy ions bombarding the electrode material degrade the detector over time, necessitating frequent maintenance or replacement. In general, these varying methods have allowed for development of non-destructive detectors with high sensitivity down to a few picograms[28,34,37,38,40], achieving near or subsecond peak widths[28,33,37,38,40], and linear dynamic range up to 7 decades[50], which allows for competitive performance compared to other GC detectors like flame ionization detectors and thermal conductivity detectors.

While the HDPID's high energy makes it a nearly universal detector for gas analysis, in contrast to regular PIDs, most HDPIDs are not applicable to portable GC systems. In an optimized device, the power consumption of the detector itself can be reduced to as low as 1.4 mW[38], but the total system power consumption (measured at the supply) is typically high (up to 12.5 W)[32,42,45,48]. Likewise, the auxiliary helium flow may be reduced to as low as 1 mL/min with specialized designs[38,40], but most systems are relatively helium intensive (up to 300 mL/min)[33,42,46,50], which is prohibitive for portable devices. Additionally, most HDPIDs are bulky in size and weight (comparable to typical FIDs)[33,34,39,42,46,50], especially considering necessary auxiliary system components, such as plasma generation supplies, transformers, and readout circuits. For a portable HDPID system, low power and helium consumption, small footprint, and device robustness are all important characteristics for practical use.

Zhu et al. previously addressed several of these issues by developing a hand-assembled microfluidic HDPID featuring low power consumption (<400 mW), helium consumption (5.8 mL/min), and small size and weight (15 mm x 10 mm x 0.7 mm, 0.25 g), while maintaining picogram-level sensitivity and a dynamic range of over 4 orders of magnitude[36]. The characteristics and performance of this HDPID are well suited for portable GC development, but

the hand-crafted nature of this device greatly reduces fabrication repeatability, robustness, and scalability; such an assembly process cannot be automated for mass-scale production. When factoring in variability due to human assembly, device sensitivity, bias voltage, optimal auxiliary flow, optimal carrier gas flow, and response time become variables as well, meaning that two such HDPIDs may require quite different parameters in order to obtain similar results. Thus, extensive optimization was required for even a single device to operate well.

This section details a method for repeatable, robust microfabrication of integrated microfluidic µHDPIDs. Compared to the previous hand-assembled design, this work allows for high yield and low variability between devices, alleviating the need for extensive optimization on each individual chip. The additional use of in-house designed circuits and miniature power supply (see *3.1.2 Circuit configuration*) enables truly portable operation for *in situ* experiments (as compared to the previous design[36], which used external power supplies and readout circuits). Further comparison between the current work and other HDPIDs is provided in **Table 3.1**.

3.2.2 µHDPID fabrication

The µHDPID fabrication process is shown in **Figure 3.2(A)**. The µHDPID pattern is provided in the schematic shown in **Figure 3.2(B)** and each individual section (*e.g.* plasma collection chamber, collection electrodes, auxiliary and analyte flow inlets, etc.) is labeled. A 175 µm thick Borofloat 33 glass wafer was bonded to a 400 µm thick silicon wafer at 330 °C under vacuum in order to reduce wafer bowing from thermal stress. Subsequently, 100 Å Cr followed by 5000 Å Au were deposited on a fresh 175 µm thick Borofloat 33 glass wafer and Si side of the bonded wafer. The two wafers were patterned with standard lithography processes with mirrored patterns and the Au and Cr were subsequently etched. The Si was then etched away completely (400 µm in depth) using deep reactive ion etching (DRIE) to form the fluidic chamber and channels. The photoresist was stripped from both wafers and the gold sides were bonded via eutectic bonding at 425 °C. A photograph of a single µHDPID chip is provided in **Figure 3.2(C)**. The final chip was 10 mm x 7 mm x 0.75 mm (L x W x H) in size. Additional chip dimensions are provided in **Figure 3.3**.

	PD-HID[28]	VICI PD-D2-IM	Shimadzu BID[50]	Integrated μDPID[19,38,40]	Handmade HDPID[36]	Fabricated μHDPID (current work)
Auxiliary He flow rate (mL/min)	>11.8	10	50-100	1	>5.8	5.2-10.5
Limit of detection	Few pg	~1 pg	~1 pg	~10 pg	Few pg	Few pg
Detector size	10 mL	~400 mL	~400 mL	0.1 mL	0.1 mL	0.1 mL
Power consumption	Not known	Not known	Not known	1.4 mW (power supply not considered)	385 mW total, ~3 mW consumed by HDPID	393 mW (with low power transformer)
Electrode maintenance required?	Yes	Yes	No	Yes	No	No
Warmup time	Not known	Few min	Few hours	Not known	<5 min	<15 s
Response/rise time	Not known	Not known	Not known	>200 ms	~400 ms	~98 ms
Advantages	Low LoD	Low LoD, low He flow needed	Low LoD	Low aux He flow, small footprint, low plasma power consumed	Low LoD, quick warmup, small footprint	Low LoD, very rapid warmup and response times, small footprint, fully self-contained system
Disadvantages	Large size, high He flow needed	Electrode degrades, very large size	Very large size, long warmup time	Electrode degrades, external voltage generator, negative signal observed	Variability and low yield due to hand-assembly, external power supply and readout circuits	Medium aux He flow required, medium power consumed by voltage transformer

Table 3.1. Comparison of fabricated μHDPID with other helium ionization detectors.

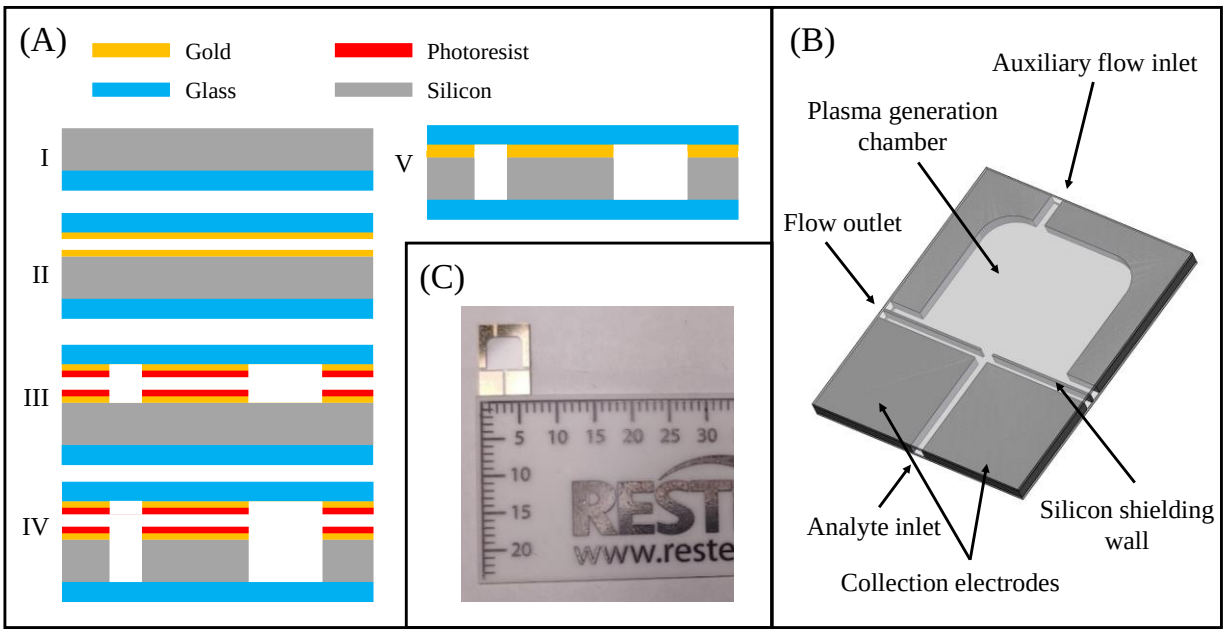

Figure 3.2 (A) µHDPID fabrication procedure. I. Anodic bonding between glass and silicon. II. Gold deposition on bonded wafer and fresh glass wafer. III. Patterning and gold etching. IV. DRIE to etch channels in silicon. V. Photoresist stripping and eutectic bonding. (B) SolidWorks® schematic of single µHDPID chip. (C) Photograph of µHD-PID (eutectically-bonded side facing up). The final chip was 10 mm x 7 mm x 0.75 mm (L x W x H) in size. Detailed chip dimensions are provided in **Figure 3.3**.

After dicing the chips, fluidic connections were formed by inserting guard columns into the inlet and outlet and sealing with Hysol® epoxy. Two pairs of electrodes were made for plasma generation and electrical readout by depositing MG Chemicals silver conductive epoxy on the top and bottom glass surfaces of the plasma chamber and the silicon readout electrodes, respectively. Wires were attached to these electrodes also using MG Chemicals silver conductive epoxy. The µHDPID was flushed with acetone and baked out at 200 °C for 1 hour prior to use. Although plasma excitation electrodes could be deposited during microfabrication, no difference in performance was observed between the microfabricated electrodes and the epoxy electrodes. While solder offers some improvement in mechanical robustness, deposition of appropriate metal pads for wire soldering (instead of silver epoxy) would require additional microfabrication steps, since solder cannot easily adhere to silicon or Pyrex glass.

The total system power consumption was measured to be 1.2 W, the majority of which was consumed by the transformer circuit as heating (note that using an unbranded transformer purchased from eBay, the power consumption can be reduced down to ~393 mW with no loss in performance). The auxiliary helium flow rate was set to 10.5 mL/min for improved device performance, although the µHDPID can be operated with auxiliary flows as low as 5.2 mL/min. The entire device (including circuit and power supply) is contained within a copper shielding mesh of dimensions 11.5 cm x 9 cm x 5 cm, weighing 141 g (**Figure 3.4**).

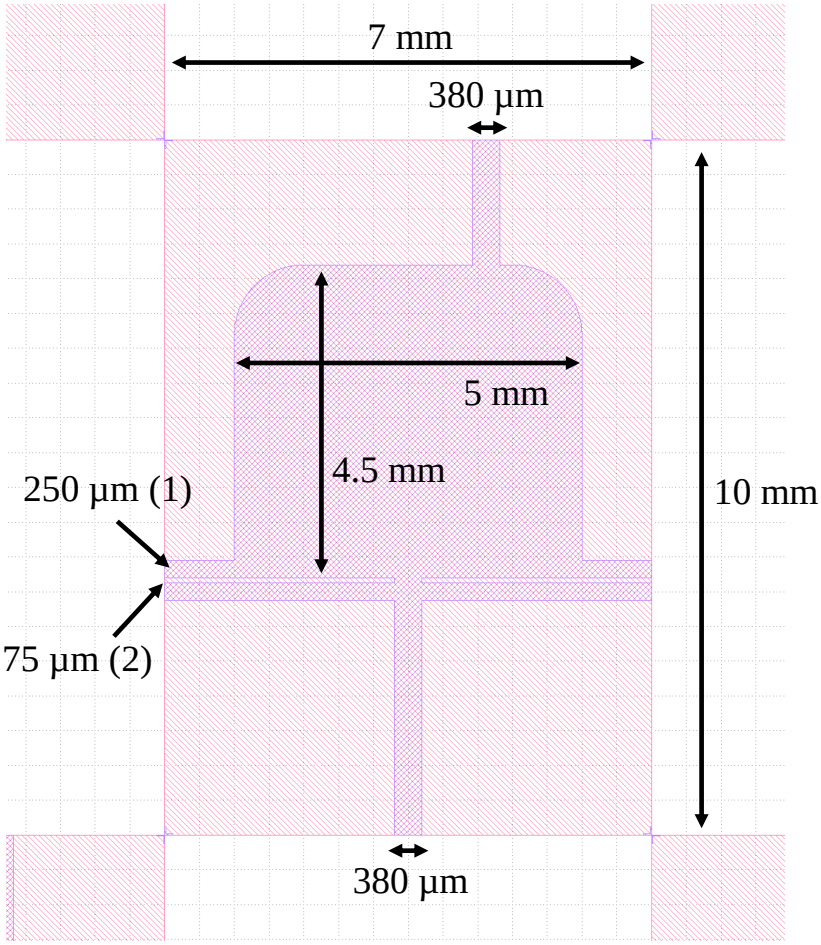

Figure 3.3. µHDPID chip dimensions. (1) Auxiliary and analyte outlet channel width. (2) Silicon ion shield width. See **Figure 3.2** for chip description. The chip height was 750 µm.

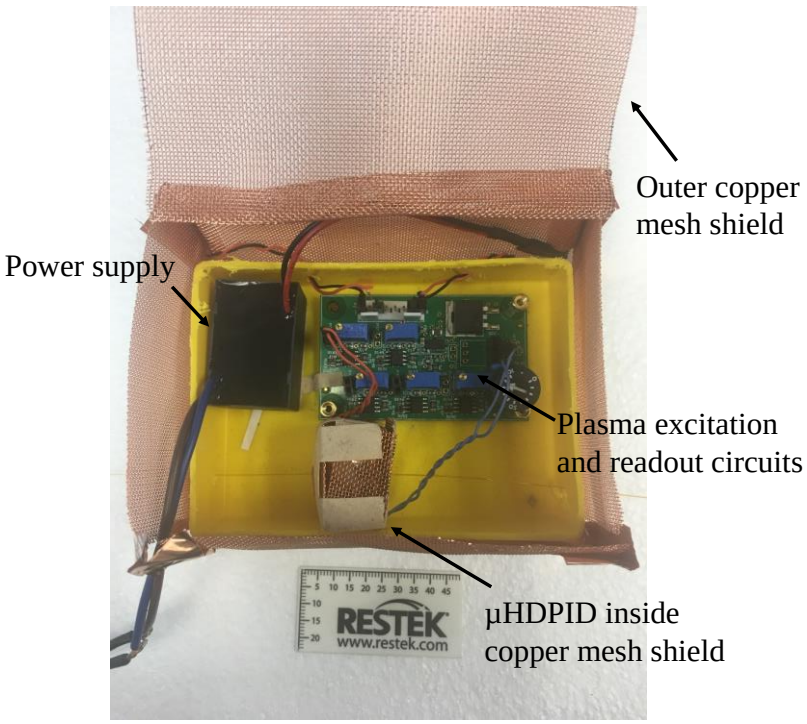

Figure 3.4. Photograph of the µHDPID system, including power supply, plasma excitation and readout circuits, and µHDPID. The entire system size is 11.5 cm x 9 cm x 5 cm and weighs 141g.

3.2.3 Experimental

The µHDPID was evaluated on all separations using an Agilent 6890 benchtop GC equipped with a split/splitless injection port. Manual injections of analytes were made using the injection port and separated using either a 5 m RTX-5 column (pentane, heptane, benzene, toluene, pyridine, tetrahydrofuran, ethyl acetate, acetone, isopropanol), 3 m Rt-Q-BOND column (dichloromethane, chloroform, carbon tetrachloride, methanol, formic acid, formaldehyde solution, acetaldehyde, water), 1 m deactivated fused silica capillary (oxygen, argon, carbon dioxide, methane, ethane, hydrogen, nitrogen), or ShinCarbon ST micropacked column (permanent gas mixture). All analytes were separated under isothermal conditions unless otherwise stated. The temperature was controlled by the GC oven. Ultra-high purity 5.0 grade helium was used as the carrier gas.

3.2.4 µHDPID characterization

3.2.4a Warm-up and response time

For a portable device, both the warm-up time and the response time are important parameters to ensure rapid responses to injected samples. The warm-up time was estimated by repeated injections of pure nitrogen directly after µHDPID plasma ignition (**Figure 3.5**). No peaks were observed within the first 10 s of plasma ignition. However, the first peak could be observed within 15 s after plasma ignition (**Figure 3.5**), demonstrating the µHDPID's rapid startup time.

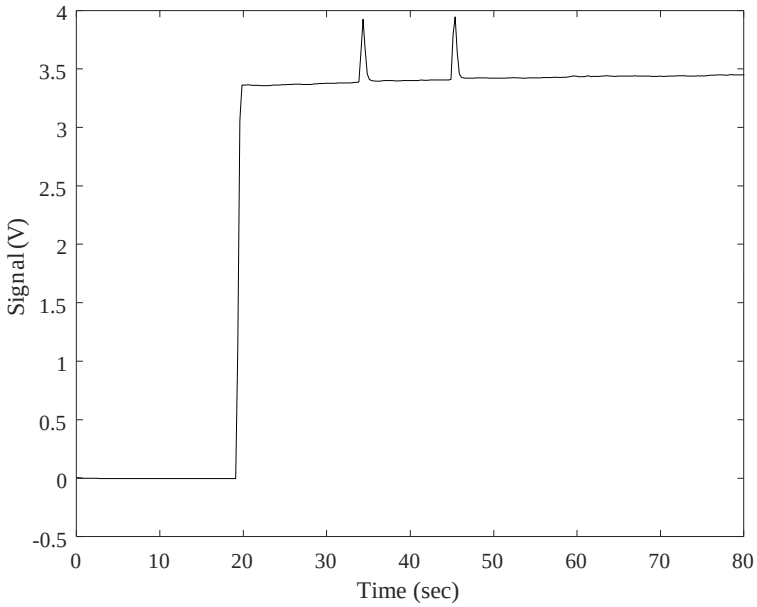

Figure 3.5. µHDPID warm-up time. The plasma voltage and helium were turned on simultaneously at 20 s. Injections of pure nitrogen were made subsequent to plasma ignition. No peaks were observed within the first 10 s after plasma ignition, however, the first peak was observed within 15 s.

The response time (defined as time taken for signal to rise from 10% of peak height to 90% of peak height) was estimated by repeated injections of methane into the µHDPID at a helium flow rate of 1.5 mL/min. Using a sampling rate of 4 Hz, the response time was estimated to be ~320 ms (average of 5 repetitions). However, if the sampling rate was increased to 200 Hz, the response time could be reduced to ~98 ms at the cost of a three times increase in noise (from 0.304 mV to 0.898 mV, 1σ). This response time is less than half of other reported micro HDPIDs (about ~200 – 400 ms)[36,38,40], demonstrating the capability for rapid responses suitable for fast

GC. A sample overlay of the µHDPID methane responses with FID methane response is provided in **Figure 3.6**.

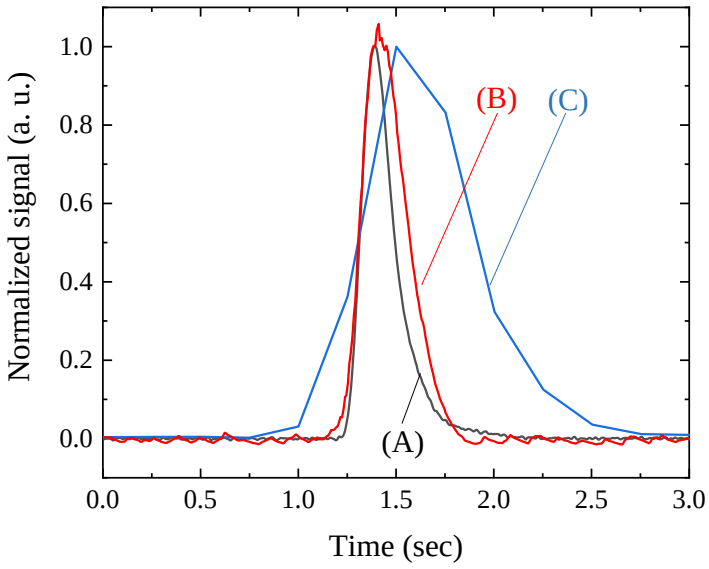

Figure 3.6. µHDPID response to methane (B/C) overlaid with FID methane response (A). The carrier gas flow rate was 1.5 mL/min. (B) µHDPID with a sampling rate of 200 Hz (followed by a 5-point Savitzky–Golay digital smoothing). Response time: ~98 ms. (C) µHDPID with a sampling rate of 4 Hz. Response time: ~320 ms.

3.2.4b Detection limit characterization

In order to characterize the µHDPID's ability to accurately detect low concentration samples, the detection limits of 17 compounds of varying ionization potentials were obtained, including values obtained with the lowest injection mass (**Table 3.2**). Example separations of nitrogen, heptane, methane, and formaldehyde are shown in **Appendix C**. Detection limits were obtained by first calculating the signal to noise ratio (SNR) of peaks obtained from injection masses ranging from 360 to 600 pg (except for pyridine, injection mass was 1163 pg). The noise was calculated based on averaging the standard deviation noise (1σ) of ten 3 second segments of baseline signal, yielding σ = 0.304 mV. Detection limits were calculated by dividing injection masses by corresponding SNRs (3σ noise level).

Compound	DL (pg)	IA (pg)	IP (eV)
Toluene	5.1	513	8.82
Benzene	5.9	513	9.25
Pyridine	6.8	1163	9.32
Tetrahydrofuran	6.5	526	9.54
Acetone	6.5	464	9.69
Heptane	9.0	405	10.08
Ethyl acetate	6.1	534	10.11
Isopropanol	9.9	465	10.12
Acetaldehyde	6.4	467	10.21
Pentane	8.9	556	10.35
Methanol*	11.2	469	10.85
Formaldehyde*	13.4	476	10.87
Formic acid*	13.4	361	11.05
Dichloromethane*	12.3	525	11.35
Chloroform*	12.3	441	11.37
Carbon tetrachloride*	14.2	471	11.47
Water*	11.5	592	12.59

Table 3.2. μHDPID detection limits (DL) of various VOCs taken at 3σ, with σ = 0.304 mV. Detection limits were calculated as averages based on 5 measurements. Ionization potentials (IPs) and injection amounts (IAs) are also reported for convenience. * compounds cannot be detected with regular 10.6 eV krypton lamps. Water cannot be detected with an 11.7 eV argon lamp.

Table 3.2 shows that compounds with ionization potentials above 10.6 eV (or even 11.7 eV in the case of water) can be detected with detection limits close to ~10 pg. Detection limits below 10 pg can also be achieved for compounds with lower ionization potentials, such as pentane or benzene. The low detection limit is facilitated by two factors in the μHDPID design. As compared with the previous HDPID[36], the plasma chamber volume is increased in the new design, meaning that helium ions are not as likely to be injected into the collection channel. In

the original design, the plasma was generated inside a volume with a circular cross-sectional area 380 µm in diameter, resulting in high auxiliary flow speeds of over 100 cm/s. This created a plasma jet that could easily flow over into the collection electrodes, thereby increasing noise. The new increased plasma chamber volume greatly reduces the auxiliary flow to less than 1 cm/s at the boundary between plasma generation and analyte flow, which is nearly negligible compared to the carrier gas flow speed from the analyte side. Additionally, a silicon wall was added between the plasma discharge chamber and the collection electrodes (see **Figure 3.2(B)**), acting as an ion and arc shutter to further reduce the amount of helium ions that could potentially be injected into the collection side. In combination with circuit optimization, these allowed for lowering of the µHDPID noise level and improvement of the detection limit.

3.2.4c Detection of light hydrocarbons and permanent gases

To further demonstrate the µHDPID's capability to serve as a universal detector for gas analysis, light hydrocarbons and permanent gases were injected and their detection limits were calculated (**Table 3.3**). Despite argon's high ionization potential (15.76 eV), the µHDPID was still capable of detecting it with a detection limit of lower than 20 pg, considering the injection volume of 1 µL at a split ratio of 209:1 (concentration 1.784 g/L). The same was true for all other permanent gases and light hydrocarbons. A sample pulse response is provided in **Appendix C**, demonstrating strong responses with 3.5 ng of pure nitrogen and 3 ng of pure methane.

3.2.4d Linearity

In **Figure 3.7**, device linearity was examined for nine compounds of varying ionization potentials, with injection masses ranging from 50 pg to 10 ng for each compound. Highly linear responses were observed over the entire range, corroborating previously obtained results for the hand-assembled HDPID. Notably, the µHDPID was not adversely affected by injections of large amounts of moisture (methanol and water, up to 10 ng), suggesting that vapor condensation is not an issue in the present design. A linear dynamic range of ~4 orders of magnitude was observed for all nine compounds.

Gas	DL (pg)	IA (pg)	IP (eV)
Ethane	11.3	200	11.65
Oxygen	11.3	7000	12.08
Methane	11.8	3000	12.98
Carbon dioxide	14.7	10000	13.79
Hydrogen	18.8	3600	15.43
Nitrogen	18.5	3500	15.58
Argon	19.8	8500	15.76

Table 3.3. µHDPID detection limits (DL) of various gases taken at 3σ, with σ = 0.304 mV. Detection limits were calculated as averages based on 5 measurements. Ionization potentials (IPs) and injection amounts (IAs) are also reported for convenience.

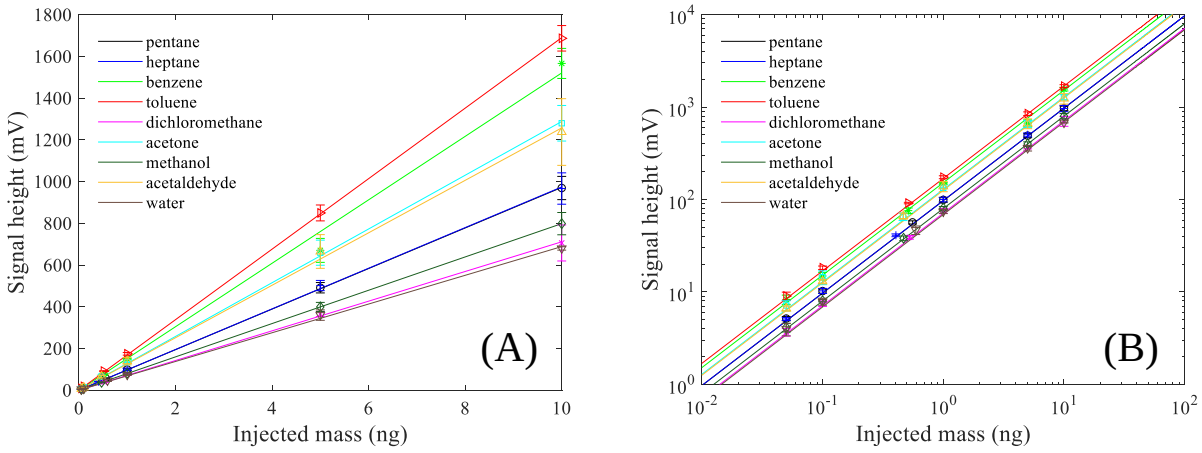

Figure 3.7. µHDPID linearity on nine compounds with injection masses ranging from 50 pg to 10 ng. (A) Signal heights vs. injected masses plotted in linear-linear scale. (B) Signal heights vs. injected masses plotted in log-log scale. Error bars are obtained from five measurements. The R^2 values for the nine linear fits are 0.9999, 0.9996, 0.9945, 1.0000, 0.9996, 0.9997, 1.0000, 0.9985, and 0.9990 from pentane to water, respectively.

3.2.4e Repeatability between devices

The main advantage of the µHDPID is the robust microfabrication process, allowing for high repeatability among different devices. To examine this, the detection limits of heptane, benzene,

dichloromethane, and nitrogen were examined for five different devices (5 repeated injections at each data point). **Figure 3.8** shows that the standard deviation of the detection limits for the five devices are 0.35 (3.9%), 0.54 (8.4%), 1.36 (10.6%), and 0.38 (2.0%) pg for heptane, benzene, dichloromethane, and nitrogen respectively. Values in percentages are calculated as deviation divided by the average of the detection limits of the five devices. The maximum deviation observed was 2.6 pg, or 20.3% for dichloromethane, while on average, the deviation between devices was only 6.2% (calculated as the average of the standard deviations divided by their respective detection limits). Notably, these results were obtained using the same operating parameters for all devices (i.e., auxiliary flow rate, carrier gas flow rate, plasma excitation voltage, readout electrode bias voltage), demonstrating low inter-device variance. Further improvements to repeatability would involve more robust methods for electrode formation, such as deposition of gold-tin electrodes during microfabrication (for both readout electrodes and plasma generation) and soldering shorter, fixed-length wire interconnections.

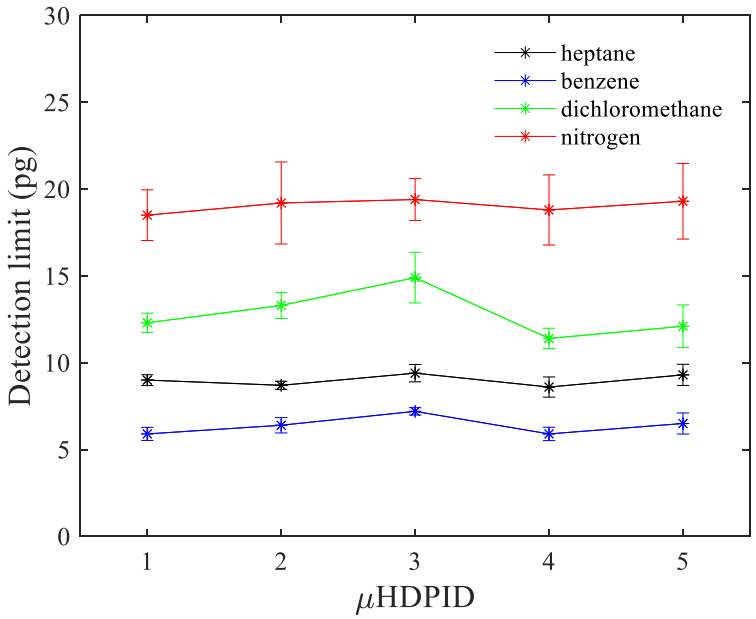

Figure 3.8. μHDPID repeatability. The detection limits of heptane, benzene, dichloromethane, and nitrogen were measured (5 repeated injections for each data point) for 5 different devices. The detection limit variation between devices was no larger than 2.6 pg, or 20.3% for dichloromethane.

3.2.4f GC chromatograms

In order to demonstrate the μHDPID's applicability to GC detection, two separations of formaldehyde solution and permanent gases were performed. The formaldehyde solution—consisting of methanol, water, and formaldehyde—was separated using a 3 m Rt-Q-BOND column with a temperature ramping profile of 70 °C ramped to 145 °C at a rate of 30 °C/min. The flow rate was 3 mL/min, and the split ratio was 20:1. The resulting chromatogram is shown in **Figure 3.9(A)** and demonstrates sharp peaks with peak widths (at half height) close to ~1-2 s.

A mixture of hydrogen, oxygen, argon, nitrogen, methane, and carbon dioxide was prepared for the permanent gas separation. This mixture was separated using a ShinCarbon ST micropacked column using a temperature ramping profile of 30 °C held for 3 minutes, then ramped to 180 °C at a rate of 15 °C/min. The flow rate was set to 6.5 mL/min and the split ratio was set to 20:1. Five of the six permanent gases were separated by the column (**Figure 3.9(B)**), with oxygen and argon coeluted as the second peak. This separation confirms the μHDPID's capability to detect high ionization potential permanent gases.

3.2.5 μHDPID summary

The development and fabrication of an integrated μHDPID has been detailed herein. The entire detector system was shown to be contained within a copper mesh of dimensions 11.5 cm x 9 cm x 5 cm, and only weighing 141 g. Analysis of permanent gases, light hydrocarbons, and formaldehyde was performed, demonstrating detection limits less than 10 pg for various volatile compounds and less than 20 pg for even high ionization energy permanent gases. High linearity for injections ranging from 50 pg to 10 ng was also observed, along with low warm-up time (within 15 s), and high repeatability between devices. Compared to the prior HDPID, the current μHDPID design offers the greatest advantages in ease of fabrication, fabrication yield and robustness, and repeatability. This on-chip, integrated fabrication allows for large-scale production of high quality μHDPIDs, which can be produced in bulk and used alongside or replacing the current lamp-based PID (ionization up to 11.7 eV) technology commonly used in portable GC systems.

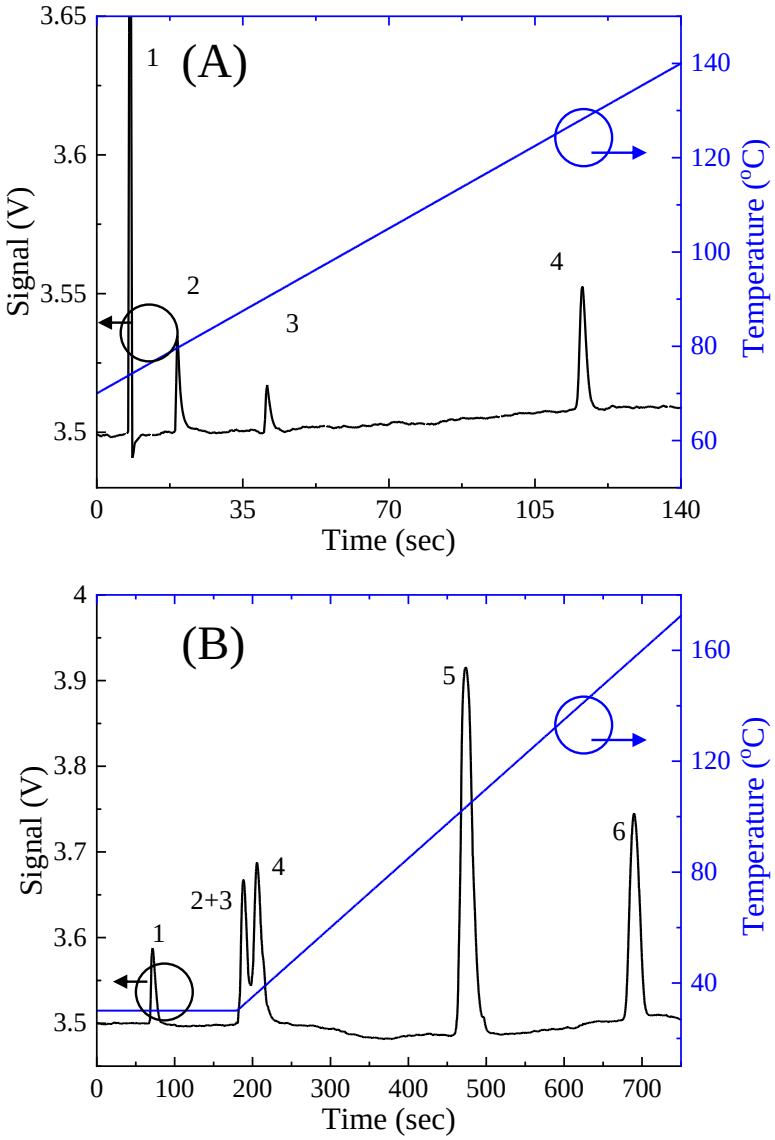

Figure 3.9. (A) Separation of formaldehyde solution (methanol, water, and formaldehyde) using a 3 m Rt-Q-BOND column. An injection of 3 µL of headspace from the solution was made at a split ratio of 20:1 using a carrier gas flow rate of 3 mL/min at 70 °C. 1. Air; 2. Methanol; 3. Water; 4. Formaldehyde. (B) Separation of permanent gases using a ShinCarbon ST micropacked column. An injection of 50 µL of gas mixture was made using a carrier gas flow rate of 6.5 mL/min at 30 °C with a split ratio of 20:1. 1. Hydrogen; 2. Oxygen; 3. Argon; 4. Nitrogen; 5. Methane; 6. Carbon dioxide.

3.3 High sensitivity μGC-PID for trace vapor detection

3.3.1 Background

Current PIDs provide wide-ranging detection with low detection limits compared to many other miniaturized GC-compatible detectors. Their use in portable GC systems has been directed toward diverse *in situ* chemical analyses. A particular point of interest is trace VOC detection for applications such as indoor air screening or detection of explosives and narcotics, which critically require highly sensitive vapor detectors which ultimately determine the sensitivity of μGC systems. However, the relatively poor performance of current μPIDs (compared to FIDs) presents a problem for trace vapor analysis applications, which require near pg detection limits, corresponding to ppt to sub-ppb concentration levels (~ng/L or sub ng/L). **Table 3.4** provides an example list of target detection or screening levels set by the EPA for the investigation of regional screening of carcinogens.

Compound	**EPA regional screening level ($ng \cdot L^{-1}$)**	**EPA regional screening level (ppb)**
Acetaldehyde	5.57	3.09
Aniline	4.38	1.15
Benzene	1.57	0.49
Bromoform	11.1	1.06
Dichlorobenzene	1.11	0.18
Formaldehyde	0.94	0.77
Nitrobenzene	0.31	0.06
Nitropropane	0.02	0.005
n-nonane	87.6	16.7
Safrole	0.19	0.03
Vinyl chloride	2.79	1.09

Table 3.4. EPA regional screening levels at Superfund sites of various carcinogens at a target risk of 10^{-6} and hazard quotient of 1.

This section details the development of a highly sensitive chip-based μPID with a sub-pg detection limit and a wide linear dynamic range. In particular, side-by-side comparison shows that the detection limit of the μPID is 2-4 times better than a commercial Agilent FID over a broad range of VOCs. Based on this μPID, a complete, automated, highly robust μGC-PID system was constructed using in-house fabricated micro-components, including miniaturized preconcentrator, micro-column (μcolumn), and μPID, as well as in-house developed PID circuits. The whole system is self-contained within a box of dimensions 27 cm x 24 cm x 10 cm and can be independently operated without the use of any benchtop equipment (besides a laptop for readout). Due to the highly sensitive μPID, this system is capable of detecting sub-ppt concentrations of VOCs with a 200 mL sample volume, which is enabled by the miniaturized preconcentrator. Details on the μPID fabrication procedure and characterization along with system-level assembly are provided, with emphasis on μPID and μGC-PID performance for detection of trace VOCs. Both standard sample chromatograms and practical chromatograms are also provided. This exhibits the capability of the μGC-PID to match or even surpass the benchtop GC-FID detection limit, enabling use of this μGC-PID system to supplement or replace the need for conventional benchtop GC analysis for on-site low concentration VOC analysis.

3.3.2 Component fabrication

3.3.2a μPID fabrication

The μPID chip was fabricated according to the fabrication process and pattern shown in **Appendix D**, which were adapted from our previous work[21]. The pattern was modified to form a circular spiral with a wider channel width of 400 μm. This allowed for a larger illumination area of ~14 mm^2 from 3.5 mm^2 in the previous design[21], as well as increased flow rates through the channel. After dicing, the chip was immersed in acetone and baked out at 80 °C for 1 hour. A photograph of the μPID chip is also provided in **Appendix D**. Subsequently, a VUV krypton lamp was then mounted atop the microchannel and sealed with Norland optical adhesive, with fluidic connections simultaneously formed by inserting guard columns into the inlet and outlet and sealing with the same optical adhesive. Prior to electrode formation, the silicon contact resistance was reduced to 10 kΩ, critically improving μPID's sensitivity. Readout electrodes were then formed by depositing MG Chemicals silver conductive epoxy and attaching wires. The

electrode bias voltage was notably increased to 24 V to from 6 V[21] to accommodate the wider channel width.

3.3.2b µcolumn fabrication

5 m and 10 m µcolumns were fabricated according to the fabrication process provided in Chapter 2. The columns were deactivated by 8 repeated injections of hexamethyldisilazane (HMDS) at 120 °C over 2 hours. The columns were both dynamically coated with a 3% (w/w) solution of OV-1 in dichloromethane by injecting 1 mL of solution and pushing out at a rate of 5 cm/min. The columns were subsequently treated with HMDS again (8 injections at 120 °C over 2 hours), then baked out at 220 °C for 2 hours prior to use. The resistance of the integrated heater was measured to be 22 Ω for the 5 m column and 28 Ω for the 10 m column and wire bonded to a PCB board to allow for pulse-width-modulated heating using a peak voltage of 24 V. The maximum temperature ramping rate was estimated to be around 10 °C/sec (up to 150 °C), although typical temperature ramping rates used ranged from around 30 °C/min to 60 °C/min.

3.3.2c Preconcentrator assembly

The stainless steel preconcentrator was made by first cutting a 21.5 gauge stainless steel tube to 4.5 cm in length. One end was first plugged with glass wool. Subsequently, the tube was filled with 0.75 mg of Carbopack B, followed by 0.75 mg of Carbopack X, and the other end was then plugged with glass wool again. Two universal press-tight connectors were attached to both ends of the stainless steel tube after loading and fixed using Hysol epoxy. A very thin layer of epoxy (~0.2 mm) was also applied to the outer surface of the stainless steel tube body. The entire preconcentrator was placed into an oven at 120 °C and left to dry for 12 hours. Finally, 32 gauge nickel chromium wire (resistance ~ 7 Ω) was wrapped around the stainless steel tube body for heating.

3.3.3 System setup and experimental conditions

The µGC-PID system was assembled by forming fluidic connections using universal press-tight connectors and deactivated fused silica capillaries between the injector, µcolumn, and µPID. Both the plasma excitation voltage and baseline voltage trimming were carefully tuned to improve the signal-to-noise-ratio of the system. Furthermore, relevant electronic components

(especially the µPID) were shielded with copper mesh to further reduce the noise. A fluidic diagram is provided in **Figure 3.10**, and a picture of the system is provided in **Figure 3.11**. The whole system is self-contained within a box of dimensions 27 cm x 24 cm x 10 cm (excluding a laptop for readout). The system was evaluated using either a 12 cm (1.875 µL) sampling loop or preconcentrator injector. Analytes were sampled into the sampling loop or preconcentrator and injected into the µcolumn, with separation conducted under isothermal conditions for single analytes, or with corresponding temperature ramping rates for chromatograms (*i.e.*, analyte mixtures). The 5 m µcolumn was used for all in laboratory experiments (*i.e.*, detection limit, linearity, and standard samples), while the 10 m µcolumn was used for practical chromatograms (*i.e.*, breath and car exhaust). Heating was controlled by the integrated heater on the column surface. All heating, pumping, and valve switching was controlled via in-house developed LabVIEW software. The only required user input was setting relevant temperature programming parameters and initiating the program; once started, the µGC-PID system could sample and run autonomously. 99.5% purity helium was used as the carrier gas. Finally, considering a carrier gas flow rate of 2 mL/min, the 95 mL (2.4 g of helium) cartridges used were capable of lasting >100 hours of operation, more than enough for a day trip in the field.

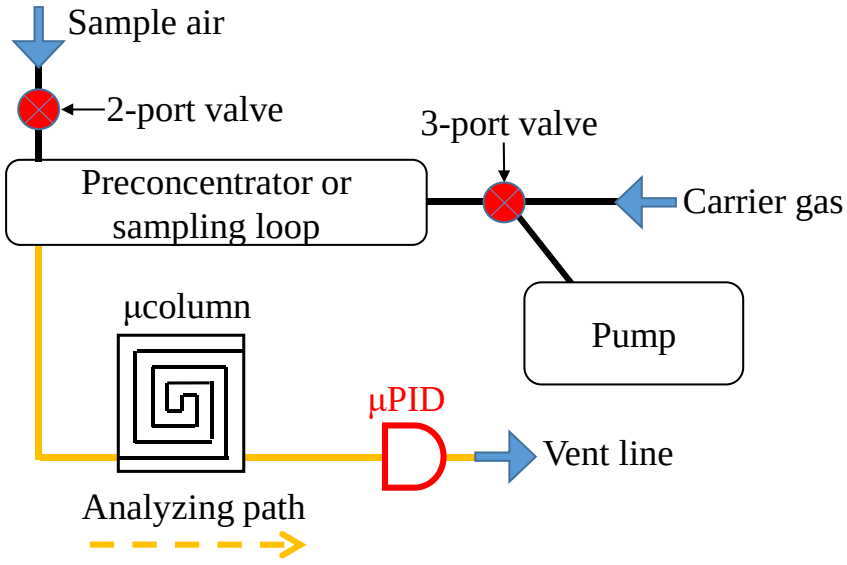

Figure 3.10. µGC-PID system fluidic diagram. The system is entirely self-contained excluding the computer at signal output. Either a sampling loop or preconcentrator can be used for sample

injection. The µcolumn was coated with a 3% (w/w) solution of OV-1. A picture of the µPID system is provided in **Figure 3.11**.

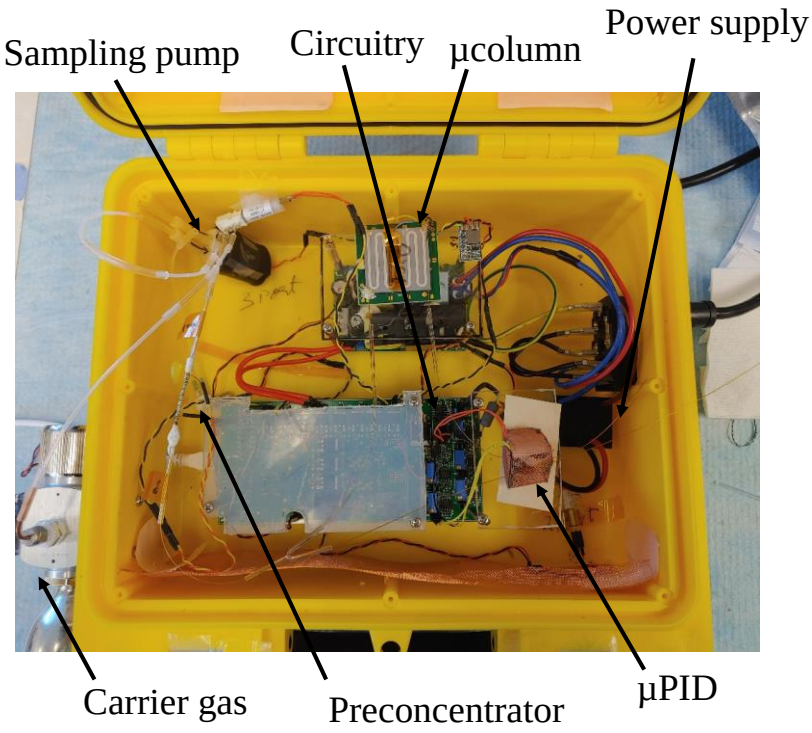

Figure 3.11. Photograph of the µGC-PID system with components labeled. The system has dimensions 27 cm x 24 cm x 10 cm and is entirely self-contained excluding the computer at signal output.

3.3.4 Results and discussion

3.3.4a Detection limit characterization

For trace vapor analysis, low limits of detection are required for accurate analysis. The µPID's detection limit was thus characterized on 14 compounds (**Table 3.5**) and compared to a conventional benchtop FID (Agilent 6890N). Injections on the FID were made using a gas-tight syringe in split mode. Sample separations of hexane and octane with comparison to FID signals are shown in **Figure 3.12**. Detection limits were obtained by first calculating the signal to noise ratio (SNR) of peaks obtained from injection masses ranging from 100 to 200 pg (except for o-xylene, injection mass was 432.2 pg). The noise was calculated based on averaging the standard deviation noise (1σ) of ten 3 second segments of baseline signal, yielding σ = 0.0162 mV. Detection limits were calculated by dividing injection masses by corresponding SNRs (3σ noise

level). Notably, these detection limits were obtained *without* any preconcentration (*i.e.*, only a 12 cm long 1.875 µL sampling loop was used) in order to examine the µPID's intrinsic performance. The µPID detection limit for many compounds with ionization potentials below ~10.1 eV is around 0.2-0.3 pg (**Table 3.5**), outperforming the commercial FID that has detection limits around 0.7 pg. The µPID detection limit is increased for compounds with ionization potentials closer to 10.6 eV, such as ethyl acetate, isopropanol, and hexane.

Compound	µPID DL (pg)	FID DL (pg)	IA (pg)	IP (eV)
Hexane	0.92	0.73	12.3	10.18
Hexane	0.93	0.73	125.5	10.18
Heptane	0.18	0.75	135.4	10.08
Octane	0.20	0.84	10.1	9.82
Octane	0.21	0.84	125.8	9.82
Benzene	0.23	0.49	129.0	9.25
Toluene	0.21	0.77	9.8	8.82
Toluene	0.19	0.77	173.4	8.82
Ethylbenzene	0.26	0.58	116.9	8.77
o-Xylene	0.22	0.67	432.2	8.56
Ethyl acetate	0.58	0.82	10.2	10.11
Ethyl acetate	0.61	0.82	113.4	10.11
Butyl acetate	0.24	0.60	127.9	10.01
2-pentanone	0.20	0.39	7.6	9.40
2-pentanone	0.22	0.39	100.8	9.40
Tetrahydrofuran	0.26	0.76	128.7	9.40
Isopropanol	0.58	0.64	11.1	10.12
Isopropanol	0.65	0.64	104.9	10.12
2-butanol	0.24	0.66	117.6	10.10
Acetone	0.16	0.40	9.8	9.69
Acetone	0.21	0.40	143.9	9.69

Table 3.5. µPID detection limits (DL) of various VOCs taken at 3σ, with σ = 0.0162 mV, and using lowest injection amounts made. FID detection limits are provided for comparison (σ_{FID} = 0.0059 pA). Detection limits were calculated as averages based on 3 measurements. Ionization potentials (IPs) and injection amounts (IAs) are also reported for convenience.

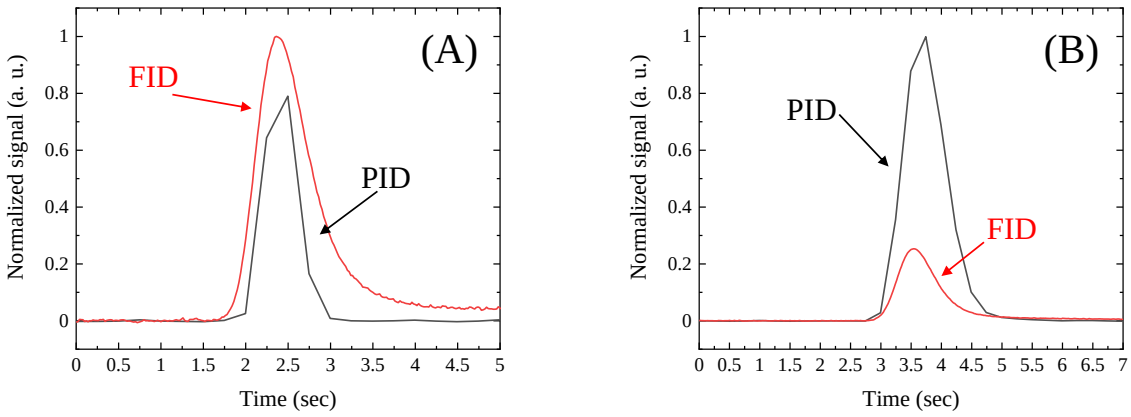

Figure 3.12. µPID response to hexane (A) and octane (B) overlaid with FID hexane and octane response. The carrier gas flow rate was 1.2 mL/min.

As compared to the previously reported µPID[21], the current µPID exhibited a ~20-fold improvement in the detection limit, which was facilitated by the following factors. First, the VUV illumination area was increased to ~14 mm^2 from 3.5 mm^2, which is nearly the same as the total area of the VUV lamp window. This allows almost all of the photons emitted from the lamp to be utilized for analyte ionization, especially considering the short illumination path of 400 µm. Additionally, although the distance between the electrodes is increased to 400 µm from 150 µm, the bias voltage was quadrupled to 24 V (corresponding to an electric field of 600 V/cm) allowing for efficient capture of ions in the collection channel; in other words, the ion transit time was maintained to be very short, resulting in high ion collection efficiency. Combined with the low contact resistance, optimized circuit, and component shielding, these parameters resulted in both increased signal strength and decreased noise level, resulting in a sub-pg detection limit.

3.3.4b Linearity

In **Figure 3.13**, µPID linearity was examined for seven compounds with injection masses ranging from as low as 10 pg to 10 ng for each compound. Highly linear responses were observed over the entire range, with a linear dynamic range of at least 4 orders of magnitude observed for all compounds. Notably, the µPID was linear even for low injection amounts around 10 pg, showing that even extremely low injection amounts could be detected by the system. µPID sensitivity and sensitivity normalized by molecular weight is provided in **Table**

3.6, which shows that slopes of compounds with similar ionization potentials are close to one another and that the µPID detects the molar concentration of analyte in the fluidic channel.

3.3.4c System robustness

For a portable system, robustness and stability over device lifetime are important in order to avoid unnecessary maintenance and calibration due to drift. The entire µGC-PID system was run for 3 months without replacement or maintenance of any parts and exhibited no difference in performance at the end of the 3 month period compared to at the start of the period. Analysis on stability was performed by assessing the baseline and noise levels of the µPID readout signal over a 12 week period, as well as examining the system's detection limit on heptane over the µPID run lifetime (**Figure 3.14**). The baseline and noise levels demonstrated low variability over the 12 week period, with the baseline level varying from 0.1370 to 0.1372 V, and the noise varying from 0.0138 mV to 0.0189 mV (average 0.0165 mV), suggesting that system drift over time was minimal.

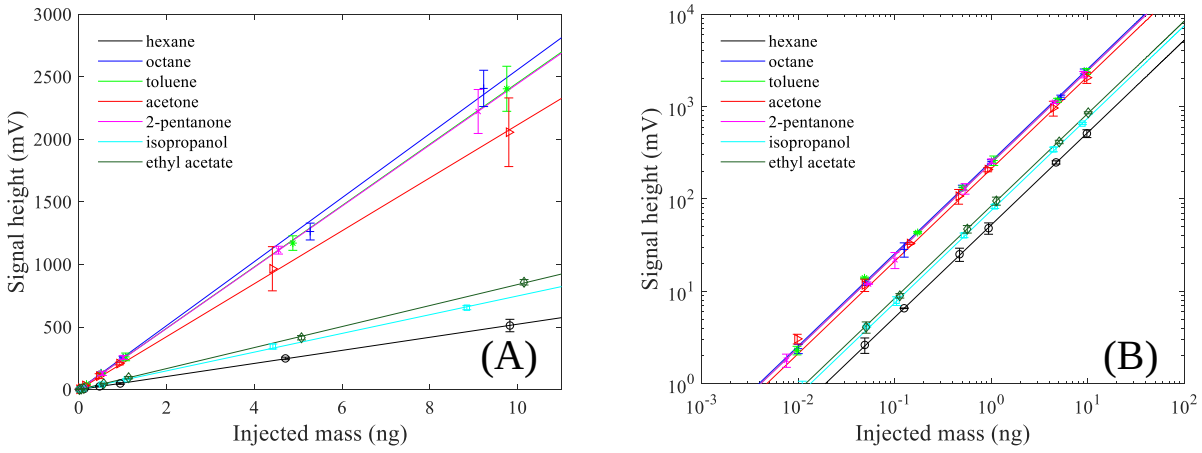

Figure 3.13. µPID linearity on seven compounds with injection masses ranging from ~10 pg to ~10 ng. (A) Signal heights vs. injected masses plotted in linear-linear scale. (B) Signal heights vs. injected masses plotted in log-log scale. Error bars are obtained from 3 measurements. The R^2 values for the seven linear fits are 0.9999, 0.9981, 0.9998, 0.9996, 1.0000, 0.9994, and 0.9997 from hexane to ethyl acetate, respectively.

Compound	Sensitivity (Vs/pg)	Normalized sensitivity (Vs/mol)
Hexane	0.24	2.07×10^{13}
Octane	1.56	1.78×10^{14}
Toluene	1.43	1.32×10^{14}
Acetone	1.08	6.27×10^{13}
2-pentanone	1.93	1.66×10^{14}
Isopropanol	0.36	2.16×10^{13}
Ethyl acetate	0.44	3.88×10^{13}

Table 3.6. Sensitivity and normalized sensitivity to molecular weight for various compounds. The slopes of compounds with similar ionization potentials (*e.g.*, octane, toluene, 2-pentanone and hexane, isopropanol, ethyl acetate) are close to one another.

The system was also analyzed over 200 hours of µPID operation in which the plasma was active in order to assess degradation due to plasma etching of the krypton lamp as well as photon bombardment of the microfluidic chip. The system detection limit on heptane showed no significant differences over these 200 hours of µPID operation, ranging from only 0.168 pg to 0.181 pg. This further demonstrates the µGC-PID system's overall stability and capability to run without maintenance or calibration.

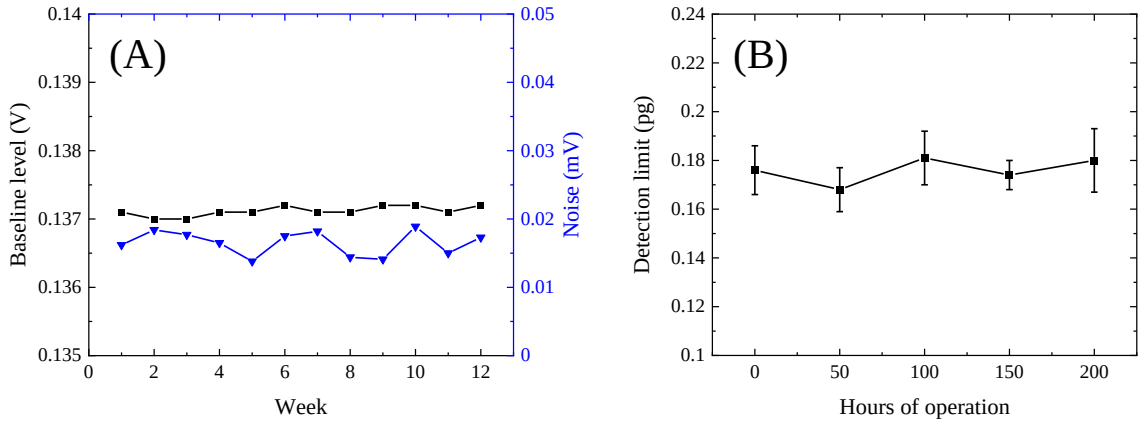

Figure 3.14. System repeatability. (A) The baseline and noise levels were examined over a 12 week period with low variation over the entire period. Each data point is an average of ten 3s time samples. (B) µPID detection limit on heptane over 200 hours of operation. No significant

differences in detection limit were observed. Data points were calculated from 3 repeated injections. Error bars represent one standard deviation.

3.3.4d GC standard chromatograms

The µGC-PID capability for GC separation was examined by analysis of three different standard samples, as shown in **Figure 3.15**. Three different samples of alkanes, aromatics, and ketones and acetates were performed at low sample concentrations of around ~3 ng/L (low ppb-level concentrations) and sampled using an in-house developed stainless steel preconcentrator. These low concentrations are similar to required levels for trace vapor analysis, such as for indoor air screening. The temperature ramping was controlled by pulse width modulation of the integrated heater, with approximate temperatures given in blue. The carrier gas flow rate was set to 2.1 mL/min. The sampling rate was set to 20 mL/min and the sampling time was 10 min, allowing for clear signals as shown in **Figure 3.15**. Considering the sampling volume of 200 mL, concentration of 3 ng/L, and the signal to noise ratios observed in **Figure 3.15**, the µGC-PID detection limit can reach as low as 0.14 ppt (by volume) on o-xylene, or below ~1 ppt for aromatic compounds, ketones and acetates, and alkanes larger than hexane (**Table 3.7**). This single digit to sub-ppt detection limit (in only 200 mL sample volume) is a significant improvement over previous sub-ppb detection limit systems[26,52-54] and is mainly facilitated by the high sensitivity of the µPID.

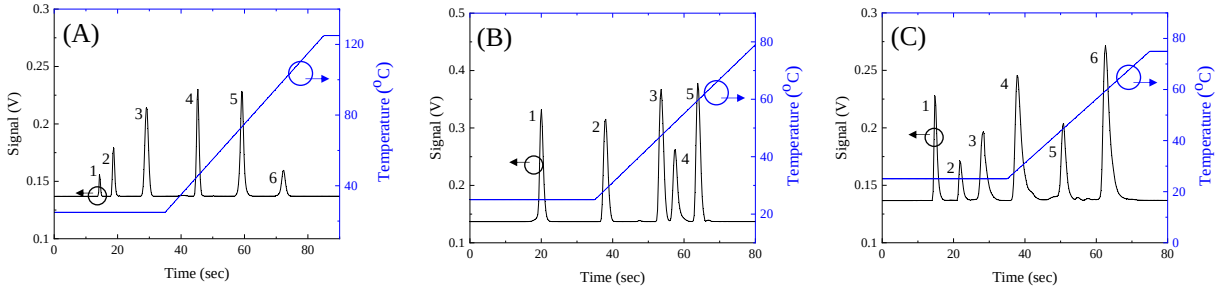

Figure 3.15. Chromatograms of various sample mixtures (each compound ~3 ng/L) with approximate temperature profiles. The flow rate was 2.1 mL/min. The sampling rate was ~20 mL/min and the sampling time was 10 min. (A) Alkanes. 1. Hexane; 2. Heptane; 3. Octane; 4. Nonane; 5. Decane; 6. Undecane. (B) Aromatics. 1. Benzene; 2. Toluene; 3. Ethylbenzene; 4.

Chlorobenzene; 5. o-Xylene. (C) Ketones and acetates. 1. Acetone; 2. Ethyl acetate; 3. Methyl isobutyl ketone; 4. Butyl acetate; 5. 2-hexanone; 6. 2-heptanone.

An additional separation of EPA 502/524.4 VOC mix was performed in **Figure 3.16**. The mixture was diluted to approximately ~10 ng/L, sampled at 20 mL/min for 10 min, and injected into the system. For this chromatogram, the flow rate was reduced to 1.2 mL/min, but the temperature ramping was increased to allow for complete separation within only 2 min. **Figure 3.16** demonstrates the μGC-PID system's applicability to environmental analysis, especially trace vapor analysis, due to the PID's high sensitivity. For alternative or more exotic separations such as polar or chiral compounds, other columns such as high polarity columns or ionic liquid-based[55] columns can be used to replace the OV-1 column used in this system.

Compound	Signal to noise ratio (SNR)	Detection limit (pptv)
Hexane	385	2.21
Heptane	864	0.85
Octane	1582	0.41
Nonane	1916	0.30
Decane	1883	0.27
Undecane	467	1.00
Benzene	4012	0.23
Toluene	3679	0.22
Ethylbenzene	4741	0.15
Chlorobenzene	2588	0.25
o-xylene	4961	0.14
Acetone	1874	0.67
Ethyl acetate	698	1.19
Methyl isobutyl ketone	1206	0.61
Butyl acetate	2165	0.29
2-hexanone	1346	0.54
2-heptanone	2761	0.23

Table 3.7. Signal to noise ratios (taken at 3σ) and detection limits in parts-per-trillion by volume (pptv) of all compounds separated in **Figure 3.15**. The lowest detection limit observed was 0.14 ppt for o-xylene.

3.3.4e Practical chromatograms

In order to assess the μGC-PID system's capability for *in situ* analysis, practical chromatograms were obtained on breath and car exhaust. For these chromatograms, the 5 m OV-1 μcolumn used in the prior sections was replaced with a 10 m OV-1 μcolumn of the same stationary phase thickness. **Figure 3.17** shows a chromatogram of human breath sampled from a Tedlar bag at a rate of 20 mL/min for 1 min. The flow rate was set to 2.1 mL/min. C_6 to C_{11} alkane marker retention times are also labeled on the chromatogram for reference. The chromatogram presented in **Figure 3.17** matches closely with previously reported breath chromatograms[56], demonstrating the capability for rapid separation and detection of a complex practical sample with minimal sampling time.

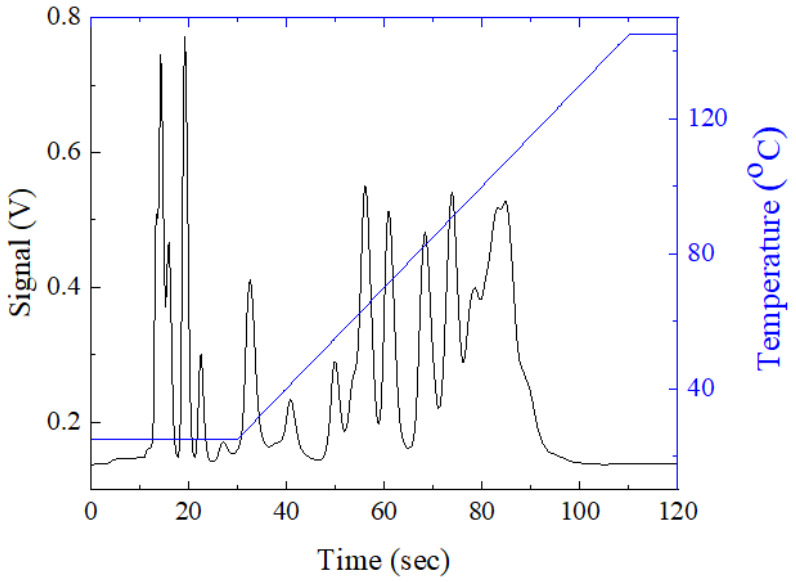

Figure 3.16. Separation of EPA 502/524 VOC mix (each component ~10 ng/L). The flow rate was 1.2 mL/min. The sampling rate was ~20 mL/min and the sampling time was 10 min. The entire separation time was less than 2 min.

An additional separation of car exhaust was performed by sampling pure car exhaust from a Hyundai Accent 2019 at a rate of 20 mL/min for 1 min. The carrier gas flow rate was again set to 2.1 mL/min, resulting in the chromatogram shown in **Figure 3.18**. Benzene, toluene, ethylbenzene, and xylene (BTEX) marker retention times are labeled on the chromatogram for reference. The peak height in **Figure 3.18** tends to increase near the BTEX markers, which are

commonly and expectedly found in most car exhaust. This suggests that this μGC-PID system could be used for toxic vapor analysis in areas with large quantities of motor vehicle emissions, such as near highways or in large cities. Overall, these chromatograms demonstrate the capability of this system for practical analysis of vapor samples outside of the lab.

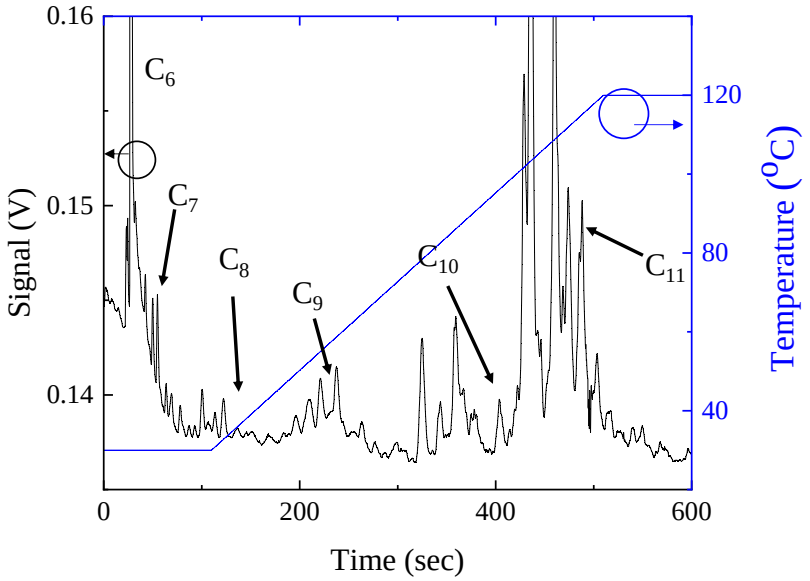

Figure 3.17. Separation of human breath. The flow rate was 2.1 mL/min. The sampling rate was ~20 mL/min and the sampling time was 1 min. Retention times of C_6-C_{11} alkane markers are provided for reference.

3.3.5 μGC-PID summary

The development of a highly sensitive μPID with sub-pg detection limit and large dynamic range for a wide range of VOCs has been detailed herein, demonstrating comparable or better detection limit compared to benchtop FID. This device was used to construct a complete automated μGC-PID system (including miniaturized preconcentrator and microfabricated column along with μPID) capable of detecting sub-ppt concentrations of VOCs in a 200 mL sample volume. Furthermore, standard GC chromatograms were analyzed along with practical complex separations of breath and car exhaust, demonstrating the capability of this μGC-PID system to enable rapid *in situ* trace VOC analysis.

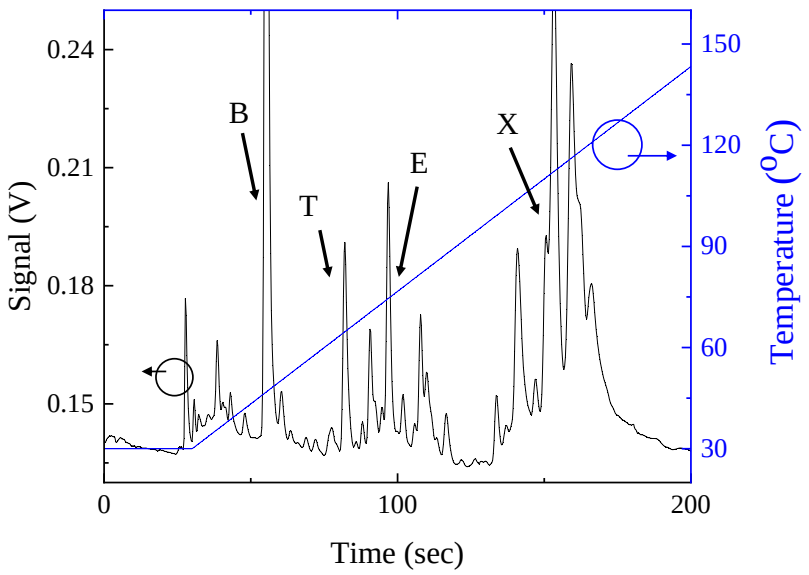

Figure 3.18. Separation of car exhaust. The flow rate was 2.1 mL/min. The sampling rate was ~20 mL/min and the sampling time was 1 min. Retention times of aromatic markers are provided for reference. B: benzene; T: toluene; E: ethylbenzene; X: xylene.

3.4 Conclusion

This chapter has summarized the development of μPIDs for higher sensitivity and broader scale volatile gas analysis. The assembly of low cost in-house developed circuits allow for reduction of the system size and operating voltage, improving the overall portability and sensitivity of various μPID systems. The development of a μHDPID demonstrated universal detection of virtually all VOCs of interest, including light hydrocarbons and even permanent gases, with low detection limits ranging less than 10 pg or 20 pg for high ionization energy gases. This allows for portable detection of compounds with high ionization potentials for applications such as light hydrocarbon analysis for the petroleum industry, formaldehyde detection, or permanent gas sensing. The additional demonstration of a high sensitivity μGC-PID system shows applicability to trace vapor detection, with sub-pg (and sub-ppt) level detection along with separation of complex standard samples and practical *in situ* chemical samples. These developments improve the overall sensing capabilities of portable GC systems, which also complements the wider range of compound separation demonstrated in the prior microcolumn chapter.

Additional future work is mainly directed toward further lowering μPID detection limits in order to improve the sensitivity, to sub-pg levels in the case of the μHDPID and even to tens of fg for regular μPID devices. This may involve further circuit optimization, especially use of fixed circuit components (*e.g.*, fixed resistors instead of trimmers), better electrode contacts with the readout silicon electrodes, and use of highly doped silicon. This would allow for development of ultra-sensitive μGC-PIDs, possibly with detection limits rivaling that of benchtop mass spectrometry equipped with electron multiplier tubes.

3.5 Experimental materials

Benchmark materials: analytical standard grade pentane, hexane, heptane, octane, nonane, decane, undecane, benzene, toluene, ethylbenzene, o-xylene, chlorobenzene, ethyl acetate, butyl acetate, methyl isobutyl ketone, 2-pentanone, 2-hexanone, 2-heptanone, dichloromethane, chloroform, carbon tetrachloride, acetone, tetrahydrofuran, pyridine, isopropanol, methanol, formic acid, formaldehyde, acetaldehyde, 2-butanol, isopropanol, hexamethyldisilazane, and EPA 502/524.4 VOC mix (Sigma Aldrich; St. Louis, MO). Oxygen, argon, carbon dioxide, methane, ethane, hydrogen, and nitrogen (Gasco; Oldsmar, FL). Argon (Cryogenic Gases; Ann Arbor, MI).

Hysol® 1C™ Epoxy (Ellsworth Adhesive; Germantown, WI). Deactivated fused silica tubing (P/N 10010), RTX-5 column (P/N 10208, cut to 5 m in length), Rt-Q-BOND column (P/N 19765, cut to 3 m in length) all with 250 μm inner diameter (Restek; Bellefonte, PA). ShinCarbon ST micropacked column (P/N 19808) (Restek). N-type silicon wafers (P/N 1095, 100 mm diameter, 500 μm thickness) and Borofloat 33 glass (P/N 517) (University Wafer; South Boston, MA). Carbopack B (P/N 20273) and X (P/N 10437-U), and glass wool (P/N 20411) (Sigma Aldrich). Norland optical adhesive 61 (P/N 6101) (Norland; Cranbury, NJ). 21.5 gauge stainless steel tubing (P/N 8988K54) (McMaster-Carr; Aurora, OH). 32 gauge nickel chromium wire (P/N 32BNC) (Consolidated; Franklin Park, IL). All materials were used as purchased without further purification or modification. Ultra-high purity 5.0 grade helium (P/N UN1046) was used as the auxiliary gas for the μHDPID (PurityPlus; Indianapolis, IN). 99.5% purity helium (P/N 49615He) (Leland Gas Technologies; South Plainfield, NJ).

3.6 References

(1) Grate, J. W. Acoustic wave microsensor arrays for vapor sensing. *Chem Rev* **2000**, *100*, 2627-2648.

(2) Kauffman, D. R.; Star, A. Carbon nanotube gas and vapor sensors. *Angew Chem Int Ed Engl* **2008**, *47*, 6550-6570.

(3) Albert, K. J.; Lewis, N. S.; Schauer, C. L.; Sotzing, G. A.; Stitzel, S. E.; Vaid, T. P.; Walt, D. R. Cross-reactive chemical sensor arrays. *Chem Rev* **2000**, *100*, 2595-2626.

(4) Szulczyński, B.; Gębicki, J. Currently Commercially Available Chemical Sensors Employed for Detection of Volatile Organic Compounds in Outdoor and Indoor Air. *Environments* **2017**, *4*, 21.

(5) Mirzaei, A.; Leonardi, S. G.; Neri, G. Detection of hazardous volatile organic compounds (VOCs) by metal oxide nanostructures-based gas sensors: A review. *Ceram Int* **2016**, *42*, 15119-15141.

(6) Cho, B.; Lee, K.; Jo, E.; Kim, J. Detection of Mixed BTEX With Suppressed Reaction Specificity Using Tin Oxide Nanoparticles Functionalized by Multi-Metalloporphyrins. *IEEE Sens J* **2019**, *19*, 11791-11796.

(7) Singh, E.; Meyyappan, M.; Nalwa, H. S. Flexible Graphene-Based Wearable Gas and Chemical Sensors. *ACS Appl Mater Interfaces* **2017**, *9*, 34544-34586.

(8) Wales, D. J.; Grand, J.; Ting, V. P.; Burke, R. D.; Edler, K. J.; Bowen, C. R.; Mintova, S.; Burrows, A. D. Gas sensing using porous materials for automotive applications. *Chem Soc Rev* **2015**, *44*, 4290-4321.

(9) Bai, H.; Shi, G. Q. Gas sensors based on conducting polymers. *Sensors* **2007**, *7*, 267-307.

(10) Sun, Y. F.; Liu, S. B.; Meng, F. L.; Liu, J. Y.; Jin, Z.; Kong, L. T.; Liu, J. H. Metal oxide nanostructures and their gas sensing properties: a review. *Sensors (Basel)* **2012**, *12*, 2610-2631.

(11) Zhou, X.; Lee, S.; Xu, Z.; Yoon, J. Recent Progress on the Development of Chemosensors for Gases. *Chem Rev* **2015**, *115*, 7944-8000.

(12) Mirzaei, A.; Kim, J.-H.; Kim, H. W.; Kim, S. S. Resistive-based gas sensors for detection of benzene, toluene and xylene (BTX) gases: a review. *Journal of Materials Chemistry C* **2018**, *6*, 4342-4370.

(13) Spinelle, L.; Gerboles, M.; Kok, G.; Persijn, S.; Sauerwald, T. Review of Portable and Low-Cost Sensors for the Ambient Air Monitoring of Benzene and Other Volatile Organic Compounds. *Sensors (Basel)* **2017**, *17*.

(14) Carapezza, E. M.; Patel, S. V.; Hobson, S. T.; Cemalovic, S.; Mlsna, T. E. Chemicapacitive microsensors for detection of explosives and TICs. **2005**, *5986*, 59860M.

(15) Qin, Y.; Gianchandani, Y. B. A fully electronic microfabricated gas chromatograph with complementary capacitive detectors for indoor pollutants. *Microsyst Nanoeng* **2016**, *2*, 15049.

(16) Freedman, A. N. The photoionization detector: Theory, performance and application as a low-level monitor of oil vapour. *J Chromatogr A* **1980**, *190*, 263-273.

(17) Driscoll, J. N.; Duffy, M. Photoionization detector: A versatile tool for environmental analysis. *Chromatography* **1987**, *2*, 21-27.

(18) Verner, P. Photoionization detection and its application in gas chromatography. *J Chromatogr A* **1984**, *300*, 249-264.

(19) Narayanan, S.; Rice, G.; Agah, M. A micro-discharge photoionization detector for micro-gas chromatography. *Microchimica Acta* **2013**, *181*, 493-499.

(20) Coelho Rezende, G.; Le Calvé, S.; Brandner, J. J.; Newport, D. Micro photoionization detectors. *Sensors Actuators B: Chem* **2019**, *287*, 86-94.

(21) Zhu, H.; Nidetz, R.; Zhou, M.; Lee, J.; Buggaveeti, S.; Kurabayashi, K.; Fan, X. Flow-through microfluidic photoionization detectors for rapid and highly sensitive vapor detection. *Lab Chip* **2015**, *15*, 3021-3029.

(22) Soo, J. C.; Lee, E. G.; LeBouf, R. F.; Kashon, M. L.; Chisholm, W.; Harper, M. Evaluation of a portable gas chromatograph with photoionization detector under variations of VOC concentration, temperature, and relative humidity. *J Occup Environ Hyg* **2018**, *15*, 351-360.

(23) Price, J. G. W.; Fenimore, D. C.; Simmonds, P. G.; Zlatkis, A. Design and operation of a photoionization detector for gas chromatography. *AnaCh* **2002**, *40*, 541-547.

(24) Zhang, W.-q.; Li, H.; Zhang, Y.-j.; Bi, F.; Meng, L.-s.; Zhang, X.-m.; Mao, J.-y.; Cheng, N.-l.; Fang, B.; Yang, Y.; Chen, C.; Guo, K.-x.; Zhan, G.-e.; Sha, J.; Wang, X.-z. Fast Determination of Monocyclic Aromatic Hydrocarbons in Ambient Air Using a Portable Gas Chromatography–Photoionization Detector. *Chromatographia* **2017**, *80*, 1233-1247.

(25) Lee, J.; Zhou, M.; Zhu, H.; Nidetz, R.; Kurabayashi, K.; Fan, X. In situ calibration of micro-photoionization detectors in a multi-dimensional micro-gas chromatography system. *Analyst* **2016**, *141*, 4100-4107.

(26) You, D. W.; Seon, Y. S.; Jang, Y.; Bang, J.; Oh, J. S.; Jung, K. W. A portable gas chromatograph for real-time monitoring of aromatic volatile organic compounds in air samples. *J Chromatogr A* **2020**, *1625*, 461267.

(27) Mendonca, S.; Wentworth, W.; Chen, E. C. M.; Stearns, S. D. Relative responses of various classes of compounds using a pulsed discharge helium photoionization detector - Experimental determination and theoretical calculations. *J Chromatogr A* **1996**, *749*, 131-148.

(28) Wentworth, W. E.; Cai, H. M.; Stearns, S. Pulsed Discharge Helium Ionization Detector Universal Detector for Inorganic and Organic-Compounds at the Low Picogram Level. *J Chromatogr A* **1994**, *688*, 135-152.

(29) Freeman, R. R.; Wentworth, W. E. Helium Photoionization Detector Utilizing a Microwave Discharge Source. *AnaCh* **1971**, *43*, 1987-+.

(30) Jin, Q. H.; Yang, W. J.; Yu, A. M.; Tian, X. D.; Wang, F. D. Helium direct current discharge ionization detector for gas chromatography. *J Chromatogr A* **1997**, *761*, 169-179.

(31) Winniford, B. L.; Sun, K.; Griffith, J. F.; Luong, J. C. Universal and discriminative detection using a miniaturized pulsed discharge detector in comprehensive two-dimensional GC. *J Sep Sci* **2006**, *29*, 2664-2670.

(32) Jalbert, J.; Gilbert, R.; Tetreault, P. Simultaneous determination of dissolved gases and moisture in mineral insulating oils by static headspace gas chromatography with helium photoionization pulsed discharge detection. *Anal Chem* **2001**, *73*, 3382-3391.

(33) Cai, H.; Stearns, S. D. Pulsed discharge helium ionization detector with multiple combined bias/collecting electrodes for gas chromatography. *J Chromatogr A* **2013**, *1284*, 163-173.

(34) Mowry, C. D.; Pimentel, A. S.; Sparks, E. S.; Moorman, M. W.; Achyuthan, K. E.; Manginell, R. P. Pulsed Discharge Helium Ionization Detector for Highly Sensitive Aquametry. *Anal Sci* **2016**, *32*, 177-182.

(35) Golubovskii, Y. B.; Maiorov, V. A.; Behnke, J.; Behnke, J. F. Modelling of the homogeneous barrier discharge in helium at atmospheric pressure. *J Phys D Appl Phys* **2003**, *36*, 39-49.

(36) Zhu, H.; Zhou, M.; Lee, J.; Nidetz, R.; Kurabayashi, K.; Fan, X. Low-Power Miniaturized Helium Dielectric Barrier Discharge Photoionization Detectors for Highly Sensitive Vapor Detection. *Anal Chem* **2016**, *88*, 8780-8786.

(37) Poole, C. F. Ionization-based detectors for gas chromatography. *J Chromatogr A* **2015**, *1421*, 137-153.

(38) Akbar, M.; Shakeel, H.; Agah, M. GC-on-chip: integrated column and photoionization detector. *Lab Chip* **2015**, *15*, 1748-1758.

(39) Dojahn, J. G.; Wentworth, W. E.; Deming, S. N.; Stearns, S. D. Determination of percent composition of a mixture analyzed by gas chromatography. Comparison of a helium pulsed-discharge photoionization detector with a flame ionization detector. *J Chromatogr A* **2001**, *917*, 187-204.

(40) Narayanan, S.; Rice, G.; Agah, M. Characterization of a micro-helium discharge detector for gas chromatography. *Sensors Actuators B: Chem* **2015**, *206*, 190-197.

(41) Fu, Y. M.; Chu, S. C.; Lu, C. J. Characteristic responses of an atmospheric pressure DC micro-plasma detector for gas chromatography to organic functional groups. *Microchem J* **2008**, *89*, 7-12.

(42) Andrade, F. J.; Shelley, J. T.; Wetzel, W. C.; Webb, M. R.; Gamez, G.; Ray, S. J.; Hieftje, G. M. Atmospheric pressure chemical ionization source. 1. Ionization of compounds in the gas phase. *Anal Chem* **2008**, *80*, 2646-2653.

(43) Lasa, J.; Mochalski, P.; Lokas, E.; Kedzior, L. Application of a pulse-discharge helium detector to the determination of neon in air and water. *J Chromatogr A* **2002**, *968*, 263-267.

(44) Gremaud, G.; Wentworth, W. E.; Zlatkis, A.; Swatloski, R.; Chen, E. C. M.; Stearns, S. D. Windowless pulsed-discharge photoionization detector - Application to qualitative analysis of volatile organic compounds. *J Chromatogr A* **1996**, *724*, 235-250.

(45) Meyer, C.; Muller, S.; Gurevich, E. L.; Franzke, J. Dielectric barrier discharges in analytical chemistry. *Analyst* **2011**, *136*, 2427-2440.

(46) Han, B.; Jiang, X.; Hou, X.; Zheng, C. Dielectric barrier discharge carbon atomic emission spectrometer: universal GC detector for volatile carbon-containing compounds. *Anal Chem* **2014**, *86*, 936-942.

(47) Jafari, M. T. Low-temperature plasma ionization ion mobility spectrometry. *Anal Chem* **2011**, *83*, 797-803.

(48) Bogaerts, A.; Neyts, E.; Gijbels, R.; van der Mullen, J. Gas discharge plasmas and their applications. *Spectrochim Acta Part B At Spectrosc* **2002**, *57*, 609-658.

(49) Gras, R.; Luong, J.; Monagle, M.; Winniford, B. Gas chromatographic applications with the dielectric barrier discharge detector. *J Chromatogr Sci* **2006**, *44*, 101-107.

(50) Shinada, K.; Horiike, S.; Uchiyama, S.; Takechi, R.; Nishimoto, T. Development of New Ionization Detector for Gas Chromatography by Applying Dielectric Barrier Discharge. *Shimadzu Review* **2012**.

(51) Forsyth, D. S. Pulsed discharge detector: theory and applications. *J Chromatogr A* **2004**, *1050*, 63-68.

(52) Lara-Lbeas, I.; Rodriguez-Cuevas, A.; Andrikopoulou, C.; Person, V.; Baldas, L.; Colin, S.; Le Calve, S. Sub-ppb Level Detection of BTEX Gaseous Mixtures with a Compact Prototype GC Equipped with a Preconcentration Unit. *Micromachines (Basel)* **2019**, *10*, 187-199.

(53) Zhou, Q.; Zhang, S.; Zhang, X.; Ma, X.; Zhou, W. Development of a Novel Micro Photoionization Detector for Rapid Volatile Organic Compounds Measurement. *Appl Bionics Biomech* **2018**, *2018*, 5651315.

(54) Pang, X.; Nan, H.; Zhong, J.; Ye, D.; Shaw, M. D.; Lewis, A. C. Low-cost photoionization sensors as detectors in GCxGC systems designed for ambient VOC measurements. *Sci Total Environ* **2019**, *664*, 771-779.

(55) Li, M. W.; Huang, X.; Zhu, H.; Kurabayashi, K.; Fan, X. Microfabricated ionic liquid column for separations in dry air. *J Chromatogr A* **2020**, *1620*, 461002.

(56) Zhou, M.; Sharma, R.; Zhu, H.; Li, Z.; Li, J.; Wang, S.; Bisco, E.; Massey, J.; Pennington, A.; Sjoding, M.; Dickson, R. P.; Park, P.; Hyzy, R.; Napolitano, L.; Gillies, C. E.; Ward, K. R.; Fan, X. Rapid breath analysis for acute respiratory distress syndrome diagnostics using a portable two-dimensional gas chromatography device. *Anal Bioanal Chem* **2019**, *411*, 6435-6447.

Chapter 4 Portable µGC Systems

4.1 Introduction

4.1.1 Background

With tremendous advances having been made on miniaturized gas chromatography (GC) components, especially columns and detectors, assembly into small scale systems with unique analytical capabilities and high performance has become the next important step in the development of micro gas chromatography (µGC) technology. Portable µGC systems have already demonstrated some success for on-site analysis[1-18], which enables chemical analysis in field applications, such as for volatile organic compounds (VOCs). Devices of only several liters in volume and weighing only several kg have been reported, with pg (sub ppb)-level detection limits as well as the capability for simultaneous separation of tens of compounds at once using both one dimensional and multidimensional µGC[1-18]. Several applications, including breath analysis[18], plant VOC analysis[16], and general environmental monitoring[1,19,20] have been explored, demonstrating the promise for rapid *in situ* VOC studies.

Despite the numerous advances made on µGC systems, further development is needed for the practical use of this technology. Devices of the current size and weight can be considered semi-portable, capable of being carried to different stations and quickly set up for use. However, most current µGC devices are not at the level of handheld vapor sensors, which are battery powered and can quickly perform analysis within a couple minutes while mobile. Additionally, due to limitations in current microcolumn and detector technology, most portable GC devices are limited to more rudimentary analysis due to using standard PDMS and 5% phenyl columns and 10.6 eV photoionization detectors (PIDs). Diverse applications especially requiring analysis of lighter compounds such as permanent gases are not suited for µGC analysis, due to the incapability for separation and detection. Furthermore, while preliminary results for *in situ* analysis have been provided, overall µGC robustness has not been well tested outside of

laboratory settings. Further experiments are needed to transition μGC technology from the proof of concept stage to widely useable devices.

This chapter discusses the development complete μGC systems using some of the components developed in the previous chapters. A preliminary system for hydrogen and methane detection is presented herein, using the μHDPID developed in Chapter 3 for the permanent gas detection. An additional ultra-compact μGC is demonstrated using the miniaturized ionic liquid column developed in Chapter 2 for separation. These systems aim to demonstrate how μGC can be further miniaturized and be applied to additional compounds beyond the typical alkane or BTEX markers used for environmental analysis. Together, these show how the range of applications for future μGC devices can be broadened, enabling their use for general purpose chemical analysis.

4.1.2 μGC system considerations and auxiliary components

Besides the core three μGC components (preconcentrator/sampling loop, column, detector), miniaturized auxiliary components are required for the assembly of small scale systems. Microfluidic tubing is necessary for interconnections between components. While inert polymer-based tubes can be used (*e.g.,* polytetrafluoroethylene or polyether ether ketone), any tubing used in the μGC flow path should ideally be of non-retaining materials, either passivated metal or fused silica (*e.g.,* guard column). Miniaturized pumps are required for sampling and require low voltage supplies, typically either 12 or 24 V, although lower voltages should be used for systems that use only a few batteries. Pumps that can be operated with voltages as low as 1.5 V are available, but this can result in low sampling rates for preconcentrators with higher resistances, diminishing overall system sensitivity. Similar, if pumps are used for carrier gas flows, sufficient voltages and flow rates are required for proper operation. Finally, miniaturized valves are required for controlling flow paths. Because most miniature valves are made using polytetrafluoroethylene or ethylene tetrafluoroethylene, samples passing through valve control paths may be retained within and contaminate the system. Ideally, μGC systems should be designed in a way that removes valves from the flow path.

Compared to a benchtop system, the proximity of the μGC components can present some difficulties for miniaturization. As discussed in Chapter 3, the proximity of the μPID to other electronics and to the ambient can result in electronic noise, increasing the system detection

limit. Proper shielding of the μPID is required to remove the noise for improved sensitivity. Additionally, the close proximity of the preconcentrator and column to other components can result in thermal crosstalk, which can be especially detrimental to integrated systems (either on the same chip or with components otherwise mechanically linked). Thermal insultation between components becomes important in these cases to prevent undesired component heating. If a pump is used for the carrier gas, mechanical vibrations may cause similar issues and also requires mechanical padding to prevent excess noise during analysis.

4.2 Portable hydrogen and methane breath analysis

4.2.1 Background

Breath analysis by micro gas chromatography (μGC) has previously shown promising results as a diagnostic aid using breath samples[18,21,22]. In particular, data analysis on μGC breath chromatograms has demonstrated the capability for robust detection of acute respiratory distress syndrome (ARDS), with an accuracy of up to 87.1%[18]. However, previous systems were limited by the usage of regular 10.6 eV photoionization detectors (PIDs), which cannot sense light high ionization potential compounds. This can be problematic for the analysis of particular compounds of interest for breath, especially hydrogen and methane[23-26].

Measurement of hydrogen in breath is often used to diagnose several conditions that cause gastrointestinal symptoms. Large amounts of hydrogen may be produced where there is a problem with the digestion or absorption of food in the small intestine that allows more unabsorbed food to reach the colon or when the colon bacteria move back into the small intestine. Some of the hydrogen produced by the bacteria, whether in the small intestine or the colon, is absorbed into the blood flowing through the wall of the small intestine and colon. The hydrogen-containing blood travels to the lungs where the hydrogen is released and exhaled in the breath where it can be measured[23-26]. The same is true for methane, which like hydrogen, is another byproduct of saccharide fermentation of gut bacteria in humans. The usefulness of analysis of these compounds has led to the development of several systems, which are summarized in **Table 4.1**. While some of these systems provide high performance detection of hydrogen and methane (<1 ppmv), most of these systems are benchtop equipment, especially relying on GC-MS methods, and the smallest system being 18 L in size. Truly portable systems

for hydrogen and methane detection would be desirable to allow for *in situ* monitoring of human gastrointestinal conditions using these known volatile gases of interest.

Hydrogen–methane breath testing results influenced by oral hygiene[24]	Testing of the commercialized Model SC from Quintron Instruments, Milwaukee, WI, USA. The accuracy of the detector was ± 3 ppm with detection limits in the range of 10 ppm. Oral hygiene was shown to interfere with testing results.
A simple and rapid GC/MS method for the simultaneous determination of gaseous metabolites[26]	A benchtop GC-MS QP2010 system using a CP-PoraPLOT Q-HT column. H_2, N_2, O_2, CH_4, CO_2, and N_2O were analyzed with sensitivities sufficient metabolic monitoring.
Simultaneous detection of hydrogen and methane in breath for the diagnosis of small intestinal bacterial overgrowth by fast gas chromatography[25]	Fast GC with detection ranging from 2–200 ppm, resolution of 1 ppm, and precision <10%. MOS sensors were used, and the entire system size was 18 L.
Evaluation of the pulsed discharge helium ionization detector for the analysis of hydrogen and methane in breath[23]	Pulsed discharge helium ionization detector used for detection with sensitivity over an order of magnitude better than published methods using FID and TCD. Limits of detection were 0.3 ppmv for both hydrogen and methane and the method had a linear dynamic range of three orders of magnitude (0.3–400 ppm, v/v). A molecular sieve 5A PLOT column was used.

Table 4.1. Summary of hydrogen-methane analysis systems with reported performances and instrumentation used.

This section reports preliminary results from a portable system with dimensions 20 cm x 25 cm x 10 cm (5 L) weighing 2.5 kg. In particular, a previously developed microfabricated helium

ionization detector (μHDPID) was used for detection of hydrogen and methane[27], allowing for system size reduction. Preliminary results showed automated portable separation of hydrogen and methane by the μHDPID, with further discussion and assembly of a more advanced system having been designed and planned for construction.

4.2.2 Experimental

4.2.2a Initial system setup

Due to hydrogen and methane being difficult to trap, a sampling loop was used for injection. A 2 m Restek molecular sieve 5A Shincarbon ST column (P/N 19808) was used for separation of permanent gases. The column heater was prepared by wrapping with 32 gauge nickel chromium wire and covering with shrink wrap tubing. The column was baked out at 200 °C for 2 hours at a flow rate of 1 mL/min prior to use. The detector was a μHDPID which was operated using an auxiliary flow rate of 13 mL/min[27]. The system was assembled by forming fluidic connections using universal press-tight connectors and deactivated fused silica capillaries between the components. Unlike a regular preconcentrator, the sampling loop was enclosed on both sides by valves to prevent analytes from preemptively leaking into the system. A system block diagram is provided in **Figure 4.1**. The entire system was contained within a box of 20 cm x 25 cm x 10 cm (5 L) and weighed 2.5 kg. Heating of the column was controlled by the wrapped heater. All heating, pumping, and valve switching was controlled by in-house developed LabVIEW software. The system was capable of operating autonomously without any benchtop equipment. A picture of the system is provided in **Figure 4.2**. 99.5% purity helium was used as the carrier gas at a head pressure of 25 psi, corresponding to 2.1 mL/min.

4.2.2b Two channel system setup

In a practical breath analysis system, any and all compounds in human breath are trapped in the injector and injected into the column. However, since the Shincarbon ST column is only capable of handling light compounds (*i.e.*, molecular weight lower than ethane), injecting all compounds into the column would result in permanent contamination. Thus, a proposed practical system involves a two channel μGC utilizing a standard PDMS column to separate the heavier compounds, while only allowing light compounds into the Shincarbon ST column. The proposed system diagram is provided in **Figure 4.3**.

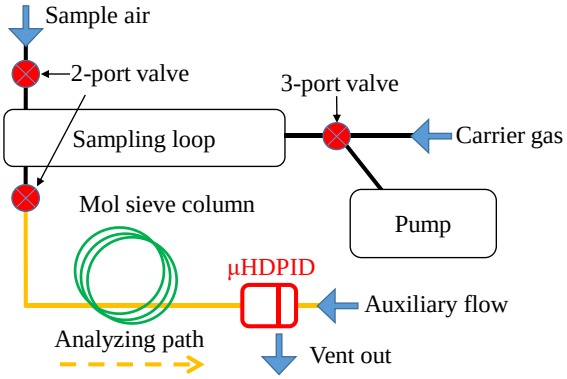

Figure 4.1. Hydrogen methane system fluidic diagram. A picture of the system is provided in **Figure 4.2**.

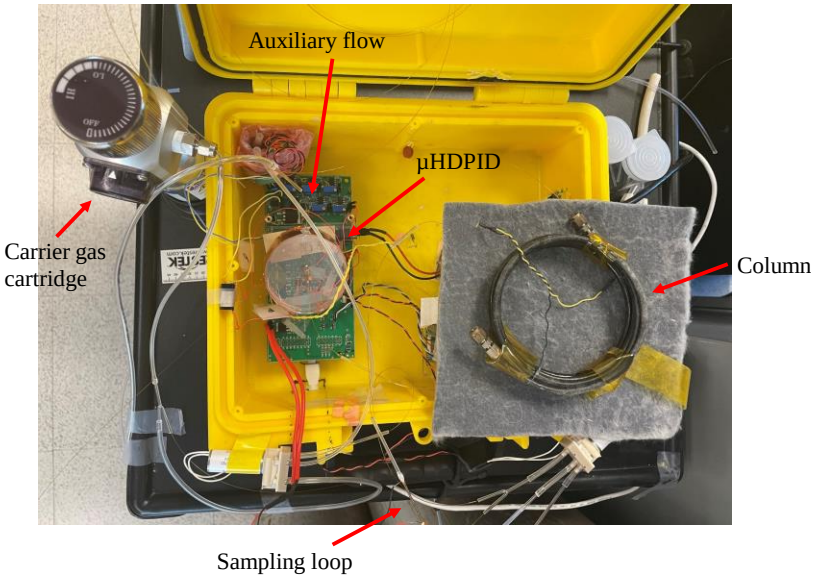

Figure 4.2. Photograph of prototype hydrogen methane analysis system.

While the first channel operates like a regular miniaturized µGC, the sample passed into the second channel requires special treatment. The sample is passed through the pump and critically through a filter packed with sorbents, which absorb all compounds of greater molecular weight than ethane to prevent column contamination. The sample then passes through a 3 port valve and is trapped within a sampling loop just as in the prior section. Simultaneous analysis in both channels is therefore possible, allowing for complete breath analysis including regular mid-range compound separation (*i.e.*, C_6-C_{11}), along with separation of light gases such as the

aforementioned hydrogen and methane. Splitting off the second channel by itself also allows for standalone separation of hydrogen and methane without the regular breath analysis. However, this places additional emphasis on the filter's capability for trapping compounds heavier than ethane.

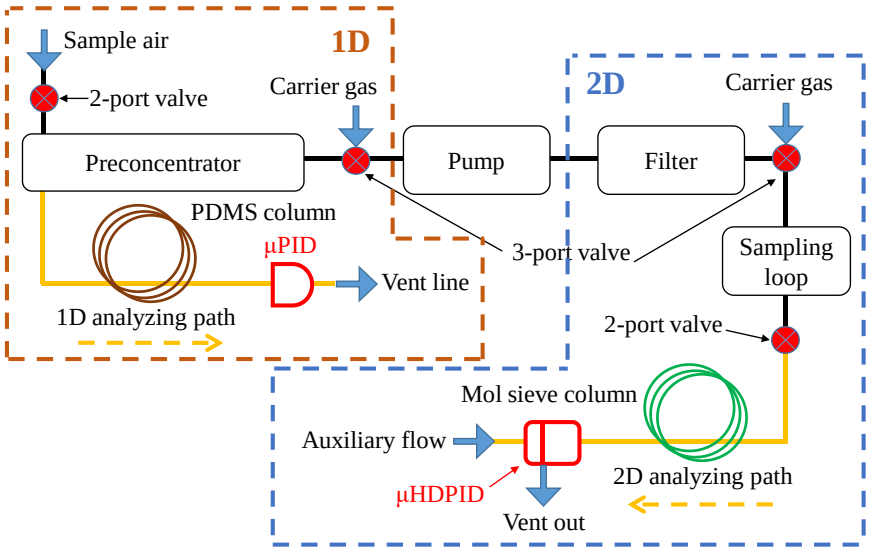

Figure 4.3. Two channel μGC with PDMS and molecular sieve 5A columns.

4.2.3 System characterization

4.2.3a Hydrogen and methane separation on prototype 1D system

The prototype system described in section *4.2.2a Initial system setup* was operated autonomously to separate a standard sample of hydrogen and methane. For this experiment, a sampling loop was made using a guard column of 4 cm in length (250 μm i.d.), corresponding to a volume of 2 μL. Sample chromatograms are provided in **Figure 4.4**. Hydrogen and methane are well separated and match well with the elution temperatures provided by Restek. This further suggests that these compounds are also well separated from CO_2, which is of particular importance when analyzing breath. This also demonstrated that heating of the column was feasible using the wrapped heater without the GC oven, and that the portable μGC was capable of delivering the high head pressure (~25 psi) required to drive the column at 2.1 mL/min.

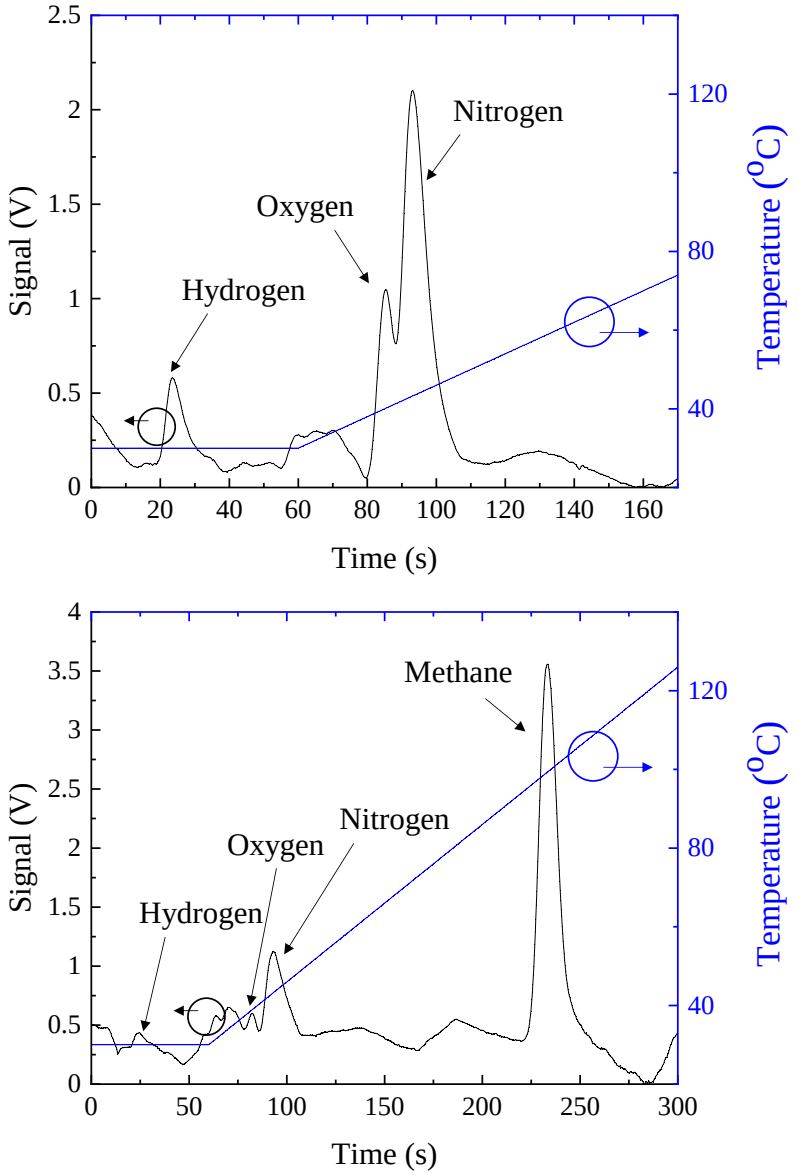

Figure 4.4. Separation of hydrogen and methane with approximate temperature profiles. The flow rate was 2 mL/min at room temperature. A sampling loop of 2 µL in volume was used for injection.

4.2.3b Breath analysis by one channel µGC

The first channel of the setup described in *4.2.2b Two channel system setup* was built using a regular PID and demonstrated for regular breath analysis and a 10 m long DB-1ms column. A sample chromatogram is provided in **Figure 4.5**, along with C_6-C_{11} breath markers, with

temperature ramping again controlled by the wrapped heater and using a flow rate of 1.8 mL/min of helium. The result matches with previously reported breath analysis chromatograms[18]. Hydrogen and methane were also sampled by the first channel of the setup and showed no signal (*i.e.*, flat baseline), demonstrating the necessity of the µHDPID.

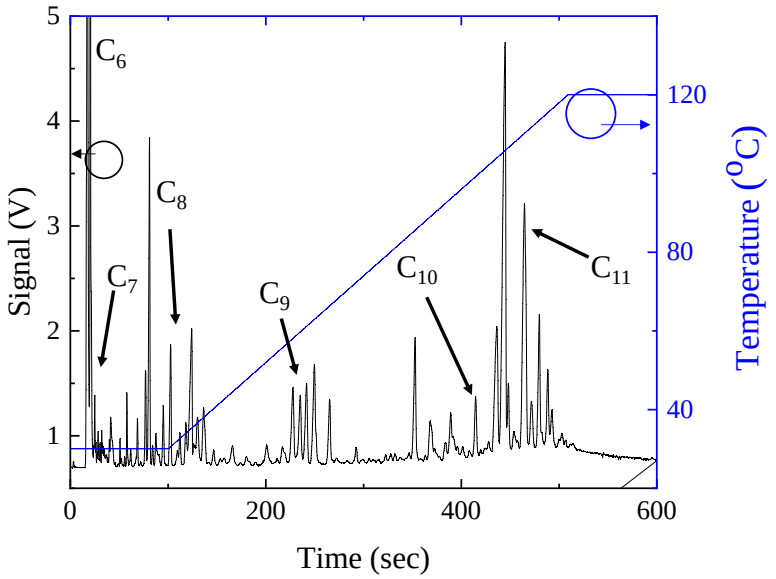

Figure 4.5. Human breath separation using one channel µGC system with DB-1ms column. The flow rate was 2 mL/min at room temperature.

4.2.4 Summary and next steps

Preliminary results from a portable system hydrogen and methane breath analysis system have been reported. Portable analysis using a miniature µHDPID was demonstrated, with automated separation of hydrogen and methane accomplished with a one dimensional system. A separate one dimensional system was also constructed using a 10 m DB-1ms column and demonstrated repeatable separation of human breath. This µGC used a regular PID and showed no response to hydrogen and methane, thus demonstrating the necessity of the µHDPID.

The next steps include assembly of the two separate one channel systems into the two channel hydrogen methane system. Currently, the key component that requires further testing is the filter, which is required to ensure that heavy compounds are not injected into the molecular sieve column. A number of proposed sorbents are already currently undergoing testing, with a critical sorbent being Carboxen 1018, which is capable of trapping alkanes C_2-C_5. Upon

assembly into a complete two channel μGC, standard sample chromatograms demonstrating the efficacy of the filter and hydrogen methane separation in the two channel system will be obtained. Subsequently, testing on human breath samples and examination of typical hydrogen and methane concentrations in said samples can be accomplished. Additional items that require tuning are the μHDPID, which may require better detection performance, along with the sampling loop, whose volume may currently be too low to allow for detection limits in the ~1 ppm range due to the lack of preconcentration. Experimenting with the sampling loop volume is also of interest, although there is a tradeoff between increased sampling loop volume and injection peak width. Further testing after two channel system assembly is needed to optimize the detection limit and separation performance for practical breath analysis. Finally, a coating method can be developed for a molecular sieve 5A microfabricated column, which would allow for a more compact and lower footprint means for separation. This would replace the Shincarbon ST column, enabling the entire system to be miniaturized further.

4.3 Ultra compact portable μGC

4.3.1 Background

Compared to other portable vapor sensors such as electronic noses or standalone optical or ion mobility spectrometers, current μGC devices are somewhat larger and more cumbersome. Despite the great advances made in the development of individual microcomponents (*i.e.* miniature preconcentrators, columns, and detectors), the large number of accessory components and difficulties in overall system miniaturization have prevented the further downscaling of μGC from the few liter scale to hand-held or even smaller devices[2,3,6-8,10,14,17,28-36]. The need for wall power as well as the still comparatively large size of these μGC systems prevents their use for truly mobile applications, such as downstream wastewater analysis, residential VOC monitoring, pipeline leak checking, and in field food and drug testing[1,4,5,14,16,37-51].

Some of the difficulties in system miniaturization were discussed in ***4.1.2 μGC system considerations and auxiliary components***, most of which become more challenging as system size is further reduced. In particular, electronic interference and mechanical vibrations between components is more of a concern for smaller systems, while thermal crosstalk is more severe when components are in closer proximity. On the flip side, shorter interconnections and the same

thermal crosstalk is an advantage for preventing cold spots where heavier chemicals can become trapped, potentially allowing for improved chromatographic performance. Shorter electrical connections can also be an advantage for electronic noise reduction, which improves the overall signal to noise ratio (SNR). Other considerations must be made for devices aimed at hand-held use. For a battery-powered device, the required voltage and peak power draw should be as low as possible to reduce the number of batteries needed. Higher voltages and currents should be avoided whenever possible both to reduce electronic interference as well as allow for safer operation. Likewise, while benchtop and some portable instruments use high column operating temperatures up to or even above 200 °C, hand-held instruments should ideally operate with lower temperatures to prevent the need for extensive thermal insulation to protect the user. The use of pressurized carrier gas cartridges is also difficult for hand-held or wearable devices due to size and weight along with safety design challenges. This necessitates the use of components that can function with dry air as the carrier gas.

This section reports the design and assembly of an ultracompact 1D μGC system. A microfabricated preconcentrator was used for injection, while an ionic liquid microcolumn was used for separation due to its high oxygen resilience, as reported in Chapter 2[52]. A microfluidic photoionization detector (PID) was used for readout. The system is entirely contained within a box of size 17 cm x 9 cm x 7 cm (~1.1 L), with only a laptop for signal viewing. The system is otherwise capable of running autonomously on batteries. The μGC weighs a total of 0.9 kg including batteries and can be operated hand-held. Preliminary data demonstrate characterization on standard lab mixtures, including alkanes and benzene, toluene, ethylbenzene, and o-xylene. Discussion on future testing is also provided.

4.3.2 Experimental

4.3.2a Microfabricated preconcentrator

The preconcentrator was fabricated using a similar process to the microcolumn. The fabrication process is provided in **Figure 4.6**. A 3 μm thick layer of thermal oxide was grown on a double side polished silicon wafer and subsequently patterned using standard lithography processes. The exposed oxide was etched away in buffered hydrofluoric acid. The photoresist then was removed, and the wafer was aligned and patterned again to expose the inlets and outlets. A 120 μm deep trench was created via deep reactive ion etching. The photoresist was

stripped again, and deep reactive ion etching was applied to the entire pattern area. The final sorbent bed depth was 250 µm, and the width and depth of the inlets and outlets were 400 µm. The wafer was subsequently anodically bonded with Borofloat 33 glass at 350 °C under vacuum. The heater was deposited on the back side of the column through physical vapor deposition and patterned by lift-off.

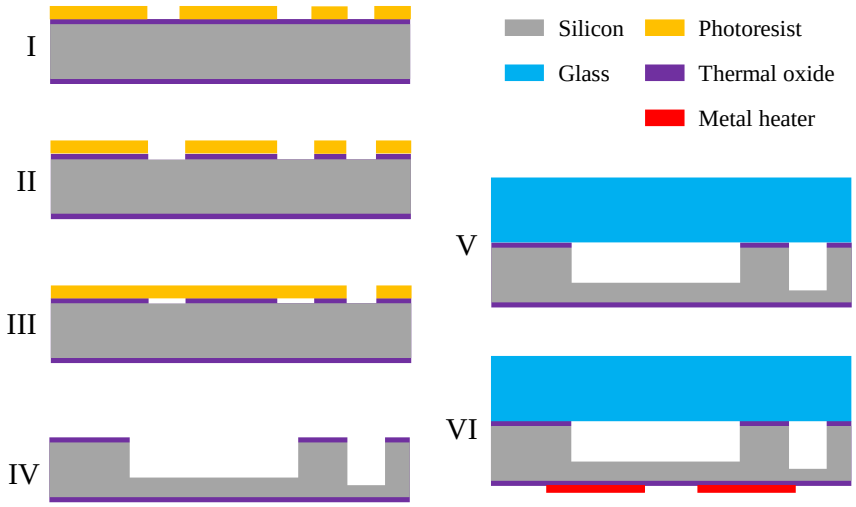

Figure 4.6. Preconcentrator microfabrication process. I. Soft mask of photoresist exposing both column and inlets/outlets. II. Creation of oxide hard mask through DRIE. III. Soft mask exposing only inlets/outlets for DRIE etching to 120 µm. IV. DRIE on the entire pattern area to etch inlets/outlets to 400 µm and sorbent bed to 250 µm. V. Anodic bonding with Pyrex glass to seal the preconcentrator. VI. Metal heater deposition on preconcentrator backside.

After fabrication, the preconcentrator was flushed with acetone and dried with nitrogen. Interconnections were made by the same two-step gluing method developed for microcolumns, using polyimide and Hysol® epoxy to fix guard columns to the inlets and outlets. Sorbents could then be loaded into the preconcentrator. Any different types of sorbents may be used: this system had Carbopack X and Carbopack B loaded equally into the sorbent bed. The sorbent loading port was then sealed with polyimide and Hysol® epoxy. The preconcentrator was baked out at 250 °C for 1 hour under a helium flow of 1 mL/min prior to use.

4.3.2b System setup

The system was assembled using a microfabricated preconcentrator, ionic liquid microcolumn, and miniaturized PID. The microcolumn[52] and PID[53] were made as previously reported, with the only difference being the column length being increased to 10 m. Fluidic connections were made using universal press-tight connectors and deactivated fused silica capillaries between the components. The components were placed into a 3D printed box that was electromagnetically shielded in order to reduce the noise. Analytes were sampled into the preconcentrator and injected by rapid heating into the microcolumn. The column was heated on-chip for temperature programmed separations. The column carrier flow was provided by a miniature pump and was 2.1 mL/min at room temperature (~19 °C). All heating, pumping, and valve switching was controlled via in-house developed LabVIEW software. The only required user input was setting relevant temperature programming parameters and initiating the program; once started, the µGC-PID system could sample and run autonomously. A fluidic diagram is provided in **Figure 4.7**, and a picture of the system is provided in **Figure 4.8**. The entire system is self-contained within a box of dimensions 17 cm x 9 cm x 7 cm (~1.1 L) and weighs a total of 0.9 kg (excluding a laptop for readout). The system is capable of running on a pack of 8 batteries to generate the necessary voltage and power, which are included in the size and weight.

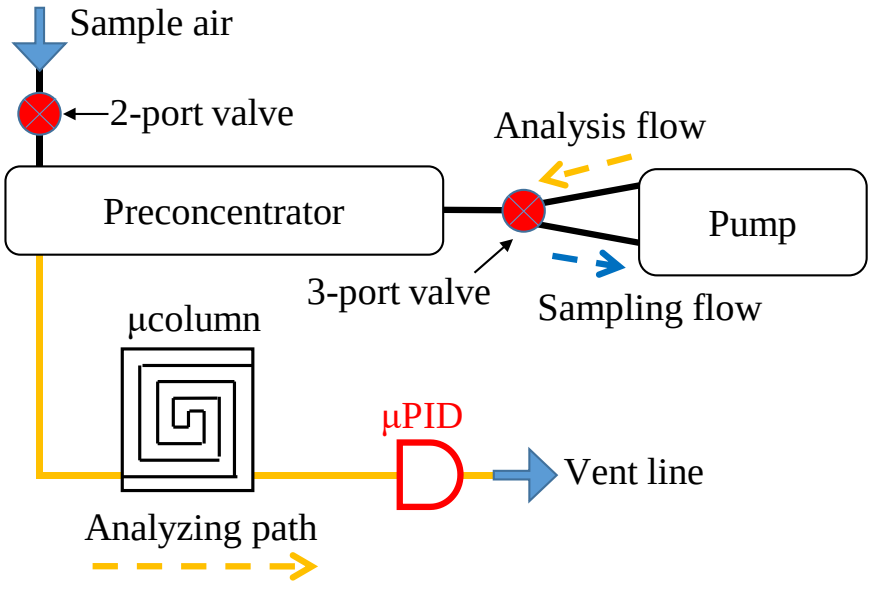

Figure 4.7. Ultracompact 1D µGC system fluidic diagram. The system is entirely self-contained excluding the computer at signal output. A picture of the system is provided in **Figure 4.8**.

4.3.3 System characterization

4.3.3a Separation of alkanes

This benchmark presents analysis of standard C_6 to C_{13} alkanes. Analytes were sampled using the preconcentrator at a sampling rate of 6 mL/min. Each analyte's concentration was 1 µg/L, and the sampling time was 5 seconds, giving an injection amount of ~500 pg of each of the alkanes. The resulting chromatogram is provided in **Figure 4.9** along with the approximate ramping rate. Retention times are provided in **Table 4.2**. The average noise is 2.6 mV. Using this, detection limits for each of the alkanes were calculated, which are also provided in **Table 4.2**. These results show that the detection limit of the system can be as low as 2 pg. While the noise is relatively high compared to previous results[54], this can be the result of the closer proximity of the PID to the other components, as well a lack of electronic shielding and mechanical vibrations from the pump carrier gas. Better component shielding and vibration padding would allow for reduction of the system noise and thus improvement of the detection limit for future systems.

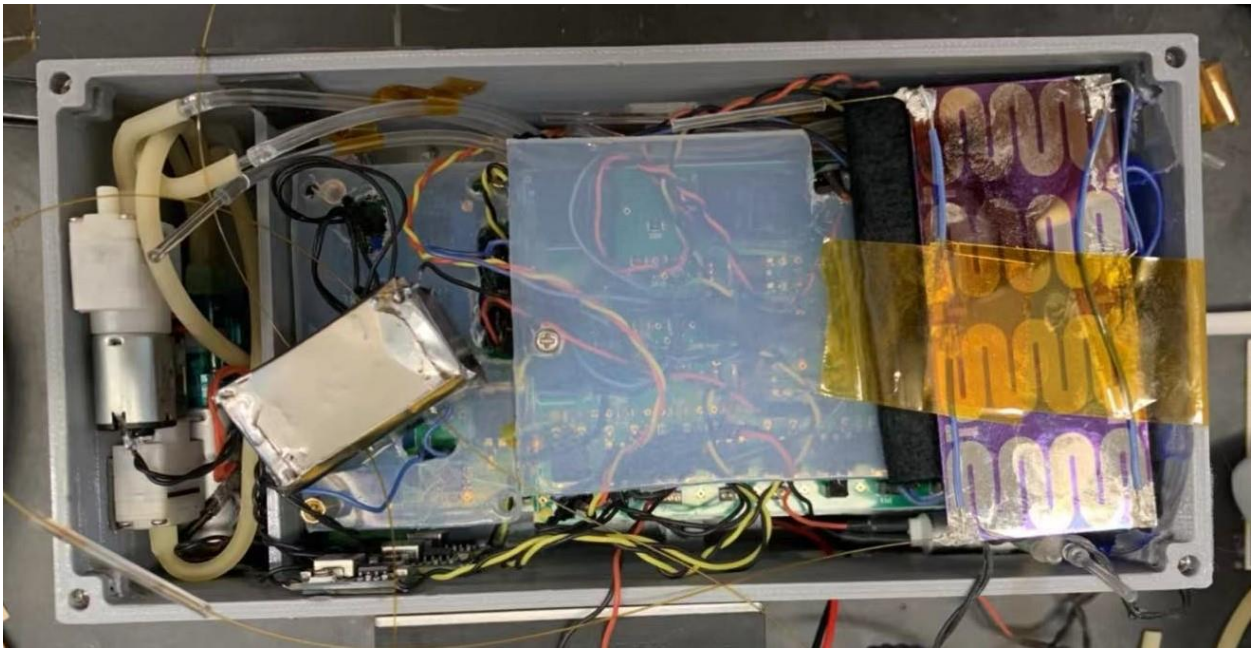

Figure 4.8. Photograph of the ultracompact system with components labeled. The system has dimensions 17 cm x 9 cm x 7 cm (~1.1 L) and weighs a total of 0.9 kg (excluding a laptop for readout).

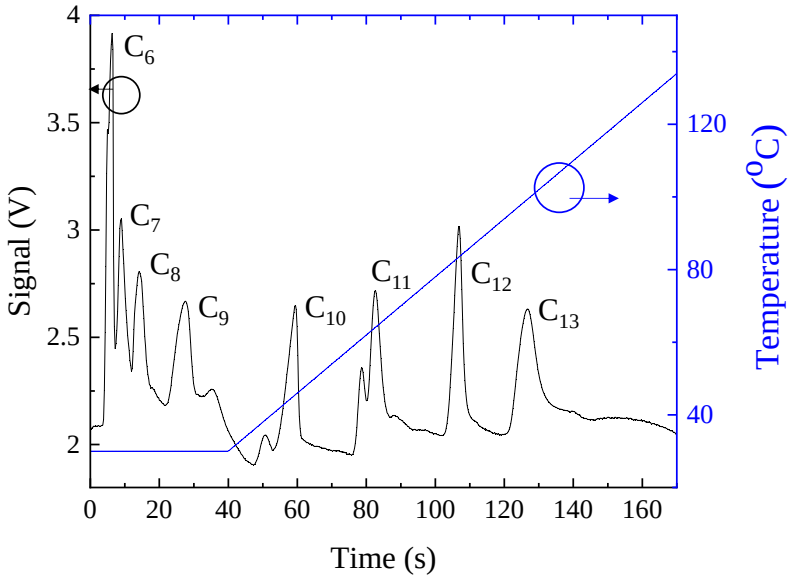

Figure 4.9. C_6 to C_{13} alkane separation with approximate temperature ramping profile. Each alkane was injected with a mass of ~500 pg. Retention times and limits of detection are provided in **Table 4.2**.

	RT (s)	DL (pg)
(1) Hexane	6.3	2
(2) Heptane	8.9	5
(3) Octane	14.1	5
(4) Nonane	27.4	6
(5) Decane	59.3	6
(6) Undecane	82.4	6
(7) Dodecane	106.6	4
(8) Tridecane	126.6	6

Table 4.2. Retention times (RTs) and detection limits (DLs) of C_6 to C_{13} alkanes. The detection limit was as low as 2 pg.

4.3.3b Separation of BTEX

This benchmark presents analysis of standard benzene, toluene, ethylbenzene, and o-xylene (BTEX). Analytes were sampled using the preconcentrator at a sampling rate of 6 mL/min. Each analyte's concentration was again 1 µg/L, and the sampling time was 5 seconds, giving an injection amount of ~500 pg of each analyte. The resulting chromatogram is provided in **Figure 4.10** along with the approximate ramping rate. Retention times and detection limits are provided in **Table 4.3**.

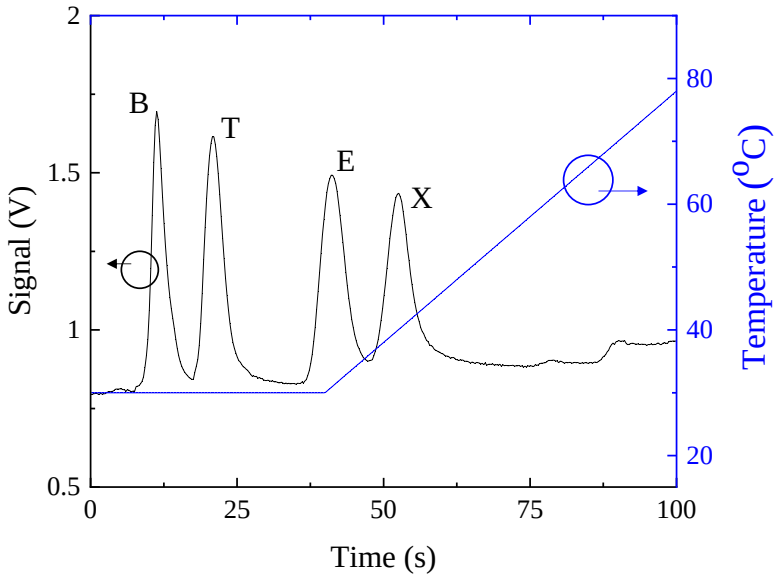

Figure 4.10. BTEX separation with approximate temperature ramping profile. Each compound was injected with a mass of ~500 pg. Retention times and limits of detection are provided in **Table 4.3**.

	RT (s)	DL (pg)
(1) Benzene	46.0	4
(2) Toluene	84.6	4
(3) Ethylbenzene	165.1	5
(4) o-Xylene	211.0	5

Table 4.3. Retention times (RTs) and detection limits (DLs) of BTEX.

4.3.4 Summary and next steps

An ultracompact 1D µGC system with a size of 17 cm x 9 cm x 7 cm (~1.1 L) and weight of 0.9 kg was assembled. The entire system could be run autonomously (excluding computer for readout) and operated handheld using batteries. The system was made using microfabricated GC components, including preconcentrator, ionic liquid column, and PID. The system was tested on a mix of C_6 to C_{13} alkanes and BTEX, with separation of all of the above compounds along with detection limits as low as 2 pg all while operated on battery power.

Since the system is already fully functional, the next steps are to test the device with additional laboratory standard samples to demonstrate the capability for system-level trapping and separation. Subsequently, *in situ* experiments with real chemical samples can be performed, such as on environmental samples like industrial or construction zone air. The system robustness and battery lifetime under different conditions can also be tested to determine how the device performance may change in the field compared to in the laboratory. These would demonstrate the practical applicability of ultracompact µGC devices to highly mobile in field testing. Future improvements may target increasing the device sensitivity by reducing the system noise with better component shielding, including electronic shielding and mechanical vibration padding. Additionally, future systems may be miniaturized even further using integrated µGC components, which would reduce the number of interconnections needed.

4.4 Conclusion

This chapter has presented two preliminary portable µGC systems capable of *in situ* analysis. A portable system utilizing a miniaturized µHDPID and Shincarbon ST molecular sieve column demonstrated separation and detection of hydrogen and methane with a sampling loop used as an injector. Preliminary data showed on column heating and autonomous operation without human intervention and without benchtop components inside a ~5 L system. An additional one channel µGC using a DB-1ms column was replicated as in previous work to allow for regular breath analysis using a regular microfluidic PID. The next steps for this project were proposed, targeting combining both systems into a two channel µGC system for “complete” simultaneous analysis of hydrogen and methane along with normal breath biomarkers. The main component to test will be a filter to prevent compounds heavier than ethane entering the Shincarbon ST

column. Subsequently, testing on real human breath both in the lab and *in situ* can be performed to demonstrate the system's portable breath analysis capabilities.

A second ultracompact 1D µGC was assembled using a microfabricated preconcentrator, ionic liquid column, and PID. The system had a size of 17 cm x 9 cm x 7 cm (~1.1 L) and weight of 0.9 kg and could be run autonomously using batteries. The system was tested on a mix of C_6 to C_{13} alkanes and BTEX, with separation of all of the above compounds along with detection limits as low as 2 pg all while operated on battery power. The next steps are to test the system on additional laboratory standard samples along with *in situ* experiments with real chemical samples. The system robustness and battery lifetime under different conditions will also be tested to determine how the device performance may change in the field compared to in the laboratory. These would demonstrate the practical applicability of ultracompact µGC devices to highly mobile in field testing. Additional shielding between components to reduce electronic interference and mechanical vibrations would also allow for reduction of the noise level and improvement of the detection limit and overall system performance.

4.5 Experimental materials

All benchmark reagents were purchased from Sigma-Aldrich (St. Louis, MO), Cal Gas Direct (Huntington Beach, CA), and Restek (Bellefonte, PA). Benchmark reagents: analytical standard grade hexane, heptane, octane, nonane, decane, undecane, dodecane, tridecane, benzene, toluene, ethylbenzene, o-xylene (Sigma Aldrich). Hydrogen, methane (Cal Gas Direct).

Hysol® 1C™ Epoxy (Ellsworth Adhesive; Germantown, WI). Polyimide sealing resin (P/N 23817) (Sigma-Aldrich). Deactivated fused silica tubing (P/N 10010) with 250 µm inner diameter (Restek). Shincarbon ST molecular sieve 5A column (P/N 19808) (Restek). DB-1MS column (P/N 122-0162, cut to 10 m in length with 250 µm inner diameter and 0.25 µm film thickness) (Agilent; Santa Clara, CA). N-type silicon wafers (P/N 1095, 100 mm diameter, 500 µm thickness) and Borofloat 33 glass (P/N 517) (University Wafer). All materials were used as purchased without further purification or modification.

4.6 References

(1) Gallego, E.; Roca, F. J.; Perales, J. F.; Sanchez, G.; Esplugas, P. Characterization and determination of the odorous charge in the indoor air of a waste treatment facility through

the evaluation of volatile organic compounds (VOCs) using TD-GC/MS. *Waste Manag* **2012**, *32*, 2469-2481.

(2) Wang, J.; Bryant-Genevier, J.; Nuñovero, N.; Zhang, C.; Kraay, B.; Zhan, C.; Scholten, K.; Nidetz, R.; Buggaveeti, S.; Zellers, E. T. Compact prototype microfabricated gas chromatographic analyzer for autonomous determinations of VOC mixtures at typical workplace concentrations. *Microsystems & Nanoengineering* **2018**, *4*, 17101.

(3) Skog, K. M.; Xiong, F.; Kawashima, H.; Doyle, E.; Soto, R.; Gentner, D. R. Compact, Automated, Inexpensive, and Field-Deployable Vacuum-Outlet Gas Chromatograph for Trace-Concentration Gas-Phase Organic Compounds. *Anal Chem* **2019**, *91*, 1318-1327.

(4) Pirsa, S. Design of a portable gas chromatography with a conducting polymer nanocomposite detector device and a method to analyze a gas mixture. *J Sep Sci* **2017**, *40*, 1724-1730.

(5) Soo, J. C.; Lee, E. G.; LeBouf, R. F.; Kashon, M. L.; Chisholm, W.; Harper, M. Evaluation of a portable gas chromatograph with photoionization detector under variations of VOC concentration, temperature, and relative humidity. *J Occup Environ Hyg* **2018**, *15*, 351-360.

(6) Lee, J.; Zhou, M.; Zhu, H.; Nidetz, R.; Kurabayashi, K.; Fan, X. Fully Automated Portable Comprehensive 2-Dimensional Gas Chromatography Device. *Anal Chem* **2016**, *88*, 10266-10274.

(7) Zhou, M.; Lee, J.; Zhu, H.; Nidetz, R.; Kurabayashi, K.; Fan, X. A fully automated portable gas chromatography system for sensitive and rapid quantification of volatile organic compounds in water. *RSC Advances* **2016**, *6*, 49416-49424.

(8) Qin, Y.; Gianchandani, Y. B. A fully electronic microfabricated gas chromatograph with complementary capacitive detectors for indoor pollutants. *Microsyst Nanoeng* **2016**, *2*, 15049.

(9) Akbar, M.; Shakeel, H.; Agah, M. GC-on-chip: integrated column and photoionization detector. *Lab Chip* **2015**, *15*, 1748-1758.

(10) Yutao, Q.; Gianchandani, Y. B. iGC1: An Integrated Fluidic System for Gas Chromatography Including Knudsen Pump, Preconcentrator, Column, and Detector Microfabricated by a Three-Mask Process. *JMemS* **2014**, *23*, 980-990.

(11) Collin, W. R.; Serrano, G.; Wright, L. K.; Chang, H.; Nunovero, N.; Zellers, E. T. Microfabricated gas chromatograph for rapid, trace-level determinations of gas-phase explosive marker compounds. *Anal Chem* **2014**, *86*, 655-663.

(12) Manginell, R. P.; Bauer, J. M.; Moorman, M. W.; Sanchez, L. J.; Anderson, J. M.; Whiting, J. J.; Porter, D. A.; Copic, D.; Achyuthan, K. E. A monolithically-integrated μGC chemical sensor system. *Sensors (Basel)* **2011**, *11*, 6517-6532.

(13) Lee, J.; Sayler, S. K.; Zhou, M.; Zhu, H.; Richardson, R. J.; Neitzel, Richard L.; Kurabayashi, K.; Fan, X. On-site monitoring of occupational exposure to volatile organic compounds by a portable comprehensive 2-dimensional gas chromatography device. *Analytical Methods* **2018**, *10*, 237-244.

(14) You, D. W.; Seon, Y. S.; Jang, Y.; Bang, J.; Oh, J. S.; Jung, K. W. A portable gas chromatograph for real-time monitoring of aromatic volatile organic compounds in air samples. *J Chromatogr A* **2020**, *1625*, 461267.

(15) Zhu, H. B.; She, J. Y.; Zhou, M. L.; Fan, X. D. Rapid and sensitive detection of formaldehyde using portable 2-dimensional gas chromatography equipped with photoionization detectors. *Sensors Actuators B: Chem* **2019**, *283*, 182-187.

(16) Sharma, R.; Zhou, M.; Hunter, M. D.; Fan, X. Rapid In Situ Analysis of Plant Emission for Disease Diagnosis Using a Portable Gas Chromatography Device. *J Agric Food Chem* **2019**, *67*, 7530-7537.

(17) Garg, A.; Akbar, M.; Vejerano, E.; Narayanan, S.; Nazhandali, L.; Marr, L. C.; Agah, M. Zebra GC: A mini gas chromatography system for trace-level determination of hazardous air pollutants. *Sensors Actuators B: Chem* **2015**, *212*, 145-154.

(18) Zhou, M.; Sharma, R.; Zhu, H.; Li, Z.; Li, J.; Wang, S.; Bisco, E.; Massey, J.; Pennington, A.; Sjoding, M.; Dickson, R. P.; Park, P.; Hyzy, R.; Napolitano, L.; Gillies, C. E.; Ward, K. R.; Fan, X. Rapid breath analysis for acute respiratory distress syndrome diagnostics using a portable two-dimensional gas chromatography device. *Anal Bioanal Chem* **2019**, *411*, 6435-6447.

(19) Peng, C.; Qian, K.; Wang, C. Design and Application of a VOC-Monitoring System Based on a ZigBee Wireless Sensor Network. *IEEE Sens J* **2015**, *15*, 2255-2268.

(20) Bocos-Bintintan, V.; Smolenschi, A.; Ratiu, I. A. Rapid Determination of Indoor Air Contaminants in Shoe Shops Using Photoionization Detectors. *Studia Universitatis Babes-Bolyai Chemia* **2016**, *61*, 203-212.

(21) Haick, H.; Broza, Y. Y.; Mochalski, P.; Ruzsanyi, V.; Amann, A. Assessment, origin, and implementation of breath volatile cancer markers. *Chem Soc Rev* **2014**, *43*, 1423-1449.

(22) Konvalina, G.; Haick, H. Sensors for breath testing: from nanomaterials to comprehensive disease detection. *Acc Chem Res* **2014**, *47*, 66-76.

(23) Roberge, M. T.; Finley, J. W.; Lukaski, H. C.; Borgerding, A. J. Evaluation of the pulsed discharge helium ionization detector for the analysis of hydrogen and methane in breath. *J Chromatogr A* **2004**, *1027*, 19-23.

(24) Erdrich, S.; Tan, E. C. K.; Hawrelak, J. A.; Myers, S. P.; Harnett, J. E. Hydrogen-methane breath testing results influenced by oral hygiene. *Sci Rep* **2021**, *11*, 26.

(25) Gao, F.; Wang, M.; Zhang, X.; Zhang, J.; Xue, Y.; Wan, H.; Wang, P. Simultaneous detection of hydrogen and methane in breath for the diagnosis of small intestinal bacterial overgrowth by fast gas chromatography. *Analytical Methods* **2018**, *10*, 4329-4338.

(26) Isobe, K.; Koba, K.; Ueda, S.; Senoo, K.; Harayama, S.; Suwa, Y. A simple and rapid GC/MS method for the simultaneous determination of gaseous metabolites. *J Microbiol Methods* **2011**, *84*, 46-51.

(27) Li, M. W.-H.; Ghosh, A.; Sharma, R.; Zhu, H.; Fan, X. Integrated microfluidic helium discharge photoionization detectors. *Sensors Actuators B: Chem* **2021**, *332*, 129504.

(28) Akbar, M.; Restaino, M.; Agah, M. Chip-scale gas chromatography: From injection through detection. *Microsyst Nanoeng* **2015**, *1*.

(29) Sun, J.; Xue, N.; Wang, W.; Wang, H.; Liu, C.; Ma, T.; Li, T.; Tan, T. Compact prototype GC-PID system integrated with micro PC and micro GC column. *Journal of Micromechanics and Microengineering* **2019**, *29*, 035008.

(30) Defiant Technologies, I. *FROG-4000TM Chemical Analysis System*2015.

(31) Agah, M.; Lambertus, G. R.; Sacks, R.; Wise, K. High-speed MEMS-based gas chromatography. *JMemS* **2006**, *15*, 1371-1378.

(32) Sun, J.; Guan, F.; Cui, D.; Chen, X.; Zhang, L.; Chen, J. An improved photoionization detector with a micro gas chromatography column for portable rapid gas chromatography system. *Sensors Actuators B: Chem* **2013**, *188*, 513-518.

(33) Lee, J.; Zhou, M.; Zhu, H.; Nidetz, R.; Kurabayashi, K.; Fan, X. In situ calibration of micro-photoionization detectors in a multi-dimensional micro-gas chromatography system. *Analyst* **2016**, *141*, 4100-4107.

(34) Lussac, E.; Barattin, R.; Cardinael, P.; Agasse, V. Review on Micro-Gas Analyzer Systems: Feasibility, Separations and Applications. *Crit Rev Anal Chem* **2016**, *46*, 455-468.

(35) Lara-Lbeas, I.; Rodriguez-Cuevas, A.; Andrikopoulou, C.; Person, V.; Baldas, L.; Colin, S.; Le Calve, S. Sub-ppb Level Detection of BTEX Gaseous Mixtures with a Compact Prototype GC Equipped with a Preconcentration Unit. *Micromachines (Basel)* **2019**, *10*, 187-199.

(36) Bryant-Genevier, J.; Zellers, E. T. Toward a microfabricated preconcentrator-focuser for a wearable micro-scale gas chromatograph. *J Chromatogr A* **2015**, *1422*, 299-309.

(37) Hobbs, P. J.; Misselbrook, T. H.; Pain, B. F. Assessment of Odors from Livestock Wastes by a Photoionization Detector, an Electronic Nose, Olfactometry and Gas-Chromatography Mass-Spectrometry. *JAER* **1995**, *60*, 137-144.

(38) Frink, L. A.; Armstrong, D. W. Determination of Trace Water Content in Petroleum and Petroleum Products. *Anal Chem* **2016**, *88*, 8194-8201.

(39) Lord, H.; Pawliszyn, J. Evolution of solid-phase microextraction technology. *J Chromatogr A* **2000**, *885*, 153-193.

(40) Jia, M. Y.; Koziel, J.; Pawliszyn, J. Fast field sampling/sample preparation and quantification of volatile organic compounds in indoor air by solid-phase microextraction and portable gas chromatography. *Field Anal Chem Technol* **2000**, *4*, 73-84.

(41) Frink, L. A.; Armstrong, D. W. Water Determination in Solid Pharmaceutical Products Utilizing Ionic Liquids and Headspace Gas Chromatography. *J Pharm Sci* **2016**, *105*, 2288-2292.

(42) Pinalli, R.; Pedrini, A.; Dalcanale, E. Environmental Gas Sensing with Cavitands. *Chemistry* **2018**, *24*, 1010-1019.

(43) Pejcic, B.; Eadington, P.; Ross, A. Environmental monitoring of hydrocarbons: a chemical sensor perspective. *Environ Sci Technol* **2007**, *41*, 6333-6342.

(44) Singh, E.; Meyyappan, M.; Nalwa, H. S. Flexible Graphene-Based Wearable Gas and Chemical Sensors. *ACS Appl Mater Interfaces* **2017**, *9*, 34544-34586.

(45) Tang, X.; Bai, Y.; Duong, A.; Smith, M. T.; Li, L.; Zhang, L. Formaldehyde in China: production, consumption, exposure levels, and health effects. *Environ Int* **2009**, *35*, 1210-1224.

(46) Baldwin, E. A.; Bai, J.; Plotto, A.; Dea, S. Electronic noses and tongues: applications for the food and pharmaceutical industries. *Sensors (Basel)* **2011**, *11*, 4744-4766.

(47) Thungon, P. D.; Kakoti, A.; Ngashangva, L.; Goswami, P. Advances in developing rapid, reliable and portable detection systems for alcohol. *Biosens Bioelectron* **2017**, *97*, 83-99.

(48) Weatherly, C. A.; Zhang, Y.; Smuts, J. P.; Fan, H.; Xu, C.; Schug, K. A.; Lang, J. C.; Armstrong, D. W. Analysis of Long-Chain Unsaturated Fatty Acids by Ionic Liquid Gas Chromatography. *J Agric Food Chem* **2016**, *64*, 1422-1432.

(49) Pello-Palma, J.; Gonzalez-Alvarez, J.; Gutierrez-Alvarez, M. D.; Dapena de la Fuente, E.; Mangas-Alonso, J. J.; Mendez-Sanchez, D.; Gotor-Fernandez, V.; Arias-Abrodo, P. Determination of volatile compounds in cider apple juices using a covalently bonded ionic liquid coating as the stationary phase in gas chromatography. *Anal Bioanal Chem* **2017**, *409*, 3033-3041.

(50) Li, Z.; Askim, J. R.; Suslick, K. S. The Optoelectronic Nose: Colorimetric and Fluorometric Sensor Arrays. *Chem Rev* **2019**, *119*, 231-292.

(51) Delmonte, P.; Fardin Kia, A. R.; Kramer, J. K.; Mossoba, M. M.; Sidisky, L.; Rader, J. I. Separation characteristics of fatty acid methyl esters using SLB-IL111, a new ionic liquid coated capillary gas chromatographic column. *J Chromatogr A* **2011**, *1218*, 545-554.

(52) Li, M. W.; Huang, X.; Zhu, H.; Kurabayashi, K.; Fan, X. Microfabricated ionic liquid column for separations in dry air. *J Chromatogr A* **2020**, *1620*, 461002.

(53) Zhu, H.; Nidetz, R.; Zhou, M.; Lee, J.; Buggaveeti, S.; Kurabayashi, K.; Fan, X. Flow-through microfluidic photoionization detectors for rapid and highly sensitive vapor detection. *Lab Chip* **2015**, *15*, 3021-3029.

(54) Wei-Hao Li, M.; Ghosh, A.; Venkatasubramanian, A.; Sharma, R.; Huang, X.; Fan, X. High-Sensitivity Micro-Gas Chromatograph-Photoionization Detector for Trace Vapor Detection. *ACS Sens* **2021**, *6*, 2348-2355.

Chapter 5 Conclusion and Future Work

5.1 Summary

This dissertation has discussed the development of individual micro gas chromatography (μGC) components (*i.e.*, microcolumns and miniaturized photoionization detectors) along with assembly into small scale miniaturized portable systems targeted at *in situ* vapor and volatile organic compound (VOC) analysis. A review and comparison of μGC technology to other sensing technologies has been provided, along with background on separation and detection principles. A review of core μGC components was also provided.

Three microcolumn development projects were detailed and aimed to broad the range of compounds suitable for microcolumn analysis, as well as providing a method for improving column separation performance. The development of a porous layer open tubular microcolumn specifically targeted separation of light compounds, such as light hydrocarbons, solvents, and formaldehyde, and additionally demonstrated high moisture resilience. A phosphonium ionic liquid based microcolumn also showed separation of a broad range of compounds including simultaneous separation of polar and nonpolar VOCs. This coating also demonstrated high resilience to oxygen and moisture, which are useful traits for portable systems that potentially encounter harsh ambient conditions and may aim to use air as the carrier gas. Both coatings additionally demonstrated high temperature resilience even up to 350 °C in the case of the ionic liquid column. The development of these coatings expands the range of practical applications that portable μGC systems can target, as well as reduce the number of accessory components required for carrier gas and air filtering if the μIL column is used. Furthermore, a film thickness gradient coating technique was demonstrated to allow for improvement of column performance without increasing the column length or involving extra active components such as for negative temperature gradient separation, both of which are challenging or not practical for portable μGC.

Altogether, these developments are aimed at improving the separation capabilities and performance of microcolumns for miniaturized gas analysis systems.

Two plasma-based photoionization detector (PID) projects aimed to complement the development of microcolumn coatings by increasing the range of compounds for detection by PID, as well as improve the overall sensitivity of these detectors. The development and fabrication of a miniaturized integrated μHDPID system allowed for analysis of permanent gases, light hydrocarbons, and formaldehyde, demonstrating detection limits less than 10 pg for various volatile compounds and less than 20 pg for even high ionization energy permanent gases. High linearity for injections ranging from 50 pg to 10 ng was also observed, along with low warm-up time (within 15 s), and high repeatability between devices due to the microfabricated nature of the HDPID chip. The μHDPID design was shown to offer advantages in ease of fabrication, fabrication yield and robustness, and repeatability. The development of a highly sensitive μPID with sub-pg detection limit and large dynamic range for a wide range of VOCs demonstrated comparable or better detection limit compared to benchtop FID. This device was used to construct a complete automated μGC-PID system (including miniaturized preconcentrator and microfabricated column along with μPID) capable of detecting sub-ppt concentrations of VOCs in a 200 mL sample volume. Standard GC chromatograms were analyzed along with practical complex separations of breath and car exhaust, demonstrating the capability of this μGC-PID system to enable rapid *in situ* trace VOC analysis. Both systems utilized in-house developed plasma excitation and readout circuits, allowing for drastic reduction of the system size, as well as capability of operation with only a 24 V input, thus allowing for increased portability and applicability to μGC systems. These developments improve the overall sensing capabilities of portable GC systems, which also complements the wider range of compound separation demonstrated in the prior microcolumn chapter.

Two preliminary portable μGC systems capable of *in situ* analysis were assembled and preliminary testing was performed. A portable system utilizing a miniaturized μHDPID and Shincarbon ST molecular sieve column demonstrated separation and detection of hydrogen and methane with a sampling loop used as an injector. Preliminary data showed on column heating and autonomous operation without human intervention and without benchtop components. A one channel μGC was replicated as in previous work to allow for regular breath analysis. The next step for this project is to combine both systems into a two channel μGC system for “complete”

simultaneous analysis of hydrogen and methane along with normal breath biomarkers. Subsequently, testing on real human breath both in the lab and *in situ* will demonstrate the system's portable breath analysis capabilities. An ultracompact 1D μGC was assembled with a total size of 17 cm x 9 cm x 7 cm (~1.1 L) and weight of 0.9 kg. The system could be run autonomously using batteries to test mixtures of C_6 to C_{13} alkanes and BTEX, with separation of all of the above compounds along with detection limits as low as 1 pg. Further standard samples along with *in situ* experiments with real chemical samples will be performed to demonstrate system level separation and detection capabilities. The system robustness and battery lifetime under different conditions will also be tested to determine how the device performance may change in the field compared to in the laboratory. These μGC devices aim to demonstrate the assembly of individually improved microcomponents into portable technology capable of real *in situ* measurements.

5.2 Future work

The various component and system-level advancements for μGC detailed within this dissertation allow for the development of future miniaturized portable GC with greatly improved analytical capabilities. The improvements detailed herein introduce several main paths along which future developments may be made:

1. Specialized and selective analysis can be accomplished by coupling highly tunable stationary phase microcolumns to universal detection via μHDPID.
2. Further improvements on sensing performance can be made with additional design and circuit developments.
3. Additional reduction of component and system footprint may allow for increased portability.
4. Introduction of additional GC dimensions and/or channels would improve the analytical capabilities for highly complex samples.

Further projects pertaining to the above are detailed subsequently.

5.2.1 Specialty compound analysis

Some applications require specialized columns for analysis of specific groups of chemicals. These may include separation of toxic volatile sulfur compounds, or chiral compounds, which are useful in forensic chemistry. Tunable PLOT and ionic liquid coatings are powerful tools that can achieve such separations. For example, highly volatile sulfur compounds like H_2S or SO_2 can be analyzed by highly retaining polar PLOT columns (as opposed to the nonpolar divinylbenzene column developed in this dissertation) coupled to μHDPID due to the high ionization potential of some of these compounds. Chiral compound separation is a little trickier and requires a stationary phase with chirality. Chiral ionic liquid columns can provide an avenue for such analysis, given their ability to differentiate between enantiomeric species. These may become especially useful in multidimensional GC, when coupled to a more standard column stationary phase such as polydimethylsiloxane, which allows for a general purpose reference separation as well as simultaneous analysis of the specialized sample.

5.2.2 Ultracompact ultrasensitive portable gas chromatograph

Some goals of state of the art μGC are to both further lower the system level detection limit and overall system footprint to improve the portability. While a preliminary ultracompact system was already presented in this thesis, additional improvements can be made to reduce the overall system size, including integration of microcomponents, and shortening of interconnections. Decreasing the voltage required from the batteries would also reduce the number of batteries needed. This mainly requires lower power for heating the preconcentrator and column, which can be achieved by reducing the preconcentrator thermal mass, and reducing the column heat requirement with relatively small compromises in performance. The latter can be accomplished using a thinner coating with a film thickness gradient. Further improvements of the μPID circuitry and fabrication would aim to improve the detection limit to the femtogram range and involves further circuit optimization, especially use of fixed circuit components (*e.g.*, fixed resistors instead of trimmers), better electrode contacts with the readout silicon electrodes, use of highly doped silicon, and better sensor shielding. These improvements would allow for the assembly of a handheld, ultracompact μGC system with extremely high sensitivity, rivaling even that of some benchtop GC-MS systems.

5.2.3 Multichannel and multidimensional µGC

While a 2D 1x1 µGC was proposed in this thesis for "complete" breath analysis of regular breath biomarkers and hydrogen and methane, additional multidimensional or multichannel µGC devices can be developed for more advanced separation of complex mixtures. For analysis of lighter compound mixtures such as volatile inorganic compounds (VICs) but excluding permanent gases, a 1x1 heartcutting system using a regular OV-1 or OV-5 column along with a µPLOT column as the second dimension coupled to a µHDPID would allow for separation and detection of a very broad range of analytes without the limitations of using a molecular sieve column (*i.e.,* requiring a filter). Another mode of 2D µGC is comprehensive GC, which involves sending all peaks from the first dimension to a short second dimensional column which can simultaneously separate any coeluted peaks. In both cases, a general 2D µGC would ideally use µcolumns with orthogonal separation capabilities, which this thesis has demonstrated the capability for. Columns with similar retentions (*i.e.,* compound ranges for separation) but different elution orders can also be run in parallel as multichannel µGC, which reduces the analysis time compared to multidimensional GC while potentially increasing the burden of data analysis. In all cases, the use of multiple columns for separation of the same sample would be aimed at improving the overall analytical capabilities of a µGC device.

Appendix A Additional µPLOT Moisture Analysis

Separation of methanol, ethanol, and formaldehyde with and without moisture added were analyzed on the µPLOT (**Figure A.1**). Retention times and full widths at half maxima (FWHMs) were analyzed, showing no significant differences in peak width, and only a small decrease in the methanol retention time (0.024 min) with added moisture (**Table A.1**).

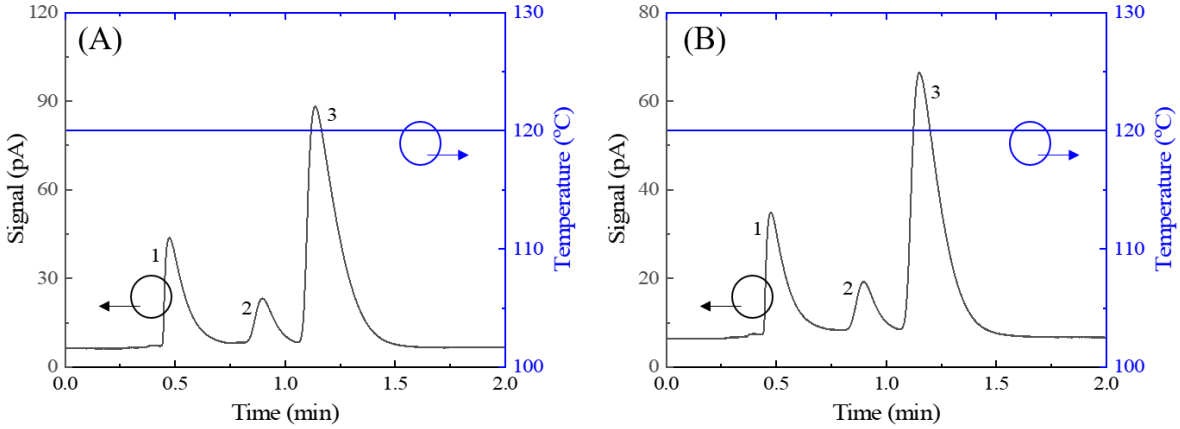

Figure A.1. Separation of methanol[(1)], ethanol[(2)], and formaldehyde[(3)] with no added moisture (A) and with 1 µL of additional liquid water (B). A solution of formaldehyde, methanol, and ethanol was heated to 80 °C and 50 µL of headspace vapor was subsequently drawn for injection. Carrier gas flow rate: 1.3 mL/min at 120 °C. Analysis is provided in **Table A.1**.

Moisture was also analyzed on an OV-5 column for comparison to the µPLOT. For the coating, OV-1 (75% w/w), OV-17 (10% w/w), and Dow SYLGARD™ 184 reagent B (15% w/w, crosslinker) were dissolved in dichloromethane to create a 2% (w/w) coating solution (5% phenyl solute). A 5 m long capillary (250 µm i.d.) was first silanized by 8 injections of HMDS vapor. Subsequently, an 80 µL coating solution was loaded into the capillary from the column inlet and driven out through a 1 m dummy column. After coating, dry air was continuously flowed through the column for 2 hours, followed by crosslinking at 80 °C for another 2 hours

and subsequent deactivation using HMDS. The column was then aged at 230 °C for 3 hours under a helium flow of 0.5 mL/min. Nonane and dodecane were injected into the column with and without moisture (**Figure A.2)**. Peak retention times and FWHMS changed significantly with added moisture (**Table A.2**), demonstrating that the OV-5 does not have the same moisture resilience as compared to the µPLOT.

	Dry	1 µL	p-value
Methanol[(1)] RT	0.477±0.0026	0.453±0.0066	0.0005
Methanol[(1)] FWHM	0.102±0.0011	0.108±0.0099	0.2202
Ethanol[(2)] RT	0.898±0.0019	0.885±0.0127	0.0798
Ethanol[(2)] FWHM	0.080±0.0002	0.083±0.0828	0.1918
Formaldehyde[(3)] RT	1.148±0.0075	1.149±0.0147	0.9119
Formaldehyde[(3)] FWHM	0.145±0.0008	0.148±0.0061	0.4272

Table A.1. p-values between retention times (RTs) and FWHMs of methanol, ethanol, and formaldehyde with no added moisture and 1 µL of added moisture (5 runs each). Significance was taken at p = 0.05. Methanol's retention time was significantly lower with added moisture. All other p-values are over 0.5, showing no significant differences (notably, added moisture did not significantly broaden any peaks).

	Dry	50 µL	p-value
Nonane[(1)] RT	0.563±0.005	0.552±0.004	0.051
Nonane [(1)] FWHM	0.084±0.006	0.095±0.002	0.049
Dodecane[(2)] RT	1.038±0.004	1.032±0.003	0.088
Dodecane[(2)] FWHM	0.113±0.003	0.141±0.004	0.016

Table A.2. p-values between retention times (RTs) and FWHMs of nonane and dodecane with no added moisture and 50 µL of added moisture (5 runs each). Significance was taken at p = 0.05. Both peaks were significantly broadened with added moisture, showing that the OV-5 column does not exhibit the same moisture resistance that the µPLOT does.

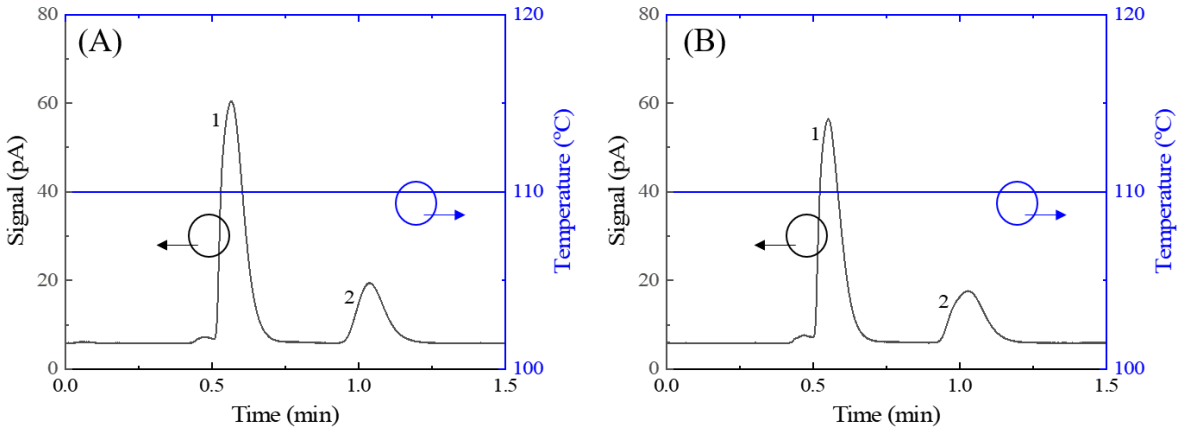

Figure A.2. Separation of nonane[(1)] and dodecane[(2)] using an in-house coated OV-5 column (coating procedure detailed below). An injection of 100 µL of headspace vapor from a mixture of the two analytes was made with no added moisture (A) and with 50 µL of additional water vapor (B). The water was heated to 80 °C in order to increase the partial pressure in the headspace. Carrier gas flow rate: 1.3 mL/min. Analysis is provided in **Table A.2**.

Appendix B FTGC Simulation and Uniform Column Thickness

Derivation of Eq. 2.9

Equation 2.8 was given as

$$k(x,t) = A\exp\left(\frac{\Delta G}{RT(x,t)}\right) \times d_f(x). \quad (2.8)$$

Taking the derivative with respect to x yields

$$\frac{\delta k(x,t)}{\delta x} = A\left[\frac{\delta \exp\left(\frac{\Delta G}{RT(x,t)}\right)}{\delta x} d_f(x) + \exp\left(\frac{\Delta G}{RT(x,t)}\right)\frac{\delta d_f(x)}{\delta x}\right],$$

by applying product rule. Applying chain rule to the first term on the right hand side yields

$$\begin{aligned}\frac{\delta k(x,t)}{\delta x} &= A\left[\delta\frac{\frac{\Delta G}{RT(x,t)}}{\delta x} d_f(x)\exp\left(\frac{\Delta G}{RT(x,t)}\right) + \exp\left(\frac{\Delta G}{RT(x,t)}\right)\frac{\delta d_f(x)}{\delta x}\right] \\ &= A\exp\left(\frac{\Delta G}{RT(x,t)}\right) d_f(x)\left[\delta\frac{\frac{\Delta G}{RT(x,t)}}{\delta x} + \frac{\delta d_f(x)/\delta x}{d_f(x)}\right] \\ &= k(x,t)\left[\delta\frac{\frac{\Delta G}{RT(x,t)}}{\delta x} + \frac{\delta d_f(x)/\delta x}{d_f(x)}\right]\end{aligned}$$

by applying Eq. (6) in the third step. Using the definition of ΔG

$$\frac{\delta k(x,t)/\delta x}{k(x,t)} = \frac{\delta \frac{\Delta H - T(x,t)\Delta S}{RT(x,t)}}{\delta x} + \frac{\delta d_f(x)/\delta x}{d_f(x)} = \frac{\delta \left(\frac{\Delta H}{RT(x,t)} - \frac{\Delta S}{R}\right)}{\delta x} + \frac{\delta d_f(x)/\delta x}{d_f(x)}$$

$$= -\frac{\Delta H}{RT(x,t)} \frac{\delta T(x,t)}{T(x,t)} + \frac{\frac{\delta d_f(x)}{\delta x}}{d_f(x)}, (2.9)$$

with chain rule applied again in the third step to yield Eq. 2.9.

Simulation parameters

The retention factor $k(x,t)$ is dependent on K and β. While β can be directly calculated from column inner diameter and film thickness, K is determined based on analyte interactions with the stationary phase material. The temperature dependent K is approximated by $\ln(K) = Ae^{BT}$, where A and B are constants and T is temperature in °C. This is an exponential fit based on previously reported $\ln(K)$ values[1]. These can be approximated using the values provided in **Table B.1**. Additional auxiliary simulation parameters are provided in

Table B.2 and were chosen to mimic the actual dimensions of the FTGC.

	D_C	A	B
C_8	1.2435e-4	8.637	-0.00616
C_9	1.1600e-4	9.762	-0.00609
C_{10}	1.0901e-4	11.05	-0.00615
C_{11}	1.0305e-4	12.20	-0.00608
C_{12}	9.7890e-05	13.30	-0.00605
C_{13}	9.3374e-05	14.53	-0.00606
C_{14}	8.9380e-05	15.74	-0.00605
C_{15}	8.5814e-05	16.89	-0.00604

Table B.1. Simulation values for C_{10} to C_{15}.

These simulation parameters were used to simulate the FTGC at different temperature ramping conditions. Temperatures were held isothermally at 70 °C (**Table B.3**) and ramped at 20

°C/min (**Table B.5**) and 30 °C/min (**Table B.7**) as well as isothermally at 120 °C (**Table B.9**). Analysis of each condition is provided as well in

Table B.4,

Table B.6,

Table B.8, and **Table B.10**, respectively. Resolutions in forward mode are always higher than in backward mode (or for uniform thickness), demonstrating that focusing is achieved under all conditions (varying temperature ramping rate or starting temperature).

η_0	8.411e-6
T_0	273.15 K
α_n	0.695
σ	1 mm
Δx	1 cm
Δt	0.005 s
p_{in}	124.8 kPa
p_{out}	101.3 kPa
L	5 m

Table B.2. Auxiliary simulation values.

	RT_{fwd}	$FWHM_{fwd}$	RT_{bkwd}	$FWHM_{bkwd}$	RT_{uni}	$FWHM_{uni}$
C_8	0.319	0.0385	0.303	0.0507	0.311	0.0441
C_9	0.462	0.0498	0.427	0.0763	0.445	0.0617
C_{10}	0.797	0.0766	0.718	0.1368	0.758	0.1030
C_{11}	1.518	0.1322	1.344	0.2666	1.431	0.1908
C_{12}	2.961	0.2370	2.597	0.5238	2.780	0.3628
C_{13}	6.349	0.4698	5.534	1.1228	5.942	0.7599
C_{14}	13.888	0.9553	12.067	2.4436	12.974	1.6268
C_{15}	29.522	1.5017	25.603	5.1577	27.544	3.3899

Table B.3. Simulated retention times (RTs) and FWHMs for isothermal separation of C_8 to C_{15} alkanes at 70 °C with a head pressure of 3.45 psi (forward, uniform, and backward modes). Column length was 5 m. All values are provided in minutes. Analysis is provided in **Table B.4**.

	R_{fwd}	R_{bkwd}	R_{uni}
C_8/C_9	1.910	1.154	1.491
C_9/C_{10}	3.127	1.610	2.243
C_{10}/C_{11}	4.076	1.832	2.707
C_{11}/C_{12}	4.615	1.870	2.874
C_{12}/C_{13}	5.656	2.105	3.323
C_{13}/C_{14}	6.243	2.162	3.477
C_{14}/C_{15}	7.509	2.101	3.427
PC	33.136	12.834	19.542

Table B.4. Simulated resolutions (R) and peak capacities (PC) between adjacent peaks for C_8 to C_{15} in forward and backward modes for isothermal separation. Forward mode resolutions are all larger than backward mode resolutions (and uniform resolutions).

	RT_{fwd}	$FWHM_{fwd}$	RT_{bkwd}	$FWHM_{bkwd}$	RT_{uni}	$FWHM_{uni}$
C_8	0.307	0.0364	0.005	0.0483	0.301	0.0419
C_9	0.422	0.0432	0.006	0.0669	0.412	0.0538
C_{10}	0.648	0.0551	0.007	0.0996	0.630	0.0744
C_{11}	1.010	0.0700	0.006	0.1407	0.982	0.0999
C_{12}	1.471	0.0831	0.004	0.1766	1.436	0.1218
C_{13}	2.052	0.0943	0.003	0.2037	2.012	0.1386
C_{14}	2.667	0.1027	0.000	0.2198	2.625	0.1493
C_{15}	3.248	0.1086	0.008	0.2286	3.206	0.1558

Table B.5. Simulated retention times (RTs) and FWHMs for separation of C_8 to C_{15} alkanes. Temperature was ramped at 20 °C/min from 70 °C (no hold) with a head pressure of 3.45 psi (forward, uniform, and backward modes). Column length was 5 m. All values are provided in minutes. Analysis is provided in

Table B.6.

	R_{fwd}	R_{bkwd}	R_{uni}
C_8/C_9	1.706	1.075	1.357
C_9/C_{10}	2.718	1.488	2.010
C_{10}/C_{11}	3.413	1.681	2.385
C_{11}/C_{12}	3.553	1.656	2.415
C_{12}/C_{13}	3.861	1.770	2.610
C_{13}/C_{14}	3.685	1.700	2.513
C_{14}/C_{15}	3.246	1.525	2.245
PC	22.182	10.895	15.535

Table B.6. Simulated resolutions (R) and peak capacities (PC) between adjacent peaks for C_8 to C_{15} in forward and backward modes for temperature ramped separation. Forward mode resolutions are all larger than backward mode resolutions (and uniform resolutions).

	RT_{fwd}	$FWHM_{fwd}$	RT_{bkwd}	$FWHM_{bkwd}$	RT_{uni}	$FWHM_{uni}$
C_8	0.302	0.0357	0.293	0.0473	0.297	0.0410
C_9	0.407	0.0410	0.390	0.0636	0.399	0.0512
C_{10}	0.602	0.0497	0.575	0.0893	0.589	0.0670
C_{11}	0.893	0.0596	0.856	0.1180	0.875	0.0843
C_{12}	1.240	0.0676	1.196	0.1401	1.219	0.0978
C_{13}	1.653	0.0744	1.606	0.1553	1.631	0.1073
C_{14}	2.078	0.0798	2.029	0.1644	2.055	0.1137
C_{15}	2.472	0.0836	2.424	0.1695	2.450	0.1177

Table B.7. Simulated retention times (RTs) and FWHMs for separation of C_8 to C_{15} alkanes. Temperature was ramped at 30 °C/min from 70 °C (no hold) with a head pressure of 3.45 psi (forward, uniform, and backward modes). Column length was 5 m. All values are provided in minutes. Analysis is provided in

Table B.8.

	R_{fwd}	R_{bkwd}	R_{uni}
C_8/C_9	1.614	1.038	1.296
C_9/C_{10}	2.538	1.426	1.899
C_{10}/C_{11}	3.146	1.598	2.233
C_{11}/C_{12}	3.216	1.554	2.226
C_{12}/C_{13}	3.435	1.638	2.371
C_{13}/C_{14}	3.250	1.563	2.265
C_{14}/C_{15}	2.851	1.395	2.014
PC	20.050	10.212	14.304

Table B.8. Simulated resolutions (R) and peak capacities (PC) between adjacent peaks for C_8 to C_{15} in forward and backward modes for temperature ramped separation. Forward mode resolutions are all larger than backward mode resolutions (and uniform resolutions).

	RT_{fwd}	$FWHM_{fwd}$	RT_{bkwd}	$FWHM_{bkwd}$	RT_{uni}	$FWHM_{uni}$
C_8	0.244	0.0390	0.240	0.0415	0.242	0.0403
C_9	0.268	0.0404	0.261	0.0451	0.265	0.0426
C_{10}	0.312	0.0440	0.299	0.0525	0.306	0.0478
C_{11}	0.393	0.0516	0.370	0.0673	0.381	0.0585
C_{12}	0.526	0.0643	0.485	0.0921	0.506	0.0762
C_{13}	0.775	0.0886	0.702	0.1390	0.739	0.1095
C_{14}	1.231	0.1323	1.098	0.2246	1.166	0.1699
C_{15}	2.006	0.2043	1.772	0.3692	1.891	0.2712

Table B.9. Simulated retention times (RTs) and FWHMs for isothermal separation of C_8 to C_{15} alkanes at 120 °C with a head pressure of 3.45 psi (forward, uniform, and backward modes). Column length was 5 m. All values are provided in minutes. Analysis is provided in **Table B.10**.

	R_{fwd}	R_{bkwd}	R_{uni}
C_8/C_9	0.360	0.287	0.323
C_9/C_{10}	0.609	0.458	0.533
C_{10}/C_{11}	1.000	0.694	0.842
C_{11}/C_{12}	1.352	0.855	1.089
C_{12}/C_{13}	1.923	1.108	1.483
C_{13}/C_{14}	2.435	1.286	1.801
C_{14}/C_{15}	2.718	1.340	1.941
PC	10.397	6.028	8.012

Table B.10. Simulated resolutions (R) and peak capacities (PC) between adjacent peaks for C_8 to C_{15} in forward and backward modes for isothermal separation. Forward mode resolutions are all larger than backward mode resolutions (and uniform resolutions).

Uniform column film thickness

The uniform column was frozen with liquid nitrogen and cut open to examine the thickness. The average thickness at the inlet was measured to be 130.6 nm and the outlet thickness was 130.8 nm, demonstrating a mostly uniform thickness over the column's length.

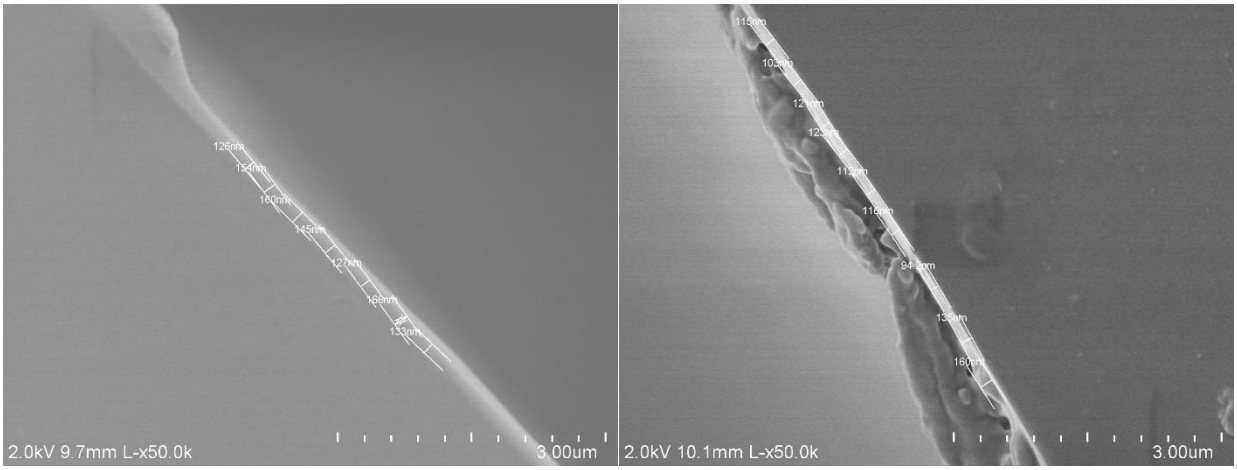

Figure B.1. SEM image of film thickness at column inlet. The average film thickness was 130.6 nm.

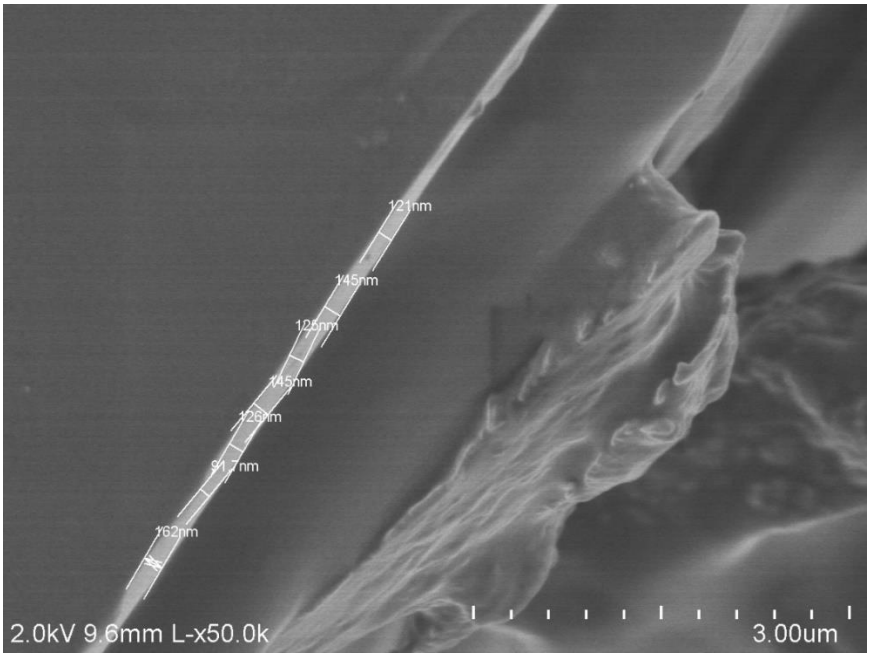

Figure B.2. SEM image of film thickness at column outlet. The average film thickness was 130.8 nm.

References

(1) Contreras, J. A.; Rockwood, A. L.; Tolley, H. D.; Lee, M. L. Peak sweeping and gating using thermal gradient gas chromatography. *J Chromatogr A* **2013**, *1278*, 160-165.

Appendix C μHDPID Sample Injections

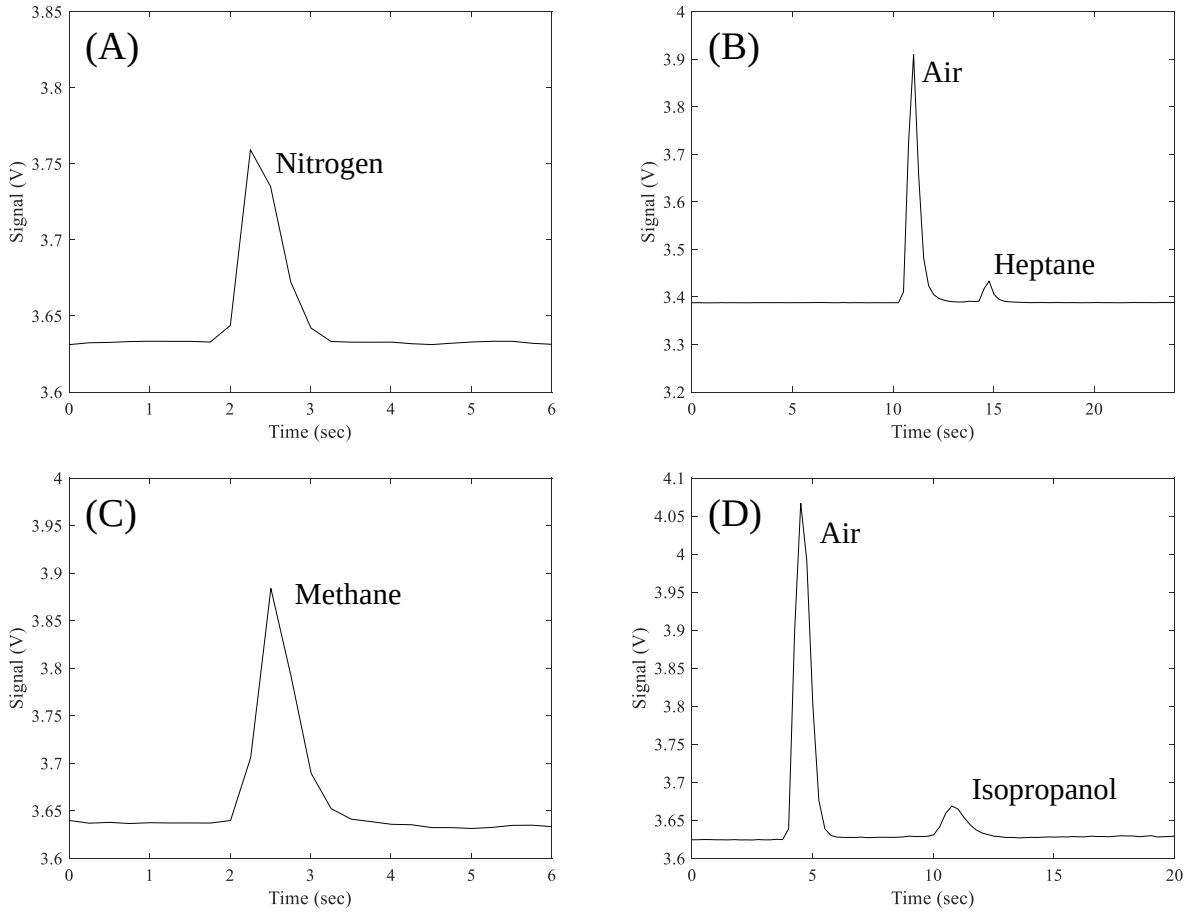

Figure C.1. μHDPID pulse response to (A) 3.5 ng injection of pure nitrogen, (B) 405 pg of heptane, (C) 3 ng of pure methane, and (D) 465 pg of isopropanol. The separation temperature was set to 30 °C for (A), (C), and (D), and 50 °C for (B). The carrier gas flow rate was 4.8 mL/min for (A) and (C), 1.5 mL/min for (B), and 1 mL/min for (D).

Appendix D µPID Fabrication Procedure

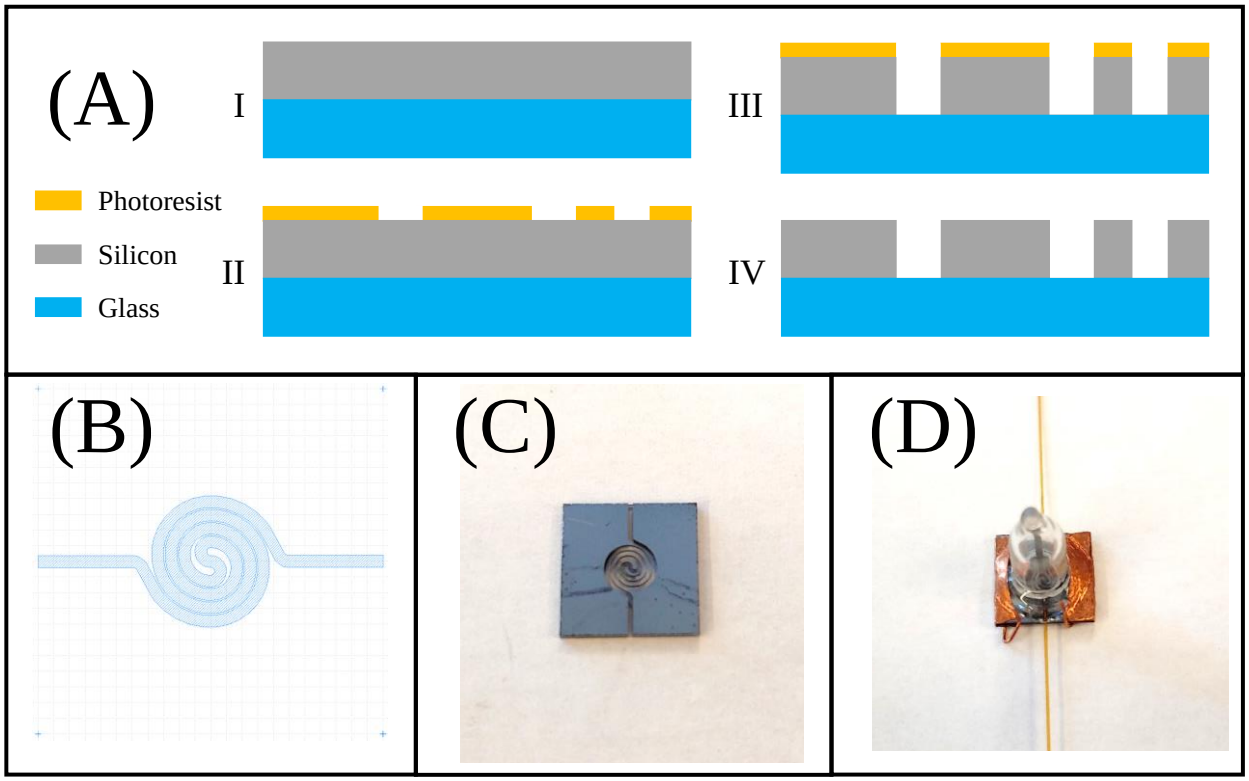

Figure D.1. (A) µPID fabrication processes. I. Anodic bonding with Pyrex glass to Si wafer. II. Soft mask of photoresist exposing PID channels. III. DRIE on the entire pattern area to etch the silicon completely through across the entire channel area. IV. Stripping of photoresist to produce final chip. (B) Single µPID pattern. (C) Photograph of µPID chip. The final channel width and depth were both 400 mm. (D) Photograph of µPID with lamp mounted.